Characterisation and Prediction of State of Health of Rechargeable Batteries

A thesis submitted in fulfilment
of the requirements for the degree of

Doctor of Philosophy

in Electronics
University of Waikato
by

Christopher John Dunn

THE UNIVERSITY OF
WAIKATO
Te Whare Wānanga o Waikato

2024

Acknowledgements

The author thanks Professor Jonathan Scott, Dr Marcus Wilson, Associate Professor Michael Cree and Associate Professor Michael Mucalo for their advice, guidance and support throughout the various stages of this research.

Thanks are also due to the University of Waikato for the award of a Doctoral Scholarship, without which this work would not have been possible, and to Dr Anna Henning and colleagues at Waikatolink for assistance with equipment. The author also thanks Professor Karin Bryan and colleagues at the School of Graduate Research for advice and support, and Vance Farrow, Levinia Paku, Mary Dalbeth and Natalie Shaw at the School of Engineering for their friendship and help with matters too numerous to list. Thanks also to Dr Lee Streeter for his invaluable teaching of signal theory.

I am also deeply grateful to my wife Martina for her encouragement and support along this journey.

Abstract

Electrochemical impedance spectroscopy (EIS) is used extensively in battery research, but usually at frequencies that do not reflect real-world usage patterns. This has resulted in equivalent circuit models (ECMs) that are over-complicated, and suboptimal battery management systems. It is logical to measure batteries at frequencies reflecting their daily or weekly charge-discharge cycles, i.e., of the order of microhertz. This is generally not done, however, because of difficulties that include extreme measurement durations and the need for care to avoid issues such as charge distribution problems, charge drift, and the risk of overcharging or flattening the battery. This research demonstrates the feasibility of extra-low frequency (ELF) EIS measurement using standard, non-specialised measurement equipment, and the optimisation of frequency domain data through the superimposition of small-signal measurement tones on larger square wave currents.

Study of charge movement rates in the frequency domain and voltage responses in the time domain in batteries indicates connections between voltage sweep rate in cyclic voltammetry (CV) and current magnitude in incremental capacity analysis (ICA). The key factor determining what the investigator sees, e.g., reversibility of electrode processes or evidence of individual electrochemical reactions, is rate of movement of charge. Thus, controlled current can be used to obtain CV-type data from a battery, something that would be hazardous if done conventionally using a voltage ramp.

Repeatable, low-error EIS measurements at ELFs are essential for inferring battery ECM components, including constant phase elements (CPEs). The fractional order of a CPE is linked to battery state of health (SoH) and energy efficiency. This thesis shows that efficiency measurements with waveforms representative of real battery usage can be used to track battery SoH accurately.

Contents

Glossary

Abbreviations

CC-CV, constant current-constant voltage
CPE, constant phase element
CV, cyclic voltammetry
DFT, discrete Fourier transform
DVA, differential voltage analysis
ECM, equivalent circuit model
EIS, electrochemical impedance spectroscopy
ELF, extra-low frequency
EV, electric vehicle
ICA, incremental capacity analysis
OCV, open-circuit voltage
SEI, solid electrolyte interface
SoC, state of charge
SoH, state of health

Battery Types

AGM, absorbent glass mat lead-acid battery
ICR, lithium cobalt oxide (also known as LCO or Li-cobalt): $LiCoO_2$
INR, lithium nickel manganese cobalt oxide (NMC, NCM): $LiNiMnCoO_2$
LTO, lithium titanate: Li_2TiO_3
NCA, lithium nickel cobalt aluminium oxides (NCR, Li-aluminium): $LiNiCoAlO_2$

See `https://batteryuniversity.com/article/bu-205-types-of-lithium-ion`

List of Figures

List of Tables

Chapter 1

Introduction

1.1 Rechargeable Batteries and State of Health

Rechargeable battery systems have become the most important means of delivering readily convertible chemical energy to, for example, electric vehicles (EVs) [1]. They are also used in critical systems where reliable and predictable supply are crucial [2]. Despite advances that have led to improvements in battery capacity and power density, however, universally accepted methods for reliable and consistent characterisation of battery state of health (SoH) remain elusive [3]. A rechargeable battery is a nonlinear and time-variable system with internal electrochemical processes that cannot be directly observed. Parameters are subject to interference from the battery's environment and mode of usage, and lack of clarity pertaining to battery characteristics and performance has major implications for battery management [3].

What do we mean by SoH? Battery SoH reflects general condition, and the ability of the battery to deliver its specified performance when compared with a new unit. During the lifetime of a battery, its performance deteriorates due to age- and usage-related changes. Eventually, the battery will reach the end of its life and will have to be retired and if necessary replaced. SoH gives us information about the condition of the battery and the point it is likely to have reached in its life cycle, factors of paramount importance to an EV owner or prospective purchaser, or laptop computer users who needs to know that the batteries in their machines will not require replacement shortly after purchase. Note here that SoH needs to be contrasted with state of charge (SoC), which describes the battery's short-term capabilities, and which can be described by measuring actual charge [4].

There is no official definition of SoH, and no universally agreed set of rules for its measurement [4]. A number of of approaches are currently used, although none appears wholly satisfactory. They include measurements of either cell impedance or conductance, or measurement of several parameters that might be lumped together and assigned a score, for example capacity, internal resistance, self-discharge, charge

acceptance, discharge capabilities, mobility of electrolyte, or cycle counting [4]. Results may depend on cell chemistry. Weighting of individual factors may be based on experience, cell chemistry and battery application.

The uncertainty and lack of agreement across the research community and industry pertaining to battery characterisation and SoH prediction is problematic for manufacturers and consumers alike, and has been a barrier to uptake of new technologies, notably EVs. Moreover, premature retirement of batteries in critical settings such as data centres because of uncertainty over service life is costly and wasteful. The research presented here represents part of a wider and ongoing effort by the Battery Modelling Group at the University of Waikato to contribute to the overcoming of these problems.

1.2 Statement of Originality

The author declares that this thesis is his original work. Assistance with equipment, software and measurement algorithms, etc., is acknowledged where appropriate.

1.3 Thesis Outline

This thesis consists of six main chapters, including this introduction and an overall discussion and conclusion with recommendations for future work. The second chapter overviews the current battery measurement landscape with a particular focus on the limitations of methods commonly used by researchers to characterise rechargeable batteries. There follows a discussion of battery impedance, its relationship to SoH, its measurement using electrochemical impedance spectroscopy (EIS), and the use of EIS in battery equivalent circuit modelling. The concept of and reasons for measurement of batteries at extra-low frequencies (ELFs) are also introduced.

The original research component of this thesis is in three parts, described in the third, fourth and fifth chapters. The first part takes place in the frequency domain and deals with the development of methods to overcome difficulties in obtaining reliable and repeatable EIS of rechargeable batteries at ELFs. It concludes that such measurements are best made under working conditions in the presence of charge movement at rates of the order we would expect to see when using the battery. It also confirms the need to use constant phase elements (CPEs) in battery equivalent circuit models (ECMs).

The second part moves to the time domain, and extends observations relating to rate of movement of charge when cycling batteries to those made by electrochemists when performing cyclic voltammetry (CV) and incremental capacity analysis (ICA), demonstrates relationships between the two methods that are not widely appreciated, and provides insight into how they relate to EIS at ELFs. A method is also

described for performing analysis analogous to CV on an intact battery by using an incremental capacity approach. CV analysis of a battery (as opposed to an electrochemical reaction system in a laboratory) would normally be inadvisable at best and extremely hazardous at worst because of the risk of uncontrolled currents being drawn by a battery subjected to a linear voltage ramp. Ultimately, the research demonstrates that, although CV and ICA are usually treated in the literature as two completely different methods, they are in fact more closely related than is generally realised, with the key underlying consideration being rate of charge movement.

The third part was prompted by the above observations in the frequency and time domains which underlined the significance of the CPE in a battery ECM, and by the need to explore how this relates to SoH. There appears to be an association between battery SoH and energy efficiency, i.e., the difference between energy (power integrated over time) put into the battery when charging and the energy released when the battery is called upon to deliver that charge, with energy efficiency decreasing as the battery wears out. This was investigated, together with relationships between energy efficiency and parameters used to characterise batteries and build ECMs.

The final chapter brings together overall observations from the three experimental chapters, discusses their implications for the ways in which we measure battery SoH, and suggests future directions on the basis of questions that remain unanswered.

1.4 Research Papers

The above three research topics are presented as three papers. At the time of presentation of this thesis, the first has been fully published, the second has been submitted for publication, and the third is in the form of a draft. This was originally intended for eventual submission following the availability of more data and further development, but has since been used instead to provide material for additional publications (the first of which is presented in Appendix C).

The three papers are:

- C. Dunn and J. Scott, "Achieving Reliable and Repeatable Electrochemical Impedance Spectroscopy of Rechargeable Batteries at Extra-Low Frequencies," IEEE Trans. Instrum. Meas., vol. 71, pp. 1–8, 2022. [Online]. Available: https://ieeexplore.ieee.org/document/9789195/

- C. Dunn, J. Scott, M. Wilson, M. Mucalo, and M. Cree, "Incremental Capacity and Voltammetry of Batteries, and Implications for Electrochemical Impedance Spectroscopy," submitted for publication.

- C. Dunn, J. Scott, M. Wilson, and V. Farrow, "New Theory and Efficient

Algorithm for Tracking Lithium Battery State of Health," Univ. Waikato, Hamilton, New Zealand, Oct. 2023.

Work presented in this thesis has been used in the development of three further publications (see Appendices):

- E. Poihipi, J. Scott, and C. Dunn, "Distinguishability of Battery Equivalent-Circuit Models Containing CPEs: Updating the Work of Berthier, Diard, & Michel," J. Electroanal. Chem., vol. 911, p. 116201, Apr. 2022. [Online]. Available: https://linkinghub.elsevier.com/retrieve/pii/S157266572200193X
- M. T. Wilson, C. Dunn, V. Farrow, M. Mucalo, and J. B. Scott, "Measuring Electrical Properties of Batteries at Ultra-long Timescales," NCSL Int. Meas., vol. 15, pp. 12–16, 2023.
- M. T. Wilson, C. J. Dunn, V. Farrow, M. J. Cree, and J. B. Scott, "Efficiency of Cycled Batteries Analyzed Through Voltage-Current Phase Differences," IEEE Access, vol. 12, pp. 36202–36211, 2024.

1.5 Code Repository

Programs and scripts key to the generation of data used in this work are held in a publicly accessible repository at https://github.com/CDunnNZ/Batteries

Some of these programs show user instructions when called in the command line without specifying any parameters or input files. These are shown below where relevant.

Programs include:

- bcp66.c

  Cycles batteries using a constant current-constant voltage (CC-CV) protocol on an HP/Agilent/Keysight 66332A two-quadrant source measurement unit. Reports time, voltage and current for plotting and further analysis.

```
bcp66 V1.08 jbs&cjd Nov 2020, June 2021, Sep 2021
Battery Cycler via Prologix gpib to HP/Agilent 66332A.
0 parameters is illegal.
Usage: bcp66 USB Vmax Vmin Ich Idis I+end I-end tdwell+ tdwell- ncyc Qfinal tfinal baseName [fsmax [Addr]]
where-  USB is the rPi USB address (/dev/ttyUSB0, etc);
        Vmax/Vmin are charge/discharge 'CV' voltages;
        Ich/Idis are the charge and discharge 'CC' currents;
        I+end/I-end are currents at which to end the CV phases;
        tdwell+ is the max period (s) to wait at CV for I+end;
        tdwell- is the max period (s) to wait at CV for I-end;
        Qfinal is the % charge in Ah at the end of cycling;
        ncyc is the # cycles to perform;
        tfinal is the period (s) to digitise after current is zero;
        baseName is the file string to be used;
```

```
        optionally Addr is the GPIB bus address, def=5.
        optionally fsmax is the max sample frequency, def=0.94.
Cycles the battery by the CCCV method, while measuring V & I,
~8 samples/second, tvi file entries limited by fsmax.
If tdwell+/- is <0, the period is set and current is set to zero (CV->rest).
Assuming a 66332A instrument on Prologix/Fenrir USB-GPIB interface.
Requires no drivers, controls prologix using ++cmd protocol.
Creates basename.log & baseName.tvi with time-volts-amps-dQ-cyc quintuples.
Displays: #points, elapsed time, V, I, cycle, Tsample, CV time, dQ, and CC/CV mode.
```

- bz3p66.c

  Measures battery impedance on a 66332A unit by sourcing a multitone current signal, and measuring and reporting time, voltage and current (see Chapter 3). Inserts a triphasic pulse of frequency and magnitude set by the user into the source signal. The software includes the option to call software ("dftv"; see [5]) to perform a discrete-time Fourier analysis on the data for impedance magnitude and phase determination.

```
bz3p66 V6.04 jbs&cjd, Dec 2020 -> Oct 2021
Battery Z measurement with triphasic pulses via Prologix/Fenrir GPIB-USB & 66332A.
Usage: bz3p66 USB Vmin Vmax Imax dQmax ncyc fmin fmax Xcyc Pf Pw Ip tr baseName [Addr [dftp [ff]]]
where-  USB is the rPi USB address (/dev/ttyUSB0, /dev/ttyACM0, etc);
        Vmin/Vmax are voltage limits (aborts outside this range);
        Imax is the maximum permitted current (-value => only sinks I);
        dQmax is the total charge in Ah that can be sourced or sunk (-val => equal I tones);
        ncyc is the # cycles at fmin (typically 2.01-6.00);
        fmin/fmax are the lowest and highest freqs;
        Xcyc is the # cycles at fmin of data to discard before logging.
        Pf is the frequency of pulse occurences in multitone time, =1/Ttp seconds;
        Pw is the period of the triphasic pulse, in seconds;
        Ip is the peak current of the triphasic pulses;
        tr is the rest period after the triphasic pulse before resuming multitone;
        baseName is the file string to be used;
        Addr is the optional GPIB bus address, def=5.
        dftp is the [path]name of Scott/Farrow dft program (dftp,dftv,etc);
        ff is the [path]name of the Scott/Finer multitone optimiser program.
Makes a multitone tvi/Z measurement by sourcing current, measuring V & I.
If the USB parameter is set to "skip" the tvi measurement is skipped.
Creates baseName.tvi, basename.log, [.bat, .fmp, [.ffz]] files.
Z optionally computed by calls to dftp [& ff] at each frequency.
.bat file is dft script, fmp has dft's z values, ffz is refined fmp.
Frequencies are a 1-2-5 sequence between fmin and fmax;
if fmax<0 frequencies are read from baseName.frq file, up to 32 freqs.
Requires no drivers, communicates using ++cmd protocol.
Writes complete data, including pulses, to basename.ptvi file.
```

- bzdcp66.c

  Measures battery impedance on a 66332A unit by sourcing a multitone current signal, and measuring and reporting time, voltage and current (see Chapter 3). The measurement multitone is superimposed on a DC signal (the working current, actually a square wave of magnitude up to 5 A with frequency set by the user). This software also includes the optional call to dftv for impedance

magnitude and phase determination. Note that bzdcp66 is now the software of choice for battery EIS at ELFs when using the 66332A units at the University of Waikato.

```
bzdcp66 ------------  V6.21 jbs&cjd Dec 2020 -> Nov 2021
Battery Z measurement with dc, via Prologix/Fenrir GPIB-USB & 66332A, optional DFT.
Usage: bzdcp66 USB Vmin Vmax Imax dQmax ncyc fmin fmax Xcyc Idc fdc baseName [Addr [dftp]]
where-  USB is the rPi USB address (/dev/ttyUSB0, /dev/ttyACM0, etc);
        Vmin/Vmax are voltage limits (aborts outside this range);
        Imax is the maximum multitone current in the cell (if <0 only sinks I);
        dQmax is the total charge in Ah that can be sourced/sunk (-val => equal I tones);
        ncyc is the # cycles at fmin (typically 2.01-6.00);
        fmin/fmax are the lowest and highest freqs;
        Xcyc is the # cycles at fmin of data to discard before logging;
        Idc is the magnitude of the added dc current component, and
        fdc is the frequency of the squarewave at Idc;
        baseName is the file string to be used;
        Addr is the optional GPIB bus address, def=5.
        dftp is the [path]name of Scott/Farrow dft program (dftp,dvtv,etc);
Makes a multitone tvi/Z measurement by sourcing current, measuring V & I.
If the USB parameter is set to "skip" the tvi measurement is skipped.
NB: If Imax<0 battery is discharging, so dQmax boundary checking is ignored.
Creates baseName.tvi, basename.log, [.bat, .fmp] files.
Z optionally computed by calls to dftp at each frequency.
The .bat file is dft script, fmp has dft's z values.
Frequencies are a 1-2-5 sequence between fmin and fmax;
if fmax<0, frequencies are read from baseName.frq file, up to 32 freqs.
fdc should be chosen so that none of its harmonics clash with multitones.
Requires no drivers, communicates using ++cmd protocol.
Measures for (ncyc+Xcyc)/fmin seconds, then does dft calls.
Corrects for 1/2 LSB DAC error in 66332.
```

- bap66.c

  Also for use with 66332A units, bap66 sources any arbitrary current signal provided by a *.ti (time and current) file, and then measures and reports time, voltage and current when the source signal is passed through a battery (see Chapter 5).

```
bap66 V1.50 jbs&cjd Jan 2021, Apr 2023
Battery arbitrary waveform measurement via Prologix/Fenrir GPIB-USB & 66332A.
Usage: bap66 USB Vmin Vmax baseName [Addr]
where-  USB is the rPi USB address (/dev/ttyUSB0, /dev/ttyACM0, etc);
        Vmin/Vmax are voltage limits (aborts outside this range);
        baseName is the file string to be used;
        Addr is the optional GPIB bus address, def=5.
Sources current described by a .ti file, measuring V & I to .tvi file.
Creates baseName.tvi, basename.log, reads basename.ti file.
Assumes ti file contains seconds-amps pairs (or blank lines).
Requires no drivers, communicates using ++cmd protocol.
```

- tvi2ica.awk

  This script takes a *.tvi (time, voltage and current) file from a battery slow cycling measurement on a 66332A unit (or similar measurement equipment), and calculates and reports rates of charge movement for voltage increments set by the user (see Chapter 4).

- Cyc_tvi2ica_Plot.m

A MATLAB® script that performs the same task as tvi2ica.awk, but with added functionality for data plotting.

- tvi2u.awk

  This script multiplies voltage, current and time elapsed for each row of a *.tvi file and keeps two running totals, E_{in} (energy in) where current is positive (charging) and E_{out} (energy out) when current is negative (discharging). The script calculates E_{out}/E_{in} and outputs the result as energy efficiency u together with the timestamp for each line of the input file (see Chapter 5).

- tvi2u.c

  A small C program that performs the same tasks as tvi2u.awk.

```
tvi2u                  V3.0 CJD & JBS August 2023
Usage: tvi2u file.tvi >file.tu
Takes in a 3-col ascii file giving time, voltage, current,
writes same time steps and device cycle efficiency to stdout.
```

- getURegCyc.awk

  Takes a *.tvi file from a regular cyclic waveform and calculates energy efficiency u for each cycle and overall u across all cycles, and reports these with a variety of other parameters including number of cycles, times, voltages, charge moved, energy and loss, and u variance.

```
getURegCyc version 1.10 Chris Dunn July 2023
Usage: getURegCyc inputfile.tvi >outputfile.tu 2>resultsfile.txt
Takes a .tvi (3-column ascii) file for a regular waveform,
works out 'u' for each period and overall 'U' across all periods,
and writes period start times and u values to stdout.
Note: suitable only for regular waveforms.
For irregular and self-similar cycles use 'getSoH'.
```

- getUTheta.c

  Primarily for use with single sinusoid stimuli in a modelled CPE. Performs the same tasks as getURegCyc.awk but also calculates and writes out the CPE phase angle and fractional order α as derived using energy efficiency u (see Chapter 5).

```
getUTheta version 1.10 Chris Dunn July 2023
Usage: getUTheta inputfile.tvi [Rs] >outputfile.tu 2>resultsfile.txt
Rs (optional) = series resistance.
Takes a .tvi (3-column ascii) file for a regular waveform,
works out 'u' for each period and overall 'U' across all periods,
and writes period start times and u values to stdout.
getUTheta also calculates and writes out the phase angle for the CPE,
from which we may infer alpha, and adds theta (in radians) and alpha to stdout.
Note: suitable only for regular waveforms.
For irregular and self-similar cycles use 'getSoH'.
```

A further program, getSoH.c, is not listed here for intellectual property reasons. However, details of this program and its operation can be found in Chapter 5 of this thesis.

Some of these programs, notably those designed for use with the 66332A units, are collaborative efforts, used and contributed to by several members (including the author) of the Battery Modelling Group at the University of Waikato. They are also subject to ongoing development.

1.6 MATLAB® Functions

A number of MATLAB® functions were used in this work, and are briefly explained here.

1.6.1 Hilbert Transform

The function $x = hilbert(xr)$ returns the analytic signal, x, from a real data sequence, xr (https://au.mathworks.com/help/signal/ref/hilbert.html).

In practice, this means that if the original real-valued signal in the time domain is referred to as $f(t)$, the Hilbert transform provides a unique analytic signal $z(t)$ from which the signal's instantaneous properties can be derived. This analytic signal will have a real part, which is the original signal, and an imaginary part, which will consist of the Hilbert-transformed data $H[f(t)](t)$. Thus,

$$z(t) = f(t) + jH[f(t)](t) = A(t) \cdot e^{j\phi(t)} \tag{1.1}$$

where j is the imaginary operator $\sqrt{-1}$, $A(t)$ is the signal's instantaneous amplitude, $\phi(t)$ the instaneous phase and $\omega(t)$ the instantaneous frequency, such that

$$A(t) = \sqrt{f^2(t) + H[f(t)]^2(t)} \tag{1.2}$$

$$\phi(t) = arctan\left(\frac{H[f(t)](t)}{f(t)}\right) \tag{1.3}$$

$$\omega(t) = \frac{d\phi(t)}{dt} \tag{1.4}$$

The Hilbert transform itself is defined in the time domain as

$$H[f(t)](t) = \frac{1}{\pi} P \int_{-\infty}^{\infty} \frac{f(\tau)}{t-\tau} d\tau \tag{1.5}$$

where P is the Cauchy principle value and t and τ are time variables.

MATLAB® calculates the Hilbert transform in Fourier space by first calculating the Fourier components with a discrete Fourier transform (DFT), then multiplying by $-jsgn(\omega)$ (where sgn is the signum function and ω is the angular frequency), so

that

$$sgn(\omega) = \begin{cases} -1, & \text{if } \omega < 0 \\ 0, & \text{if } \omega = 0 \\ +1, & \text{if } \omega > 0 \end{cases} \tag{1.6}$$

The inverse Fourier transform then gives the Hilbert transform.

1.6.2 polyval (Polynomial Evaluation)

$y = polyval(p, x)$ evaluates the polynomial p at each point in x. The argument p is a vector of length $n + 1$ whose elements are the coefficients (in descending powers) of an nth-degree polynomial (https://au.mathworks.com/help/matlab/ref/polyval.html).

$$p(x) = p_1 x^n + p_2 x^{n-1} + ... + p_n x + p_{n+1} \tag{1.7}$$

For example, the polynomial $3x^2 + 2x + 1$ can be represented as a vector of coefficients [3 2 1], and *polyval* then used to evaluate the polynomial for specific values of x. Thus

$$p = [3\ 2\ 1]$$
$$x = 2$$
$$y = polyval(p, x)$$

outputs a value of 17.

1.6.3 polyfit (Polynomial Curve Fitting)

$p = polyfit(x, y, n)$ returns the coefficients for a polynomial $p(x)$ of degree n that is a best fit (in a least-squares sense) for the data in y. The coefficients in p are in descending powers, and the length of p is $n + 1$ as shown in Equation 1.7 above (https://au.mathworks.com/help/matlab/ref/polyfit.html). x and y are vectors of the same length that represent x- and y- coordinates, and p is the vector of coefficients representing the fitted polynomial.

For example, consider the following data points:

$$(1, 2)\ (2, 3)\ (3, 4)$$

$polyfit$ can be used to fit a polynomial to these points, so

$$x = [1\ 2\ 3]$$
$$y = [2\ 3\ 4]$$
$$p = polyfit(x, y, 1)$$

outputs

$$p = 1.0000\ 1.0000$$

which means that the fitted polynomial is of degree 1 (a straight line) with the form $y = x + 1$.

Note that *polyval* (Section 1.6.2) can then be used to evaluate this polynomial at any specific point x.

Chapter 2

Background and Literature Review

2.1 Estimating State of Health

The ability to characterise and model rechargeable battery SoH is key to the development of an effective and reliable battery management system, and many estimation methods have accordingly been investigated. According to a recent state-of-the-art review [6], these methods fall into four main types (**Figure 2.1**):

- Direct measurement methods
- Indirect analysis methods
- Adaptive algorithms
- Data-driven methods

These approaches have been discussed extensively in the literature, and the reader is referred to relevant reviews for further information [3, 6, 7]. This part of the present thesis illustrates the variety of approaches to the problem of characterising battery SoH, and the dilemma faced by a researcher seeking reliable and efficient methods that work across different battery chemistries.

While a number of comprehensive reviews describing the many SoH analysis and characterisation techniques and their relative merits are available (see above and **Table 2.1**), authors appear reluctant to make unequivocal recommendations. Xiong et al. state that "Although a large number of SoH estimation methods have been studied, each method has its deficiencies and possibilities for improvement" [6]. These authors suggest that data-driven methods (see **Figure 2.1**) are increasingly popular, and the Battery Modelling Group at the University of Waikato is investigating optimisation and data fitting algorithms as part of its overall work. However, Xiong et al. admit that these algorithms are only as good as the data upon which

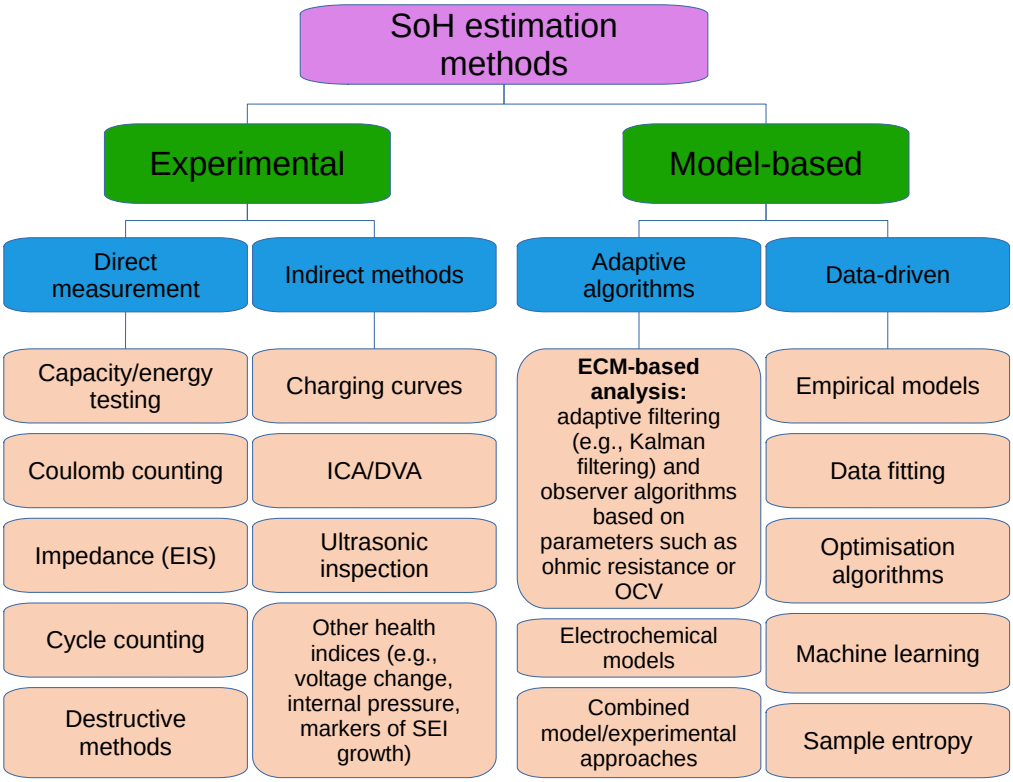

Figure 2.1: Classification of battery SoH estimation methods. DVA, differential voltage analysis; ECM, equivalent circuit model; EIS, electrochemical impedance spectroscopy; ICA, incremental capacity analysis; OCV, open-circuit voltage; SEI, solid electrolyte interface. Adapted from Xiong et al. [6].

they are based, which brings us back to the need for reliable and consistent measurements coupled with an accurate circuit model.

As an illustration, techniques that are popular among researchers, frequently discussed in the literature and apparently straightforward, but that are nevertheless associated with problems likely to render them unsuitable for universal adoption in battery SoH determination, are highlighted here.

2.1.1 Coulomb Counting

Of all the methods described, coulomb counting is stated to be one of the most commonly used for SoH estimation [7]. This method is superficially attractive. Integration of battery current over time has low computational complexity [8, 9]:

$$Q_{discharge} = \int_0^T I(t)dt \tag{2.1}$$

and

$$SoH(\%) = \frac{Q_{discharge}}{Q_{rated}} \times 100 \tag{2.2}$$

where $Q_{discharge}$ is the charge obtained by integrating the discharge current $I(t)$ over time T, and Q_{rated} is the rated charge capacity.

Table 2.1: Comparison of battery state of health (SoH) estimation methods.

Method	Advantages	Disadvantages	Future direction
Direct measurement	• Simplest and most direct • Can be combined with model-based methods • Accurate in the laboratory • Ageing mechanisms can be studied using EIS and destructive methods	• Online measurement may be difficult • Specialised equipment needed for EIS and destructive methods • Destructive methods irreversible, not suitable for real-time use	• Simple online EIS implementation methods needed, with efficient offline maintenance and troubleshooting • Better battery models needed
Indirect analysis	• Can measure external characteristics to get ageing information • ICA/DVA and ultrasonic methods can show ageing mechanisms in real time • Accurate in a laboratory environment	• Not suitable for all battery types • Temperature affects accuracy • Not suitable for online application; needs controlled and strictly specified conditions	• Online ICA, etc. methods with minimal computational complexity (difficult to envisage) • Combine applied and machine learning methods • Consider influence of temperature
Adaptive filtering	• Accurate and robust • Easy online implementation	• Needs extensive algorithm validation and debugging • Needs high performance controllers • Dependent on model accuracy	• Improve ECM by further physical characterisation • Improve ECM by incorporating ageing mechanisms • Fusion-model methods to improve generalisability
Data driven	• Less pre-testing required • Precise estimation of slowly changing parameters	• Requires efficient and portable algorithm • High dependence on magnitude, sampling frequency, completeness, etc. of data	• Improve real-time accuracy and robustness by combining machine learning, big data mining and on-board adaptive filtering algorithms

DVA, differential voltage analysis; ECM, equivalent circuit model; EIS, electrochemical impedance spectroscopy; EM, electrochemical model; ICA, incremental capacity analysis. Adapted from Xiong et al. [6].

Moreover, online application is feasible. However, estimation precision has been reported to be low, and variable with respect to cycling (e.g., approximately 9% after 21 cycles as opposed to 2.43% after eight cycles in lithium-ion batteries in one study [9]). The degree of error may be improved by combination with other methods such as Kalman filtering (KF) [10], but at the expense of increased complexity and processing times.

KF algorithms require two steps for implementation. Firstly, a prediction state is needed, where the filter estimates the output variable of interest; secondly, the estimate is updated to obtain greater accuracy and improve certainty. There are many derived and improved algorithms based on KF, including extended KF (EKF), unscented KF (UKF), particle filtering (PF), adaptive EKF (AEKF), and sigma point KF (SPKF), which represent attempts to deal with nonlinearity and high

computational requirements (see **Figure 2.1**). Detailed discussion of these is beyond the scope of this thesis.

Coulomb counting may be unreliable for three reasons. First, current is measured by a piece of hardware, typically an analog-to-digital converter reading voltage across a resistor or across a Hall effect sensor. This might have errors or drifts. To capture all the information the current must be sampled with sufficient resolution at a sufficiently high frequency. A good digitiser will integrate the signal in analog fashion with wide bandwidth and will digitise the integrated value with good precision, but many systems simply sample the instantaneous value at some rate. The currents involved may have very wide dynamic range, and might have sharp pulses with wide bandwidth.

Second, batteries have history and long, non-exponential memories [11]. A good early example of this unexpected behaviour was reported in capacitors by Westerlund in 1991 [12]. It is possible to demonstrate different charges entering and exiting a battery over subsequent charge-discharge cycles on the bench, simply with a misleading pre-charge sequence. This might account for coulomb miscounts.

Third, charge leaks through the cell, and there may be a mechanism at work by which charge pushed into the battery bypasses the chemistry responsible for energy storage. All these require further investigation, and could form part of future research.

2.1.2 Open-Circuit Voltage and Charging Curves

Open-circuit voltage (OCV)-based methods seek to link the battery's OCV (i.e., the potential difference between the battery's terminals with no load connected) with its SoH. OCV develops as a result of electrochemical reactions within the battery, and varies with the metals and electrolytes used [13]. Identifying this relationship so that it can be expressed via a function can be an extensive process involving offline battery cycling [7]. These methods are applicable to differing battery chemistries, but the relationship between OCV and SoH varies with battery chemistry and cycling history [7, 14, 15].

The definition of the open-circuit terminal voltage U_{OCV} is based on a simplified battery model as shown in **Figure 2.2** [7, 16].

$$U_{OCV} = U + IR \tag{2.3}$$

Xing et al. [16] acknowledged the influence of temperature when attempting to construct SoH-SoC curves. These authors used extensive offline laboratory testing and suggested an online variant of their method. Waag et al. [17] used an online OCV method in combination with a nonlinear (current-dependent) battery model (**Figure 2.3**) to estimate SoC and SoH.

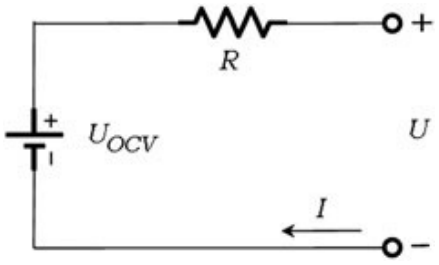

Figure 2.2: Simplified battery model showing open circuit voltage (OCV) [7, 16].

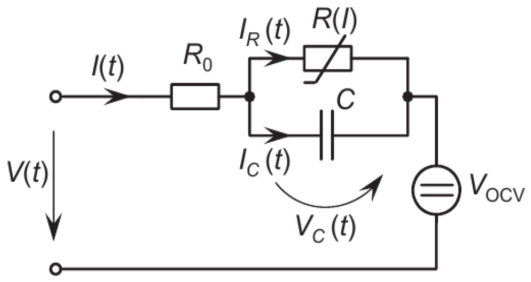

Figure 2.3: Equivalent nonlinear circuit model used for power prediction [17].

Other authors [18] used a constant current-constant voltage (CC-CV) charging method, with an ECM (**Figure 2.4**) to characterise the constant current portion of the charging curve. They then used a transfer function and time-based parameter to estimate SoH via a nonlinear least squares method to identify model parameters.

Charging curves have been used in this way because researchers perceive that they change as the battery degrades, although interfering factors are likely to include temperature and charging rate. The effective capacity of a cell is not constant under all conditions, and is dependent on, for example, discharge rate [19]. This phenomenon is known as capacity offset, is common across cell chemistries, and is expressed by Peukert's law, which describes a power relationship between the discharge current (normalised to some base-rated current) and delivered capacity (normalised to rated capacity) over some specified range of discharge currents [20].

A related complication is seen when cell terminal voltage as a function of charge delivered is examined. When current flows through a cell, a voltage drop across its internal resistance decreases the terminal voltage during discharge and increases the voltage needed to charge the cell. This reduces effective capacity and decreases charge-discharge efficiency. Higher discharge rates give rise to higher internal voltage drops, which may explain capacity offset [19]. In addition, charge-discharge meas-

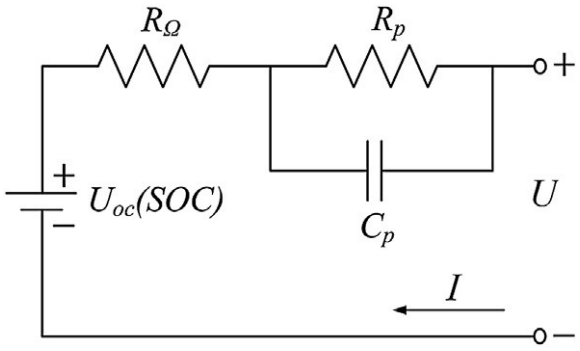

Figure 2.4: Equivalent circuit model of lithium-ion battery used to represent constant current charging profiles [18].

urements show a hysteresis in the charge capacity-terminal voltage characteristic, with no single open circuit potential, and variation of both terminal voltage and curve separation with charging rate relative to the rated capacity of the battery (C-rate). **Figure 2.5** shows measurements obtained by the Battery Modelling Group at the University of Waikato to illustrate this.

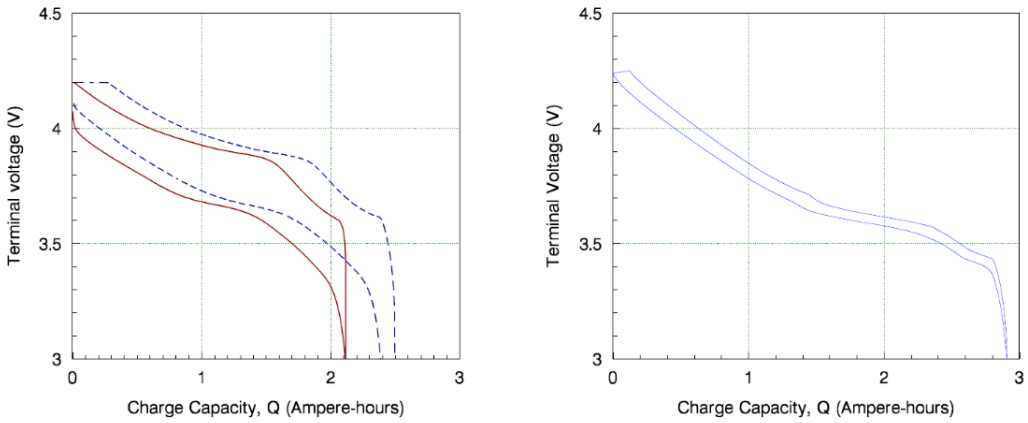

Figure 2.5: Measured charge-voltage characteristic of a lithium-ion 18650 cell. Left: measured at C/2 using a constant current-constant voltage regime (dashed trace), and then a constant current regime without a constant voltage equilibration period (solid red trace). Right: measured at C/100, constant current-constant voltage regime.

The constant voltage step has also been used as a health indicator, with battery current behaviour during the CV phase being simulated by:

$$I(t, C_{loss}) = A(C_{loss})e^{-B(C_{loss})t} + C(C_{loss})$$

where C_{loss} represents capacity loss, and A, B and C are parameters related to

C_{loss} [21]. The authors stated that they were able to determine these parameters and hence C_{loss} from the current curve at the constant voltage step.

As in most areas of battery research, the heterogeneity of approaches and models makes objective comparison, or the recommendation of one system over another, extremely difficult.

2.1.3 Incremental Capacity and Differential Voltage Analyses

As voltage curve analysis reveals very little information relating to the internal characteristics of a battery, some researchers have attempted to use electrochemical characterisation in combination with ICA to process voltage data [22, 23]. This is done by integrating capacity corresponding to small voltage intervals (dQ/dV) via charging and discharging the battery using very small currents. Lithium intercalation reactions are associated with complex phase transformations in lithium-ion batteries; popular cathode materials such as transition metal oxides show two-phase separation across porous electrodes, whereas graphite (the standard anode material) passes through at least three phases [24]. The process of constructing an ICA plot converts the voltage plateaus of a two-phase transition into recognisable incremental capacity peaks.

In differential voltage analysis (DVA; dV/dQ), distances between peaks of the differential voltage curve represent the amount of charge participating in the two-phase transition. This facilitates quantitative analysis of capacity fading [25].

Figure 2.6 shows changes in incremental capacity and differential voltage curves cycled at 40°C with 50% depth of discharge. The shapes, amplitudes and positions of the curves characterise the battery at different ageing states.

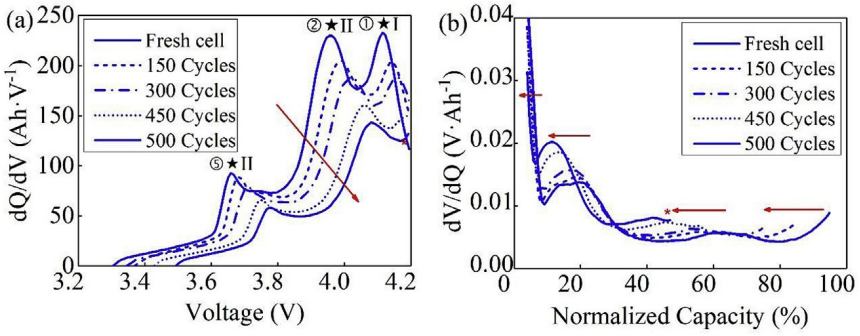

Figure 2.6: Evolution of incremental capacity and differential voltage curves in a lithium-ion battery cycled at 40°C with 50% depth of discharge. Reproduced from Xiong et al. [6] with permission.

A number of published papers have reported ICA peak position [15, 26, 27, 28]

or the interval between peaks of the DVA curve [29] as markers of battery ageing. Interestingly, one of these groups [28] used a fractional order battery model (**Figure 2.7**; see also Section 2.2.2).

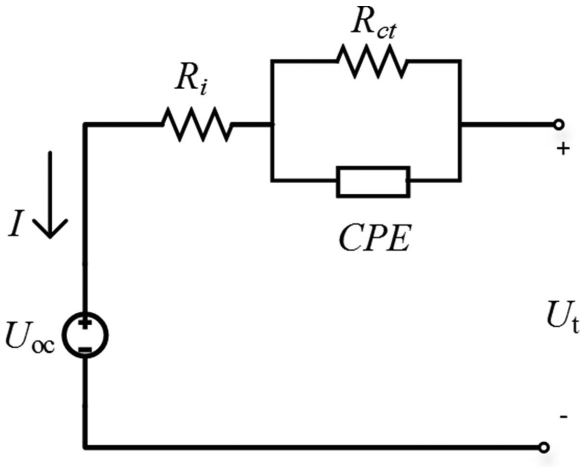

Figure 2.7: First-order fractional model as proposed by Tian et al. for use with incremental capacity analysis [28]. CPE, constant phase element.

These authors demonstrated better agreement with dynamic stress testing voltage data than was achieved with an integer order circuit model in which the CPE was replaced by a capacitor (i.e., a CPE in which $\alpha = 1$, where α is the dispersion coefficient or fractional order which represents non-uniform boundary conditions and distributed intercalation/de-intercalation processes in porous electrodes [30, 31]). Fractional order models, CPEs, and the non-ideal capacitative characteristics of the electrode-electrolyte interface will be discussed in more detail later.

ICA and DVA are subject to a number of limitations, chief of which are the conditions and C-rates under which the curves are obtained (typically of the order of C/25). Real-world SoH determination involves the movement of much larger amounts of charge; under these conditions, terminal voltages cannot be considered as OCV and parameters based on ICA or DVA may not apply. Moreover, charging currents encountered in environments beyond the laboratory may be variable, depending on the type of battery management system in use [32, 33, 34].

2.1.4 Cycle Counting

This is the simplest method of all, involving a counter that keeps track of the number of charge and discharge cycles undergone by the battery [6]. It is commonly used in laptop computers or small electronic products such as cellphones. If the total number of cycles that the battery can be expected to undergo across its life is provided by the manufacturer, and the current cycle number is known or can be calculated, battery SoH can theoretically be determined. However, the method is based on numbers of complete charge-discharge cycles, whereas batteries are frequently charged after only

partial discharge. Conversion coefficients, determined experimentally, are generally used to circumvent this problem, although it remains unclear as to how accurate these are. Another problem lies in the inability of cycle counting to account for extreme operating conditions that may affect the battery's functionality, or other aspects of any single battery's individual usage history [4].

2.1.5 Other Methods

Other methods mentioned in **Figure 2.1** include ultrasonic inspection, which uses wave reflection, refraction and pattern transformation to characterise internal degradation processes in a battery. Electrochemical models attempt to describe the internal electrochemical dynamics of the cell, while destructive methods involve battery disassembly and use of methods such as spectroscopy, X-ray diffraction and scanning electron microscopy. Obviously, this involves permanent damage to cells, and is suitable only for laboratory investigations. Sample entropy relates to a system of measures of system complexity, originally developed for use with noisy data sets from biological systems (e.g., cardiovascular studies) [35]. Further discussion of these methods is beyond the scope of this review, and the reader is referred to papers covering these topics [6, 7]. They are mentioned here to illustrate the wide variety of approaches to the measurement of battery SoH.

2.2 Battery Impedance and State of Health

We know that the ability of a rechargeable battery to store energy and provide power decreases over the lifetime of the battery. However, as indicated above, SoH definition and characterisation lack clarity, despite over a century of battery development and decades of discussion in the literature. Nevertheless, there is a consensus, exemplified by recent reviews such as that of Xiong et al. [6], that battery SoH can be characterised by a unit's capacity and internal resistance, which are stated to reflect energy capability and power capability, respectively [36, 37].

Studies of internal ageing mechanisms in lithium-ion batteries (for example) indicate that capacity loss is chiefly due to loss of lithium inventory, active material decomposition and structural changes [38, 39, 40], while increasing internal resistance is attributed mainly to growth of the solid electrolyte interface (SEI: to be discussed in more detail later).

2.2.1 Electrochemical Impedance Spectroscopy

Notwithstanding the wide variety of direct and indirect methods briefly discussed above (Section 2.1), impedance measurement has become well established as the method of choice for the characterisation of battery behaviour and properties, and thereby the estimation of SoH. The preferred approach is electrochemical impedance

spectroscopy (EIS), a powerful and non-destructive tool in which the properties of a battery (or a variety of other systems) can be deduced by characterising impedance over a wide frequency range. EIS possesses a number of features that underlie its popularity and utility when compared with other methods: it provides a great deal of useful information suitable for further analysis [41], can be used to separate and quantify impedances related to the cell bulk, interfacial layer, charge transfer reaction, and diffusion processes with a single experiment, can be carried out under operating conditions, and is relatively straightforward and inexpensive [31]. It is also highly accurate, is a reliable indicator of SoC, and provides information that can be used to predict SoH [7].

Details of EIS and its applications are available from a number of good sources (e.g., the text by Lasia [41] and several recent reviews [31, 30, 42]), and a brief overview of the technique and how it applies to our research is given here.

Impedance (Z) of an electrochemical system around some steady or quasi-steady state can be determined by [30]:

1. Applying a sequence or set of small-signal AC currents, expressed (for sinusoidal signals) as the complex exponential $I(t) = |I|e^{j(\omega t+\phi_I)}$;

2. Measuring the voltage response $V(t) = |V|e^{j(\omega t+\phi_V)}$;

3. Calculating $Z(\omega) = \frac{|V|}{|I|}e^{j(\phi_V-\phi_I)} = \frac{|V|}{|I|}[\cos(\phi) + j\sin(\phi)]$.

The complex impedance $Z(\omega)$ is made up of real and imaginary parts:

$$Z(\omega) = Z_0\cos(\phi) + jZ_0\sin(\phi)$$

where $Z'_{real} = Z_0\cos(\phi)$ is the real part of the complex exponential, which represents the resistance of the system; $Z''_{imag} = Z_0\sin(\phi)$ is the imaginary part of the complex exponential, which is related to capacitance or inductance and represents energy storage [31].

Impedance spectra can be produced in two different ways: Bode plots, showing magnitude and phase shift across the measured frequency range, and Nyquist plots (also known as Argand diagrams) that show the real and imaginary parts of $Z(\omega)$ using cartesian coordinates (**Figure 2.8**). Nyquist plots are more commonly used by electrochemists, and are seen more frequently in the literature, because of a prevailing consensus that ECMs can be more easily deduced from them [41]. However, frequency information is implied only, not shown clearly (see **Figure 2.9**), and this has implications for the present research.

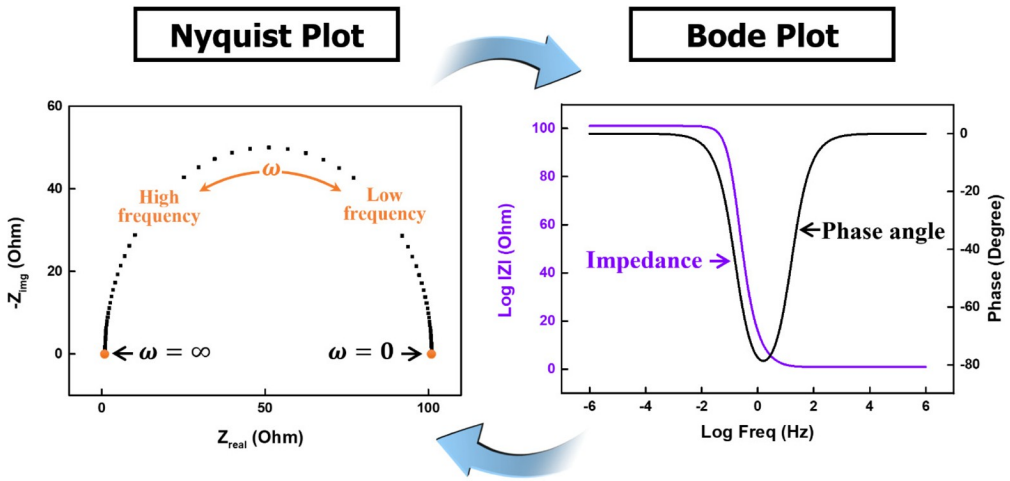

Figure 2.8: EIS spectroscopy representation according to Nyquist (Argand) and Bode plots. These diagrams indicate a parallel RC circuit with $R = 100\,\Omega$ and $C = 20\,\mu$F. Reproduced from Choi et al. [31] with permission.

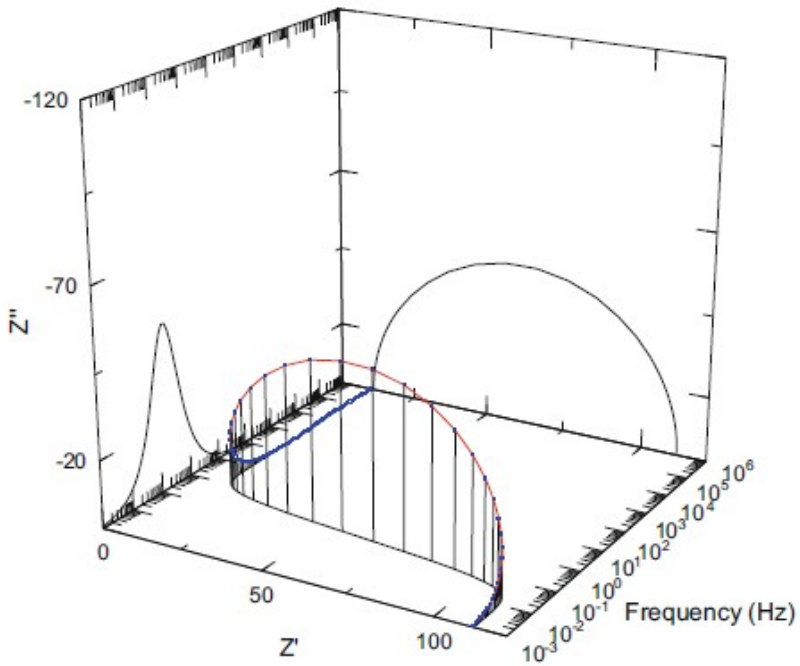

Figure 2.9: Tridimensional EIS impedance plot. Note the relationship of the real and imaginary impedance to frequency, which is implied but not readily evident on the more usually seen two-dimensional Nyquist plot. Reproduced from Lasia [41] with permission.

2.2.2 Electrochemical Impedance Spectroscopy and Equivalent Circuit Modelling

The shape of and the relative positions of elements in a Nyquist plot show how Z'_{real} and Z''_{imag} change relative to each other with decreasing frequency, and thus suggest the likely components that might be used to construct an ECM that mimics the measured behaviour. For example, the diameter of the semicircle in **Figure 2.10** indicates the resistance of the parallel resistor (100 Ω) on the real axis, while the maximum point on the imaginary axis is observed at $\omega = 1/RC$, where RC is the time constant of the system.

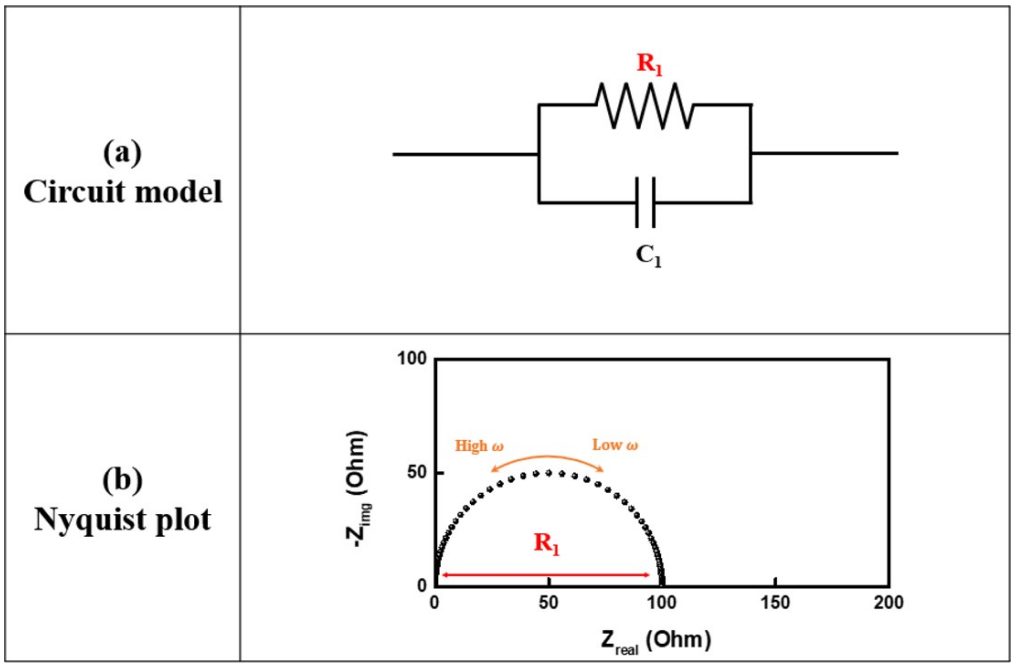

Figure 2.10: (a) Equivalent circuit model and (b) Nyquist plot of a parallel RC circuit. Reproduced from Choi et al. [31] with permission.

Addition of a series resistance to the parallel RC circuit yields the Nyquist plot in **Figure 2.11**. The series resistance shifts the starting point of the semicircle to higher Z'_{real} values.

Before discussing ECMs and their relationship to Nyquist plots further, we note that modern electrochemical ECMs are generally based on the seminal work of Randles [43], who proposed in 1947 that a battery ECM should consist of a network consisting of two capacitors and two resistors to represent the capacity and resistance equivalent to the electrode reaction, the ordinary double layer capacity of the electrode surface, and the electrolyte resistance.

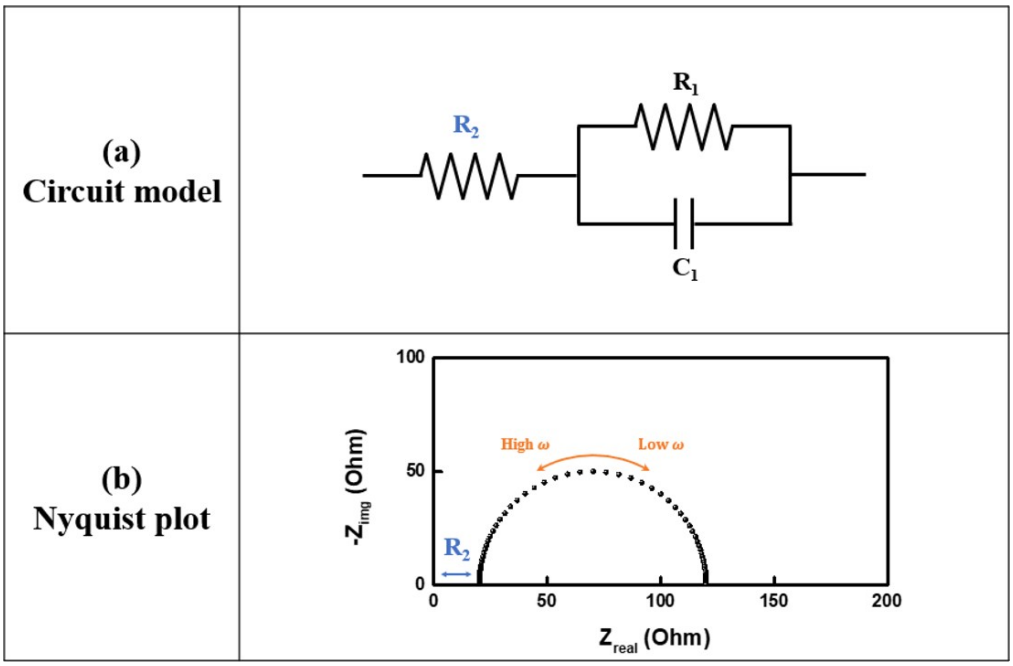

Figure 2.11: (a) Equivalent circuit model and (b) Nyquist plot of a parallel RC circuit with series resistance. $R_2 = 20\Omega, R_1 = 100\Omega$. The semicircle x-axis intercept at 120Ω represents the sum of the polarisation and bulk resistances; the diameter of the semicircle represents the polarisation resistance (100Ω). Reproduced from Choi et al. [31] with permission.

Randles used a capacitor to model the electrical double layer (the Gouy-Chapman-Stern layer) between the electrode and the electrolyte on the assumption that an electrode is ideally polarisable. We now know this not to be the case for solid electrodes. At such electrodes, the double-layer capacitance is not purely capacitative, and may display frequency dispersion [41]. This is attributed to dispersion of time constants, $\tau = R_s C_{dl}$, and dispersion due to surface adsorption and diffusion processes (kinetic dispersion) [44]. Such behaviour cannot be modelled by simple RC circuits, and in such cases Randles' double-layer capacitor is replaced by a CPE, or fractional capacitor, as originally proposed by Cole and Cole in 1941 [45]. Brug et al. suggested in 1984 that the interface between a solid electrode and an electrolyte can be mathematically described by an equivalent circuit consisting of a faradaic resistance in series with a CPE [46].

A fractional order capacitative element can be characterised by its impedance as

$$Z_{CPE} = \frac{1}{C_f(j\omega)^\alpha} \quad \text{for} \quad \alpha \in (0,1) \tag{2.4}$$

where α is a fractional order exponent, and C_f, the pseudo- or fractional capacitance, is a constant with dimensions $\mathrm{Fs}^{\alpha-1}$ [47]. As 1 F is equal to $1\,\mathrm{CV}^{-1}$, and 1 A is equal to $1\,\mathrm{Cs}^{-1}$, these units may alternatively be expressed as $\mathrm{As}^{\alpha}\mathrm{V}^{-1}$.

Z_{CPE} has a constant phase angle at $\alpha\pi/2$ [48], whereas the phase shift in pure capacitors (where $\alpha = 1$) is $\pi/2$. α is related to the deviation of the straight capacitative line from 90 degrees by angle $90(1-\alpha)$ degrees [44].

When we consider that $j^{-\alpha} = \cos(\alpha\pi/2) - j\sin(\alpha\pi/2)$, then Z_{CPE} (see above) may be expressed as

$$Z_{CPE} = \left[\frac{\cos(\alpha\pi/2)}{(C_f)\omega^{\alpha}}\right] - j\left[\frac{\sin(\alpha\pi/2)}{(C_f)\omega^{\alpha}}\right] \tag{2.5}$$

which means that the impedance of this element is no longer purely imaginary. Thus, the CPE represents a non-ideal or leaking capacitor, and causes energy dissipation because of the presence of a real impedance [44].

If $j\omega = s$, then:

$$Z(s) = \frac{V(s)}{I(s)} = \frac{1}{C_f s^{\alpha}} \tag{2.6}$$

and

$$I(s) = C_f s^{\alpha} V(s) \tag{2.7}$$

The inverse Laplace transform of (2.7) gives the current through a CPE in the time domain:

$$i(t) = C_f \frac{d^{\alpha} v(t)}{dt^{\alpha}} \tag{2.8}$$

After a potential step, current decreases proportionally to $t^{-\alpha}$. Thus, it never reaches zero, which means the electrode charge goes to infinity. Obviously, this is impossible, the electrode cannot be called ideally polarisable, and cannot physically exist. Also, it must become ideally polarisable somewhere beyond the measured low frequency range [44]. A more detailed discussion of CPE behaviour in the time domain can be found in a recently published review by Gateman et al. [49].

The name "constant phase element" originates from behaviour on the complex plane and in Bode plots (**Figure 2.12**). The complex plane plots deviate from the ideal capacitor case by 9° for $\alpha = 0.9$ and by 18° for $\alpha = 0.8$ (note that Lasia refers to α as ϕ [44]). The Bode phase angle is always constant and equal to 90α degrees, and the slope of the logarithmic Bode magnitude plot equals α. For a series R-CPE circuit (**Figure 2.13**), the slopes in the complex plane are the same as in **Figure 2.12**, and the Bode plots approach those for the CPE only at lower frequencies [44]. This has implications for frequencies of measurement, and we will return to this later.

This brings us to Randles' cell model [43], which models interfacial electrochem-

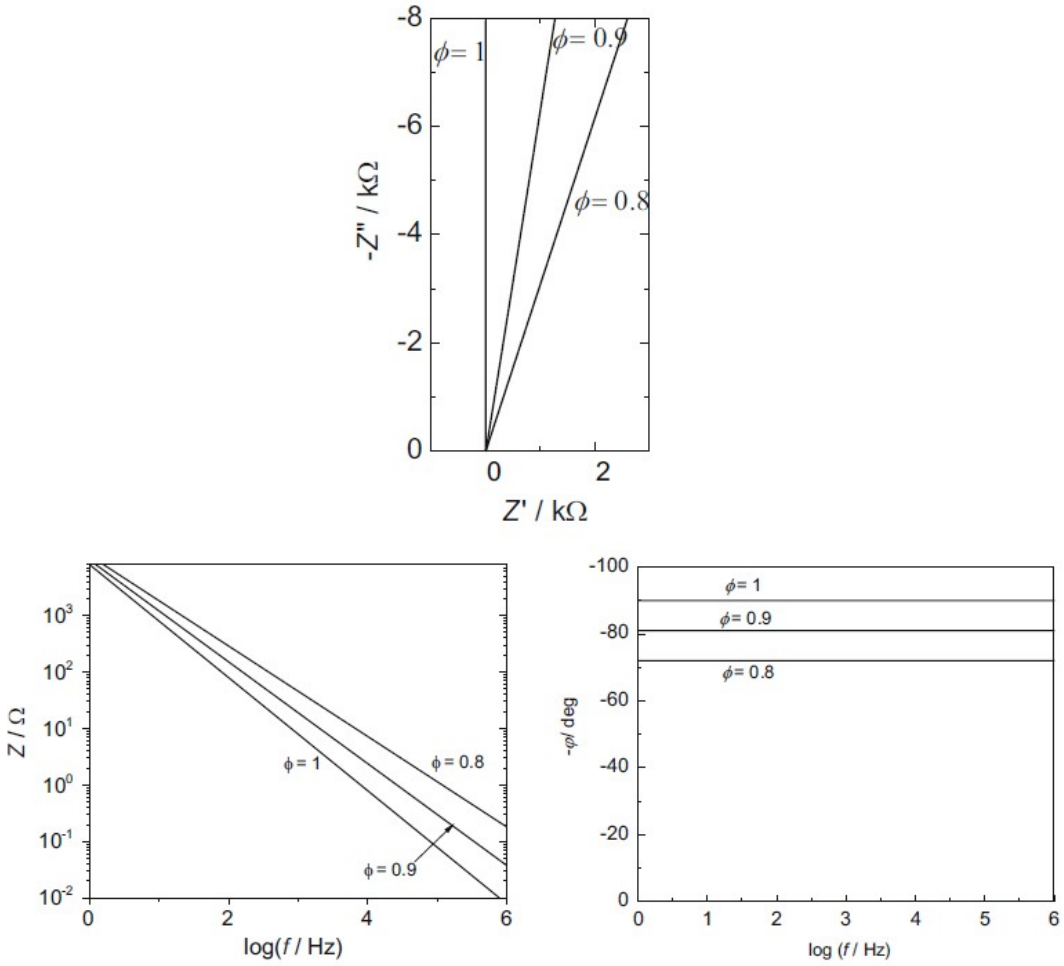

Figure 2.12: Complex plane and Bode plots for a CPE, $Z_{CPE} = \frac{1}{C_f(j\omega)^\alpha}$ where C_f = 20 μAs$^\alpha$V^{-1} per cm^2 of electrode surface area. Reproduced from Lasia [44] with permission.

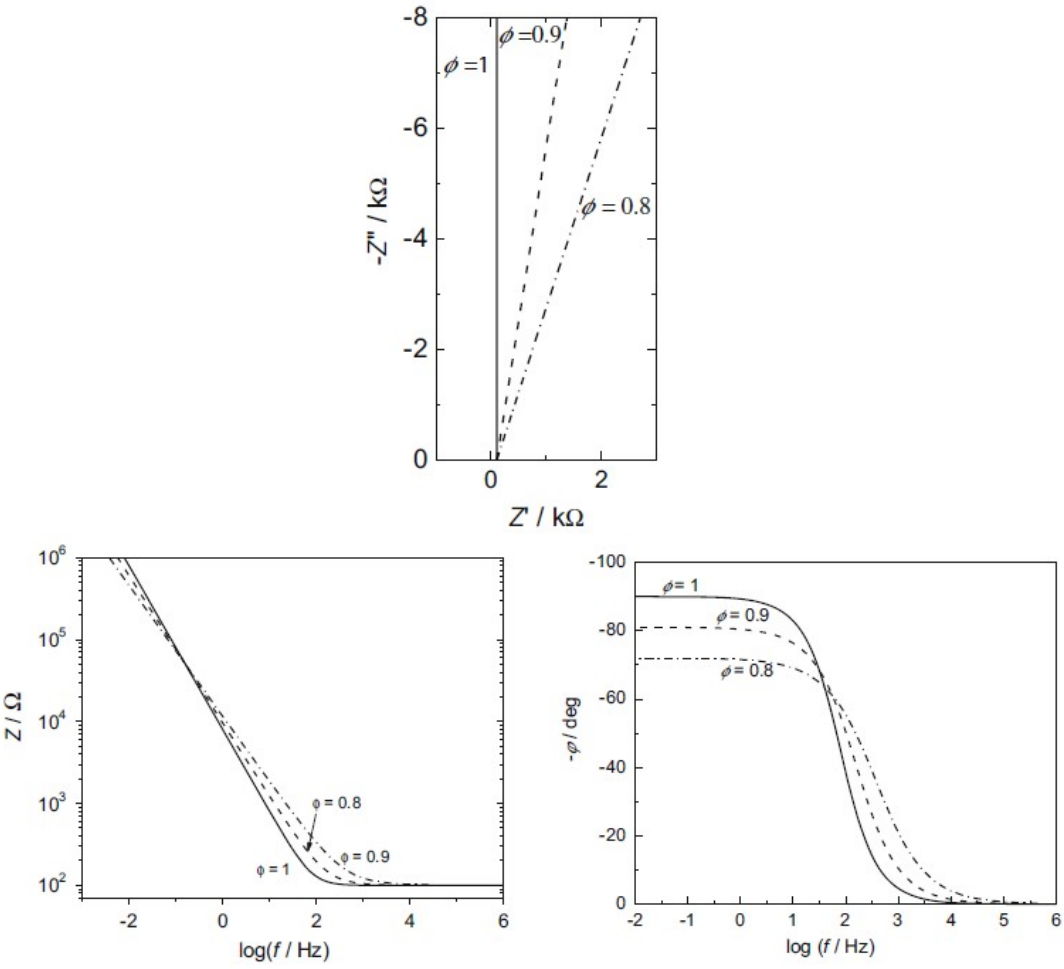

Figure 2.13: Complex plane and Bode plots for a series R-CPE circuit, $R = 100\Omega$, $Z_{CPE} = \dfrac{1}{C_f(j\omega)^{\alpha}}$ where $C_f = 20\,\mu\text{As}^{\alpha}\text{V}^{-1}$ per cm^2 of electrode surface area. Reproduced from Lasia [44] with permission.

ical reactions in the presence of semi-infinite linear diffusion of electroactive particles to flat electrodes. The basic model consists of ionic resistance in series with a double layer capacitance which is in parallel with a charge transfer resistance associated with a faradaic reaction [50] (**Figure 2.14**). The key assumption is that the rate of the faradaic reaction is controlled by diffusion of reactants to the electrode surface. The diffusional resistance is represented by a Warburg impedance in series with the charge transfer resistance. The Warburg impedance is a function of $\omega^{-0.5}$ [51], such that

$$Z_{Warburg} = \sigma/(j\omega)^{0.5} \tag{2.9}$$

where σ is the Warburg coefficient [50].

The Warburg impedance cannot be represented by simple R, C, and L parameters, has real and imaginary parts of the same value [51], and is essentially a CPE with α fixed at 0.5.

As discussed earlier, modern electrochemical and distributed time constant theory accepts that Randles' double layer capacitor will become a CPE [12, 47]. Thus, a Randles circuit will contain two fractional elements, and it becomes clear that any useful battery model must be fractional in nature.

2.2.3 Measurements, Interpretation and Model Complexity

Battery research literature in which characterisation is based on interpretation of EIS spectra has tended to focus heavily on modelling based on Nyquist plots, where each shape or pattern in the plot signifies a circuit element (**Figure 2.15**).

This has resulted in the generation of complicated ECMs with many elements, each representing a battery component or characteristic (**Figure 2.16**).

The level of complexity needed in a battery model remains a contentious topic in the literature. The choice of ECM, informed by Nyquist EIS spectra, has been stated to depend heavily on cell chemistry and detailed characteristics [52]. Some authors assert that there is no standard model that can fit all battery types [31, 52], and that it is necessary to customise models by adding and subtracting circuit elements, depending on cell characteristics (e.g., [53, 54, 55, 56]). Nevertheless, the need to minimise circuit elements for practical impedance analysis has also been pointed out [31]. Berthier et al. suggested in 2001 that most ECMs containing CPEs are only distinguishable in a noise-free experimental environment [57]. When noise is introduced, theoretically distinguishable two-terminal circuits frequently become numerically non-distinguishable.

In the meantime, the literature continues to fill with various ECMs which differ greatly in their physical significance but which often produce very similar EIS spectra [58]. In an attempt to rationalise this confused state of affairs, some researchers

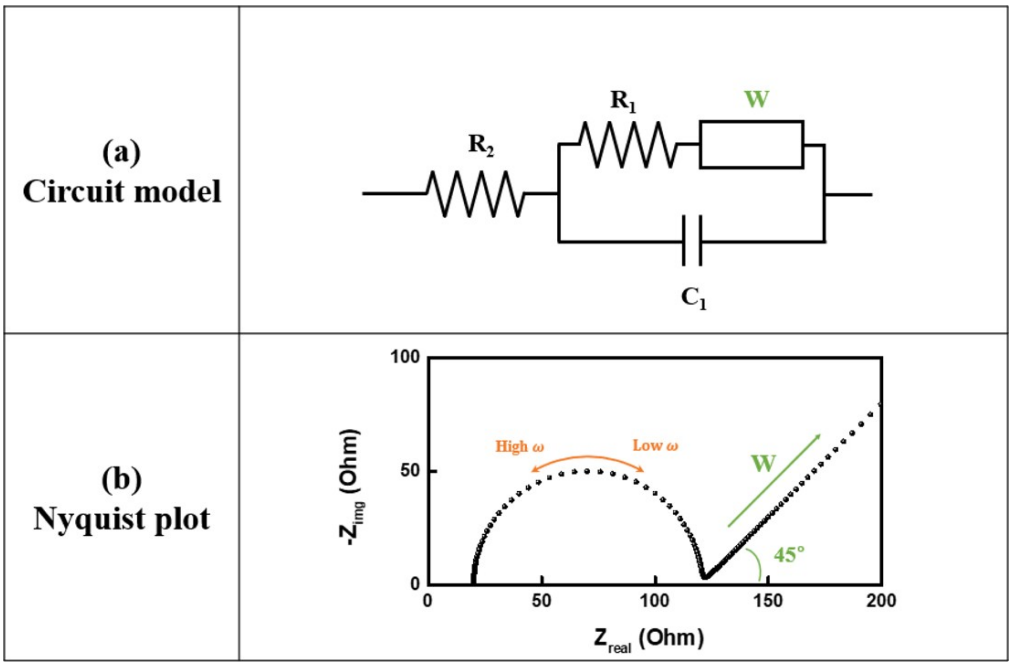

Figure 2.14: (a) Equivalent circuit model and (b) Nyquist plot of a Randles circuit. Note that R_1 represents the charge transfer resistance, which in series with the Warburg element (W) presents the diffusional resistance, C_1 is the double layer capacitance (often replaced by a CPE), and R_2 is the ionic (solution) resistance. The Warburg impedance appears as a straight line, starting at the charge transfer resistance, with a 45 degree slope. The total impedance shows as a semicircle due to coupling of the charge transfer resistance with the double layer capacitance at high frequencies and a straight line due to $Z_{Warburg}$ at low frequencies. Reproduced from Choi et al. [31] with permission.

have developed formulae to convert between different circuit models that produce identical spectra [58], or to automate via machine learning the fitting of measured data to physical models [59].

Furthermore, many ECMs still consist of a voltage source with a network of elements fitted to a cell impedance; several models of this type are illustrated in Section 2.1.2. These Thévenin-type RC models have been preferred by researchers because they offer an additional degree of freedom when characterising SoC, but have been shown to be unsuitable for modelling the runtime characteristics of a cell [60, 61].

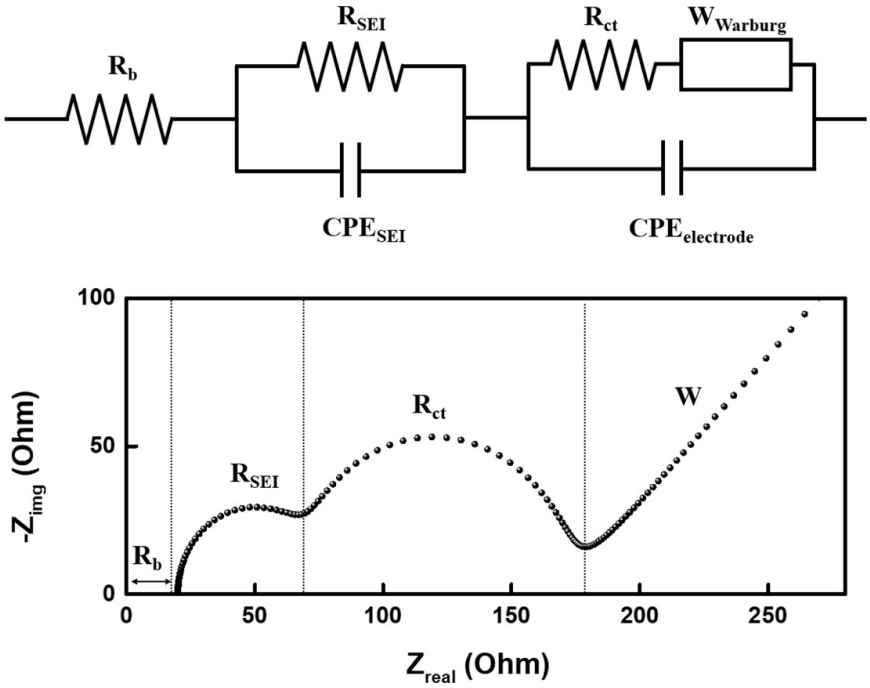

Figure 2.15: Equivalent circuit model of a lithium-ion battery half-cell system. R_b, bulk resistance of the cell (electrolyte, separator and electrodes; R_{SEI}, CPE_{SEI}, resistance and capacitance of the interfacial layer; $R_{ct}, CPE_{electrode}$, charge transfer resistance and double layer capacitance; W, Warburg element, diffusional effects of lithium ions on the host material. Reproduced from Choi et al. [31] with permission.

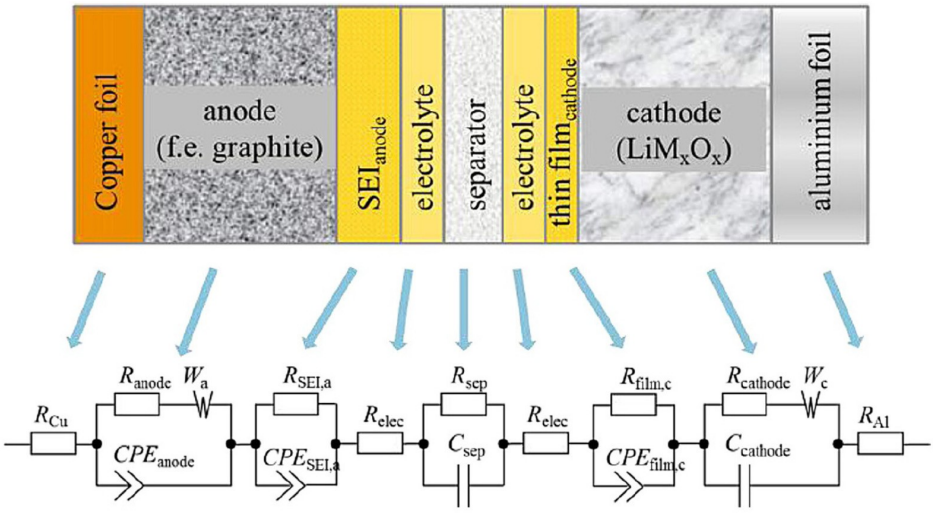

Figure 2.16: Suggested entire circuit model of a lithium-ion battery. Reproduced from Westerhoff et al. [52] with permission.

2.2.4 Electrochemical Impedance Spectroscopy and Battery State of Health

Studies such as those of Wang et al. [62] and Westerhoff et al. [52] are good examples of the use of EIS to model SoH. Wang's group fitted an impedance model while attempting to account for temperature and SoC. Impedance of the battery was mapped over the temperature range 5°C to 45°C, and SoC from 10% to 90%, while varying SoH from 1.0 to 0.8 (by using ageing cycles) to represent the typical life cycle of a battery. No fewer than 200 impedance sweeps covered a frequency range from 10 mHz to 1 kHz, but nevertheless resulted in an inadequate model with an error of 10% or more under most scenarios [62].

Westerhoff et al. [52] used EIS spectra with circuit model parameter estimation guided by the Levenberg-Marquardt algorithm (which is stated to be particularly robust against poor starting parameters). Experiments were performed across the temperature range 50°C to −20°C, SoC 100% to 0%, and SoH 100% to 86% after cycling at 1C. The lower limit of frequency measurement was 5 mHz. Evolution of Nyquist plots (**Figure 2.17**) showed increasing resistance with ageing, which was stated to be irreversible, with expansion of the second semicircle in the plot indicating increased charge transfer resistance. Increasing impedance caused by depletion of free lithium ions in the electrolyte and growth of the SEI layer shifted the entire impedance spectrum further into the capacitative range of impedance, with an increase in the zero crossing frequency.

These authors fitted no fewer than nine circuit models of progressively increasing complexity to their measured data. A simple resistance-only model was deemed suitable for high voltage grid applications, RC circuits with up to five parallel elements arranged in series were suggested for smart grid integration or EV use, and one to three R-CPE elements were recommended for EV or diagnostic use. Fits of R-CPE model data to measured data are shown in **Figure 2.18**, with good agreement by standard and average deviations. Despite the apparent complexity of their work, Westerhoff et al. acknowledged the utility of CPE-based models for diagnostic use, and warned against the assignment of excessive numbers of circuit elements [52].

These papers illustrate the issues encountered when attempting to characterise battery SoH, especially when models are expanded to include other parameters such as SoC and temperature.

A literature search using the University of Waikato's library search engine with the search string "'battery' AND 'impedance' AND 'state of health'" yielded over a thousand hits from the most recent five years alone. Despite the number of publications and obvious keen interest from many centres in rechargeable battery characterisation and SoH prediction, there is still no clear direction.

A selection of papers flagged as most relevant is summarised in **Table 2.2**. For example, Cui et al. [63] claim to have developed a model based on impedance and

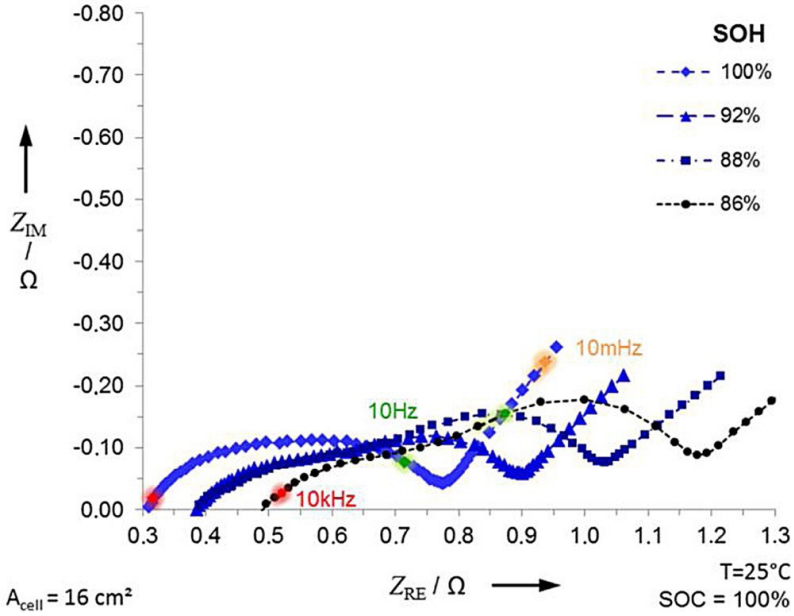

Figure 2.17: Change in impedance spectrum showing dependence on state of health (SoH) at $T = 25°C$, state of charge (SoC) 100%, frequency range 100 kHz to 5 mHz, signal amplitude C/20. Reproduced from Westerhoff et al. [52] with permission.

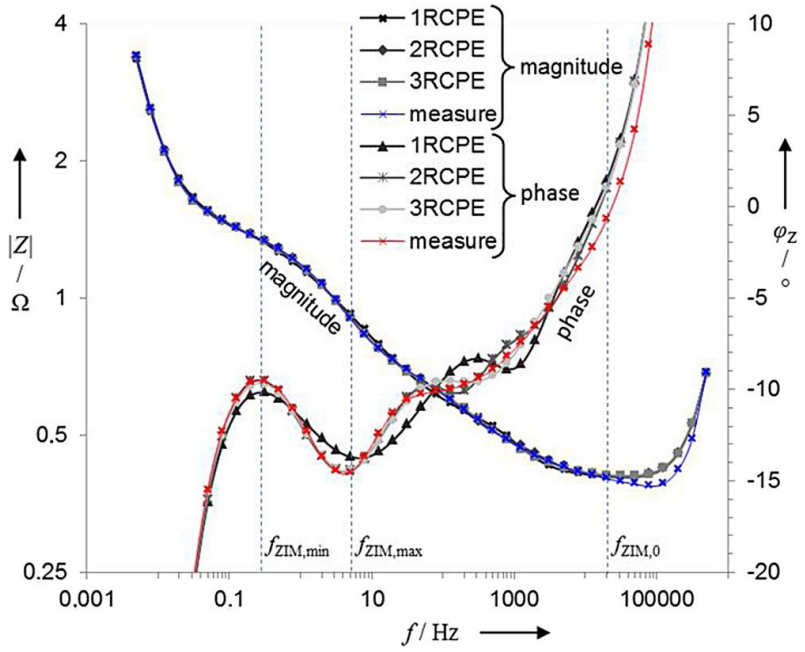

Figure 2.18: Magnitude (blue) and phase (red) responses of measured impedance spectra at $T = 25°C$, state of charge (SoC) 10%, and state of health (SoH) 98% against simulated responses of R-CPE circuit models. Reproduced from Westerhoff et al. [52] with permission.

OCV determination using charging curves that is suitable for battery management system implementation, notwithstanding the problems with voltage-capacity characterisation alluded to in Section 2.1.2 of this review. Yang et al. [64] used a fractional approach, using terminal voltage to approximate OCV. However, the state of a fractional element cannot be described by its terminal voltage, as demonstrated using Laplace circuit theory by Hartley et al. [65]. The terminal voltage of a capacitor reflects the energy stored within it through

$$E = \frac{1}{2}CV^2 \tag{2.10}$$

and charge stored through

$$Q = CV \tag{2.11}$$

but, as illustrated in Section 2.1.2, no such single-value functions exist for a fractional device, and therefore a battery.

Some authors have experimented with alternatives to the usual multisine stimuli used with EIS. Locorotondo et al. [66] used pseudo-random binary sequence (PRBS) excitation (a deterministic and periodic sequence of length M that switches between two logic levels {0,1}), while Mingant et al. [67] studied the power spectral density of a "quasi-EIS" (QEIS) spectrum based on free current and voltage signals arising from acceleration and regenerative braking in an EV. Alternative approaches such as these have not been widely accepted, however, and do not address the fundamental problems relating to battery characterisation as discussed here. Moreover, past experiments using daily driving and charging cycles with an electric scooter failed to yield useful spectral data [68].

2.2.5 Electrochemical Impedance Spectroscopy, Battery Modelling and the Solid Electrolyte Interface

The first semicircle visible on a Nyquist plot obtained using EIS (see **Figures 2.15 and 2.16**) represents the impedance of a layer that forms on the interface between the electrode and the electrolyte in a lithium-ion battery. This layer is called the SEI, is generated via decomposition of the electrolyte, and provides a protective film to suppress further decomposition of the electrolyte. It also protects the anode [71], and is known to be a key physical marker of battery ageing and degradation [72] (**Figure 2.19**).

Zhang et al. [73] conducted EIS studies on the surface of graphite in lithium-ion cells and reported the formation of a relatively resistive preliminary SEI at approximately 0.15 V, followed by a highly conductive layer at 0.15–0.04 V. Thus, SEI layers with two different characteristics are formed, according to the voltage region in the anode [73]. Furthermore, the resistance of the SEI layer (R_{SEI}) was found to be very sensitive to the reactivity of the electrolyte during the first lithiation cycle [73].

Table 2.2: Studies relating electrochemical impedance spectroscopy (EIS) to battery state of health (SoH).

Reference	Methods	Conclusions and comments
Cui et al. [63]	• Real-time parameter identification based on voltage response to charging curves to identify ohmic and charge transfer impedance • Fast OCV determination based on short charge-discharge (2 minutes each) current pulses • Real-time impedance and OCV data used to develop an "SoH diagnosis ECM" • Ageing experiments conducted by cycling 1.15 Ah prismatic $LiCoO_2$/MCMB (mesocarbon microbead) batteries • Impedance measured with Solartron 1250B frequency response analyser, 5 mHz to 20 kHz, amplitude 5 mV	• Rapid identification of impedance and OCV based on charge-discharge curves stated to be effective for development of SoH diagnosis model • The authors state: "This method can identify ohmic impedance and charge transfer impedance from internal impedance and realize the transformation of Warburg diffusion impedance from frequency domain to time domain" • "Fast determination method of OCV is proposed based on the short-time and low current pulse to realize real-time measurement and identification of the OCV"
Jiang et al. [69]	• $LiMnNiCoO_2 + LiMn_2O_4$ 35 Ah batteries • Cycled up to 520 times at C/3 to simulate ageing • EIS measured from 10 mHz to > 100 Hz after cycling at C/20, C/2 and 2.5C	• Both impedance and available capacity should be taken into account in the evaluation of SoH, especially with high discharge current • The authors state: "The ageing of the batteries has a significant impact on the impedance characteristic" • At frequency > 100 Hz, "there is a significant difference between the phase angles of different aging impedance. The absolute value of the impedance increases constantly with the batteries (*sic*) aging"
Kim et al. [70]	• Compared cell impedances at different SoCs, SoHs and temperatures • EIS with IM6ex unit (Zahner-Elektrik GmbH & CoKG), 200 mHz to 2 kHz, 100 mA, lithium-ion 18650-26F 2.6 Ah batteries • Cells cycled to simulate ageing to 80% nominal capacity • Also presented test system to measure impedance during charging and discharging (1C) at frequencies from 1 Hz to 250 Hz	• Lower impedances and less impedance change between different SoCs at higher frequencies • Impedance increased linearly as SoH decreased • Charge-discharge test system not suitable for online use because DC bias was fixed at 1C, whereas in a real-world system operating current changes frequently
Locorotondo et al. [66]	• EIS using PRBS as a rapid test alternative to a multisine signal • Frequency band 4–1600 Hz • $LiMnNiCoO_2$ 20 Ah cells, ranging in condition from new to end-of-life (by repeated cycling)	• 50 Hz and 500 Hz PRBS are good indicators of battery SoH • Most reliable results obtained with batteries at 20–80% SoC, PRBS discharge current amplitude C/4

ECM, equivalent circuit model; OCV, open-circuit voltage; PRBS, pseudo-random binary sequence; SoC, state of charge.

Reference	Methods	Conclusions and comments
Mingant et al. [67]	• "Quasi-EIS" (QEIS) spectrum based on free current and voltage signals arising from acceleration and regenerative braking in electric vehicle • QEIS analysed using power spectral density (PSD); spectral results used to develop ECM based on series resistance, a capacitance and resistance in parallel, and a series CPE • $LiFePO_4$ 1.4 Ah cells (66-cell modules), subjected to ageing protocols	• Ohmic resistance and capacitance of the ECM evolved monotonically with capacity fade
Yang et al. [64]	• EIS (frequencies not apparent) with fractional Grunwald-Letnikov model • OCV, approximated by terminal voltage, included in model • $LiMnNiCoO_2$ 2950 mAh batteries	• Changing charge capacity across various voltage intervals was linked to capacity fade and used to develop a fractional model of battery ageing • The authors stated that: "A back propagation neural network method was utilized to successfully estimate battery SoH with an error margin of −1.5% to 1.5% without a special state observer or filtering approach"

ECM, equivalent circuit model; OCV, open-circuit voltage; PRBS, pseudo-random binary sequence; SoC, state of charge.

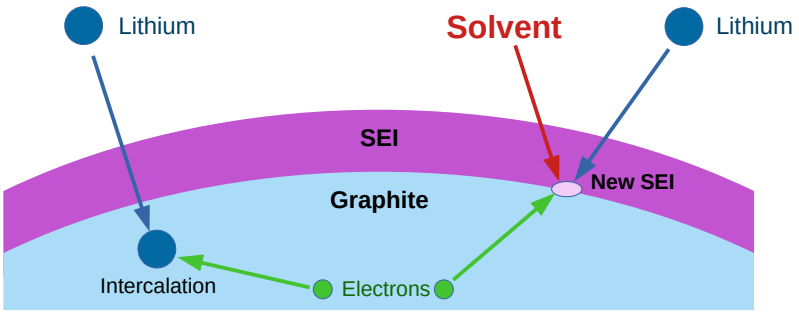

Figure 2.19: Electrochemical intercalation of lithium at a graphite electrode. Note the reaction of lithium with components of the electrolyte to form the solid electrolyte interface (SEI). Adapted from Pinson and Bazant [72].

Other authors have reported that the major component of the SEI is lithium diethylene dicarbonate (LEDC), a compound with high lithium ion conductivity but low electrolyte conductivity (hence its protective effect at the electrode) [74].

Pinson and Bazant [72] used a single-particle model (modelling capacity fade by considering only the loss of lithium to the SEI on the negative electrode on the assumption that other sources of capacity fade can be neglected). They were able to accurately model observed capacity fade, and predict future fade, in cells with graphite anodes. Extension to porous electrodes indicated homogeneous SEI growth throughout the electrode (even at high rates). The lifetime distribution across a sample of batteries was found to be consistent with Gaussian statistics, as predicted by the single-particle model [72].

The formation and cyclic performance of the SEI can be improved by the addition of agents such as vinylene carbonate to the electrolyte prior to lithiation [71]. The SEI can also be damaged by extreme operating conditions or abuse, which manifests as reduced battery performance and accelerated ageing [75]. Changes in R_{SEI} that are visible on EIS spectra can indicate failure after over-discharging leading to SEI breakdown/decomposition and reformation [76].

In addition, a number of researchers have reported the formation in some nanostructured anode materials of a reversible film which contributes to capacity beyond that reported theoretically for a battery [77, 78, 79, 80, 81]. This "reversible" SEI formation with extra capacity is not well understood. All these observations have implications for observed characteristics of batteries under different usage conditions, and would need to be accounted for in any battery model derived from conventional EIS techniques.

2.3 New Approaches with Extra-Low Frequency Measurements

The battery research community's preoccupation with the use of EIS to generate Nyquist plots in order to replicate individual electrochemical processes in batteries has resulted in a plethora of complicated and inconclusive ECMs, and has caused most workers to overlook a fundamental principle behind what is being measured and why. Lasia has pointed out that Nyquist plots lack frequency information, whereas Bode plots of magnitude and phase contain all the necessary detail [82]. Other authors concur [52, 31].

Mauracher and Karden noted as long ago as 1997 that rechargeable batteries ought to be measured and characterised at frequencies that reflected their usage patterns [83]. These authors suggested that measuring down to 1 μHz, representing a period of approximately 278 hours, yielded useful information relating to diffusion outside the electrodes in a battery. The research community appears, oddly, to have

ignored this observation, which is surprising because rechargeable batteries are often found in appliances that are charged daily, which corresponds to a cycling frequency of approximately 11.6 μHz. All publications reviewed here and previously discuss the fitting of models using impedance data obtained at frequencies no lower than 1–5 mHz. Unfortunately, however, Mauracher and Karden adopted the position that only frequencies down to 50 μHz were necessary (and subsequently modelled down to 68 μHz, although they measured down to 6.8 μHz) because EV driving does not usually take more than 2 hours. In addition, they provided incomplete descriptions of how they obtained their data, which were sparse and noisy at lower frequencies.

2.3.1 Advances in Extra-Low Frequency Battery Impedance Measurement

Scott and Hasan described in 2019 a method suitable for ELF battery impedance measurement [84]. A sinewave current was delivered using a two-quadrant power supply (Agilent 66332A) or a four-quadrant source measurement unit (SMU, Keithley 2460A or Agilent E5270). Current and voltage were logged, and magnitude and phase of both at frequencies of interest were determined using a DFT to yield complex impedances. The authors noted that decreasing frequency required decreasing stimulus current in order to limit the charge moved to a value within the capacity of the battery under test [84, 85].

The proposed method was used to measure the impedance of an 800 mAh 14500 lithium-ion battery. External temperature was maintained at 25°C, and SoC at 62%. The data yielded a Bode plot (**Figure 2.20**) with a slope that was not 1 (as would be expected for a pure capacitance) but α in accordance with the fractional theory summarised in Section 2.2.1. From Section 2.2.2 and Equation 2.8, the characteristic CPE equation is

$$i(t) = C_f \frac{d^\alpha v(t)}{dt^\alpha} \tag{2.12}$$

which is represented by an impedance in the Laplace domain of

$$Z_{CPE} = \frac{1}{C_f (j\omega)^\alpha} \quad \text{(see also Equation 2.4)} \tag{2.13}$$

while phase is constant at $\alpha\pi/2$ (Section 2.2.1).

Inspection of the figure shows how the impedance of the CPE dominates at lower frequencies, with the phase settling to approximately 76 degrees, and the slope of the magnitude showing a straight line with slope less than 20 dB/decade. The ohmic series resistance of the battery, R_S, is 0.12 Ω.

The measured data were compared with two ECMs (**Figure 2.21**) which were simulated in SPICE using the method of Scott and Single [86] with corrections by Seshadri and Scott [87]. This method uses a theoretically infinite lumped RC

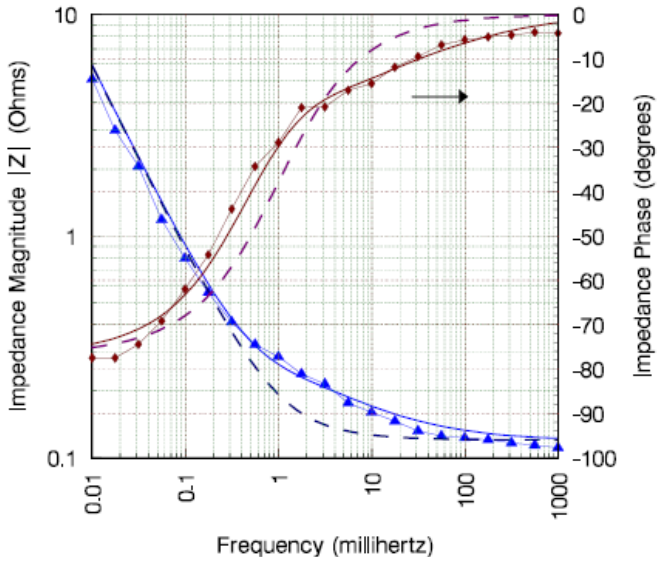

Figure 2.20: Impedance magnitude (left vertical axis, blue traces) and phase (right axis, grey traces) of a 14500 lithium-ion battery for frequencies starting at 10 μHz. Measured data (lines with symbols) compared with those generated by an R-CPE mathematical model (dashed lines) and a split-CPE model (solid lines) simulated in SPICE [84].

approximation to model the behaviour of a CPE, and is based on mathematics originally published by Morrison in 1959 [88].

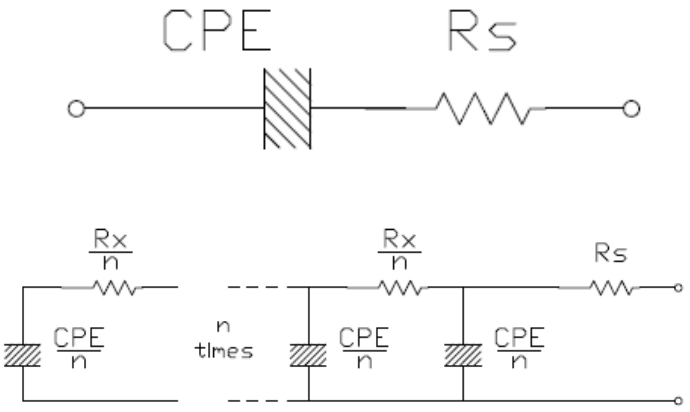

Figure 2.21: Equivalent circuit models suggested by impedance plots at extra-low frequencies [84].

Like the earlier model suggested by Brug et al. in 1984 [46], these new models [84] required few variables, but fitted measured low-frequency data accurately. Note also that the models contain only one element that is capable of storing energy: the CPE, which is described by C_f and α. This is important, because it suggests that any change in SoH should be reflected by changes in either or both of these two

parameters. Moreover, there is no need to add an arbitrary voltage source to the model (as done by many other researchers); such added sources have nothing to do with the way the battery stores and releases energy, and are unnecessary.

The results of the new experiments showed for the first time a possible connection between SoH in a rechargeable battery and the parameters C_f and α. These parameters are not readily apparent when measurements are made at high frequencies, and C_f cannot be deduced from a Nyquist plot (although a Nyquist plot may show α if measurements extend to low enough frequencies: the gradient of the straight constant phase line as illustrated for a Warburg element in **Figure 2.14** is the tangent of α). Further data obtained in lithium nickel manganese cobalt oxide batteries [89] suggest that C_f falls in conjunction with repeated cycling and falling capacity, and that the magnitude and phase of impedance change. The research described in the present thesis continues these efforts to characterise ageing in batteries.

Chapter 3

Achieving Reliable and Repeatable Electrochemical Impedance Spectroscopy of Rechargeable Batteries at Extra-Low Frequencies

3.1 Measuring Batteries at Extra-Low Frequencies

The original research component of this thesis begins in the frequency domain with a continuation of the work described in Section 2.3.1: impedance measurement by EIS of batteries at ELFs, and investigation of the connections between these measurements and battery ageing. New methods to obtain better quality EIS data and their application in the development of an improved battery model that is detectable only at ELFs and is based on only a small number of circuit elements (see Section 2.3) but that can nevertheless accurately characterise the battery and its condition are discussed. The novel EIS approaches include the use of frequency-division and time-division multiplexing of non–small-signal (working) currents with small-signal measurement tones. Note that the effects on charge movement at the electrode level in the time domain are discussed further in Chapter 4.

Following some introductory notes, this chapter presents a discussion of charge distribution difficulties that may be encountered when measuring at ELFs, and a charge leakage problem that was encountered with the 66332A units and its solution. The paper "Achieving Reliable and Repeatable Electrochemical Impedance Spectroscopy of Rechargeable Batteries at Extra-Low Frequencies" that was published in "IEEE Transactions on Instrumentation and Measurement" in June 2022 is then presented.

3.1.1 The Rationale For Extra-Low Frequency Measurements

The need to measure rechargeable batteries at frequencies that reflect their real-world usage patterns (i.e., daily or weekly cycles of charging and discharging) was acknowledged as long ago as the 1990s [83], but this need has been largely ignored by the battery research community. Among the reasons for this are the difficulties associated with making these measurements. These difficulties are addressed in the paper that follows, and include briefly poor or non-availability of suitable commercial impedance meters, very long measurement times, problems with consistency or repeatability of measurements, and interference of transient time domain phenomena.

Note that, in addition to the frequency-division and time-division multiplexing working current methods described in this section, a third method involving a high-current pilot tone was also originally tested. The pilot tone is a single frequency sinusoidal stimulus set well above the measurement frequencies of interest (e.g., 20 mHz or higher) notwithstanding the problems this might cause in terms of charge distribution (see Section 3.2). This method was found to produce poor quality and inconsistent impedance data, with erratic phase information in particular, and was abandoned. This will be discussed further in Chapter 6.

3.2 Relationship Between Charge Transfer and Frequency

A fundamental problem of making ELF impedance measurements relates to control over the movement of charge. We would like to be able to measure down to 1 μHz, or even lower. A half cycle (which would involve continuous charging or discharging) at this frequency would occupy more than 11 days. This may exceed the charge excursion capabilities of the battery, a problem which has in the past caused researchers to abandon ELF measurement attempts [90].

If a small signal being used to measure impedance has an amplitude of I_0 and frequency f, its time domain equation will be

$$I = I_0 \sin(2\pi f t) \tag{3.1}$$

As discussed by Scott and Hasan [84], the integral of current will show the amount of charge transferred to and from the cell. The area under the positive half cycle is the amount of charge moved into the cell, Q_{in} and the negative half of the cycle represents the amount of charge moved out of the cell, Q_{out}:

$$Q_{in} = \int_0^{T/2} I dt = \int_0^{T/2} I_0 \sin(2\pi f t) dt \tag{3.2}$$

and

$$Q_{out} = \int_{T/2}^{T} I dt = \int_{T/2}^{T} I_0 \sin(2\pi f t) dt \tag{3.3}$$

Integration of (3.2) and (3.3) results in

$$Q_{in} = -\frac{I_0}{2\pi f}[\cos(2\pi f t)]_0^{T/2} = -\frac{I_0}{2\pi f}[\cos(\pi f T) - 1] \tag{3.4}$$

and

$$Q_{out} = -\frac{I_0}{2\pi f}[\cos(2\pi f T) - \cos(\pi f T)] \tag{3.5}$$

However, $fT = 1$, which leads to

$$Q_{in} = \frac{I_0}{\pi f} \tag{3.6}$$

and

$$Q_{out} = -\frac{I_0}{\pi f} \tag{3.7}$$

The negative sign denotes the direction of the charge flow with respect to the source. The net overall charge movement over one complete cycle should be $\Delta Q = 0$, otherwise there may be unexpected waveform distortion.

Note that the peak amplitude of the charge delivered is dependent on the frequency of the signal. As frequency decreases, the current stimulus must be reduced to prevent the charge excursion flattening or overcharging the battery. Low current

stimuli should therefore be used at ELFs. The bzdcp66 software used by the Battery Modelling Group (see Section 1.5 and the paper presented later in this chapter) requires the user to set the total charge that may be sourced or sunk; if this limit is exceeded, the measurement will abort. When carrying out ELF measurements, current stimuli may need to be set so low that noise could potentially become a problem, but early experiments upon which the research presented here was based indicated that measurements down to at least 1 μHz would be feasible, and data discernible above the noise floor.

There is also a potential problem associated with excessive peak-to-peak amplitude of the signal when adding a number of frequencies together. This is seen in communications and in applications such as radar and sonar where there is a need to maximise average power for a given amplitude range. The problem was highlighted by Schroeder in 1970, who defined peak factor as the difference between the maximum and minimum amplitudes of the signal divided by its root mean square value, and proposed a method for adjusting the phase angles of the components of a signal to yield low peak factors (equivalent to a single sinusoid of equal power) [91]. Schroeder's equations were accordingly incorporated into the bz3p66 and bzdcp66 programs described in Section 1.5 and in the paper that follows.

3.3 Charge Leakage

A problem encountered with analog-to-digital conversion (and vice-versa) and apparent charge leakage with ELF impedance measurements should also be acknowledged here. The HP/Agilent/Keysight 66332A two-quadrant source measurement units used in these experiments admit up to 12 and 16 bits, respectively, for digital-to-analog and analog-to-digital conversion. Ideally, when constructing signals digitally, a measurement unit should round towards zero, but the 66332A units were found to round down. This becomes a problem when making very long measurements, even when 12 or 16 bits of resolution are available. The problem manifests as the battery discharging very slowly during the measurement (**Figure 3.1)**.

This type of error can be corrected by monitoring charge and adjusting for any drift during the measurement. Alternatively, the data may be adjusted to eliminate the ramp after the measurement is complete but before processing; this option is available in the discrete-time Fourier transform software used in these experiments. Any slope or offset is detected using linear regression and removed from the voltage and current data before impedance magnitude and phase are calculated.

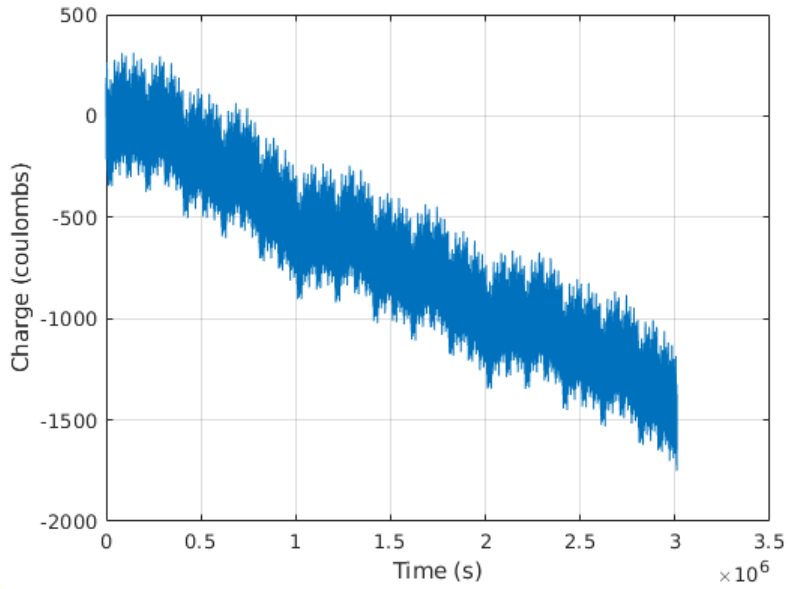

Figure 3.1: Cumulative charge during EIS measurement using a 66332A two-quadrant source measurement unit down to 1 μHz (three cycles of the lowest frequency requested) on a 2600 mAh ICR (lithium cobalt oxide) 18650 battery. Note the overall loss of charge over the course of the measurement (approximately 35 days).

Achieving Reliable and Repeatable Electrochemical Impedance Spectroscopy of Rechargeable Batteries at Extra-Low Frequencies

Christopher Dunn and Jonathan Scott, *Life Senior Member, IEEE*

***Abstract*— There is a need for techniques for efficient and accurate measurement of the impedance of rechargeable batteries at extra-low frequencies (ELFs, of the order of microhertz), as these reflect real usage and cycling patterns, and their importance in fractional battery circuit modeling is becoming increasingly apparent. Major impediments include the time required to perform such measurements and "drift" in impedance values when measurements are taken from the same battery at different times. Moreover, commercial impedance analyzers are generally unable to measure at these frequencies. We describe here our use of programmable two-quadrant power supplies to deliver multiple small-signal measurement tones in the presence of large-signal "working" currents, and our use of these data to generate impedance measurements with good precision and in reasonable time. The improvement in the quality of electrochemical impedance spectroscopy (EIS) data is verified through root-mean-square error (RMSE) when fitting equivalent-circuit models (ECMs).**

***Index Terms*— Electrochemical impedance spectroscopy (EIS), equivalent-circuit model (ECM), extra-low frequency (ELF), impedance, measurement, rechargeable batteries.**

I. Introduction

ELECTROCHEMICAL impedance spectroscopy (EIS) is a powerful and non-destructive tool by which the properties and characteristics of a battery can be deduced by determining impedance over a wide frequency range [1], [2]. EIS is claimed to be a reliable indicator of state of charge (SoC) [3], [4] and state of health (SoH) [5]. The battery research community has traditionally tended to focus heavily on equivalent-circuit models (ECMs) fitted to EIS data. These circuit models are considered key to prediction of SoC and SoH [2], [5]–[8], although the reliability of some claims, particularly around SoC, are questioned by some authors (see Mauracher and Karden [9], for example).

Impedance spectra can be presented either as Bode plots or Argand diagrams (also called Nyquist plots). The Bode plots are now considered to be more informative [1]. This is because frequency information is implied rather than shown explicitly in Nyquist plots, while the Bode plots contain all necessary detail [2], [7], [10]. This article will use Bode plots exclusively.

Manuscript received February 12, 2022; revised April 13, 2022; accepted May 17, 2022. Date of publication June 6, 2022; date of current version June 14, 2022. The Associate Editor coordinating the review process was Dr. Kamel Haddadi. *(Corresponding author: Christopher Dunn.)*

The authors are with the School of Engineering, The University of Waikato, Hamilton 3240, New Zealand (e-mail: cjdunn@xtra.co.nz).

Digital Object Identifier 10.1109/TIM.2022.3180429

Mauracher and Karden [9] noted as long ago as 1997 that rechargeable batteries ought to be measured and characterized at frequencies that reflect their usage patterns. These authors suggested that measuring down to 10 μHz, representing a period of approximately 28 h, yielded useful information relating to diffusion outside the electrodes in a battery. Measurements taken at these extra-low frequencies (ELFs) provide insights into model formulation [11] and have been shown to aid model fitting [12]. The use of ELFs is new, which is surprising because rechargeable batteries are often found in appliances that are charged daily, which corresponds to a cycling frequency of approximately 11.6 μHz.

Measuring in the ELF range is associated with a number of difficulties. These include the time needed to make the measurement. The minimum practical period for an EIS measurement is the reciprocal of its frequency. To minimize the time required, a single stimulus signal that includes all frequencies of interest can be used [13]. The magnitudes and phases of voltages and currents at these frequencies can be recovered using a Fourier transform. In this case, the stimulus is referred to as a multitone or multisine. Other complex waveforms can be used to find impedances at multiple frequencies, for example, a pseudorandom binary sequence (PRBS) [14], [15], although there is a tradeoff between increasing numbers of frequencies and the signal-to-noise ratio (SNR) of the measurement.

Researchers have been faced with difficulties in finding equipment suitable for operation at ELFs. Almost all commercial impedance meters have a lower frequency limit of 1 mHz, which may have something to do with the many investigators reporting results obtained at frequencies no lower than this [16]–[23]. The Solartron 1260A is rated to measure down to 10 μHz, but its use has been found to require great care when working with "wet" systems such as batteries [13].

Modern electrochemical theory accepts that batteries exhibit "fractional capacitance" [24], and an ECM should therefore contain constant phase elements (CPEs) to embody battery characteristics [12], [13], [25]. Fractional components are associated with long decay tails after a stimulus is applied or removed [26], [27], and these tails are thought to be among the problems encountered when measuring "wet" systems with the Solartron [13].

The impedance of a battery is known to "drift." Fig. 1 shows EIS data obtained at five frequencies from a near-new

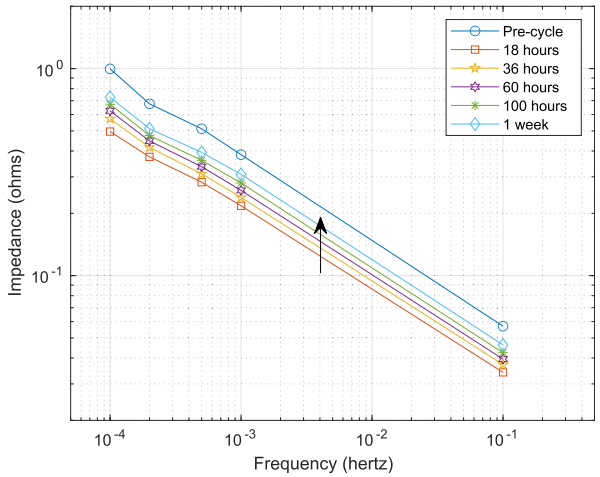

Fig. 1. Impedance (magnitude) of a 30-Ah AGM lead-acid battery at five frequencies before and at various times after a charge–discharge cycle at 5 A. The arrow shows the impedance drift over time as the battery equilibrates.

30-Ah absorbent glass mat (AGM) lead-acid battery of the type typically found in light traction and power backup applications. Measurements were made before and at several times after cycling the battery and returning it to 80% SoC. Note that small-signal impedance of the battery is halved by cycling, with over a week being required for the battery to re-equilibrate and return to its original state. Other reported transient phenomena include the "coup de fouet" ("crack of the whip"), which causes a sudden drop in voltage and change in impedance with subsequent recovery when a fully charged lead-acid battery is initially discharged [28].

We have observed impedance drifts in other battery chemistries, including the lithium family, although relaxation times seem to be much shorter. These drifts, which have been noted by other researchers [29], make observation more difficult and add to the frustration experienced by researchers seeking reliable, repeatable EIS data. This article presents novel measurement strategies that address these problems and demonstrates the importance of measured data quality in battery characterization and accurate ECM fitting.

II. New Methods for Battery Impedance Measurement

All data obtained from the new system were measured at 22 °C with two-quadrant precision sources using four-wire connections controlled via GPIB interfaces by Raspberry Pi 4 computers running custom software written in C. The software utilities are: 1) bz3p66 and 2) bzdcp66 (battery impedance with: 1) triphasic pulses or 2) added dc component on our "Prologix/66332A" hardware) [30]. These command line programs, which are called by scripts setting the parameters for each run, minimize the risk of interference between a small measurement signal and large "working" current signal using time-division or frequency-division multiplexing, respectively. Both the programs make multitone impedance measurements by sourcing and sinking current and recording times, currents, and voltages in three-column ".tvi" data files (timestamp, voltage, current). Default frequency ranges are 1-2-5 sequences between minimum and maximum specified

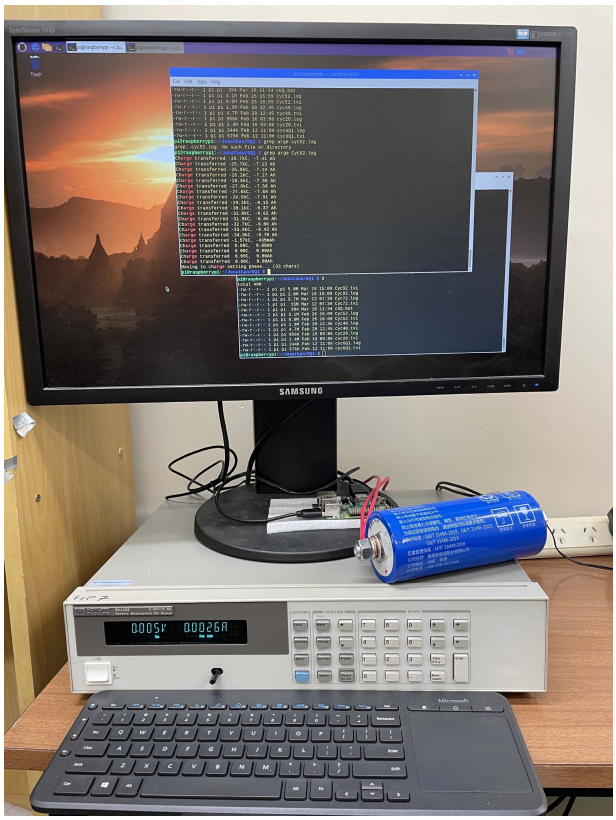

Fig. 2. Example measurement system setup to use an HP66332A. Note the unenclosed Raspberry Pi model 4 on the monitor base. The blue cylinder is the battery under test, a single 40-Ah LTO cell.

values, but any set of frequencies is possible. The complex impedance $Z(\omega)$ for each frequency of interest

$$\text{where } Z(\omega) = \frac{|V|}{|I|} e^{j(\phi_V - \phi_I)}$$

is obtained from the.tvi data by performing a discrete Fourier transform with "dftv," a program based on software originally described by Scott and Parker [31] for use with SPICE.

The battery used in new ELF experiments was a brand new lithium titanate (LTO) 40-Ah 2.3-V 66160H cell. Fig. 2 depicts the equipment setup. Fig. 3 presents a block diagram of the system. The measurement parameters were based on our experience of battery cycling and impedance measurement, the manufacturer's ratings for the battery under test, and the capabilities of the 66332A units.

A. Time-Division Multiplexing: bz3p66

bz3p66 alternately subjects the battery to a small-signal measurement multitone and a "working" stimulus signal that reflects a normal usage current. Interference is minimized by reducing as far as possible the change in terminal voltage that is seen following the application of a large working signal (i.e., minimizing the artifact or "pulse tail" that characterizes fractional elements as described earlier [27]). The working stimulus is a triphasic pulse, a stimulus believed from empirical observations in human-implanted electrodes to minimize artifact tails [26]. Some mathematics confirm that

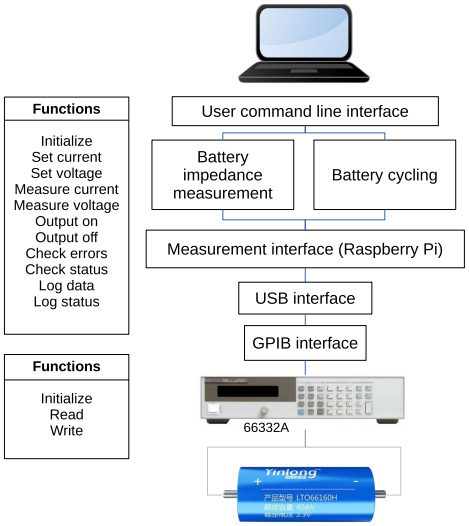

Fig. 3. Measurement system architecture.

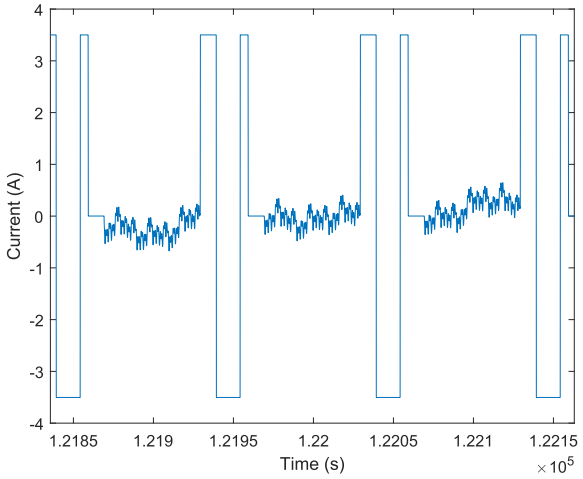

Fig. 4. Time-domain plot: bz3p66 on LTO, 30-s ±3.5-A triphasic pulse every minute. Note the 10-s "rest" after the end of each pulse to allow for the settling of the long voltage tail that characterizes fractional devices, and the small-signal measurement tones between the pulses.

the optimal pulse in a fractional derivative system consists of three equal amplitude, alternating-polarity pulses in a 2-3-1 duration sequence (see Fig. 4).

bz3p66 outputs two time-domain files, one that includes the triphasic pulse (".ptvi") and one with the pulse removed: this is the .tvi file that is used for further analysis.

The LTO battery was cycled once using a constant current-constant voltage (CCCV) regime. The maximum ($V_{\max}$) and minimum ($V_{\min}$) CV voltages were set at 2.7 and 1.8 V, respectively; the charge and discharge CC currents were 5 A (the maximum available from the 66332A units). CV phases were ended at ±1 A. The battery was rested after cycling for 10 min at a final SoC of 65%. Following this, bz3p66 was run four times with working ± 3.5-A current pulses as follows:

1) 30-s pulse every 4 min;
2) 30-s pulse every 2 min;
3) 30-s pulse every minute (see Fig. 4);
4) 60-s pulse every 2 min.

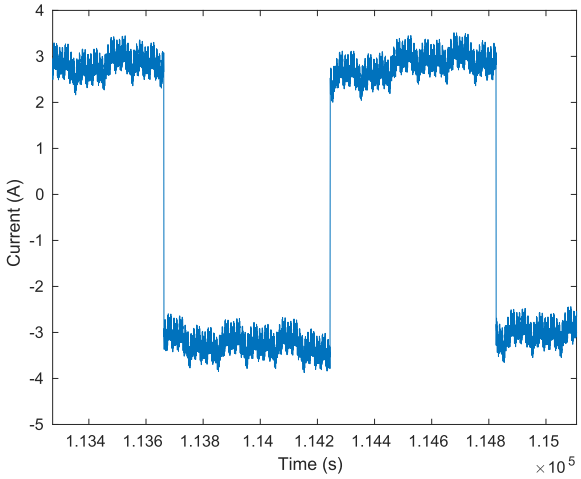

Fig. 5. Time-domain plot: bzdcp66 on LTO, ±3-A 860-μHz square wave. Note offset measurement tones.

The measurement tones were 1-2-5 sequences from 10 μHz (three cycles) to 1 Hz. The maximum total charge that could be sourced or sunk ($dQ_{\max}$) was set at 5 Ah (0.125C). This charge is distributed across all measurement tones.

B. Frequency-Division Multiplexing: bzdcp66

bzdcp66 performs battery measurements by exposing the battery to a small-signal multitone and a working stimulus signal simultaneously. This is accomplished by superimposing the EIS multitone on a periodic square wave which aims to mimic the effect of a working dc signal (see Fig. 5).

The battery was cycled to 65% SoC as for bz3p66 and then subjected to sets of consecutive bzdcp66 runs as follows:

1) three runs with 3-A square wave ($I_{\rm dc}$) at a frequency of 860 μHz ($f_{\rm dc}$), i.e., a period of approximately 20 min;
2) three runs with $I_{\rm dc}$ 35 mA with the same $f_{\rm dc}$ (i.e., negligible working current signal);
3) cycle again to reset and ensure SoC;
4) repeat.

The measurement tones were 1-2-5 sequences from 20 μHz (three cycles) to 2 Hz. $dQ_{\max}$ was 5 Ah, distributed across all measurement tones as with bz3p66.

The working and EIS signals for bzdcp66 are selected so that their spectra do not overlap. This is done by choosing EIS frequencies that are multiples of f_0, the lowest frequency, and powers of 2 or 5

$$f_{\rm test} = 2^p \times 5^q \times f_0 \tag{1}$$

where $f_{\rm test}$ is a test frequency, and p and q are integers. Thus, each frequency in the multisine has the prime factors 2 and 5 only in its multiple of f_0. The square wave is then given a frequency that is a multiple of f_0 but that does not have 2 or 5 as prime factors, for example

$$f_{\rm dc} = 7^i \times 11^j \times 13^k \times 17^l \times f_0 \tag{2}$$

where i, j, k, and l are integers. This suggests that $f_{\rm dc}$ might be a multiple of 7, 11, 13, 17, etc.

As a final check, all odd multiples of $f_{\rm dc}$ can be compared with each multisine tone, and a larger factor is chosen for $f_{\rm dc}$

if there are "near-miss" differences that might pollute adjacent tones in a windowed Fourier transform. For these experiments, 860 μHz was chosen as this is a multiple of 43 (a prime number) and the fundamental frequency of 10 μHz, and it has no harmonics close to any of the test frequencies.

C. Data Quality Evaluation: ECM Fitting

The quality of the data was evaluated via ECM fitting. The procedure used was developed at this center and has been described recently by Poihipi *et al.* [12]. Briefly, the measured data are used to generate an ECM via an optimization method based on the downhill simplex algorithm of Nelder and Mead and implemented in C as a command line program [32], [33].

The optimization target is defined as a root-mean-square error (RMSE) value calculated from complex impedances as indicated by the measured data. The final RMSE reflects how well the model fits the data: a perfect fit will yield an RMSE approaching zero; higher values indicate noisier (less stable) data. The choice of appropriate model starts with the simplest ECM which is based on a single resistor and CPE in series (R-CPE). If the resulting RMSE indicates a poor fit, selection moves to the next model in the chain of complexity, a resistor, and two CPEs in series (R-CPE-CPE). Fitting then starts with parameter values returned by the R-CPE case. If the previous fit had resulted in an RMSE dictated chiefly by noise in the data, the additional component will not improve the fit and the quality of the data can be said not to justify the more complicated model, even if that model is in fact more correct. If the additional element reduces the RMSE, however, we may conclude that the extended model represents the data better. The reader is referred to Poihipi *et al.* [12] for more details of the ECM fitting method.

III. Results

A. Time-Division Multiplexing: bz3p66

The impedance magnitude and phase curves obtained from the Fourier-transformed .tvi data generated by bz3p66 are shown in Fig. 6. Varying the duration and/or frequency of the triphasic pulse made little or no difference to magnitude and phase profiles, with consistent disturbance of the phase response around 0.1 mHz.

Different regions of the Bode plot reveal various aspects of the battery's characteristics and condition that can be represented in an ECM. Briefly, the high-frequency section of the magnitude plot approaches a horizontal asymptote that represents the series resistance (R_s) of the battery, while the region below 1 mHz is dominated by a CPE (i.e., the R-CPE model). Other behaviors of the magnitude and phase plots reveal hints as to other circuit elements that might be appropriate. For example, the rounded "knee" between the R_s and first CPE regions suggests a second fractional series element [12], [13], [27] (i.e., the R-CPE-CPE model). The results showing the relationship between the quality of the measured data and ECM determination are summarized later (see Section III-D).

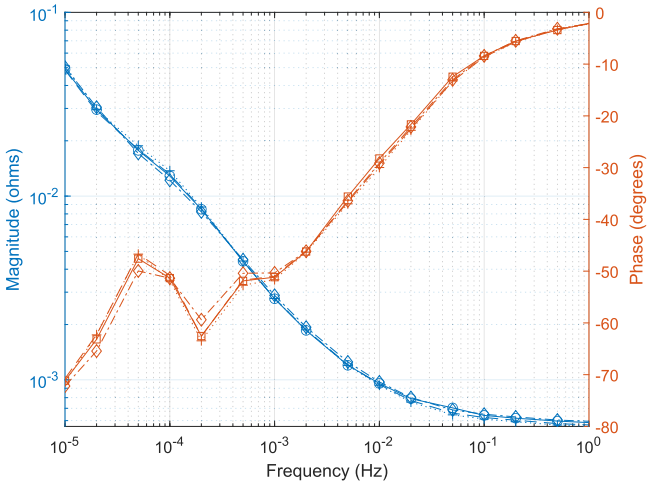

Fig. 6. bz3p66 on LTO battery: impedance magnitude and phase of four runs with differing triphasic pulse frequencies and durations. Solid lines, open circles (magnitude), or squares (phase) = 30-s pulse repeated every minute; dashed lines = 30-s pulse every 2 min; dotted lines with crosses = 30-s pulse every 4 min; dot-dash lines with open diamonds = 60-s pulse every 2 min. On this and all subsequent plots, magnitude runs from top left to bottom right, and phase from bottom left to top right.

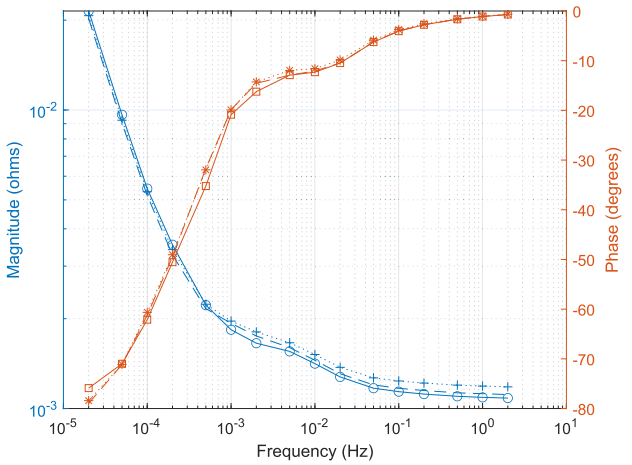

Fig. 7. Impedance magnitude and phase: bzdcp66 on LTO battery with 3-A square wave. The battery was cycled twice, with three consecutive impedance measurements after each cycling. Solid lines with open circle (magnitude) or square (phase) = first of three consecutive impedance measurements after first cycling; dashed lines = third of three consecutive measurements after first cycling; dotted lines with star/asterisk = second of three consecutive measurements after second cycling.

B. Frequency-Division Multiplexing: bzdcp66

Figs. 7 and 8 show impedance magnitude and phase curves overlaid from repeated runs (three plots per chart to maintain clarity) of bzdcp66 with a 3-A working square wave. Magnitude and phase appeared consistent and repeatable between runs, whether interspersed with additional cycling or not, and the low-frequency phase response did not show the disturbance exhibited repeatedly by bz3p66.

Similar consistency between runs was noted when bzdcp66 was run with a negligible (35 mA) square wave to mimic a small-signal measurement multitone with no working current (see Figs. 9 and 10). No impedance drift due to re-equilibration

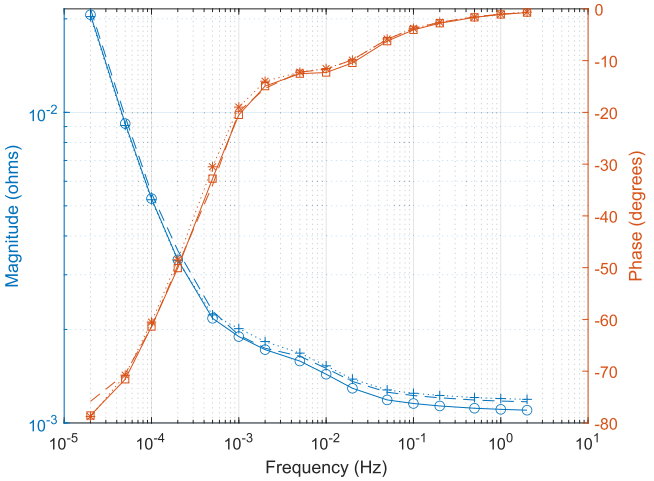

Fig. 8. Impedance magnitude and phase: bzdcp66 on LTO battery with 3-A square wave. Solid lines with open circle (magnitude) or square (phase) = second of three consecutive impedance measurements after first cycling; dashed lines = first of three consecutive measurements after second cycling; dotted lines with star/asterisk = third of three consecutive measurements after second cycling.

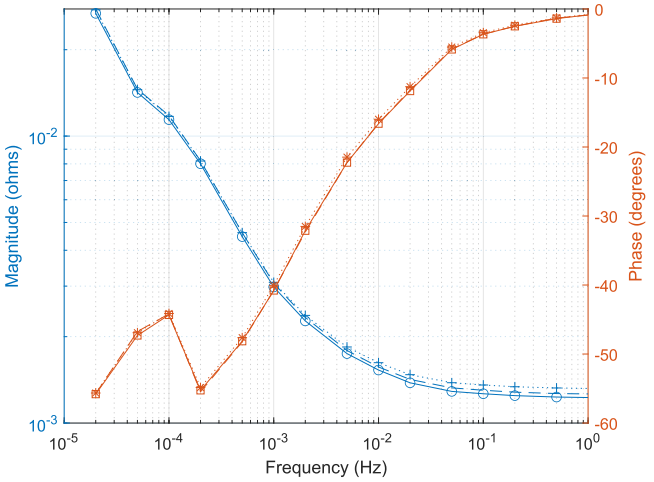

Fig. 9. Impedance magnitude and phase: bzdcp66 on LTO battery with 35-mA square wave. Solid lines with open circle (magnitude) or square (phase) = first of three consecutive impedance measurements after first cycling; dashed lines = third of three consecutive measurements after first cycling; dotted lines with star/asterisk = second of three consecutive measurements after second cycling.

after cycling as described earlier in lead-acid batteries (see Fig. 1) was evident. These results are consistent with observations that suggest very rapid re-equilibration of batteries based on lithium chemistries. Interestingly, the phase irregularity around 0.1 mHz seen with time-division multiplexing reappeared in the presence of negligible I_{dc}.

C. Comparison of Time-Division and Frequency-Division Multiplexing: bz3p66 Versus bzdcp66

In view of the homogeneity between sweeps for each type of measurement (i.e., bz3p66 and bzdcp66 with or without a working square wave), individual representative plots may be used for visual comparison of the different methods. Fig. 11 contrasts third (final) runs from one set each of bzdcp66 runs with 3-A and 35-mA working currents.

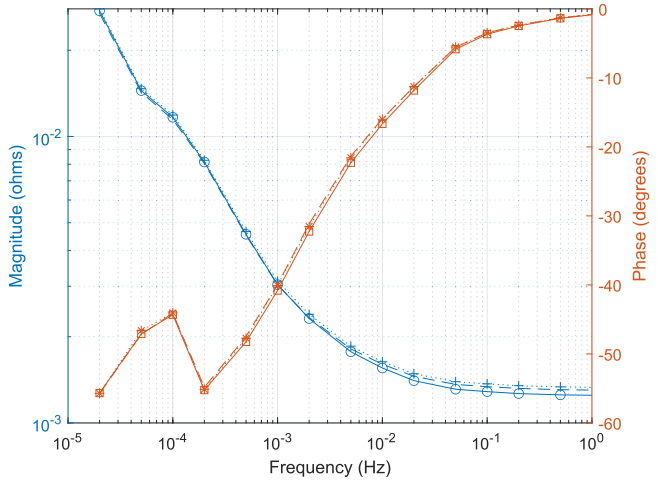

Fig. 10. Impedance magnitude and phase: bzdcp66 on LTO battery with 35-mA square wave. Solid lines with open circle (magnitude) or square (phase) = second of three consecutive impedance measurements after first cycling; dashed lines = first of three consecutive measurements after second cycling; dotted lines with star/asterisk = third of three consecutive measurements after second cycling.

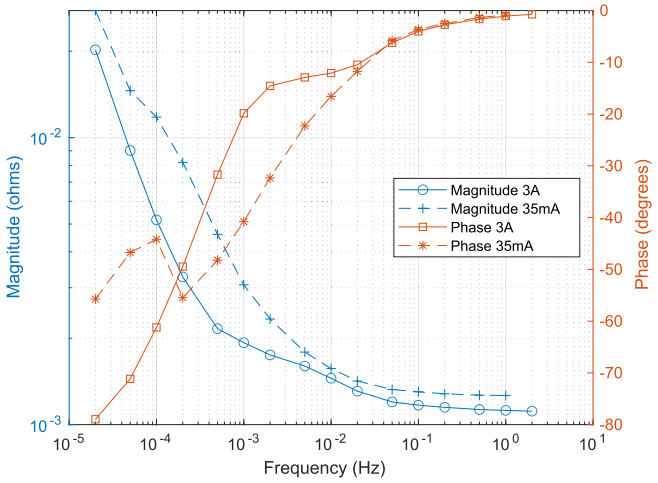

Fig. 11. Impedance magnitude and phase plots: representative bzdcp66 runs (third of three sweeps for each square wave magnitude) on LTO battery with 3-A and 35-mA square waves. The solid lines with open symbols show magnitude and phase achieved with a 3-A square wave; the dashed lines with star/asterisk show results with a 35-mA (i.e., negligible) square wave.

Note the reduction in impedance magnitude when a significant working signal is applied, particularly in the region below 0.5 mHz (e.g., 0.0052 versus 0.0118 Ω at 0.1 mHz) and the elimination of erratic behavior in the low-frequency region of the phase plot. Additional shaping of the phase curve is also evident in the region around 10 mHz in the presence of a 3-A working current. This is not visible when the square wave is effectively "turned off" and implies the availability of additional information that might be important in the development of a realistic ECM for the battery.

Finally, Fig. 12 repeats the above with the addition of magnitude and phase information from a representative bz3p66 run (30-s pulse every 2 min). The magnitude trace follows that of bzdcp66 with negligible square wave in the low-frequency

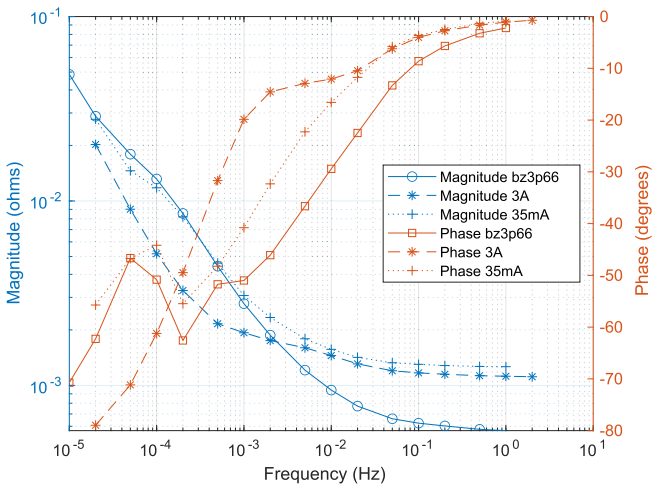

Fig. 12. Impedance magnitude and phase plots: comparison of bzdcp66 with a 3-A or 35-mA square wave and bz3p66 runs on LTO battery. Solid lines with open symbols = bz3p66 sweep with a 30-s triphasic pulse every 2 min; dashed lines with asterisks = third of three bzdcp66 sweeps with a 3-A square wave; dotted lines with crosses = third of three bzdcp66 sweeps with a 35-mA square wave.

region, but with markedly erratic phase behavior. Most notable, however, is the suppression of impedance magnitude in the higher frequency R_s region.

D. ECM Fitting

Table I summarizes the results of ECM fitting to data obtained using the three measurement techniques described above. Data from all runs with each type of measurement (bzdcp66 with 3-A square wave, bzdcp66 with 35-mA square wave, and all triphasic pulse variations of bz3p66) were, respectively, concatenated into three combined files for the analysis, one for each type of measurement.

Observing the changes in parameter values and RMSEs when attempting to develop the model from the basic R-CPE case (see Table I), only bzdcp66 with a 3-A working square wave yielded data that allowed the second CPE to be "seen." This level of model refinement was not possible with either bzdcp66 with a 35-mA square wave or bz3p66, as shown by the negligible changes in parameter values upon addition of the second CPE. Note also the identical RMSEs for the R-CPE and R-CPE-CPE models with these two last measurement techniques, with α values approaching zero for the second CPE (see Table I). In contrast, addition of the second CPE when fitting to data generated by bzdcp66 with 3-A working current resulted in a halving of the RMSE value (see Table I).

IV. Discussion

Evidently, charge density or rates of current flow must be taken into account when measuring impedance and parameterizing models. Apparent impedance decreases when higher currents are passed, an effect that is exaggerated at low frequencies. Fig. 13 shows data from an exploratory experiment in which $|Z|$ was measured using a multisine run at maximum current ($I_{\max}$) values ranging from 5 mA to 7 A on a lithium

TABLE I
ECM Parameter Estimation

ECM	R_s	α	C_F	C_2	α_2	RMSE
bzdcp66 3 A square wave (frequency multiplexing)						
R-CPE	1.252	0.80	73,270			0.1271
R-CPE-CPE	0.406	0.91	17,130	1218	0.07911	0.0651
bzdcp66 35 mA square wave (frequency multiplexing)						
R-CPE	1.228	0.63	10,280			0.0804
R-CPE-CPE	1.069	0.63	10,300	6236	0.00004	0.0804
bz3p66 (time multiplexing)						
R-CPE	0.559	0.66	11,330			0.1020
R-CPE-CPE	0.434	0.66	11,290	8042	0.00006	0.1020

CPE, constant phase element; ECM, equivalent-circuit model; RMSE, root mean square error.
R_s, series resistance ($ohm \times 10^{-3}$); C_F and C_2, fractional capacitances ($F/s^{(1-\alpha)}$) of first (R-CPE model) and second (R-CPE-CPE model) CPEs, with respective slopes denoted by α and α_2.

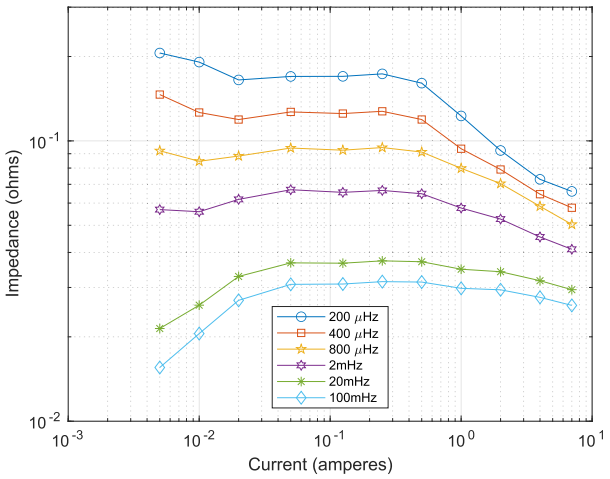

Fig. 13. Impedance of a 4-Ah LiFePO4 battery plotted against currents ranging from 5 mA to 7 A at six frequencies (see figure key). Measurements taken on a Keithley 2460A four-quadrant precision source controlled by a Raspberry Pi running custom software [30].

iron phosphate battery rated at 4 Ah. Frequencies ranged from 200 μHz to 100 mHz. Measurements from 50 to 200 mA (approximately C/50) behaved like "small" signals. At higher frequencies, increasing current had less effect, but although the 7-A maximum current had a marked effect on the low-frequency traces, it did not "pull" the impedance down to a high current asymptote, which suggests some permanent resistive mechanism that cannot be overcome. This is more apparent in Fig. 14, which shows full frequency sweeps carried out with $I_{\max}$ set at 50 mA and 7 A after cycling.

Unfortunately, it is not possible to draw substantial current from a battery for prolonged periods because the battery will run flat, a major difficulty encountered by Budde-Meiwes *et al.* [29]. As described by Scott and Hasan [13], the peak amplitude of charge delivered is dependent on the frequency of the signal. As frequency decreases, the current stimulus must be dropped significantly to prevent the charge excursion flattening or overcharging the battery. Budde-Meiwes *et al.* [29] abandoned ELF measurements because it is not possible to make a reliable measurement of battery impedance below 1 mHz without running for periods well in excess of 1000 s. Overall, the twin aims of measuring

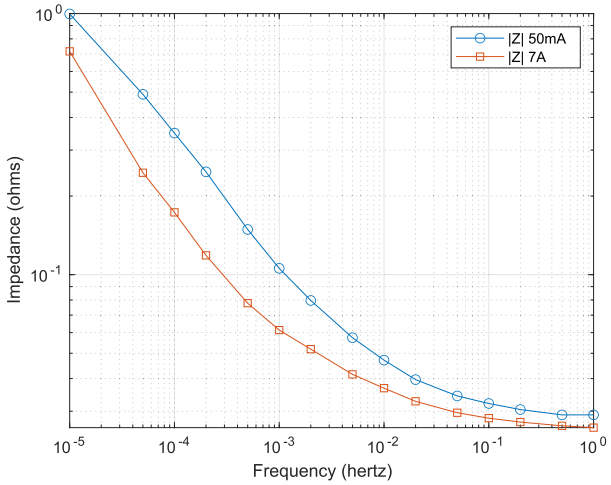

Fig. 14. Impedance versus frequency for a 4-Ah LiFePO4 battery at low (50 mA) and high (7 A) currents. Full frequency sweeps from from 10 μHz to 1 Hz.

at ELFs while the battery under test is delivering significant current cannot be met with techniques that have been available until now. In this article, we have described two methods permitting ELF measurements while the battery is delivering or receiving substantial current or charge without going flat or overcharging.

V. Conclusion

We have presented two novel methods for measuring the impedance of batteries at ELFs in the presence of substantial currents. One method time-division multiplexes EIS measurement stimuli with large "working" current bursts; the second method multiplexes in the frequency domain, relying on Fourier transformation to recover the EIS data from "underneath" the large working current. Both the methods break the fundamental limiting tradeoff noted by Budde-Meiwes *et al.* [29] between the magnitude of the "working" current that can be drawn during measurement and the lowest attainable frequency in the EIS. We show here measurements to 10 μHz, and note that exploratory measurements to below 500 nHz have been made.

Frequency-division multiplexing proves superior in stabilizing the impedance spectrum against impedance drift phenomena. That stable impedance agrees most closely with expectations from models [3], [12], [13], [27].

Thus, substantial charge displacement achieved with the frequency-domain method appears to stabilize battery impedance more effectively and maximize measured data quality when compared with large peak currents achieved with the time-domain method. This implies that it is charge displacement rather than working current value that should be maximized to expose the true working impedance of a battery and to optimize data for ECM fitting. This is consistent with the expectation that surface layer processes on the battery electrodes are responsible for impedance drift; they may also be implicated in the erratic phase behavior seen at ELFs. The exact chemical nature of these interfacial processes requires further clarification.

Acknowledgment

The authors wish to acknowledge the assistance of WaikatoLink and the Waikato University Doctoral Scholarship.

References

[1] A. Lasia, *Electrochemical Impedance Spectroscopy and Its Applications*. New York, NY, USA: Springer, 2014.
[2] W. Choi, H. C. Shin, J. M. Kim, J. Y. Choi, and W. S. Yoon, "Modeling and applications of electrochemical impedance spectroscopy (EIS) for lithium-ion batteries," *J. Electrochem. Sci. Technol.*, vol. 11, no. 1, pp. 1–13, Feb. 2020.
[3] T. J. Freeborn, B. Maundy, and A. S. Elwakil, "Fractional-order models of supercapacitors, batteries and fuel cells: A survey," *Mater. Renew. Sustain. Energy*, vol. 4, no. 3, p. 9, Sep. 2015.
[4] D. A. Howey, P. D. Mitcheson, V. Yufit, G. J. Offer, and N. P. Brandon, "Online measurement of battery impedance using motor controller excitation," *IEEE Trans. Veh. Technol.*, vol. 63, no. 6, pp. 2557–2566, Jun. 2014.
[5] L. Ungurean, G. Cârstoiu, M. V. Micea, and V. Groza, "Battery state of health estimation: A structured review of models, methods and commercial devices," *Int. J. Energy Res.*, vol. 41, no. 2, pp. 151–181, 2017.
[6] M. Cacciato, G. Nobile, G. Scarcella, and G. Scelba, "Real-time model-based estimation of SOC and SOH for energy storage systems," *IEEE Trans. Power Electron.*, vol. 32, no. 1, pp. 794–803, Jan. 2017.
[7] U. Westerhoff, K. Kurbach, F. Lienesch, and M. Kurrat, "Analysis of lithium-ion battery models based on electrochemical impedance spectroscopy," *Energy Technol.*, vol. 4, no. 12, pp. 1620–1630, Dec. 2016.
[8] C. F. Zou, L. Zhang, X. Hu, Z. Wang, T. Wik, and M. Pecht, "A review of fractional-order techniques applied to lithium-ion batteries, lead-acid batteries, and supercapacitors," *J. Power Sources*, vol. 390, pp. 286–296, Jun. 2018.
[9] P. Mauracher and E. Karden, "Dynamic modelling of lead/acid batteries using impedance spectroscopy for parameter identification," *J. Power Sources*, vol. 67, nos. 1–2, pp. 69–84, 1997.
[10] A. Lasia, "Definition of impedance and impedance of electrical circuits," in *Electrochemical Impedance Spectroscopy and Its Applications*. New York, NY, USA: Springer, 2014, pp. 7–66, doi: 10.1007/978-1-4614-8933-7_2.
[11] R. Hasan and J. B. Scott, "Fractional behaviour of rechargeable batteries," Electron. New Zealand, Victoria Univ. Wellington, Wellington, New Zealand, Nov. 2016, pp. 111–114. [Online]. Available: https://hdl.handle.net/10289/10756
[12] E. Poihipi, J. Scott, and C. Dunn, "Distinguishability of battery equivalent-circuit models containing CPEs: Updating the work of Berthier, Diard, & Michel," *J. Electroanal. Chem.*, vol. 911, Apr. 2022, Art. no. 116201. [Online]. Available: https://linkinghub.elsevier.com/retrieve/pii/S157266572200193X
[13] J. Scott and R. Hasan, "New results for battery impedance at very low frequencies," *IEEE Access*, vol. 7, pp. 106925–106930, 2019.
[14] A. Peinado and A. Fúster-Sabater, "Generation of pseudorandom binary sequences by means of linear feedback shift registers (LFSRs) with dynamic feedback," *Math. Comput. Model.*, vol. 57, nos. 11–12, pp. 2596–2604, Jun. 2013.
[15] E. Locorotondo, V. Cultrera, L. Pugi, L. Berzi, M. Pierini, and G. Lutzemberger, "Development of a battery real-time state of health diagnosis based on fast impedance measurements," *J. Energy Storage*, vol. 38, Jun. 2021, Art. no. 102566.
[16] A. Guha and A. Patra, "Online estimation of the electrochemical impedance spectrum and remaining useful life of lithium-ion batteries," *IEEE Trans. Instrum. Meas.*, vol. 67, no. 8, pp. 1836–1849, Aug. 2018.
[17] H. Chaoui, N. Golbon, I. Hmouz, R. Souissi, and S. Tahar, "Lyapunov-based adaptive state of charge and state of health estimation for lithium-ion batteries," *IEEE Trans. Ind. Electron.*, vol. 62, no. 3, pp. 1610–1618, Mar. 2015.
[18] D. V. Do, C. Forgez, K. El Kadri Benkara, and G. Friedrich, "Impedance observer for a Li-ion battery using Kalman filter," *IEEE Trans. Veh. Technol.*, vol. 58, no. 8, pp. 3930–3937, Oct. 2009.
[19] B. Saha, K. Goebel, S. Poll, and J. Christophersen, "Prognostics methods for battery health monitoring using a Bayesian framework," *IEEE Trans. Instrum. Meas.*, vol. 58, no. 2, pp. 291–296, Feb. 2009.

[20] Y. Cui *et al.*, "State of health diagnosis model for lithium ion batteries based on real-time impedance and open circuit voltage parameters identification method," *Energy*, vol. 144, pp. 647–656, Feb. 2018.
[21] J. Jiang, Z. Lin, Q. Ju, Z. Ma, C. Zheng, and Z. Wang, "Electrochemical impedance spectra for lithium-ion battery ageing considering the rate of discharge ability," *Energy Proc.*, vol. 105, pp. 844–849, May 2017.
[22] J. Kim, L. Krüger, and J. Kowal, "On-line state-of-health estimation of lithium-ion battery cells using frequency excitation," *J. Energy Storage*, vol. 32, Dec. 2020, Art. no. 101841.
[23] Q. Yang, J. Xu, X. Li, D. Xu, and B. Cao, "State-of-health estimation of lithium-ion battery based on fractional impedance model and interval capacity," *Int. J. Electr. Power Energy Syst.*, vol. 119, Jul. 2020, Art. no. 105883.
[24] A. Lasia, "Dispersion of impedances at solid electrodes," in *Electrochemical Impedance Spectroscopy and Its Applications*. New York, NY, USA: Springer, 2014, pp. 177–201.
[25] R. Hasan and J. Scott, "Application of Swingler's method for analysis of multicomponent exponentials with special attention to non-equispaced data," in *Proc. IEEE 12th Int. Colloq. Signal Process. Appl. (CSPA)*, Melaka, Malaysia, Mar. 2016, pp. 12–15. [Online]. Available: http://ieeexplore.ieee.org/document/7515794/
[26] J. Scott and P. Single, "Compact nonlinear model of an implantable electrode array for spinal cord stimulation (SCS)," *IEEE Trans. Biomed. Circuits Syst.*, vol. 8, no. 3, pp. 382–390, Jun. 2014.
[27] R. Hasan and J. Scott, "Extending Randles's battery model to predict impedance, charge–voltage, and runtime characteristics," *IEEE Access*, vol. 8, pp. 85321–85328, 2020.
[28] P. E. Pascoe and A. H. Anbuky, "The behaviour of the coup de fouet of valve-regulated lead–acid batteries," *J. Power Sources*, vol. 111, no. 2, pp. 304–319, Sep. 2002.
[29] H. Budde-Meiwes, J. Kowal, D. U. Sauer, and E. Karden, "Influence of measurement procedure on quality of impedance spectra on lead–acid batteries," *J. Power Sources*, vol. 196, no. 23, pp. 10415–10423, Dec. 2011.
[30] V. Farrow, "Characterisation of rechargeable batteries: Addressing fractional ultralow-frequency devices," M.E. thesis, Dept. Electron. Eng., Univ. Waikato, Hamilton, New Zealand, Sep. 2020.
[31] J. Scott and A. Parker, "Distortion analysis using SPICE," *J. Audio Eng. Soc.*, vol. 43, no. 12, pp. 1029–1040, Dec. 1995.
[32] J. A. Nelder and R. Mead, "A simplex method for function minimization," *Comput. J.*, vol. 7, no. 4, pp. 308–313, Jan. 1965.
[33] W. H. Press, *Numerical Recipes in C: The Art of Scientific Computing*, 2nd ed. Cambridge, U.K.: Cambridge Univ. Press, 1992.

Christopher Dunn received the bachelor's degree from the Portsmouth School of Pharmacy, Portsmouth, U.K., in 1985, the master's degree from the Queen's University of Belfast, Belfast, U.K., in 1993, and the Graduate Diploma in electronics from The University of Waikato, Hamilton, New Zealand, in 2019, where he is currently pursuing the Ph.D. degree.

His background is originally in the pharmaceutical sciences, with past specialization in medicinal chemistry (notably quantitative structure–activity relationships and pharmaceutical analysis), pharmaceutical technology, small-scale and aseptic/sterile manufacturing, and quality assurance. He has also worked in scientific communications and in asset management/inspection and line structure engineering for the power supply industry.

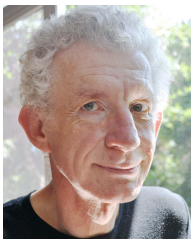

Jonathan Scott (Life Senior Member, IEEE) received the B.Sc., B.E. (Hons), M.Eng.Sc., and Ph.D. degrees from The University of Sydney in 1977, 1979, 1985, and 1997, respectively, and the PGC Management in Higher Education from Waikato University in 2014.

From 1998 to 2006, he was with Hewlett-Packard and Agilent Technologies Microwave Technology Center, Santa Rosa, CA, USA, where he was responsible for advanced measurement systems operating from dc to millimeter-wave. In 1997 and 1998, he was the Chief Engineer of RF Technology, Sydney, NSW, Australia. He was with the Department of Electrical Engineering, The University of Sydney, Sydney, prior to 1997. He is currently the Foundation Professor of electronic engineering with The University of Waikato, Hamilton, New Zealand. He has authored more than 150 refereed publications, several book chapters, and a textbook. He holds a dozen patents, several covering active products. His educational interests include threshold concepts and their application, particularly across engineering disciplines. His research interests are the characterization and modeling of implantable electrodes, semiconductor devices, batteries, and acoustic systems.

Chapter 4

Incremental Capacity and Voltammetry of Batteries, and Implications for Electrochemical Impedance Spectroscopy

4.1 Linking Electrochemical Impedance Spectroscopy in the Frequency Domain and Electrochemical Analysis in the Time Domain

Chapter 3 dealt with novel approaches to EIS, a type of analysis that is carried out in the frequency domain. Here we move into the time domain and discuss electrochemical observations related to rate of charge movement, and their connection with EIS carried out at ELFs.

This chapter begins with some background on our experience of slow cycling of batteries (i.e., low rates of charge movement) and observations that led to an exploration of how frequency and time domain analyses complement each other. Behaviour that is obscured in one domain may be more easily visible in the other, and investigation of time domain phenomena may shed light on what is happening in the frequency domain in the work described in Chapter 3. The electrochemical techniques of ICA and CV, which illustrate charge behaviour in the time domain, are briefly introduced, and there follows a paper that explores the relationships between ICA, CV and EIS, demonstrates the relationship between charging rate in ICA and voltage sweep rate in CV, and how they relate to behaviour seen with ELF measurements in a battery undergoing EIS.

4.2 Relationship Between Slow Cycling and Incremental Capacity

The work described in this chapter was prompted by observations during constant-current cycling experiments in batteries in which small (down to 50 mA) charge-discharge currents resulted in voltage plots that were markedly different in appearance to plots obtained at larger currents (up to 5 A). In addition to apparently higher charge capacity and reduced hysteresis in charge-discharge loops when plotted against charge moved [92], voltage responses to current stimuli also showed pronounced regular perturbations, repeating in every cycle, that smoothed out with increasing current (**Figure 4.1**).

4.2.1 Incremental Capacity Analysis

The voltage response perturbations are related to the peaks and troughs seen in ICA plots, which show incremental charge movement per unit change in voltage. This is illustrated in **Figure 4.2**. ICA was introduced in Section 2.1.3 as a potential candidate for tracking battery degradation (although its suitability for inclusion in battery management systems has been questioned on the grounds of computational complexity [93]), and is carried out by applying small (C/25 or less [94, 95]) charge-discharge currents to the device under test and tracking the voltage response. Con-

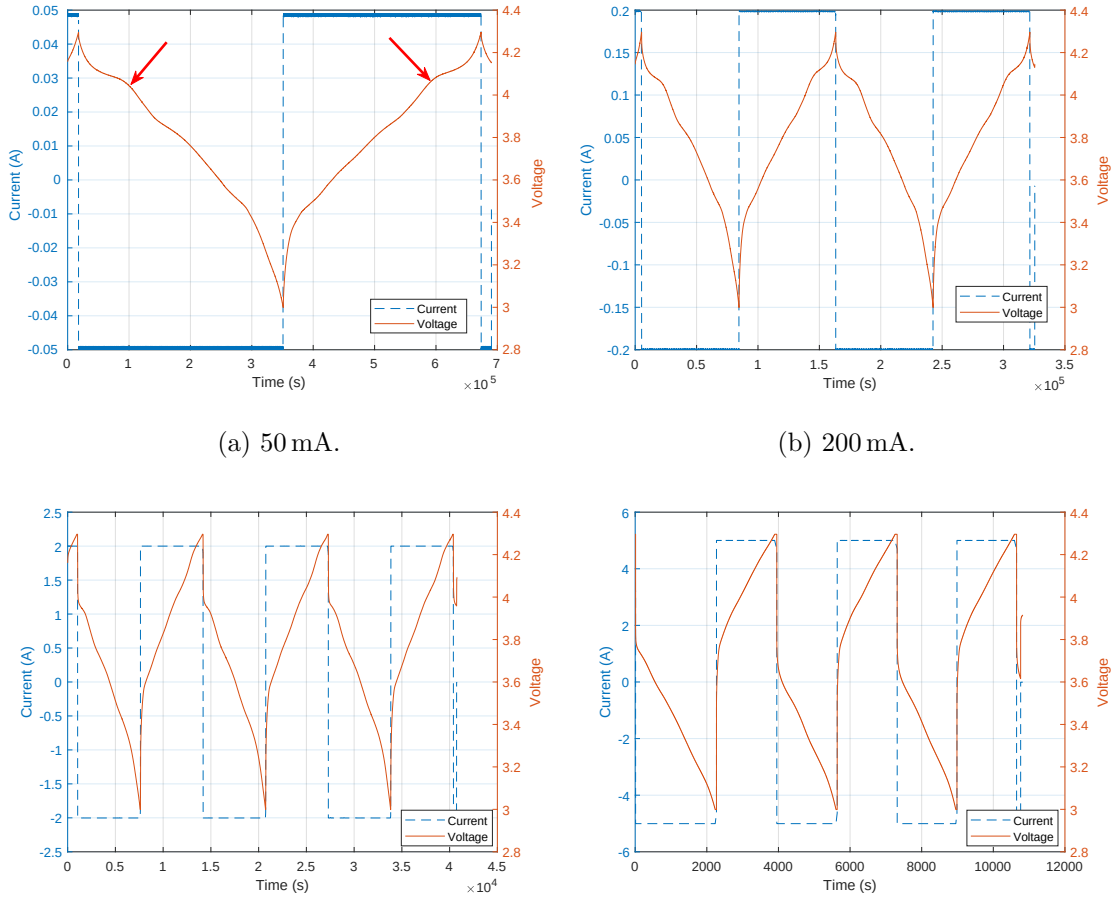

(a) 50 mA.

(b) 200 mA.

(c) 2 A.

(d) 5 A.

Figure 4.1: Cycling plots for a 4.8 Ah lithium NCA battery charged and discharged at currents ranging from 50 mA to 5 A. Examples of perturbations in the voltage response curves are indicated by arrows: note their attenuation as current (i.e., rate of charge movement) increases.

stant current in both directions is usually used, and incremental capacity is plotted by choosing a set small voltage increment (δV) and calculating (using current and time, both of which are known) the charge moved (δQ) for each successive voltage step. $\delta Q/\delta V$ is then plotted against the cell potential, which in a lithium-ion cell results in a series of peaks corresponding to reactions involving the intercalation and de-intercalation of lithium ions at the electrode (e.g., see **Figure 4.2**, second panel). Tracking the magnitudes and positions of these peaks as the battery ages reveals information pertaining to electrochemical changes and electrode degradation [96]. In addition, peak areas (each demarcated by curve inflections) correspond to phase transitions associated with the formation of solid solutions of lithium with other elements [96, 97].

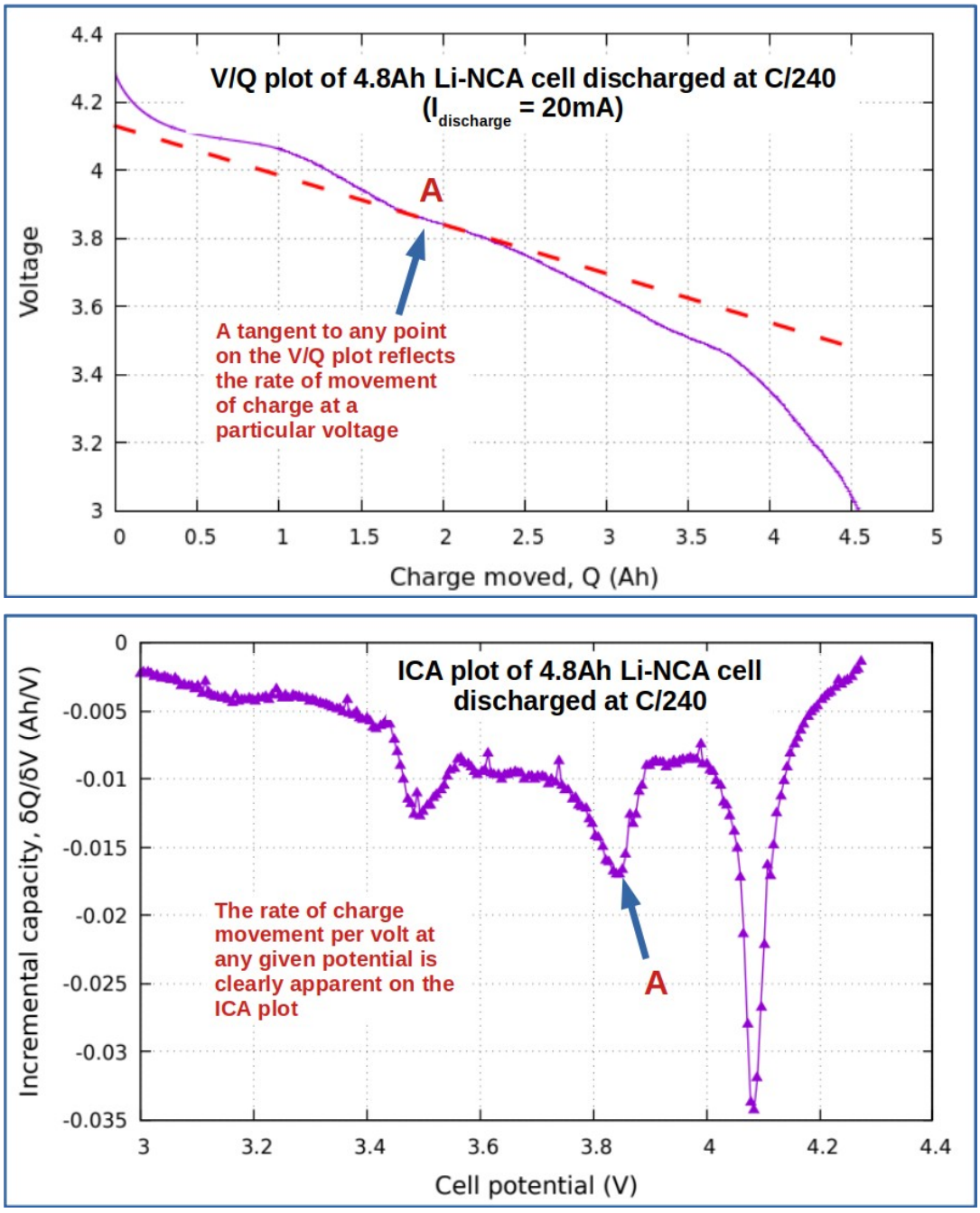

Figure 4.2: $V(Q)$ and incremental capacity plots for the discharge part of a slow cycle in a 4800 mAh lithium NCA cell. Note how the slope of the tangent to a shallow portion of the $V(Q)$ plot corresponds to a peak in the incremental capacity plot (i.e., greater charge movement for a smaller voltage increment).

4.2.2 Cyclic Voltammetry

In CV, a cyclic linear potential sweep (potential is swept up and then down at a constant rate) is applied to the electrode, and the resulting currents are recorded.

A plot of current against voltage can then be used to obtain information on the thermodynamics and kinetics of electrode reactions and mass transport in the cell. CV is widely used to investigate reduction and oxidation reactions, the reversibility of electrochemical processes, and electron transfer-initiated chemical reactions such as catalysis [98, 99, 95].

An example of a typical cyclic voltammogram is shown in **Figure 4.3** [100]. Here the forward scan is negative and proceeds in a reductive direction (note that this is the US convention; the IUPAC convention has the oxidative scan in the forward direction, with anodic currents in the top half of the plot [98]).

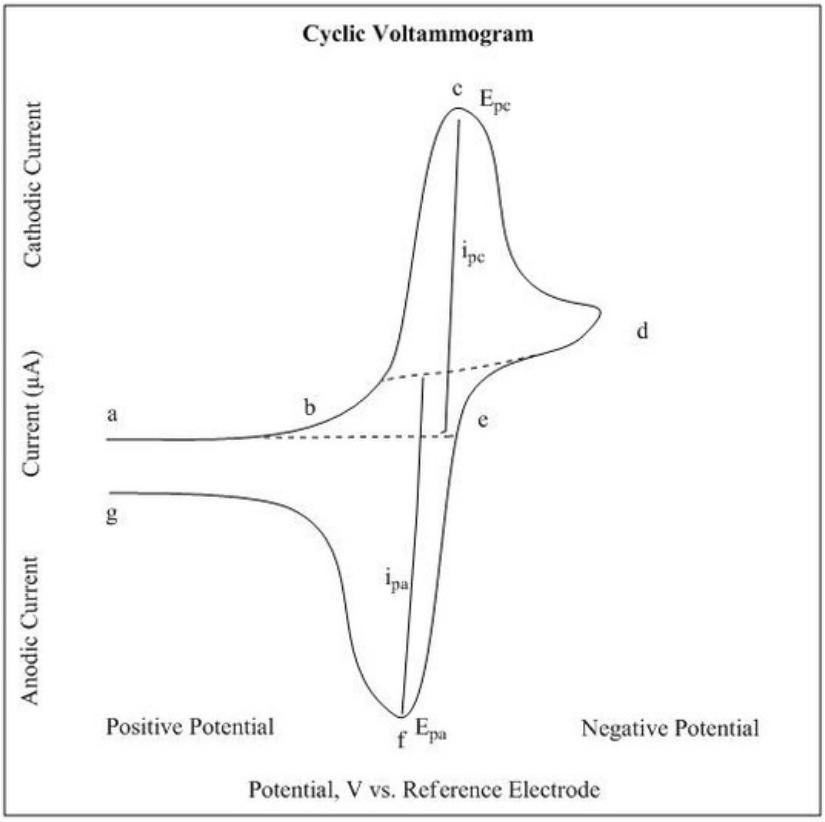

Figure 4.3: Cyclic voltammogram showing a single-electron reduction and oxidation [100]. The reduction reaction (negative scan) starts at (a), the starting potential, and runs to (d), the switching potential. E_{pc}, the cathodic peak potential at (c), is reached when the reductive current is at a maximum. After the switching potential is reached, the anodic (positive) scan runs from (d) to (g). The anodic peak potential E_{pa} is at (f). i_{pa}, anodic current; i_{pc}, cathodic current.

At first, the potential is insufficient to reduce the analyte, but it increases until the onset of reduction is reached at (b). Current then increases as cations are reduced, with current limited by speed of migration of cations (diffusion of reduced species is more rapid than ion migration). The voltammogram peaks at (c) where the reductive current is at a maximum, and the migration rate of cations is equal to

the rate of diffusion of reduced species. Current flow decreases after this point as the electrode becomes saturated with reduced species, which hinders cation approach and causes the reaction rate to be limited by diffusion [100, 101].

Scan reversal to positive potentials (the oxidative scan) from (d) continues until the potential reaches the oxidation threshold at (e). Oxidation then proceeds as a reversal of the reductive process described above. If the reaction is fully reversible, the anodic and cathodic peak currents should be of equal magnitude. If it is not, the plot will show a missing or attenuated peak on the reverse scan.

More detailed discussion of CV is beyond the scope of this brief introduction, and the reader is referred to the review by Elgrishi et al. [98] for more information.

4.2.3 Charge Rate, Sweep Rate and Extra-Low Frequency Electrochemical Impedance Spectroscopy

Charge or discharge rate in ICA is related to voltage sweep rate as used in CV. Faster sweep rates in a CV (i.e., a steeper voltage ramp) leads to a decrease in the size of the diffusion layer at the electrode, which leads to the generation of higher currents [98]. The forced change in potential in CV, which is applied regardless of the SoC of the electrode, can increase current beyond the kinetic limit of the system and thereby prevent capacity from being accessed [95]. Incremental capacity, on the other hand, is collected at constant current, which gives electrochemical processes more time to complete. This however begs the question as to what happens to an ICA plot if current is increased to the point where kinetic limits are being exceeded (as in CV). As suggested by **Figure 4.4**, in the limit, the two approaches could be viewed as essentially providing the investigator with the same information, with rate of movement of charge being the underlying factor that determines what the investigator sees. Observations hinting at these points have been published previously [95], but the measurement techniques and new EIS results at ELFs described in this thesis have allowed these ideas to be developed further.

The evolution of ICA plots and voltammograms as rate of movement of charge increases provides insight into why EIS may yield variable results, particularly at ELFs. It also indicates the importance of operating point and a possible reason for the effectiveness of the non–small-signal working current discussed in Chapter 3. These concepts are explored in the paper that follows. There is also a mathematical argument for a new way of looking at ICA and CV based on the importance of rate of charge movement, and a suggestion for an easily implemented laboratory method for safely carrying out a CV-type analysis on an intact battery.

In light of its potential interest to electrochemists as well as engineers, the paper that follows was originally submitted for publication in “The Journal of Electroanalytical Chemistry”. It was rejected after peer review, however, with reviewers raising concerns over the perceived novelty of the electrochemical work, and difficulty in see-

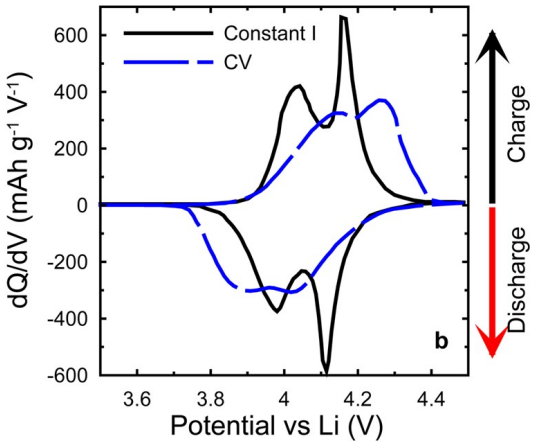

Figure 4.4: Incremental capacity plot (ICA, black solid line) and a cyclic voltammogram (CV, blue dashed line) from the same electrode (lithium manganese oxide, $Li_2Mn_2O_4$). ICA was carried out with a constant current of 0.33 mA/cm^2; CV voltage ramp was 0.04 mV/s (sweep up and down in 6.9 hours). Reproduced from Talaie et al. [95] with permission.

ing the rationale underlying measurement at ELFs. The paper was edited in light of these comments to give more emphasis to the postulated links (related to rate of charge movement) between electrochemical (time domain) measurements and our ELF (frequency domain) observations, to explain more clearly the reasoning behind ELF measurements, to highlight the hitherto underappreciated equivalence of CV and ICA when charge is moving at sufficiently high rates, and to suggest that measurement equipment and protocols described provide a straightforward and safe means of obtaining CV-type data from a battery with basic equipment. At the time of original submission of this thesis, the paper was under consideration by "IEEE Transactions on Instrumentation and Measurement".

Incremental Capacity and Voltammetry of Batteries, and Implications for Electrochemical Impedance Spectroscopy

Christopher Dunn, *Student Member, IEEE*, Jonathan Scott, *Life Member, IEEE*, Marcus Wilson, Michael Mucalo, and Michael Cree, *Senior Member, IEEE*

***Abstract*—Incremental capacity analysis (ICA), where incremental charge (Q) movements associated with changes in potential are tracked, and cyclic voltammetry (CV), where current response to a linear voltage sweep is recorded, are used to investigate the properties of electrochemical systems. Electrochemical impedance spectroscopy (EIS) is a powerful, non-destructive technique that can be used to determine small-signal ac impedance over a wide frequency range. It is frequently used to design battery equivalent circuit models.**

This manuscript explores the relationships between ICA, CV and EIS, demonstrates how sweep rate in CV is related to charging (C) rate in ICA, and shows the connection between observations linked to rate of charge movement in CV and ICA and intermittent, irregular behavior seen in EIS when performed on a battery. We explain the use of an additional dc stimulus during EIS to ensure reliability of battery impedance data and to facilitate equivalent circuit modeling, and suggest a method for obtaining CV-type data from a whole battery without risking its destruction.

***Index Terms*—Electrochemical impedance spectroscopy, cyclic voltammetry, incremental capacity analysis, equivalent circuit model, battery, nonlinear analysis**

I. Introduction

CYCLIC voltammetry (CV) and incremental capacity analysis (ICA) are widely used in the evaluation of electrochemical systems. CV measures current while potential is swept linearly as a function of time [1]–[4], whereas ICA tracks incremental charge (Q) movements associated with changes in potential (dQ/dV) when a constant current is applied [5], [6]. A related technique, differential voltage analysis (DVA), shows how potential changes with respect to charge movement (dV/dQ) [7]. While these methods provide simple but useful information about peak currents and potentials that can help to characterize the electrochemistry of a system, a further method, electrochemical impedance spectroscopy (EIS), holds a special place because it presents data as a function of frequency that can reveal a great deal of information about the electrochemical characteristics and condition of a cell and inform the development of equivalent circuit models (ECMs) [8], [9]. Accompanying all these is the most basic method of charging and discharging a cell (cycling), which allows the investigator to produce plots of potential against some other variable (typically charge moved), the shapes of which are determined by a cell's thermodynamics and kinetics [10].

Although the above methods are usually viewed as distinct techniques that give the investigator different types of data, they are related both mathematically and in terms of the information they can provide. Very slow cycling experiments and EIS at extra-low frequencies (ELFs, down to as low as 1 μHz) that reflect the real-world usage cycles of rechargeable batteries [11]–[14] have led to observations enabling us to clarify connections between the above techniques, and to suggest a simple and inexpensive method for carrying out ICA on batteries. They also explain the recently reported need to use background direct currents to suppress electrochemical behavior that interferes with EIS measurements at ELFs [14].

We report and discuss these observations in this paper, and suggest in addition how our method might be used to allow analyses analogous to CV to be carried out on intact lithium-ion batteries. Conventional CV involving the application of a voltage ramp with constant dV/dt would not be feasible because of the risk of thermal runaway, leakage of electrolyte or even explosion as a result of the uncontrolled currents that might be generated. Other problems include the relatively small active electrode area in a lithium-ion cell, which could limit sensitivity and accuracy of an attempted CV, and potential unsuitability of the battery electrolyte for this procedure.

II. Connecting Cyclic Voltammetry, Incremental Capacity Analysis and Differential Voltage Analysis

CV, ICA and DVA are all used to relate aspects of electrochemical activity to cell terminal voltage. Relationships between CV and ICA have been explored previously [10], [15], but we extend these ideas with an emphasis on the significance of very low sweep or cycling rates, and discuss their relevance to EIS, particularly when carried out at ELFs.

Assume a battery has some function relating open circuit terminal voltage to charge available, $V(Q)$. In the case of CV a linear voltage ramp is applied, so

$$\frac{dV}{dt} = k \tag{1}$$

and so

$$V(t) = kt + V_0 \tag{2}$$

Manuscript received Month XX, 2023; revised Month XX, 2023.

where k is the constant voltage sweep rate, t is time in seconds, and V_0 the battery's open circuit voltage at the start of the sweep. Also

$$I(t) = \frac{dQ}{dt} = \frac{dQ}{dV}\frac{dV}{dt} = k\frac{dQ}{dV} \tag{3}$$

In CV, current $I(t)$ is plotted against voltage $V(t)$, and the rate of change of voltage (dV/dt) is constant. Current represents rate of reaction, which varies as the absolute voltage varies. Equation 3 shows that incremental capacity dQ/dV is in fact equal to $I(t)/k$, which is current (which may vary) divided by the voltage sweep rate k, a constant that now acts as a scaling factor.

CV experiments assume that the concentration of reagents is not affected by diffusion, which is equivalent to saying that the sweep rate k is slow (so that concentration gradients that would build up by diffusion-affected processes do not form). Moreover, the peaks of a CV plot are influenced by sweep rate [1], [3].

In ICA, a constant current is used, so

$$I(t) = c \tag{4}$$

and so

$$I(t) = \frac{dQ}{dt} = \frac{dQ}{dV}\frac{dV}{dt} = c \tag{5}$$

where c is the constant current value. Then

$$\frac{dQ}{dV} = \frac{c}{\left[\frac{dV}{dt}\right]} \tag{6}$$

This value is plotted against voltage. By definition, DVA (dV/dQ) is the reciprocal of ICA (dQ/dV). Both describe cell phase transition characteristics during intercalation and de-intercalation processes at the electrodes during charging and discharging [16], but constitute different ways of viewing this information.

It is worth noting here that the assumption that a battery obeys a state equation relating open-circuit terminal voltage to charge available, $V(Q)$, is not true in general. If we accept that the battery embodies a fractional (constant phase) element, this is mathematically not the case. [1]

III. Experimental Methods

A. Hardware and Procedure

The battery used in the present experiments was a new lithium nickel cobalt aluminium oxide (NCA) $4.8\,\mathrm{Ah}$ $3.7\,\mathrm{V}$ 21700 cell. Measurements were taken at $22\,^{\circ}\mathrm{C}$ using two-quadrant precision sources (HP/Agilent/Keysight 66332A units) via four-wire connections controlled through GPIB interfaces by Raspberry Pi 4 computers running custom software written in C [14], [17] (Figure 1).

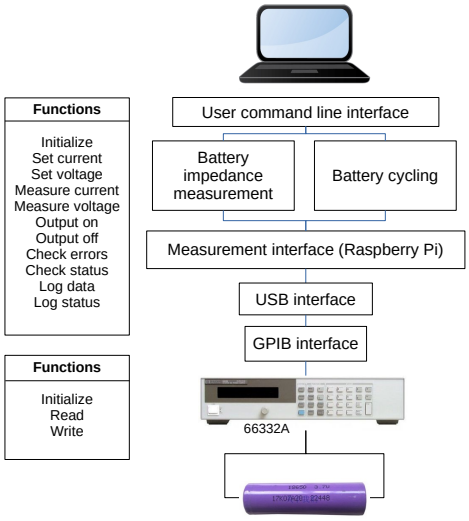

Fig. 1. System architecture.

The software utility used for battery cycling, "bcp66", is a command line program called by scripts that set parameters for each run, allowing many experiments to be queued and executed. Typically batteries are cycled according to industry standard CC (constant current) or CC-CV (constant current-constant voltage) protocols[2]. The utility allows the user to specify charge and discharge currents (cycling rate calculated with reference to the cell's nominal capacity in ampere-hours) which are applied in constant current mode until pre-specified voltage limits are reached. At this point, a constant voltage phase may begin if desired; if not, the software stays in constant current mode and switches immediately to the next charge or discharge phase. Rest periods can also be requested. The software allows the user to specify currents at which to end constant voltage phases, and dwell times, the maximum period to wait for constant voltage phases to end. Other parameters include number of cycles, the final charge (percent) at the end of cycling, and a wait time or period to continue recording after cycling is finished and current has returned to zero. Output is presented in a ".tvi" text file with time, voltage, current, charge moved (ΔQ) and repetition-number columns. The 66332A units return approximately eight records per second.

B. Data Processing

Data were processed by scripts in MATLAB® or AWK. All processing starts by importing timestamped current and voltage values from .tvi files created by the measurement system into arrays containing time, voltage and current data. An arbitrary voltage interval is specified ($5\,\mathrm{mV}$ in the examples shown in this manuscript), and a calculation performed as the script loops through the arrays to calculate the quantity of charge moved and the time taken for each voltage increment.

[1] In general, charge Q is a functional of voltage, $Q = Q\,[V(t)]$. Differentiating with respect to time yields

$$I(t) = \frac{dQ(t)}{dt} = \int_{t'=-\infty}^{t} \frac{\delta Q(t)}{\delta V(t')}\left.\frac{dV}{dt}\right|_{t=t'} dt'$$

and this full form must be evaluated. In a typical quasi-static situation this is not necessary. Discussion of this is beyond the scope of this manuscript.

[2] The acronym "CV" is used in electrochemical research to designate cyclic voltammetry, but in the industrial battery world the same acronym is used to designate "constant voltage", a part of charging and discharging protocols.

This information is then used to create three further arrays containing charge moved as a function of time, charge moved as a function of voltage (incremental capacity) and change in voltage as a function of time (k, see Equation 1) for each voltage increment. These data can be used to generate plots that are representative of ICA or a current-derived equivalent of CV. The latter are not conventional electrochemical CV plots as described earlier (Section I) because we have not applied a voltage ramp and measured the current response. Rather, we have applied constant charge and discharge currents and tracked voltage increases and decreases with time at the sample rate of the instruments. In the interests of clarity, we will therefore refer to "CV-type" or "current-derived" plots in this manuscript.

C. EIS Measurement

Full details of the procedure used to conduct EIS at ELF using the 66332A units controlled by Raspberry Pi computers via GPIB interfaces have been reported previously [14]. Briefly, a command line C program C, "bzdcp66", is used to make multitone impedance measurements by sourcing and sinking current, and recording times, currents and voltages in three-column .tvi files. The complex impedance $Z(\omega)$ for each frequency of interest

$$Z(\omega) = \frac{|V|}{|I|} e^{j(\phi_V - \phi_I)} \tag{7}$$

is obtained from the .tvi data by performing a discrete-time Fourier transform using a program based on software originally described in [18] for use with SPICE, and the magnitude and phase results presented in Bode plots (Nyquist plots convey no useful information at ELFs). The measurement software is distinguished by its ability to impose a small-signal, multiple-frequency (multitone) stimulus in addition to a "working" stimulus signal simultaneously. This is accomplished by superimposing the EIS multitone on a periodic square wave which aims to mimic the effect of a working dc signal, as reported previously [14]. This charge displacement stabilizes the impedance spectrum against impedance drift phenomena and maximizes measured data quality, showing the true working impedance of a battery and optimizing data for ECM fitting [14].

D. ECM Fitting

The ECM fitting procedure used has been described previously [9], and involves generation of an ECM via an optimization method based on the downhill simplex algorithm of Nelder and Mead [19] that is implemented in C as a command line program [20]. The optimization target is defined as a root mean square error (RMSE) value calculated from complex impedances as indicated by the available data. The final RMSE reflects how well the model fits the data, with a perfect fit defined as an RMSE approaching zero, while higher values indicate noisier, poorer quality or ambiguous data. As previously [14], modeling starts with the simplest ECM, a single resistor and CPE in series (R-CPE). If the RMSE indicates a poor fit, we move to the next model in the chain of complexity, a resistor and two CPEs in series (R-CPE-CPE). Links between these observations and electrochemical behavior suggested by cycling experiments are explored as described in Sections III-A and III-B.

IV. Results

A. Incremental Capacity and Voltammetry

Figure 2a shows a complete slow (C/48) discharge-charge cycle with its voltage response. Note the uneven voltage trace: this is characteristic of slow charging and discharging and corresponds to changes in the rate of movement of charge, which is not constant across cell potentials. Plateaus in the voltage versus time curve correspond to peaks in the dQ/dV (ICA) plot in Figure 2b, with each peak representing a different chemical reaction or intercalation environment, and the area under the peak being the capacity of that process. Thus, voltage plateaus (shallow tangents) in Figure 2a represent large capacity increments in Figure 2b (i.e., a lot of charge is moved for a small voltage change). These peaks describe cell phase transition characteristics during the intercalation and de-intercalation of lithium ions [16]. Changes in peak position and size have been investigated as potential markers of battery aging, with the literature tending to focus on $LiFePO_4$ cells [5], [6], [21]–[23], although data on NCA [24] and other chemistries [25]–[28] are also available.

We see the same pattern of peaks when charge movement is related to increments of time and presented as current in a CV-type plot (Figure 2c). This is because dQ/dt (i.e., current, as conventionally plotted in CV), is in fact dQ/dV (i.e., incremental capacity) multiplied by the scaling factor k (Equation 3). Moreover, ICA is dQ/dt (which we define as c; Equation 5) multiplied by $1/k$ (i.e., $1/\frac{dV}{dt}$; Equation 6). Although we have not carried out a true CV on the battery for reasons discussed earlier (Section I), these relationships and observations indicate that CV might yield the same information as ICA but under different circumstances.

Figure 3a shows the effect of increasing the rate of charge/discharge from $100\,\mathrm{mA}$ (C/48) to $5\,\mathrm{A}$ (approximately 1C): the voltage response to the charge/discharge current becomes smoother, reflecting increased uniformity of charge movement across the cell's terminal voltage range. In addition, the peaks in both the incremental capacity versus time and current versus time plots that correspond to the shallow portions of the charge-discharge curve flatten and become less distinct, and move apart so that the negative and positive portions are no longer symmetrical (Figures 3b and 3c). Under these conditions both types of plot begin to resemble more closely the CV traces typically seen in textbooks, in which the current change with terminal voltage has a broad anodic (charging) region, with a corresponding cathodic region upon discharge if the overall electrode process is behaving reversibly.

The conventional view is that electrochemical processes have more time to reach completion under the constant current conditions under which differential capacity is collected [10]. The constant potential sweep rates used in CV on the other hand force changes in potential regardless of the state of charge of the electrode which can increase current beyond the

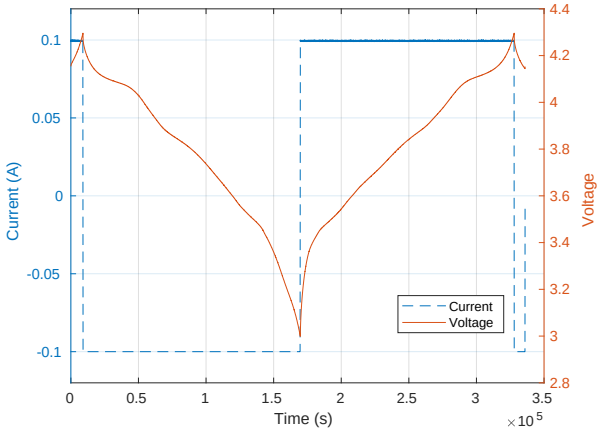

(a) Cycling plot: cell current and voltage versus time.

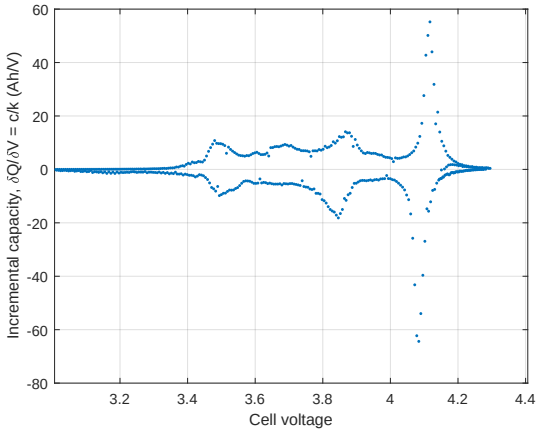

(b) Incremental capacity versus cell voltage (ICA plot).

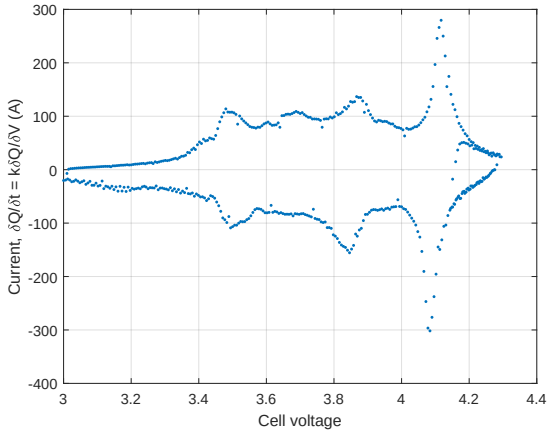

(c) Current versus cell voltage (CV-type plot).

Fig. 2. 4.8 Ah lithium NCA cell cycled with a charge/discharge current of 100 mA (C/48).

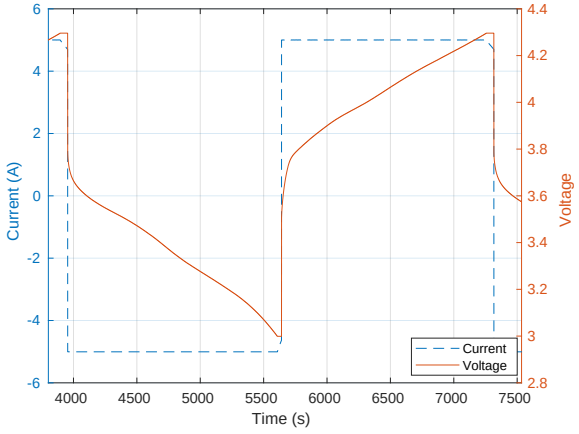

(a) Cycling plot: cell current and voltage versus time (one of three complete cycles).

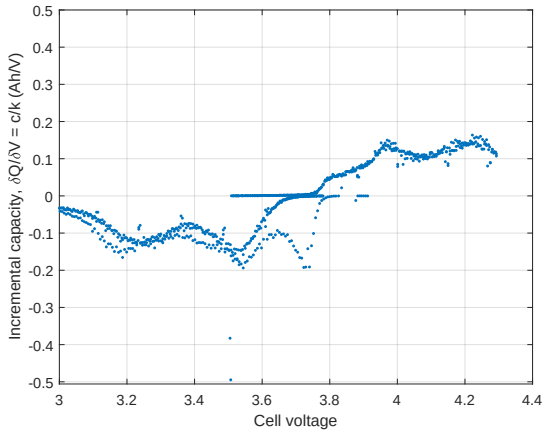

(b) Incremental capacity versus cell voltage (ICA plot).

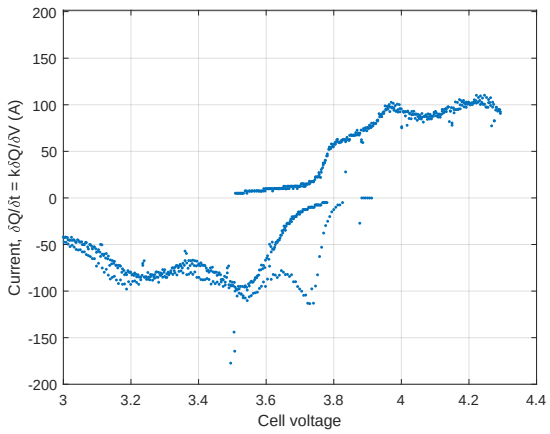

(c) Current versus cell voltage (CV-type plot).

Fig. 3. 4.8 Ah lithium NCA cell cycled with a charge/discharge current of 5 A (approximately 1C): three complete cycles.

kinetic limit of the cell and prevent some capacity from being accessed.

We contend that, regardless of whether current or potential is used as the stimulus, the key underlying factor is rate of charge movement. Under very slow charge-discharge conditions, the system can be said to be in a quasi-static state, with the electrode processes within the cell approximating a succession of equilibrium states that reveal the variable rates of charge movement. If charge and discharge rates are increased, the cell moves away from this equilibrium-like state and can no longer be described as being in a quasi-static condition.

These observations underline the interrelationships between CV and ICA, and the importance of rate of charge movement in maintaining a quasi-static measurement. They also demonstrate how a controlled current stimulus might be used to obtain CV-like data from an intact cell. One stated advantage of CV has been that it provides rate information about the full cell, while dQ/dt plots have superior resolution and are more useful to researchers focusing on electrode materials [10], [15]. However, both CV and ICA have associated rates. In one, dV/dt is constant, while in the other dQ/dt is constant, yet in both dQ/dt is sought. In the limit of δt approaching zero, they can be said to be equivalent.

It is worth noting here the very large current values indicated in Figure 2c. As explained in Section III-B, these are not actual measured currents, but result from a calculation based on charge movement. They underline the danger inherent in attempting to apply even a gentle voltage ramp to an intact battery, as we would have no control over the potentially huge currents that might eventuate at certain terminal voltages.

B. Conditions for Reliable EIS and ECM Fitting

Rate of charge movement is also crucial in EIS, particularly when carried out at the lowest frequencies. EIS measures by means of sinusoidal tones (perturbations) what amounts to the derivative dV/dI of the battery characteristic at various frequencies (rates), which essentially corresponds to the slope of the trace in a voltammogram. Traditional small-signal EIS measurement yields unreliable results especially below $100\,\mu$Hz. We suggest that this is because the slope of the voltammogram can vary sharply at low enough rates. Using an additive, large, working current in EIS measurement changes the nature of the current-voltage characteristic towards a flatter, broad peak, and impedance values become stable as a result.

Figure 2c shows, for example, that the value of impedance when the battery is at $4.0\,\mathrm{V}$ will be very different from the value at $4.1\,\mathrm{V}$, since for a given increment in voltage the increment in current will be very different. The working current pulls the battery away from the small-signal, quasi-static condition, thus smoothing out the effect of the local peaks. The current is no longer "small", and the paradox is resolved by noting that the working current may be large, but it reverses often enough that the charge displacement it produces remains small. Hence, the battery does not discharge before the measurement is complete, nor do its characteristics become nonlinear.

The implications of charge movement rates for EIS at ELFs are apparent when EIS is performed with and without working currents as described in Section III-C. As shown in Figure 4a, with no working current (small measurement tones only), poor quality magnitude and phase impedance plots are obtained. In particular, phase behavior is unclear below $20\,\mu$Hz, and series resistance above $100\,\mathrm{mHz}$ is difficult to ascertain. An ECM based on two elements (R-CPE) only can be generated (Table I), with poor fit to the measured data.

Conversely, when the same measurement is made in the presence of a $500\,\mathrm{mA}$ square wave, stable and unambiguous magnitude and phase impedance plots are obtained (Figure 4b). Using these data, a three-element ECM (R-CPE-CPE) with a good fit to the measured data can be generated (Table I). These results are concordant with earlier findings [14], and demonstrate that EIS at ELFs in an intact battery must be carried out under working conditions.

This begs the question as to whether the cell is in a quasi-static or non–quasi-static state: on one hand, there are relatively large "working" currents flowing; on the other, those large currents reverse frequently, so that net charge flow is small over a period of minutes. In answer to this question, we contend that the system should be considered quasi-static, as evidenced by the reversible peaks in CV-type plots.

The asymptotes corresponding to the circuit elements in each ECM are shown in Figures 5a and 5b. Note in particular the asymptote for CPE2 in Figure 5b. This element is discernible only through ELF measurement [14] and confirmed here to be visible only when the cell is not fully quasi-static, but also not in perfect equilibrium. We might call this a "pseudo–quasi-static" state. Certainly the data are not obscured by diffusion, but neither are the instantaneous currents small. We are in the region between "small-signal" measurements that typically apply to EIS work that assumes a linear device, and the "large-signal" regime where nonlinear effects dominate.

TABLE I
ECM PARAMETER ESTIMATION

ECM	R_s	α	C_F	C_2	α_2	RMSE
bzdcp66 with 10 mA square wave (negligible working current)						
R-CPE	38.53	0.7200	2397			0.1456
R-CPE-CPE	36.73	0.7450	3162	793.6	0.2839	0.1439
bzdcp66 with 500 mA square wave (working current)						
R-CPE	26.80	0.9053	6160			0.1479
R-CPE-CPE	18.25	0.9913	14,250	155.3	0.2402	0.0296

CPE, constant phase element; ECM, equivalent-circuit model; RMSE, root mean square error.
R_s, series resistance ($ohm \times 10^{-3}$); C_F and C_2, fractional capacitances ($F/s^{(1-\alpha)}$) of first (R-CPE model) and second (R-CPE-CPE model) CPEs, with respective slopes denoted by α and α_2.

V. CONCLUSION

These findings support the concept of equivalence of CV and ICA in terms of the information they provide to the experimenter. Both methods have associated rates and, in both cases, rate of charge movement is the key variable that determines what the investigator sees. Low rates of charge movement yield detailed peaks corresponding to individual reactions in incremental charge or current plots, while greater rates lead to loss of resolution and the generation of plots

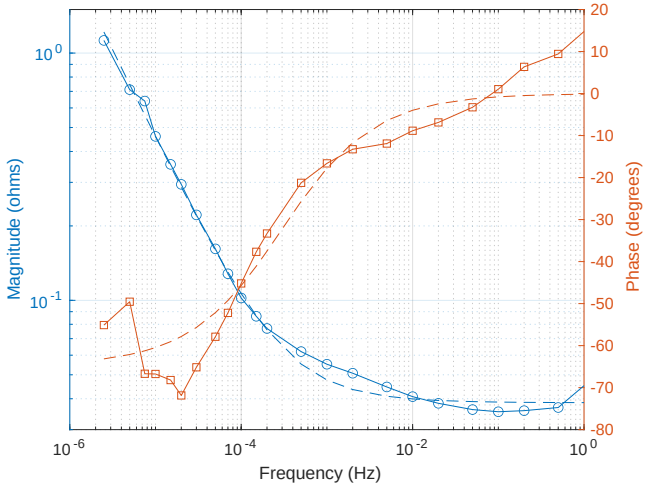

(a) Measurement multitone superimposed on a negligible (10 mA) square wave current.

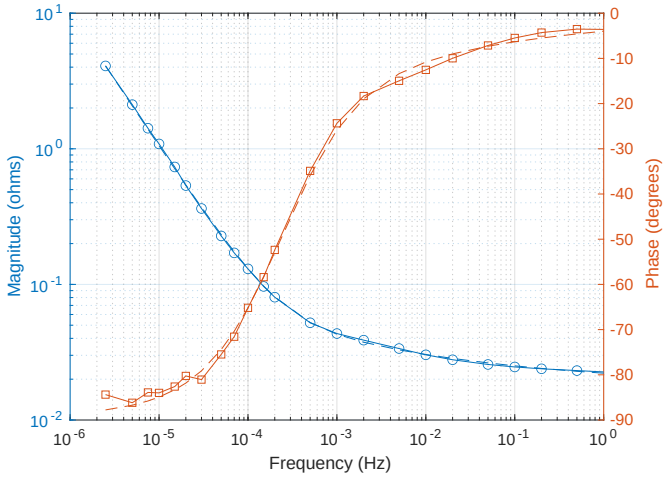

(b) Measurement multitone superimposed on a 500 mA square wave "working" current.

Fig. 4. Measured (solid lines) and fitted (dashed lines) magnitude (open circles) and phase (open squares) impedance curves: extra-low frequency (down to 2.5 μHz) electrochemical impedance spectroscopy on a 4.8 Ah lithium NCA cell.

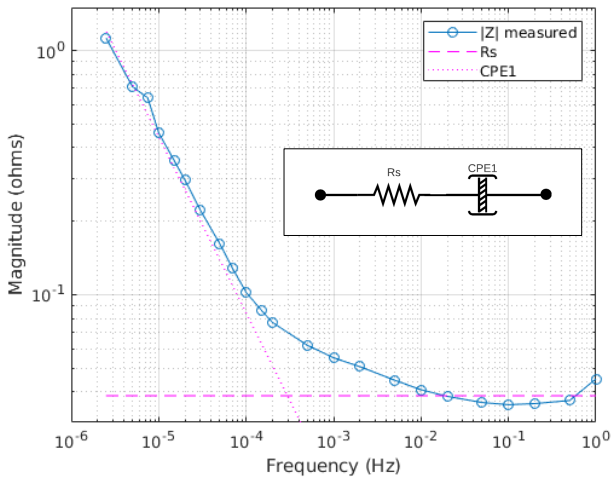

(a) Measurement multitone superimposed on a negligible (10 mA) square wave.

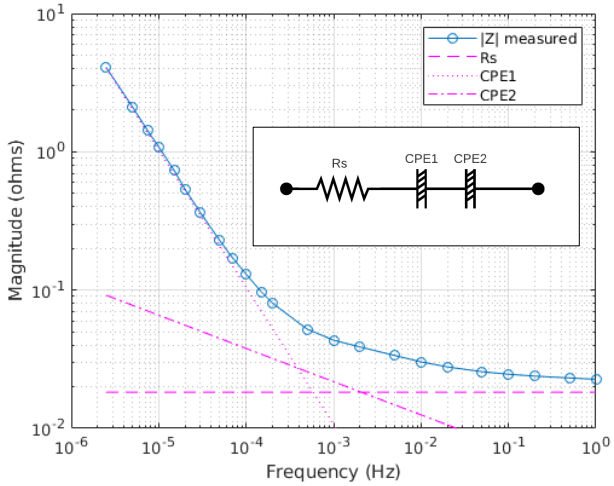

(b) Measurement multitone superimposed on a 500 mA square wave "working" current.

Fig. 5. Measured impedance magnitude with fitted asymptotes showing discernible equivalent circuit elements: 4.8 Ah lithium NCA cell.

more closely resembling CV as commonly presented in the literature. In addition, the current-controlled method with calculation of cumulative charge movement described in this manuscript offers a practical solution, using basic equipment, to the problem of performing CV, or at least a pseudo-CV analysis, on an intact battery without risking destruction of the device under test.

The near-equilibrium conditions that reveal electrode activity at different terminal voltages interfere with small signal impedance measurements, or at least make them susceptible to small changes in equilibrium point. We suggest that attempts to fit circuit models to EIS data obtained under quasi-static conditions are likely to result in unreliable models. This work is consistent with earlier observations [9], [14] suggesting that rechargeable batteries based on lithium ion chemistries are adequately characterized by relatively simple R-CPE-CPE models, and that ECMs with many components representing individual electrochemical processes within the cell [8], [29], [30] are overfitted when predicting operation under *working* conditions.

ACKNOWLEDGMENTS

The authors wish to acknowledge the assistance of WaikatoLink and a Waikato University Doctoral Scholarship.

REFERENCES

[1] P. W. Atkins and J. De Paula, *Atkins' Physical Chemistry*, 8th ed. Oxford; New York: Oxford University Press, 2006.

[2] Anon., "Linear Sweep and Cyclic Voltammetry: The Principles," Nov. 2013. [Online]. Available: https://www.ceb.cam.ac.uk/research/groups/rg-eme/Edu/linear-sweep-and-cyclic-voltametry-the-principles

[3] F. Marken, A. Neudeck, and A. M. Bond, "Cyclic voltammetry," in *Electroanalytical methods: guide to experiments and applications*, F. Scholtz, Ed. Berlin; New York: Springer, 2002.

[4] D. Y. W. Yu, C. Fietzek, W. Weydanz, K. Donoue, T. Inoue, H. Kurokawa, and S. Fujitani, "Study of $LiFePO_4$ by Cyclic Voltammetry," *J. Electrochem. Soc.*, vol. 154, no. 4, p. A253, 2007. [Online]. Available: https://iopscience.iop.org/article/10.1149/1.2434687

[5] V. Ovejas and A. Cuadras, "Battery Aging Impedance Spectroscopy and Incremental Capacity Analysis," Chemnitz, Germany, Sep. 2017.

[6] D. Anseán, V. M. García, M. González, C. Blanco-Viejo, J. C. Viera, Y. F. Pulido, and L. Sánchez, "Lithium-Ion Battery Degradation Indicators Via Incremental Capacity Analysis," *IEEE Trans. Ind. Appl.*, vol. 55, no. 3, pp. 2992–3002, May 2019. [Online]. Available: https://ieeexplore.ieee.org/document/8603757/

[7] G. Vennam, A. Sahoo, and S. Ahmed, "A survey on lithium-ion battery internal and external degradation modeling and state of health estimation," *J. Energy Storage*, vol. 52, p. 104720, Aug. 2022. [Online]. Available: https://linkinghub.elsevier.com/retrieve/pii/S2352152X22007320

[8] U. Westerhoff, K. Kurbach, F. Lienesch, and M. Kurrat, "Analysis of Lithium-Ion Battery Models Based on Electrochemical Impedance Spectroscopy," *Energy Technol.*, vol. 4, no. 12, pp. 1620–1630, 2016.

[9] E. Poihipi, J. Scott, and C. Dunn, "Distinguishability of Battery Equivalent-Circuit Models Containing CPEs: Updating the Work of Berthier, Diard, & Michel," *J. Electroanal. Chem.*, vol. 911, p. 116201, Apr. 2022. [Online]. Available: https://linkinghub.elsevier.com/retrieve/pii/S157266572200193X

[10] E. Talaie, P. Bonnick, X. Sun, Q. Pang, X. Liang, and L. F. Nazar, "Methods and Protocols for Electrochemical Energy Storage Materials Research," *Chem. Mater.*, vol. 29, no. 1, pp. 90–105, Jan. 2017. [Online]. Available: https://pubs.acs.org/doi/10.1021/acs.chemmater.6b02726

[11] P. Mauracher and E. Karden, "Dynamic modelling of lead/acid batteries using impedance spectroscopy for parameter identification," *J. Power Sources*, vol. 67, no. 1-2, pp. 69–84, 1997.

[12] J. Scott and R. Hasan, "New Results for Battery Impedance at Very Low Frequencies," *IEEE Access*, vol. 7, pp. 106 925–106 930, 2019.

[13] R. Hasan and J. Scott, "Extending Randles's Battery Model to Predict Impedance, Charge–Voltage, and Runtime Characteristics," *IEEE Access*, vol. 8, pp. 85 321–85 328, 2020.

[14] C. Dunn and J. Scott, "Achieving Reliable and Repeatable Electrochemical Impedance Spectroscopy of Rechargeable Batteries at Extra-Low Frequencies," *IEEE Trans. Instrum. Meas.*, vol. 71, pp. 1–8, 2022. [Online]. Available: https://ieeexplore.ieee.org/document/9789195/

[15] T. Kim, W. Choi, H.-C. Shin, J.-Y. Choi, J. M. Kim, M.-S. Park, and W.-S. Yoon, "Applications of Voltammetry in Lithium Ion Battery Research," *J. Electrochem. Sci. Technol*, vol. 11, no. 1, pp. 14–25, Feb. 2020. [Online]. Available: http://jecst.org/journal/view.php?doi=10.33961/jecst.2019.00619

[16] L. Zheng, J. Zhu, D. D.-C. Lu, G. Wang, and T. He, "Incremental capacity analysis and differential voltage analysis based state of charge and capacity estimation for lithium-ion batteries," *Energy*, vol. 150, pp. 759–769, May 2018. [Online]. Available: https://linkinghub.elsevier.com/retrieve/pii/S0360544218304213

[17] V. Farrow, "Characterisation of rechargeable batteries: addressing fractional ultralow-frequency devices," Master of Engineering, University of Waikato, Hamilton, New Zealand, Sep. 2020.

[18] J. Scott and A. Parker, "Distortion analysis using SPICE," *J. Audio Eng. Soc.*, vol. 43, no. 12, pp. 1029–1040, Dec. 1995.

[19] J. A. Nelder and R. Mead, "A Simplex Method for Function Minimization," *Comput. J.*, vol. 7, no. 4, pp. 308–313, Jan. 1965.

[20] W. H. Press, *Numerical recipes in C: the art of scientific computing*, 2nd ed. Cambridge, UK: Cambridge University Press, 1992.

[21] Y. Jiang, J. Jiang, C. Zhang, W. Zhang, Y. Gao, and Q. Guo, "Recognition of battery aging variations for $LiFePO_4$ batteries in 2nd use applications combining incremental capacity analysis and statistical approaches," *J. Power Sources*, vol. 360, pp. 180–188, Aug. 2017. [Online]. Available: https://linkinghub.elsevier.com/retrieve/pii/S0378775317307796

[22] T. Kalogiannis, D. I. Stroe, J. Nyborg, K. Nørregaard, A. E. Christensen, and E. Schaltz, "Incremental Capacity Analysis of a Lithium-Ion Battery Pack for Different Charging Rates," *ECS Trans.*, vol. 77, no. 11, pp. 403–412, Jul. 2017. [Online]. Available: https://iopscience.iop.org/article/10.1149/07711.0403ecst

[23] A. Krupp, E. Ferg, F. Schuldt, K. Derendorf, and C. Agert, "Incremental Capacity Analysis as a State of Health Estimation Method for Lithium-Ion Battery Modules with Series-Connected Cells," *Batteries*, vol. 7, no. 1, p. 2, Dec. 2020. [Online]. Available: https://www.mdpi.com/2313-0105/7/1/2

[24] M. Maures, Y. Zhang, C. Martin, J.-Y. Delétage, J.-M. Vinassa, and O. Briat, "Impact of temperature on calendar ageing of Lithium-ion battery using incremental capacity analysis," *Microelectron. Reliab.*, vol. 100-101, p. 113364, Sep. 2019. [Online]. Available: https://linkinghub.elsevier.com/retrieve/pii/S0026271419304731

[25] Y. C. Zhang, O. Briat, J.-Y. Delétage, C. Martin, N. Chadourne, and J.-M. Vinassa, "Efficient state of health estimation of Li-ion battery under several ageing types for aeronautic applications," *Microelectron. Reliab.*, vol. 88-90, pp. 1231–1235, Sep. 2018. [Online]. Available: https://linkinghub.elsevier.com/retrieve/pii/S0026271418305869

[26] E. Schaltz, D.-I. Stroe, K. Norregaard, L. S. Ingvardsen, and A. Christensen, "Incremental Capacity Analysis Applied on Electric Vehicles for Battery State-of-Health Estimation," *IEEE Trans. Ind. Appl.*, vol. 57, no. 2, pp. 1810–1817, Mar. 2021. [Online]. Available: https://ieeexplore.ieee.org/document/9328130/

[27] T. Plattard, N. Barnel, L. Assaud, S. Franger, and J.-M. Duffault, "Combining a Fatigue Model and an Incremental Capacity Analysis on a Commercial NMC/Graphite Cell under Constant Current Cycling with and without Calendar Aging," *Batteries*, vol. 5, no. 1, p. 36, Mar. 2019. [Online]. Available: https://www.mdpi.com/2313-0105/5/1/36

[28] M. Huang, "Incremental Capacity Analysis-Based Impact Study of Diverse Usage Patterns on Lithium-Ion Battery Aging in Electrified Vehicles," *Batteries*, vol. 5, no. 3, p. 59, Sep. 2019. [Online]. Available: https://www.mdpi.com/2313-0105/5/3/59

[29] P. Gao, C. Zhang, and G. Wen, "Equivalent circuit model analysis on electrochemical impedance spectroscopy of lithium metal batteries," *J. Power Sources*, vol. 294, pp. 67–74, 2015.

[30] W. Choi, H.-C. Shin, J. M. Kim, J.-Y. Choi, and W.-S. Yoon, "Modeling and Applications of Electrochemical Impedance Spectroscopy (EIS) for Lithium-ion Batteries," *J. Electrochem. Sci. Technol*, vol. 11, no. 1, pp. 1–13, 2020.

VI. Biography Section

Christopher Dunn (Student Member, IEEE) received the bachelor's degree from the Portsmouth School of Pharmacy, Portsmouth, U.K., in 1985, the master's degree from the Queen's University of Belfast, Belfast, U.K., in 1993, and the Graduate Diploma in Electronics from The University of Waikato, Hamilton, New Zealand, in 2019, where he is currently pursuing the Ph.D. degree. His background is originally in the pharmaceutical sciences, with past specialization in medicinal chemistry (notably quantitative structure–activity relationships and pharmaceutical analysis), pharmaceutical technology, small-scale and aseptic/sterile manufacturing, and quality assurance. He has also worked in scientific communications and in asset management/inspection and line structure engineering for the power supply industry.

Jonathan Scott (Life Member, IEEE) received the B.Sc., B.E. (Hons), M.Eng.Sc., and Ph.D. degrees from The University of Sydney in 1977, 1979, 1985, and 1997, respectively, and the PGC Management in Higher Education from Waikato University in 2014. From 1998 to 2006, he was with Hewlett-Packard and Agilent Technologies Microwave Technology Center, Santa Rosa, CA, USA, where he was responsible for advanced measurement systems operating from dc to millimeter-wave. In 1997 and 1998, he was the Chief Engineer of RF Technology, Sydney, NSW, Australia. He was with the Department of Electrical Engineering, The University of Sydney, Sydney, prior to 1997. He was the Foundation Professor of electronic engineering with The University of Waikato, Hamilton, New Zealand from 2006 to 2022. He has authored more than 150 refereed publications, several book chapters, and a textbook. He holds numerous patents, several covering active products from microwave and RF to biomedical and battery systems. His educational interests include threshold concepts and their application, particularly across engineering disciplines. His research interests are the characterization and modeling of implantable electrodes, semiconductor devices, batteries, and acoustic systems.

Marcus Wilson received the Honors degree in Physics and Theoretical Physics from the University of Cambridge in 1992, and the Ph.D. degree in Theoretical Solid State Physics from the University of Bristol in 1995. He is a Senior Lecturer in Physics and Chemistry in Te Aka Mātuatua – School of Science at The University of Waikato, Hamilton, New Zealand. He has worked in numerical modeling of physics processes in industry in the U.K. and in academia in New Zealand, the latter since 2004. His research interests include electric properties and dynamics of the human brain, transcranial magnetic stimulation, and more recently batteries.

Michael Mucalo received the bachelor's and master's degrees in Chemistry, and the Ph.D. degree in Chemistry in 1991, from the University of Auckland, New Zealand. He is an Associate Professor of Chemistry in Te Aka Mātuatua – School of Science at The University of Waikato, Hamilton, New Zealand. He has had post-doctoral appointments as a Foundation for Research, Science and Technology Fellow in the then Department of Scientific and Industrial Research in Gracefield, Lower Hutt, New Zealand, from 1991 to 1993, and as a Science and Technology Agency Fellow at the National Industrial Research Institute of Nagoya, Japan, from 1993 to 1995. He joined the University of Waikato in 1995, and has a wide area of research interests with materials chemistry as a central theme. These interests span biomedical materials based on calcium phosphate, colloid chemistry, design of matrices for water treatment, repurposing of waste materials, electrochemistry, and controlled-release drug delivery. His pursuits in electrochemistry have been in the area of infrared spectroelectrochemical characterization of corroding interfaces as a function of potential, where he has published a number of studies. More recently, he has become more interested in battery electrochemistry.

Michael Cree (Senior Member, IEEE) received the B.Sc. (Hons) degree in Physics, and the Ph.D. degree in Electrical and Electronic Engineering from the University of Canterbury in Christchurch, New Zealand, in 1990 and 1994, respectively. He is an Associate Professor of Electrical and Electronic Engineering with the University of Waikato, Hamilton, New Zealand. His research interests include medical imaging, computer vision, time-of-flight range imaging, and, more recently, equivalent circuit modeling of batteries.

4.3 Complete Incremental Capacity and Cyclic Voltammetry-Type Plot Sets

All available ICA and CV-type plots could not be shown in the paper presented in this chapter because of journal space limits. The full sets are reproduced here to show how the plots evolved with each increase in current.

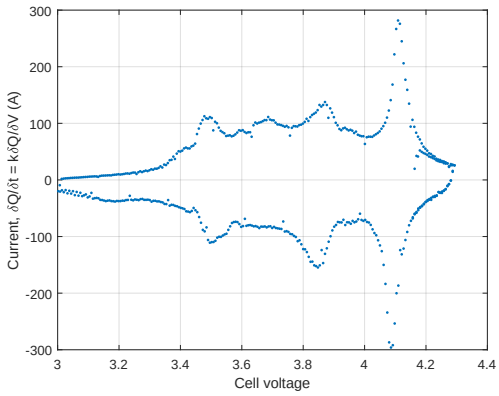

(a) 50 mA.

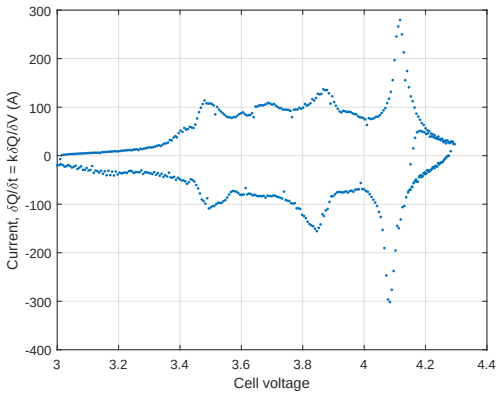

(b) 100 mA.

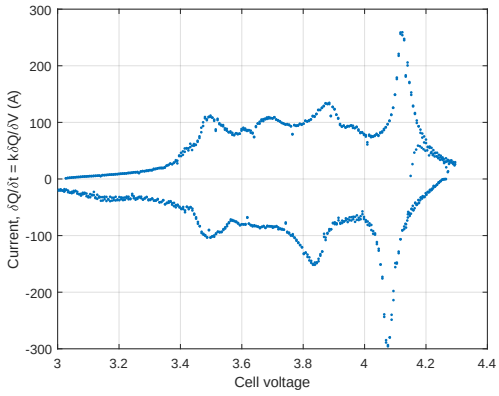

(c) 200 mA.

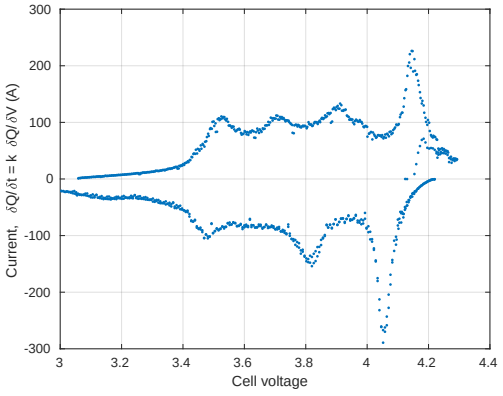

(d) 500 mA.

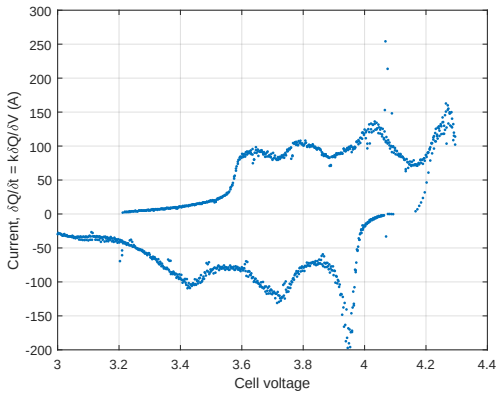

(e) 2 A.

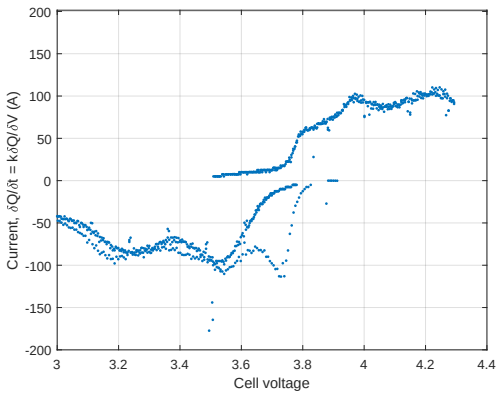

(f) 5 A.

Figure 4.6: CV-type plots for a 4.8 Ah lithium NCA battery charged and discharged at currents ranging from 50 mA to 5 A.

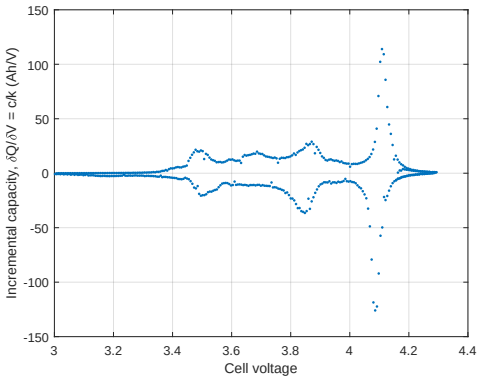

(a) 50 mA.

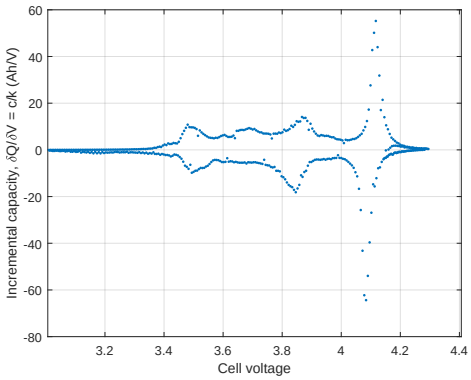

(b) 100 mA.

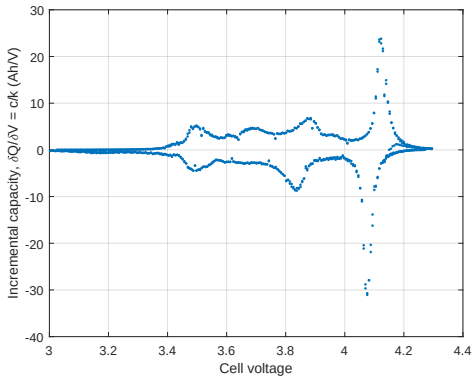

(c) 200 mA.

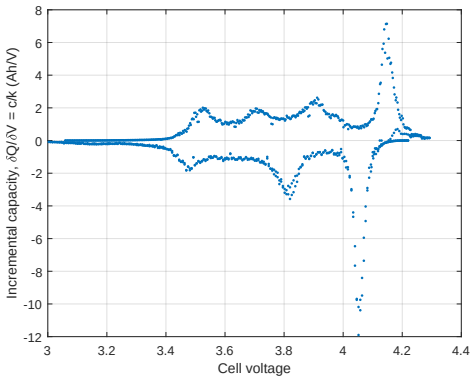

(d) 500 mA.

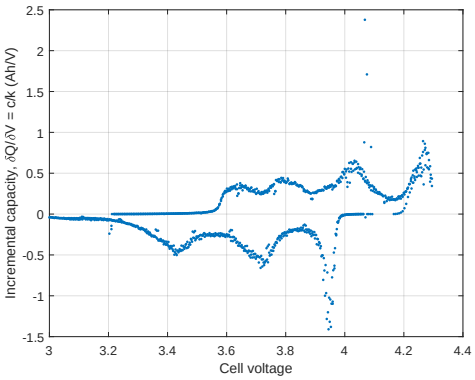

(e) 2 A.

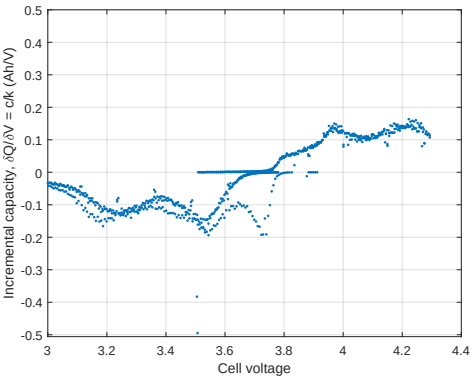

(f) 5 A.

Figure 4.5: ICA plots for a 4.8 Ah lithium NCA battery charged and discharged at currents ranging from 50 mA to 5 A.

Chapter 5

New Theory and Efficient Algorithm for Tracking Lithium Battery State of Health

5.1 The Constant Phase Element and Battery State of Health

The work reported in Chapter 3 in the frequency domain and Chapter 4 in the time domain reinforces the place of the CPE as a significant and necessary component of a battery ECM [44, 52, 31]. The discussion thus far has focused on battery characterisation, but we would like explore links between the CPE-based battery model and SoH. Importantly, for future practical application (in, for example, battery management systems), this needs to be done in realistic situations using the types of waveform encountered in real-world settings.

The research described in this chapter was initially intended for eventual publication, with "IEEE Transactions on Instrumentation and Measurement" as a likely target journal, as the work follows on from and ties in with the papers in Chapters 3 and 4. It also shows further application of the measurement techniques and equipment used by the Battery Modelling Group. A preliminary draft that required further work is presented in this chapter. A subsequent paper by Wilson et al. [102] that developed these ideas sufficiently for publication (after initial submission of this thesis in November 2023) is presented in Appendix C.

5.2 Energy Efficiency as a Marker For State of Health

In 2015, Hartley et al. [65] published observations that linked the energy efficiency of a battery (i.e., the ratio of energy put into the battery upon charging, E_{in}, to that delivered when the battery is discharged, E_{out}) to its fractional order when the battery is viewed as a single fractional element. Hartley's primary objective was to ascertain and describe the conditions under which energy efficiency could be maximised during a single charge-discharge cycle for fractional elements of order -1 (inductor) to $+1$ (capacitor), and to show that these conditions held for both constant current and constant voltage scenarios. The authors then used their findings to construct curves showing the relationship between maximum input-to-output efficiency and fractional order.

It is important to note here that Hartley et al. described a specific case where the system is charged from rest with initial voltage and charge of zero, and then discharged back to the initial zero state, using a single rectangular pulse. They did not generalise their findings to other waveforms and scenarios.

These authors demonstrated their hypothesis with an example based on a measured 1.0 F supercapacitor. The experiment was repeated here for constant current charge and discharge in simulation with an R-CPE battery model. This was done to verify that the idea of relating u to α is a practical one that extends to systems other than that described in the paper, and as an additional test of our SPICE modelling process.

5.2.1 Repeating the Work of Hartley et al. in a Battery Model

Hartley et al. [65] stated that the energy efficiency (which we call u) of a fractional element is:

$$\frac{E_{out}}{E_{in}} = [2^{\alpha} - 1]^2 \tag{5.1}$$

where α is the fractional order of the element.

If we know u, then, with rearrangement of Equation 5.1, we can estimate α.

$$\alpha = \frac{log(\sqrt{u} + 1)}{log(2.0)} \tag{5.2}$$

The above applies **only** when

- the fractional element is stimulated from rest with initial voltage and charge of zero;
- a constant current k_i is applied until time T;
- the fractional element is discharged back to its initial zero state using a constant current $-bk_i$,

where the current ratio b is given by

$$b = 2^{\alpha} - 1 \tag{5.3}$$

$-bk_i$ is applied from time T to time T_f, where

$$T_f = 2T \tag{5.4}$$

These conditions reportedly [65] confer maximum input-to-output energy efficiency for a fractional element for all α.

A simple R-CPE battery circuit was simulated in "ngspice" (https://ngspice.sourceforge.io/) according to the procedure described by Wilson et al. [103] as used by the Battery Modelling Group. This method generates a CPE subcircuit in SPICE, using software written in C, that is based on an array of RC elements in parallel as originally described by Morrison [88]. The SPICE model consisted of a CPE with $\alpha = 0.8$ and fractional capacitance $C_f = 1200\,\mathrm{As}^{\alpha}\mathrm{V}^{-1}$ in series with a resistance of $0.025\,\Omega$ (parameters that reflect real lithium-ion batteries as measured by us). An initial constant charge current of 500 mA (k_i, an arbitrary value reflecting the magnitude of cycling current that might typically be used in the laboratory) was applied for 10 000 s (T). A discharge current of −370 mA (this is $-bk_i$ as described above) was then applied for a further 10 000 s (i.e., to T_f; this was equivalent to a 50 μHz charge-discharge cycle). This was modelled in a piecewise-linear (PWL) manner as follows:

```
Istim 0 99 PWL(0 0 0.1 500mA 10000s 500mA 10000.1s -370mA 20000s -370mA 20000.1s 0)
```

where $Istim$ is the SPICE name of the current source, 0 and 99 are the nodes either side of $Istim$, and the current starts at zero amps at 0 s, then maintains 500 mA from 0.1 s to 10 000 s, then drops to −370 mA from 10 000.1 s to 20 000 s, and finally returns to zero at 20 000.1 s.

A plot of the SPICE-simulated currents and voltages (**Figure 5.1**) showed a response exactly as predicted by Hartley et al. [65].

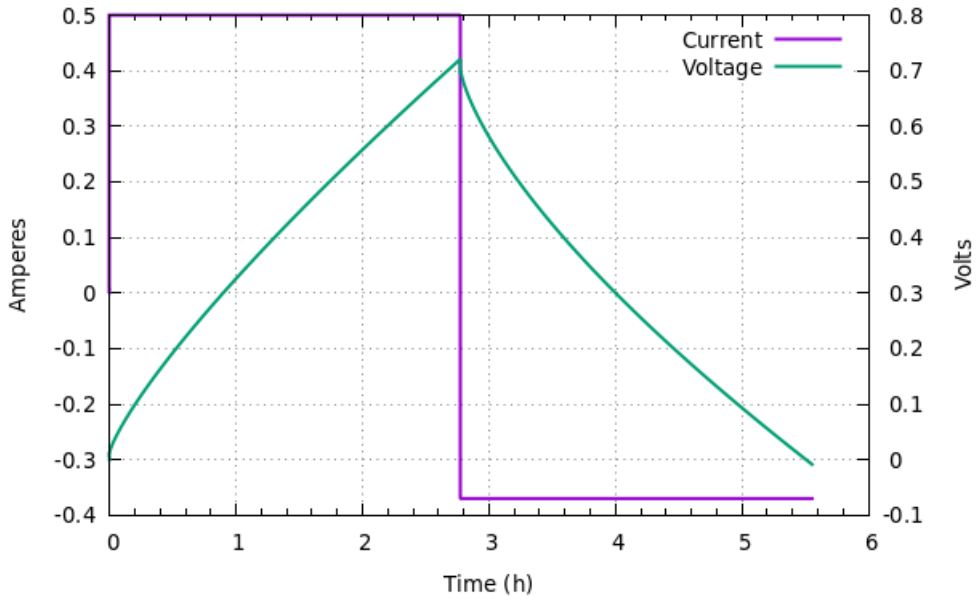

Figure 5.1: Current stimulus and voltage response in a battery with $\alpha = 0.8$ simulated in SPICE.

An AWK script (Section 1.5) was used to integrate energy in and energy out by multiplying current and voltage at each timestep and keeping cumulative totals for E_{in} and E_{out}. Calculation of $u = E_{out}/E_{in}$ at the end of the simulation yielded $u = 0.543$. Thus

$$\alpha = \frac{log(\sqrt{0.543} + 1)}{log(2.0)} = 0.796$$

which appears to validate the work of Hartley and colleagues [65] and the SPICE CPE model [103]. It also reinforces the concept of linking a CPE characteristic (in this case fractional order) to energy efficiency.

5.3 Energy Efficiency in Real-World Batteries

The idea that energy efficiency E_{out}/E_{in}, which we will call u, would decline as a battery was repeatedly cycled was initially tested on a ".tvi" file from a past bzdcp66 measurement (see Chapter 3). **Figure 5.2** shows a zoomed-in portion (for easy visualisation of the waveform) of the current against time plot for this measurement, which ran for a total of 3×10^6 seconds (34.7 days). The waveform shows the

measurement tones superimposed on a 1 A square wave (which is effectively cycling the battery).

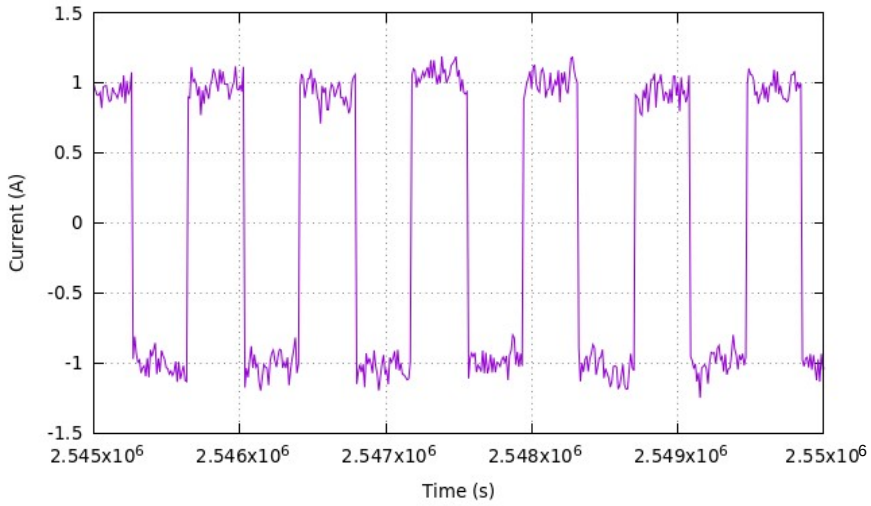

Figure 5.2: Zoomed-in current versus time plot from an impedance measurement (bzdcp66) on a 66332A source measurement unit using a 2.6 Ah ICR 18650 battery.

The result of calculation of u, data line by data line, averaged out as the measurement proceeded, is shown in **Figure 5.3**.

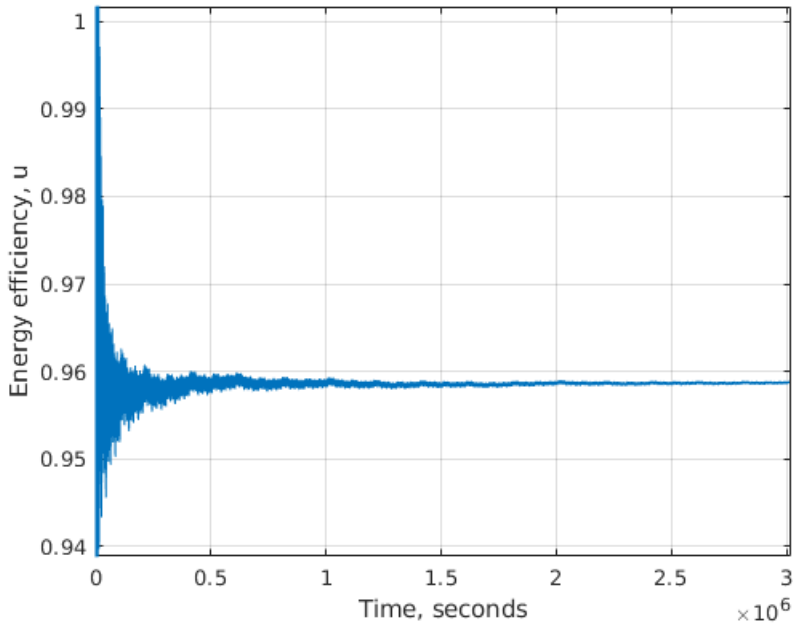

Figure 5.3: Energy efficiency u ($= E_{out}/E_{in}$) averaged over time of the 2.6 Ah lithium ICR 18650 battery of **Figure 5.2**.

The measurement settles to a u value representative of the battery under test as progressively more charge and discharge cycles are completed. Calculating u by

each line of data as the measurement proceeds is a poor method for detecting drifts in u, however, since we are averaging the result over the entire measurement time. A very long measurement time would be needed to discern declining u with this approach, as SoH deterioration in a battery in normal use is a gradual process.

It would be better to identify complete cycles and compute E_{out} and E_{in} for each complete half cycle. This is straightforward for regularly repeating waveforms like sinusoids or even waveforms that are staggered or asymmetrical (**Figures 5.4** and **5.5**), but not so for irregular or arbitrary waveforms of the type that might be produced by a battery in use. In addition, **Figure 5.5** indicates variation of u with shape, magnitude and period of waveforms, which suggests that some as-yet unknown waveshape correction factor might be required.

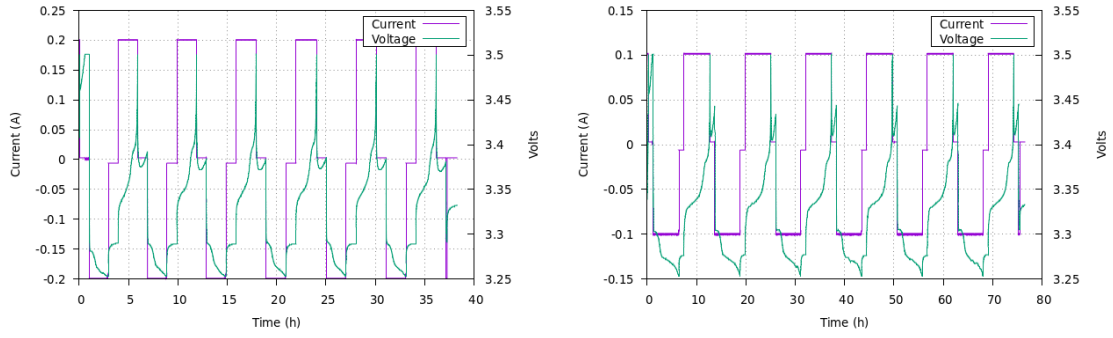

(a) Waveform 1.

(b) Waveform 2.

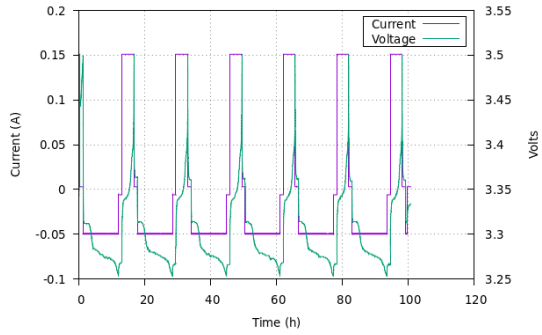

(c) Waveform 3.

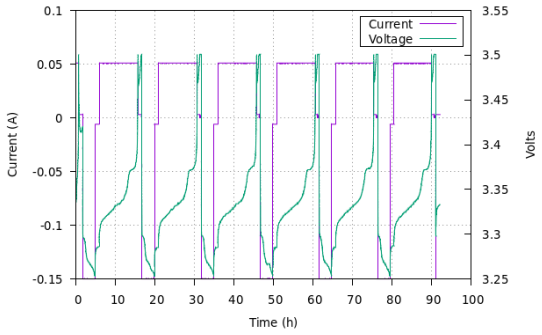

(d) Waveform 4.

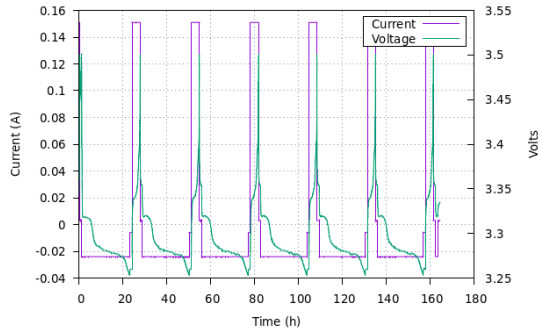

(e) Waveform 5.

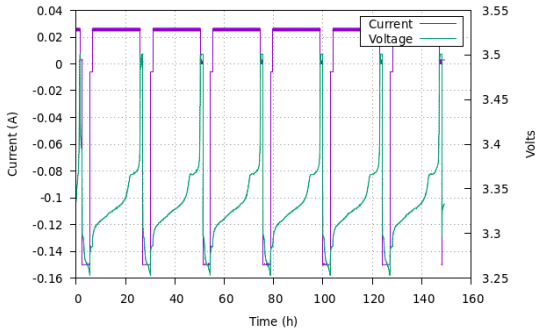

(f) Waveform 6.

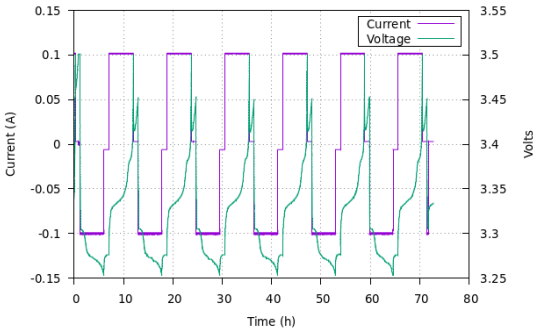

(g) Waveform 7.

Figure 5.4: Cycling plots for a range of CC-CV protocols applied to a 1.6 Ah 3.2 V lithium iron phosphate 18650 battery. Note the varying minimum and maximum currents, waveshapes and period lengths.

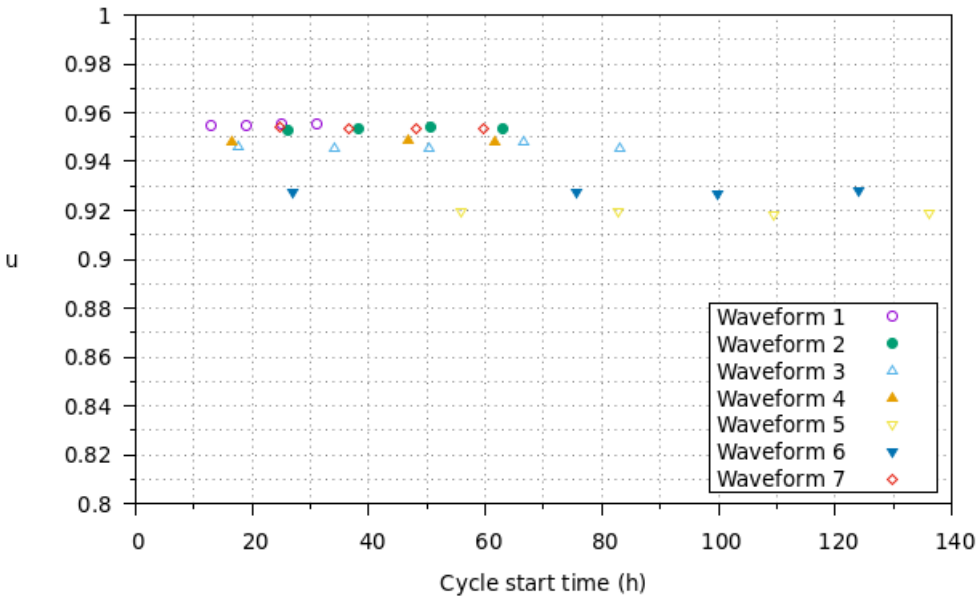

Figure 5.5: u values calculated by cycle for the waveforms in **Figure 5.4**.

5.4 Real-World Measurements: Self-Similar (Pseudo-) Cycles

In addition to exploring u as a potential marker of battery SoH, we would like to be able to calculate this parameter from waveforms that are likely to be seen in real-world environments. Consider the energy delivered by the battery of an EV. The current drawn is large when the vehicle is accelerating, modest when cruising, is reversed when braking regeneratively, and so forth. These events take place in an irregular fashion, and are influenced by factors such as traffic light timing, hills on the route taken, weight being carried, etc. On some days the user may make more trips than on others. When the vehicle's battery is being charged, current is constant (or follows a defined profile). In-use current draw, on the other hand, will occur less predictably, and will include large bursts or current spikes. Recharging might be carried out each night, or perhaps weekly, but might also sometimes be interrupted for an urgent journey. Clearly, no two days will be exactly alike, and even if the vehicle is used for regular commuting five days a week weather and other unexpected events will occasionally break the routine.

For the purposes of experimentation with real batteries in the laboratory, test sequences capable of specifying current as a function of time for periods of time ranging from days to years were required. These current profiles never repeat exactly but have a quality that we refer to as self-similarity, and return to a defined "home state" after each complete recharge cycle. This home state might have some variability to it, for example charge to 80% most days, but occasionally all the way to 100%. Cyclic behaviours that can be identified from this quality of self-similarity are referred to as pseudocycles.

A software utility named "GenDrive" was developed to generate such a waveform by Vance Farrow of the Battery Modelling Group (see author list in the paper that follows), and was used for these experiments with permission. The GenDrive waveform is based on current versus time profiles obtained from experiments originally carried out by the present author that involved weekly use of an electric scooter [104] (**Figures 5.6** and **5.7**).

GenDrive is a utility written in the MATLAB® programming language that uses the MATLAB® randn() function. It generates text files consisting of two columns, time and current (*.ti files). Waveforms created by GenDrive can be broken down into cycles, series and pulses, each of which contains multiples of the next (i.e., a cycle is made up of multiples of series, and a series is a multiple of pulses). For the experiments described in the paper presented here, negative pulses (which draw current from the battery) were set to a mean -1.5 A with standard deviation (SD) 0.12 A. Positive pulses (which push current into the battery) were a mean 0.9 A with SD 0.18 A. Each GenDrive series contains a mean of fifteen (SD = 4) negative pulses, and seven (SD = 3) positive pulses, so the combination of generally greater

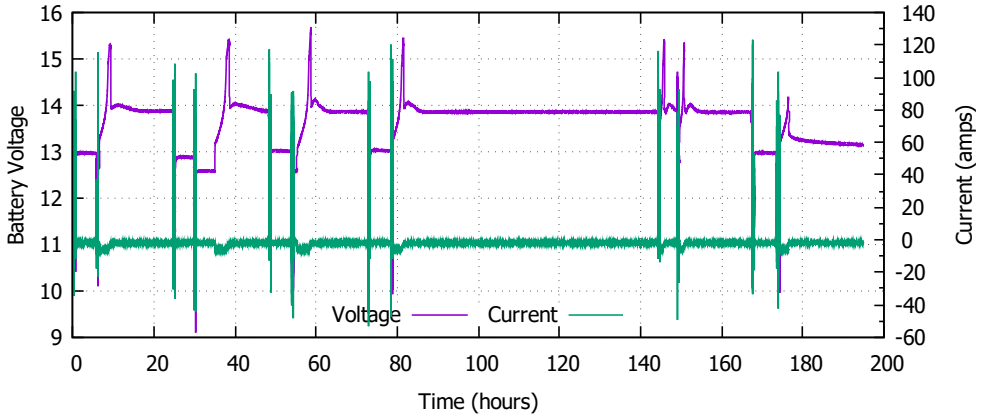

Figure 5.6: Voltage and current versus time logged during a week's use of an electric scooter powered by two 12-volt lead-acid batteries wired in series (voltage was measured at the node between the two batteries). Note the twice-daily current draws as the scooter is ridden on weekday mornings and afternoons. The period of inactivity from approximately 80 to just over 140 hours shows the scooter left over a weekend plus one day [104].

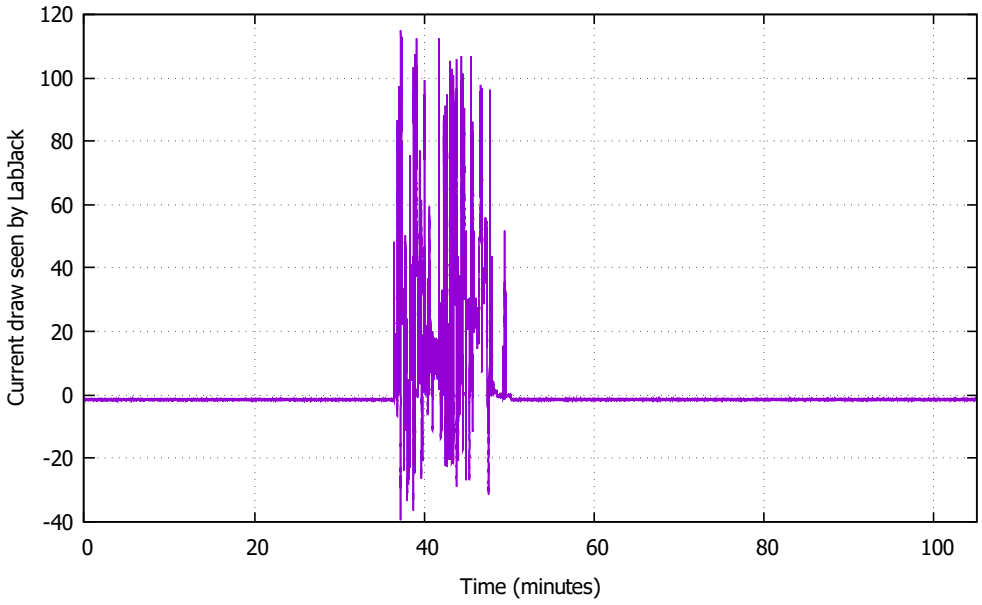

Figure 5.7: Zoomed-in plot of current (amps) versus time with scooter ride during data collection as shown in **Figure 5.6**. The y-axis label refers to the data logger used, a "LabJack" U6 device (https://labjack.com/products/u6), connected to the scooter across a 2 mΩ shunt to provide current sensing [104].

number and magnitude of negative pulses sets an overall trend of drawing current from the batteries. Each cycle contains at least two series of pulses which are randomly spaced with rest periods of between 15 minutes and 2 hours, and finishes with

a 1 A recharging period during which the net charge lost is replaced. Parameters were arrived at experimentally by setting current values suitable for batteries in use in the laboratory, and by comparing the evolving GenDrive waveform with the original scooter driving data and fine-tuning until the current excursions and frequency spectrum of the artificial waveform were deemed to match the real-world waveform closely enough.

A single series of pulses from a GenDrive *.ti file is shown below. The left-hand column shows the time in seconds, and the right-hand column the current in amps to be drawn or supplied from that time until the next listed timepoint.

```
3.312280000000e+04        -1.440000e+00
3.319260000000e+04        0
3.322930000000e+04        -2.030000e+00
3.331660000000e+04        9.300000e-01
3.338330000000e+04        0
3.341590000000e+04        -2
3.349520000000e+04        0
3.353230000000e+04        1.040000e+00
3.358190000000e+04        -1.590000e+00
3.366050000000e+04        1.100000e+00
3.372050000000e+04        1.190000e+00
3.378270000000e+04        0
3.381240000000e+04        -1.660000e+00
3.389410000000e+04        0
3.392050000000e+04        -1.540000e+00
3.400980000000e+04        -1.750000e+00
3.408900000000e+04        3.300000e-01
3.414310000000e+04        -1.450000e+00
3.422250000000e+04        8.400000e-01
3.427840000000e+04        5.500000e-01
3.433210000000e+04        -1.850000e+00
3.441160000000e+04        0
3.444330000000e+04        -1.820000e+00
3.452420000000e+04        0
3.455610000000e+04        9.900000e-01
3.464390000000e+04        -2.130000e+00
3.474970000000e+04        -1.630000e+00
3.483230000000e+04        0
3.486620000000e+04        5.300000e-01
3.493610000000e+04        0
3.583020000000e+04        0
3.670570000000e+04        0
4.192050000000e+04        -1.620000e+00
```

The pulses and series generated by this part of the file, and the five subsequent series, are shown graphically in **Figure 5.8**. The figure shows the six series making up part of a cycle, and the end of that cycle followed by the start of a 1 A recharge period.

The GenDrive *.ti file is sourced by bap66, another C program that runs in the command line on the Raspberry Pi computers controlling the 66332A units (see Section 1.5). When called without parameters, bap66 presents the following instructions to the user:

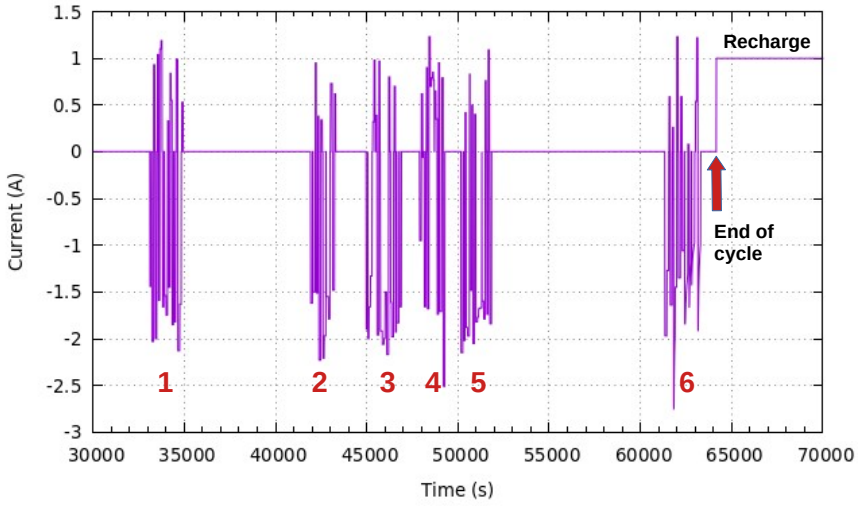

Figure 5.8: Part of a GenDrive current stimulus: 30 000 s to 70 000 s (8.3 to 19.4 hours). Each series (numbered 1 to 6 in the figure) is made up of individual positive and negative pulses, with rests of 15 minutes to 2 hours between series. Each collection of series makes up a cycle, which ends with a 1 A charging period as indicated.

```
bap66 V1.50 jbs&cjd Jan 2021, Apr 2023
Battery arbitrary waveform measurement via Prologix/Fenrir GPIB-USB & 66332A.
Usage: bap66 USB Vmin Vmax baseName [Addr]
where-  USB is the rPi USB address (/dev/ttyUSB0, /dev/ttyACM0, etc);
        Vmin/Vmax are voltage limits (aborts outside this range);
        baseName is the file string to be used;
        Addr is the optional GPIB bus address, def=5.
Sources current described by a .ti file, measuring V & I to .tvi file.
Creates baseName.tvi, basename.log, reads basename.ti file.
Assumes ti file contains seconds-amps pairs (or blank lines).
Requires no drivers, communicates using ++cmd protocol.
```

"baseName" is the name of the input file called; this name is also used for the output file (with a .tvi suffix) generated by bap66. V_{min} and V_{max} are limits set according to rating of the battery being tested.

5.4.1 Detecting Self-Similar (Pseudo-) Cycles and Measuring u

For the GenDrive waveform, u was calculated using "getSoH", a C program that searches streams of voltage and current data for pseudocycles. The utility runs in the command line, and presents the user with the following instructions when called with no parameters.

```
getSoH                  V6.10 JBS CJD May 2023
Usage: getSoH file.tvi Ithreshold Verror t_rest Qerr [Rs [t_min [t_max]]] >file.tu
where
        Ithreshold is the current considered to be close to zero;
        Verror is how close to the starting voltage one must be;
        t_rest (seconds) is the time considered enough to be at rest;
        Qerr is how close to zero the delta-Q must be;
        Rs is battery ohmic resistance (def=0.00);
        t_min (seconds) is the smallest permitted pseudocycle duration (def=3 days);
        t_max (seconds) is the longest permitted pseudocycle duration (def=14 days).
Takes in a 3-col ascii file giving time, voltage, current;
writes plottable Tstart(hr)-u-Tperiod(hr) triples to stdout at pseudocycles,
plus adjusted efficiency factor.
Cycle recognised for return close to V and Q between rests, with large enough Q
excursion plus required min and max time between matching rests.
Writes progressive pseudocycle reports to stderr.
Writes some diagnostics to getSoH.log.
If time is not monotonic (cat tvi files?) time is incremented to make it monotonic.
Start with Verror & Qerr around 0.2% of battery values.
Ithreshold depends upon hardware. t_rest will increase with battery age.
```

GetSoH runs line-by-line through the *.tvi file generated by bap66 and identifies rest periods of negligible current movement (based on the $Ithreshold$ value entered by the user) that exceed a given duration (t_rest). While doing this it accumulates charge delivered and withdrawn. Using the parameter $Verror$, it examines terminal voltages at the end of rest periods, and identifies pseudocycles as periods delineated by rests where the voltage and charge differences (based on $Qerr$) are smaller than the parameters entered. A pseudocycle search starts every time a rest is identified, coulomb counting separately for each one, and terminates when the pseudocycle completes at the next rest. The algorithm is executed sequentially (current and voltage data are processed but not stored). The process therefore requires very little memory and very modest processing power.

Note that in the experiments described in the paper that follows, a pseudocycle is in fact one or more GenDrive series (of pulses), while a GenDrive cycle is a complete set of series between recharges. Thus, in this instance, GetSoH is identifying as pseudocycles groups of series that may or may not correspond to complete GenDrive cycles. The point is made because GetSoH was written as a utility that could be used with any arbitrary waveform, not GenDrive specifically, which simply represents the first attempt to deploy it. It also does not affect the overall progression of the u calculation over the life of the battery. GetSoH can be made to identify larger groups of series as pseudocycles by increasing the length of the t_min parameter (the smallest permitted pseudocycle duration, which defaults to three days if not specified). There is also a t_max parameter that can be used to override the default 14 days for the maximum permitted pseudocycle duration. Adjustment of parameters allows the user to control the operation of the software to take account of factors such as the equipment used and the timescale of the measurement.

There is also the option to add a series resistance (Rs) for the battery. If this is

done an adjustment is made to the voltage used in the energy calculation. The adjusted efficiency factor mentioned in the instructions relates to the as-yet unidentified waveform correction factor referred to earlier, and was not used.

New Theory and Efficient Algorithm for Tracking Lithium Battery State of Health

Christopher Dunn, *Student Member, IEEE*, Jonathan Scott, *Life Member, IEEE*, Marcus Wilson, and Vance Farrow

***Abstract*—Recent observations in battery measurement studies and the representation of batteries by equivalent-circuit models (ECMs) containing constant-phase elements (fractional capacitors) suggest a powerful new measure of battery state of health (SoH) based on the evolution of energy efficiency as the battery ages. The proposed measure may be calculated from arbitrary current and voltage waveforms as seen in normal battery use, and does not require values of any model parameters. The relationship between efficiency and battery SoH is demonstrated. The algorithm requires very little data storage and only trivial computing power. Simulation and measurement confirm the accuracy and utility of the new measure. Measured data stretches over 120 days of continuous usage.**

***Index Terms*—Rechargeable batteries, state of health, fractional derivatives, equivalent-circuit model, power factor**

I. Introduction

BATTERY state of health (SoH) has been defined as "a measure that reflects the general condition of a battery and its ability to deliver specified performance in comparison with a fresh battery" [1].

Charge cycle capacity has been presented as the "gold standard" for measurement of battery health [1]. Batteries degrade and lose charge-holding capacity over time after manufacture [2] because of a variety of physical aging mechanisms [3]. When the capability of the battery to hold and deliver charge (and therefore energy) drops below a predefined threshold (typically 70% to 80% of its capacity at manufacture), many warranty providers consider it to have reached the end of life [2, 4]. SoH is a term used to express this capacity fade [2, 3]. This definition is popular because it can be measured easily on the bench.

SoH does not correspond to a single specific physical characteristic, however, and charge capacity is not the only property of a battery that changes with progressive degradation [1]. Power capability (the ability to deliver a given power) also falls. Wearing out of various internal battery components can manifest as increased charge transfer and diffusion resistance, reduced current density, decreased voltage, and heat generation [5]. Recent reports describe Tesla roadster batteries failing through loss of power capacity [6].

We seek to characterize SoH in a battery using measured arbitrary current and voltage. Because the waveform is arbitrary, any measure must be independent of frequency, wave shape and load current amplitude. It should not depend upon any particular charging behavior a user may impose. In this manuscript a parameter related to cycle energy efficiency is proposed as suitable for this purpose.

The authors are with the School of Engineering and the School of Science, University of Waikato, Hamilton, New Zealand. e-mail: cjdunn@xtra.co.nz

II. Theory

A battery may be accurately represented by an equivalent circuit model (ECM) comprising only a series resistor and constant-phase elements (CPEs; fractional capacitors) [7, 8, 9]. Hartley et al. showed the energy cycle efficiency of a charged and then discharged CPE to be a simple power function of the system order, subject to "the assumption that zero initial energy is stored" [10]. However, the authors' main stated aim was to demonstrate energy equivalence of constant current and constant voltage charging and discharging in a CPE, and to describe conditions under which energy efficiency could be maximized for a given fractional order. They did not generalize to different types of waveform or situations where there is considerable energy stored and a large dc offset.

Both the capacity of a battery and the apparent order of the CPE that models it in the simplest R-CPE equivalent circuit decrease with wear [11]. This is consistent with falling cycle capacity and power capability.

By definition, a CPE exhibits a constant phase shift between sinusoidal current and voltage across all frequencies [8, 12]. Thus, the power factor of a CPE is independent of the frequency at which it is measured. Moreover, as shown by Hartley et al. [10], energy loss in a CPE over a cycle is related to α, the order of the fractional derivative describing that CPE. Thus, the energy efficiency of the element reveals the order of the derivative. Since a CPE is linear [13], superposition holds, and we may decompose any waveform into a sum of sine functions. From this we can relate efficiency to SoH.

A. Single Sine Wave Stimulus

Let us assume that the current into a cell is a single sine wave:

$$I(t) = I_0 \sin(\omega t) \tag{1}$$

The complex impedance of a CPE is

$$Z(\omega) = \frac{1}{C_f(\jmath\omega)^\alpha} \tag{2}$$

The voltage across a CPE for this current input, assuming there is a constant starting voltage offset V_0, is:

$$V(t) = V_0 + V_a \sin(\omega t - \theta) \tag{3}$$

where $V_a = |Z(\omega)|I_0$ is the amplitude of the ac part of the waveform, $\theta = \alpha\pi/2$ is the phase, and α is the order of

the fractional derivative. Note that V_a depends on frequency through $|Z|$ and the phase delay θ depends on the order of the CPE, α.

Since the terminal voltage of a battery is always positive in a practical situation, the sign of the power, $P(t) = V(t)I(t)$, is determined by the sign of the current $I(t)$, positive in the first half-cycle and negative in the second. The energy into the CPE in the first half-cycle is given by:

$$E_{\text{in}} = \int_{t=0}^{T/2} V(t)I(t)dt$$
$$= \int_{t=0}^{T/2} \left[V_0 + V_a \sin(\omega t - \theta)\right] \left[I_0 \sin(\omega t)\right] dt \quad (4)$$

which is:

$$E_{\text{in}} = \int_{t=0}^{T/2} V_0 I_0 \sin(\omega t)dt + \int_{t=0}^{T/2} V_a I_0 \sin(\omega t)\sin(\omega t - \theta)dt \quad (5)$$

where T is the period of the sine wave. The first part integrates simply to $V_0 I_0 T/\pi$. The second part can be integrated by noting that

$$\sin\alpha \sin\beta = \frac{1}{2}\left[\cos(\alpha - \beta) - \cos(\alpha + \beta)\right] \quad (6)$$

and thus the energy into the CPE becomes

$$E_{\text{in}} = \frac{V_0 I_0 T}{\pi} + \frac{V_a I_0 T \cos\theta}{4} \quad (7)$$

The energy put *into* the CPE in the second half-cycle is given by:

$$E_{\text{out}} = \int_{t=T/2}^{T} V(t)I(t)$$
$$= \int_{t=T/2}^{T} \left[V_0 + V_a \sin(\omega t - \theta)\right] \left[I_0 \sin(\omega t)\right] dt \quad (8)$$

The quantity E_{out} is *negative*, since $I(t)$ is negative during the second half-cycle. We can perform the integration in the same way as for the previous half-cycle, giving us:

$$E_{\text{out}} = -\frac{V_0 I_0 T}{\pi} + \frac{V_a I_0 T \cos\theta}{4} \quad (9)$$

The energy taken *out* of the CPE in the second half-cycle is the negative of E_{out}.

Thus we can define the efficiency as being $u = -E_{\text{out}}/E_{\text{in}}$ which is:

$$u = \frac{V_0 I_0 T/\pi - V_a I_0 T \cos\theta/4}{V_0 I_0 T/\pi + V_a I_0 T \cos\theta/4} \quad (10)$$

Cancelling the factor of $I_0 T$ and multiplying top and bottom by π/V_0 gives:

$$u = \frac{1 - \pi V_a \cos\theta/4V_0}{1 + \pi V_a \cos\theta/4V_0} \quad (11)$$

In the limit of $\alpha \to 1$, in other words the CPE becoming a pure capacitor, $\cos\theta \to 0$ and thus $u \to 1$ as we expect since a capacitor cannot dissipate energy.

If the ratio of V_a to V_0 is rather less than one (which practically would likely be the case), then we can use the binomial theorem to approximate Equation (11) as:

$$u \approx 1 - \frac{\pi V_a \cos\theta}{2V_0} \quad (12)$$

and

$$\cos\theta \approx \frac{2V_0(1-u)}{\pi V_a} \quad (13)$$

and hence

$$\alpha \approx \frac{2}{\pi} \arccos\left[\frac{2V_0(1-u)}{\pi V_a}\right] \quad (14)$$

By measuring u experimentally we can then infer α.

B. Complex Stimulus

For multiple sinewaves let us define an applied current $I(t)$ over some time domain 0 to T:

$$I(t) = I_1 \sin(\omega_1 t + \phi_1) + I_2 \sin(\omega_2 t + \phi_2) + ...$$
$$= \sum_n I_n \sin(\omega_n t + \phi_n) \quad (15)$$

where n is an integer ≥ 0 (n.b., $I_0 = 0$ would denote no net average charge moved), I_n is a real amplitude for the nth component, $\omega_n = 2\pi n/T$, and ϕ_n is the phase of the nth component.

For the voltage over a CPE, each harmonic component is related to the equivalent harmonic component of the current, so:

$$V(t) = \sum_n V_n \sin(\omega_n t + \phi_n + \theta) \quad (16)$$

where $V_n = |Z_n| I_n$ is the (real) amplitude of the nth component and $|Z_n| = 1/C_f \omega_n^\alpha$ is the magnitude of the impedance at the nth frequency, with C_f the fractional capacitance and α the order of the CPE, and $\theta = -\pi\alpha/2$ is a constant phase difference between the V and I harmonic components.

In the case of a single sinewave it was possible to break the integration into the "adding energy" (E_{in}) and "removing energy" (E_{out}) parts. This allowed straightforward computation of efficiency, u. This is not feasible for an arbitrary waveform, however, as we cannot identify complete half-cycles to integrate from $t = 0$ to $T/2$. The determination of E_{in} and E_{out} is consequently mathematically difficult, possibly even intractable. Alternatively, therefore, we investigate the energy E dissipated over time T by integrating $I(t)$ and $V(t)$ as follows:

$$E = \int_{t=0}^{T} dt \left[\sum_n I_n \sin(\omega_n t + \phi_n)\right] \left[\sum_m V_m \sin(\omega_m t + \phi_m + \theta)\right] \quad (17)$$

Reversing the order of summation and integration:

$$E = \sum_n \sum_m I_n V_m \int_{t=0}^{T} dt \sin(\omega_n t + \phi_n) \sin(\omega_m t + \phi_m + \theta) \quad (18)$$

which will equal zero unless $m = n$, in which case (with this special case denoted by J_{nn}):

$$J_{nn} = \int_{t=0}^{T} dt \sin(\omega_n t + \phi_n) \sin(\omega_n t + \phi_n + \theta) \quad (19)$$

Using the identity $\sin(\alpha+\beta) = \sin\alpha\cos\beta + \cos\alpha\sin\beta$, with $\alpha = \omega_n t + \phi_n$ and $\beta = \theta$, we expand the second of the sines in the integral to give:

$$J_{nn} = \int_{t=0}^{T} dt \sin(\omega_n t + \phi_n)\sin(\omega_n t + \phi_n)\cos\theta$$

$$+ \int_{t=0}^{T} dt \sin(\omega_n t + \phi_n)\cos(\omega_n t + \phi_n)\sin\theta \qquad (20)$$

The sine-cosine product in the second integral goes to zero over the period; the sine-squared product in the first integrates to $T\cos\theta/2$. Then, substituting into Equation 18:

$$E = \sum_m \sum_n I_n V_m \delta_{nm} T\cos\theta/2 \qquad (21)$$

where the Kronecker delta $\delta_{mn} = 1$ if $m = n$ or 0 otherwise. Hence, carrying out the sum over m, we get the $m = n$ case (being non-zero) only, yielding

$$E = \frac{T\cos\theta}{2}\sum_n I_n V_n \qquad (22)$$

C. Self-Similar Cycles (SSCs)

Most rechargeable batteries are used in a repetitive fashion. A cell in an electric vehicle (EV) sees large current pulses as the vehicle accelerates, modest current draw while cruising, pulses of recharging when dynamically braking, periods of rest with minor current draw while stopped or parked, and episodic slow or fast charging. The pattern of such usage may change, say with the particular driver or the vehicle load or traffic conditions, but the approximate periodicity will remain. No two periods will be exactly alike, but they will resemble each other in their statistical properties, typical waveshapes, etc. A similar argument applies to batteries in power tools, mobile phones, solar-powered installations, wireless accessories, and grid storage facilities. We refer to the periods of self-similar activity as "pseudocycles".

Finding SoH via u in pseudocycles depends upon selecting intervals that capture a pseudoperiod from within the stream of current and voltage data that approximates an ideal period sufficiently closely. For example, one might consider any interval over which the charge delivered and the charge returned are equal, or close to equal, to constitute a valid pseudocycle.[1] Another condition might require that the starting and ending rest voltages of a cell be the same, or close; alternatively, perhaps both the change in charge and the change in rest voltage could be required to be small. Another condition would be that the statistical properties of the current waveform hold across the pseudocycle, or that an adjustment be made to compensate for this. Refer to Section III for details of how pseudocycles have been identified in this manuscript.

[1]Note that this definition fails with lead-acid batteries, and often with nickel metal hydride batteries. Both these chemistries are provided with a mechanism to cope with overcharging, so that they are not immediately damaged when too much charge is supplied.

D. Health via Efficiency

On the premise that declining energy efficiency tracks battery health, we require a generic indicator of SoH that follows θ independently of waveform. Equation 22 shows the overall energy dissipated in a pseudocycle. We suggest that this is proportional to $\cos\theta$, but this leaves us unsure as to how to approach the summation term (without performing Fourier transforms on $I(t)$ and $V(t)$ to obtain I_n and V_n). However, V_n depends on α via impedance, so α is involved in the summation term as well as $\cos\theta$. The research question then becomes: "How does α relate to energy dissipated?", in addition to whether it is possible to identify pseudocycles from a stream of real-world data.

Rewriting Equation 22 as

$$E = \sum_n \frac{T\cos\theta}{2} I_n V_n = \sum_n E_n \qquad (23)$$

where E_n is now defined as

$$E_n = \frac{T\cos\theta}{2} I_n V_n \qquad (24)$$

Then

$$\cos\theta = \frac{2E_n}{T I_n V_n} \qquad (25)$$

which suggests a ratio of energy dissipated by the nth harmonic component to the energy that would be dissipated by the nth component with no phase difference between I and V, i.e., energy "lost" over energy "contained".

We require a general formula that reduces back to (13) for the sinewave case, but the mathematical intractability of this process requires us to formulate a hypothesis based on what is known that can be tested empirically.

Let D be a measure of the deviation of the CPE from a pure capacitor (i.e., $D = 0$ implies pure capacitative behavior), so that

$$D = \frac{\langle V(t)\rangle (1-u)}{\sqrt{2}\sigma_V} \qquad (26)$$

where V_0 in (13) is replaced by $\langle V(t)\rangle$, the mean voltage over some chosen period, and V_a by $\sqrt{2}\sigma_V$, the peak voltage excursion across that period, and where u is the measured efficiency over that period. As a battery ages, we expect D to increase as efficiency decreases. This approach was to be explored using the present battery measurements.

III. Methods

A. Simulation

First, the relationship between u and α for the sine wave case (Section II-A) was explored using a modeled resistance in series with a CPE of known α generated by the open-source "ngspice" SPICE simulator (https://ngspice.sourceforge.io/). The CPE model was based on an array of resistors and capacitors in parallel as described by Morrison [14] and Seshadri and Scott [15], and subsequently developed and validated as a SPICE model by Wilson et al. [16].

A ".tran" analysis tracking current and voltage was run on a circuit simulation consisting of a small ($0.025\,\Omega$) series

resistance and a single CPE with $\alpha = 0.8$. A 50-μHz sine wave was simulated for 1.2×10^6 s, with an initial potential of $4.0\,\mathrm{V}$ on the CPE. The SPICE output was processed by an AWK script that detects cycles by looking for reversals in charge movement (current direction) and calculates E_{in} for each positive half-cycle and E_{out} for each negative half cycle. Total E for each half-cycle was calculated as the cumulative product of voltage and current for each recorded timestep (dt). Then, for each complete cycle:

$$u = \frac{E_{out}}{E_{in}} \tag{27}$$

B. Measurements

The initial CPE SPICE simulation was followed by battery measurements. The equipment and methods used at our center have been described in detail previously [17]. Briefly, measurements were taken at $22\,^{\circ}\mathrm{C}$ using two-quadrant precision sources (HP/Agilent/Keysight 66332A units) via four-wire connections controlled through GPIB interfaces by Raspberry Pi 4 computers running custom software written in C [11]. Three batteries were used in these experiments. Two were lithium nickel manganese cobalt oxide ($\mathrm{LiNi}_x\mathrm{Mn}_y\mathrm{Co}_{1-x-y}\mathrm{O}_2$; INR) 3500-mAh 3.6-V 18650 cells removed from an electric quad-bike battery pack, and the other was a lithium nickel cobalt aluminium oxide ($\mathrm{LiNiCoAlO}_2$; NCA) 4800-mAh 3.7-V 21700 cell.

Batteries were initially cycled using industry standard CC-CV (constant current-constant voltage) protocols using "bcp66", a command line program written in C [17]. Code is available in a repository (https://github.com/CDunnNZ/Batteries). After cycling, extra-low frequency (ELF) electrochemical impedance spectroscopy (EIS) from $5.0\,\mu\mathrm{Hz}$ to $1.0\,\mathrm{Hz}$ was carried out using the recently reported method that is now standard in our laboratory [17] to allow characterization of the cell and the fitting of an ECM as described by Poihipi et al. [7].

Another C utility, "bap66", was used to pass sinusoidal and arbitrary waveforms through the cells via the 66332A units. bap66 calls two-column ".ti" files consisting of timestamp-current pairs that can represent any desired waveform, and outputs a three-column ".tvi" file showing voltage response to the applied current. A sinusoidal current waveform was generated as a .ti file via a script written in C. u was determined as described previously (Section III-A and Equation 27) using a C program developed from the earlier AWK script with some additional capabilities including calculation (based on Equation 13) and printout of α and voltage-current phase differences.

These phase differences and α values calculated from u were verified by comparison with values determined using Fourier and Hilbert transform methods. Fourier transforms of .tvi data were performed with "dftv", a C program originally designed for use with SPICE [18] that is able to handle non-equispaced time-domain data, and the fast Fourier transform (FFT) function available in MATLAB®. Fourier analysis was applied to the voltage and current data columns in each .tvi file to reveal the phase (ϕ) associated with both parameters at frequencies of interest. The difference between ϕ_V and ϕ_I is the phase shift θ through the battery at any given frequency. This would be 90° for a capacitor, and somewhat less for a fractional system such as a battery, which acts as a "lossy" capacitor. Note also that, although a CPE displays constant θ regardless of frequency (a fundamental characteristic), a battery can show changing θ at very low frequencies [17] because the circuit describing it is not a pure CPE, but rather a fractional capacitance in series with a resistance.

Hilbert transforms involve convolution of a signal in the time domain with the Hilbert kernel $1/\pi t$ or multiplication in the Fourier domain by $-jsgn(f)$ to reveal the so-called analytical signal, which contains phase information. The "hilbert" function in MATLAB® was applied to voltage and current data to obtain ϕ_V and ϕ_I, respectively, and consequently θ.

Arbitrary waveforms intended to represent the usage cycles of electric vehicles and other equipment as described earlier (Section II-C) were generated as .ti files with "GenDrive", a utility that creates waveforms using MATLAB® and its "randn" function. These waveforms can be broken down into cycles, series and pulses, each containing multiples of the next. For these experiments, negative pulses (drawing current from the battery) were set to a mean $-1.5\,\mathrm{A}$ with standard deviation (SD) $0.12\,\mathrm{A}$. The mean positive pulse was $0.9\,\mathrm{A}$ with SD $0.18\,\mathrm{A}$. A GenDrive series contains a mean of fifteen (SD = 4) negative pulses, and seven (SD = 3) positive pulses, so the combination of generally greater number and magnitude of negative pulses sets an overall trend of drawing current from the battery. Cycles contain at least two series of pulses, randomly spaced with rest periods of between 15 minutes and 2 hours, and finish with a 1-A recharging period during which the net charge lost is replaced. Figure 1 shows a representative section of the current stimulus used in these experiments.

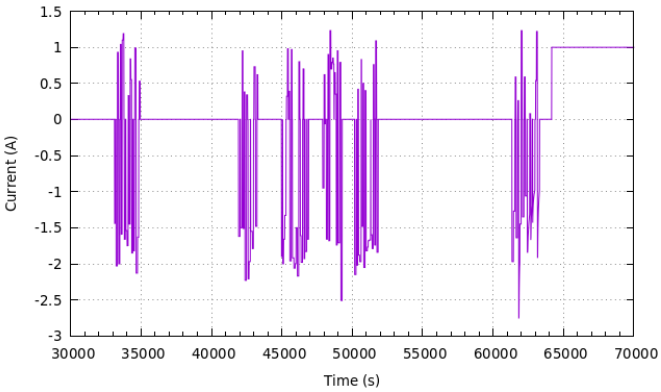

Fig. 1. GenDrive current stimulus: 8.3 to 19.4 hours.

E_{in} and E_{out} were determined with "getSoH", a C program that searches streams of voltage and current data for pseudocycles. Within the stream, it identifies rest periods of negligible current draw that exceed a given duration. By accumulating the charge delivered and withdrawn, and looking at terminal voltage at the end of rest periods, it identifies pseudocycles as periods delineated by rests where the voltage and charge differences are smaller than the parameters entered

when the program is called. Inspecting these values between every possible pair of rest periods allows pseudocycles to be identified. The algorithm is executed sequentially (current and voltage data are processed but not stored). It starts a search for a pseudocycle at each rest identified, coulomb counting separately for each one, and terminates each search when the pseudocycle completes at the next rest. This means that the process requires very little memory and very modest processing power. Parameters set by the user include threshold current (0.01 A for these measurements) and voltage (0.05 V) considered to be close to starting values, and how close to zero charge movement should be (0.01 Ah). The minimum time for the system to be considered at rest (60 s in these experiments), and the shortest and longest permitted pseudocycle durations, may also be set (these were left at their default values of 3 and 14 days, respectively). The data from getSoH can be presented as a point in time associated with the computed efficiency factor, or as a "bar" that marks the start and end point of each pseudocycle.

Regression analyses and least-squares fitting were carried out using MATLAB® "polyfit" and "polyval" functions

IV. Results

A. SPICE Sinusoid Simulation

Simulation work started with an R-CPE model with α = 0.8. The minimum (V_{min}) and maximum (V_{max}) voltage responses for a selected cycle were determined from plots constructed in MATLAB® (Figure 2), and these values used to calculate V_0 and V_a (see Equation 13). Knowing u, α could then be back-calculated.

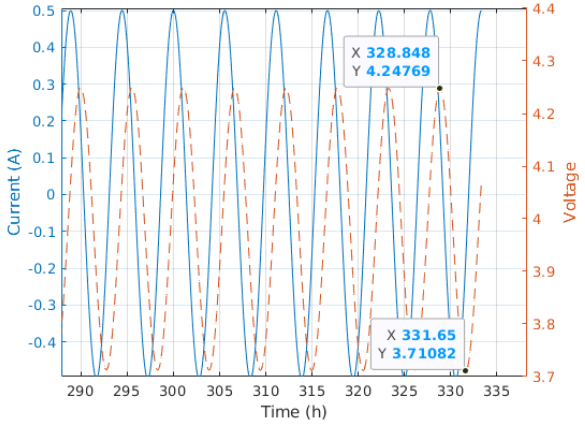

Fig. 2. Current (solid line) and voltage response (broken line) at end of simulation. R-CPE model, $\alpha = 0.8$, fractional capacitance C_f = 1200 $\mathrm{As^{\alpha}V^{-1}}$, series resistance = 0.025 Ω, 50-μHz sinusoidal stimulus.

V_a = 0.2684 V, V_0 = 3.9793 V, and $u = E_{out}/E_{in}$ = 0.9635, and therefore

$$\theta = \arccos\left[\frac{2 \times 3.9793(1 - 0.9635)}{\pi \times 0.2684}\right] = 1.22\,\mathrm{rad}\ (69.9°)$$

and

$$\alpha = \frac{2\theta}{\pi} = \frac{2 \times 1.22}{\pi} = 0.78 \qquad (28)$$

which is compared to the value of 0.80 upon which the CPE model was based. Note that the model was initialized by simply putting an initial condition of 4.0 V on all the capacitors in the Morrison array in SPICE.

In an attempt to ensure that the simulation was reaching steady state, the model was adjusted to reduce the fractional capacitance (C_f) of the CPE to 470 $\mathrm{As^{\alpha}V^{-1}}$ and to increase the stimulus frequency to 100 μHz. Under these conditions a value of α = 0.80 was obtained, confirming the association between u and α for this modeled sine wave case.

B. Measured Sinusoidal Stimulus

Figure 3 shows the voltage response to a 0.5-A 50-μHz sine wave applied to one of the INR batteries. The constant phase exponent α characterizing the fractional capacitance of the battery is related to the (purely) capacitative phase separation of 90° by an angle $\phi = 90°(1 - \alpha)$ [8].

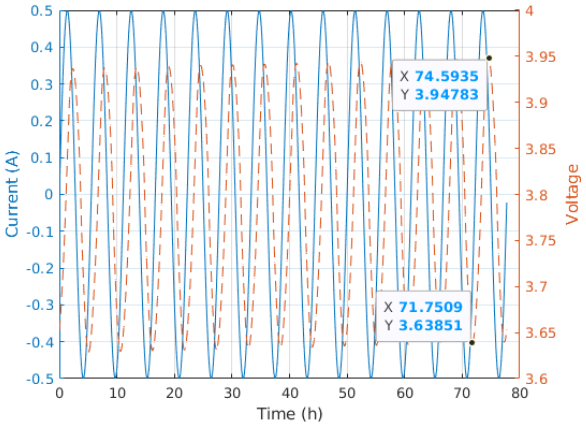

Fig. 3. Current (solid line) and voltage response (broken line) after 14 measured cycles. INR 18650 cell, 50-μHz sine wave current.

A Fourier transform using dftv showed a phase separation between current and voltage at 50 μHz of 65.93°, a difference from 90° of 24.07° (= ϕ). Thus

$$-\alpha = \frac{\phi}{90} - 1 = \frac{24.07}{90} - 1 = -0.73 \qquad (29)$$

Thus, $\alpha = 0.73$. The MATLAB® FFT and Hilbert transform (Figure 4) yielded the same result.

Calculation of E_{out}/E_{in} for each available cycle showed results ranging from 0.9760 to 0.9762; thus, u was set to 0.9761. Use of the same calculation as for the simulation in Section IV-A, and V_{min} and V_{max} values as shown in Figure 3, resulted in a phase difference of 68.11° (1.19 rad) and α = 0.76. Refinement of the program to include a small series resistance (0.01 Ω, a plausible value for a battery) reduced the value of α to 0.73 (phase difference 65.95°), in alignment with the Fourier and Hilbert approaches, and linking u and α in a measured battery. The series resistance is entered

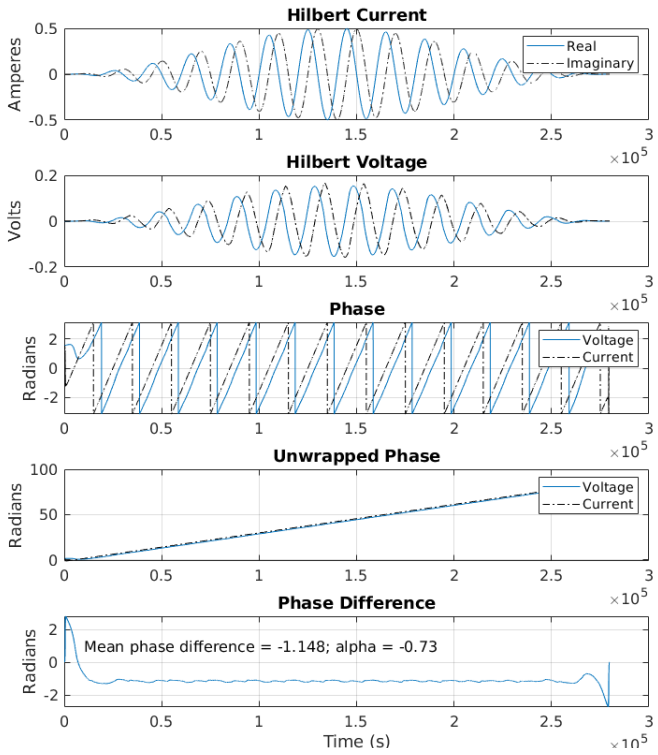

Fig. 4. Hilbert transform of time domain data with raised cosine window: INR 18650 cell, 50-μHz sine wave current. Note: 1.148 rad = 65.78°.

as a parameter when the program is called in the command line, is multiplied by current, and the result used to adjust the CPE voltage before the energy calculation is performed.

C. Self-Similar Cycles

Following repeated charging and discharging using the arbitrary waveform (SSCs), u as calculated for pseudocycles identified by getSoH showed a clear and consistent reduction over time (Figure 5). Note the reproduction of two consecutive "runs" in the figure, necessitated by memory and file size limitations in the Raspberry Pi computers used to control the 66332A units and the consequent need to restart after approximately 80 days. Note also the point estimates of u in Figure 5, and u with pseudocycle duration in Figure 6. Central clustering of longer pseudocycles, with shorter pseudocycles as outliers, suggested more reliable estimates of u with longer periods.

Least-squares fitting analysis of the first dataset (run 1) in MATLAB® showed a strong linear correlation (correlation coefficient -0.9392) with narrow 95% confidence limits (Figure 7).

D (Equation 26) increased over time for each identified pseudocycle as predicted. Results showed greater scatter and weaker linear correlation than those for u (Figure 8), but the increasing trend for D was clearly apparent.

The first run of data from the 4800-mAh NCA 21700 battery followed the same pattern of falling u when subjected to the arbitrary waveform (Figure 9), although cyclic variation

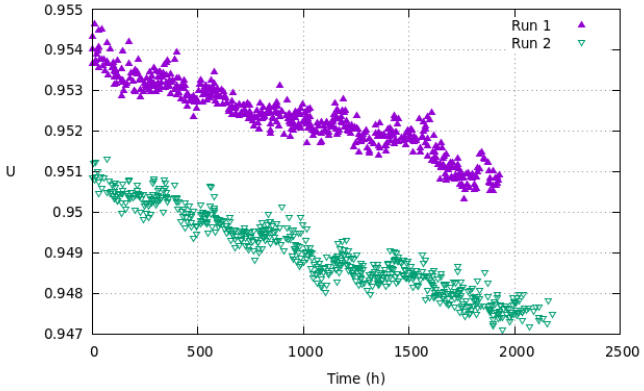

Fig. 5. Plot of energy efficiency u against time for an INR cell charged and discharged using an arbitrary waveform. Note the reduction in u with repeated cycling over time. The two data series are two consecutive parts of the same ongoing measurement, with run 2 beginning where run 1 stops, necessitated by the data storage limitations of the Raspberry Pi units executing the measurement software.

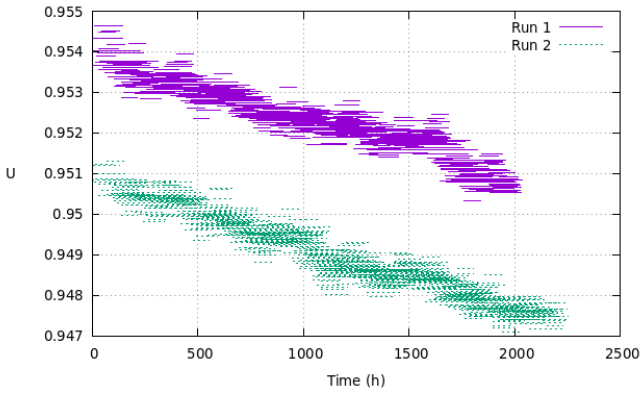

Fig. 6. Energy efficiency u against time for an INR 18650 cell plotted as bars showing pseudocycle duration for each calculated u value. Note the central clustering of longer pseudocycles, with outliers tending to be shorter pseudocycles (durations range from 3 to 14 days). The two data series are two consecutive parts of the same ongoing measurement, with run 2 beginning where run 1 stops, necessitated by the data storage limitations of the Raspberry Pi units executing the measurement software.

was apparent. There was also some evidence of this type of pattern in the INR battery (Figure 5). This effect may have been caused by the GenDrive waveform not being truly arbitrary, and we might expect to see such a pattern in a real-world waveform from an electric vehicle, as drivers tend to use their vehicles according to regular routines.

Similarly to the INR battery (Figure 6), longer pseudocycles tended to be concentrated in the middle of the u plot, with outliers being predominantly short pseudocycles (Figure 10).

The same strong linear correlation between u and time was noted in this cell (Figure 11), together with the same clear increasing trend in D (Figure 12), although correlation for D with time was again weak, with wide 95% confidence limits.

Note that it is possible to adjust input parameters in getSoH to control the length of pseudocycles to be detected (the default minimum and maximum values are 3 and 14 days, respectively). Figure 13 shows the result of repeating getSoH for run 1 in the INR battery with a minimum pseudocycle

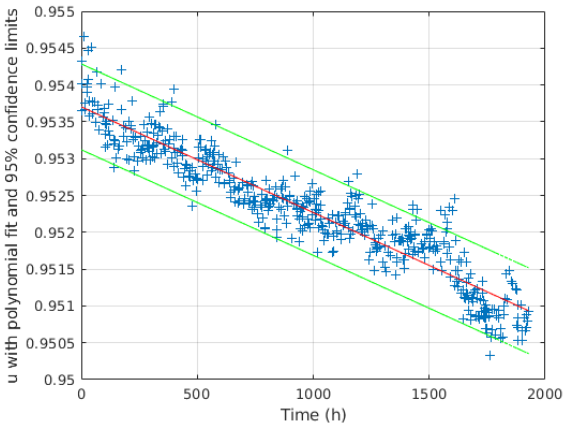

Fig. 7. INR 18650 cell arbitrary waveform run 1: u versus time t with first-order polynomial (linear) fit and 95% confidence limits. Correlation coefficient = -0.9392; $u = (-1.4354 \times 10^{-6})t + 0.9537$.

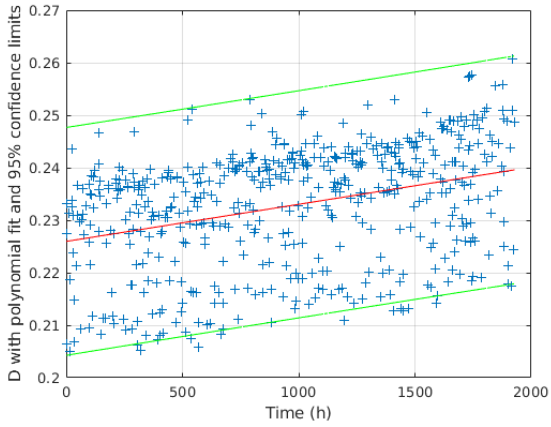

Fig. 8. INR 18650 cell arbitrary waveform run 1: D versus time t with first-order polynomial (linear) fit and 95% confidence limits. Correlation coefficient = 0.3400; $D = (7.0677 \times 10^{-6})t + 0.2260$.

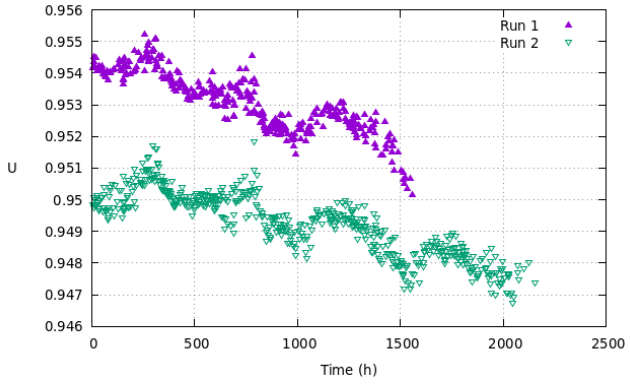

Fig. 9. Plot of energy efficiency u against time for the NCA 21700 cell charged and discharged using an arbitrary waveform.

duration of 7 days. There was a small improvement in the least-squares linear fit for D (correlation coefficient = 0.3544),

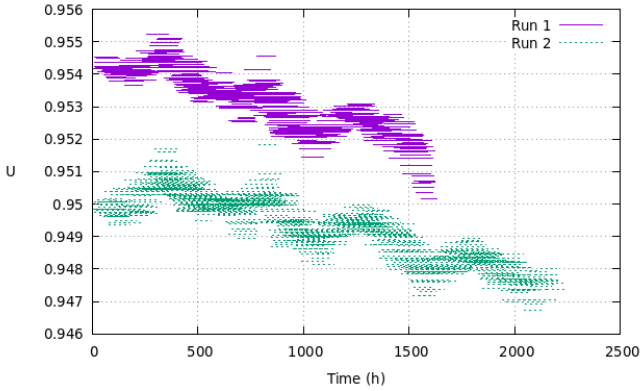

Fig. 10. Energy efficiency u against time for an NCA 21700 cell plotted as bars showing pseudocycle duration for each calculated u value. Note the central clustering of longer pseudocycles, with outliers tending to be shorter pseudocycles (durations range from 3 to 14 days).

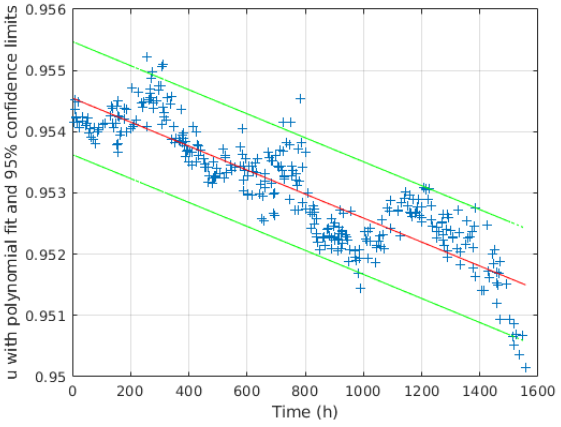

Fig. 11. NCA 21700 cell arbitrary waveform run 1: u versus time t with first-order polynomial (linear) fit and 95% confidence limits. Correlation coefficient = -0.8749; $u = (-1.9151 \times 10^{-6})t + 0.9545$.

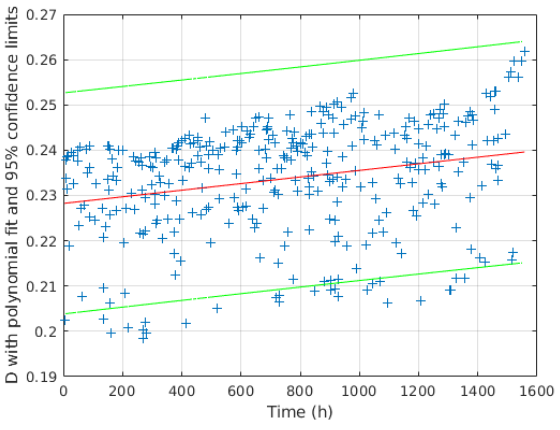

Fig. 12. NCA 21700 cell arbitrary waveform run 1: D versus time t with first-order polynomial (linear) fit and 95% confidence limits. Correlation coefficient = 0.2464; $D = (7.2904 \times 10^{-6})t + 0.2282$.

but the best-fit line was unchanged.

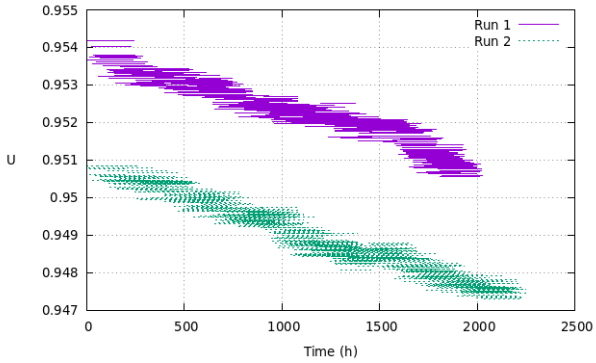

Fig. 13. Energy efficiency u against time for an INR 18650 cell plotted as bars showing pseudocycle duration for each calculated u value. Pseudocycle durations set to 7 to 14 days. Note the absence of short-cycle outliers as seen in Figure 6.

D. Relationship of D and α

To test the relationship between D and α where the waveform is not a single sine, inverse cosines of D after least-squares fitting for the batteries at the beginning of the measurements were taken, and, using the relationship shown in Equation 28, the results summarized in Table I were obtained. Values of α obtained in this way (α_D) and those obtained using extra-low frequency EIS and R-CPE model fitting [7, 19] (Figure 14) were within 2% of each other.

TABLE I
ESTIMATION OF α VIA D

Battery	$\boldsymbol{\alpha}$	$\boldsymbol{u}$	$\boldsymbol{D}$	$\boldsymbol{\theta = \cos^{-1} D}$	$\boldsymbol{\alpha_D = 2\theta/\pi}$
INR	0.869	0.9537	0.2260	1.343 rad	0.855
NCA	0.860	0.9545	0.2282	1.341 rad	0.853

α, estimate based on equivalent-circuit model with single constant-phase element (CPE) as determined using the method of Poihipi et al. [7]; α_D, estimate based on inverse cosine of D.

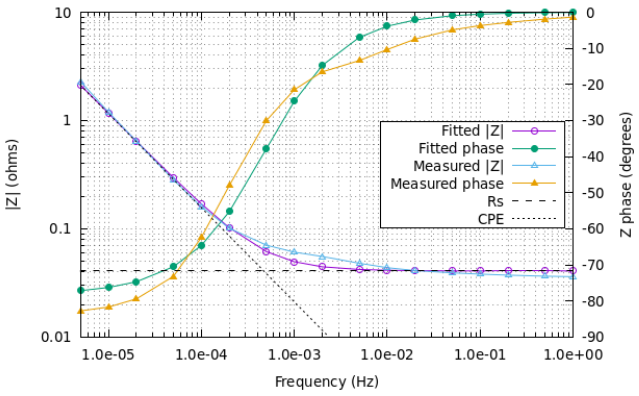

Fig. 14. R-CPE model fitting [7] for the 18650 INR battery. α (= 0.869 for this cell) is given by the slope of the CPE impedance magnitude ($|Z|$) asymptote. Rs = series resistance.

Figure 15 shows the result of applying the above to all values of D and to the best-fit line in MATLAB® for run 1 in the INR cell. We see the anticipated fall in α with repeated charging and discharging.

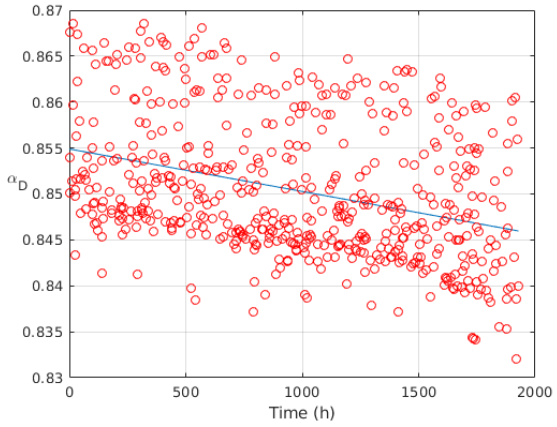

Fig. 15. α derived from D (α_D) for run 1 of the 18650 INR battery.

V. DISCUSSION

These findings demonstrate that energy efficiency u reveals SoH for a lithium-ion battery, and α specifically where the charge-discharge stimulus is a sine wave. Where this is not the case, theory predicts that we would have to know I_n and V_n (Equation 22) as well as being able to identify pseudocycles. The results presented here suggest that u can be used to track battery health without necessarily knowing these characteristics, and that we can do this with waveforms other than single sinusoids. Furthermore, we can detect phase changes following declining SoH that reflect changing α using a parameter that shows deviation of a fractional system from purely capacitative behavior.

We note that have shown this only for a single modeled arbitrary waveform which may be too "self-similar" for further generalization. A real waveform from, say, an EV in daily use might not give the same result. Many further measurements, using a variety of waveforms over prolonged periods, will be required for verification. Some sort of waveform correction might also be needed. Is there a measurable waveform property (crest factor, spectral range, spectral occupancy, envelope, etc.) that correlates with the variation in efficiency, and can therefore correct out non-health noise that we see in u or D? Such correction factors would have to be investigated through extensive simulation and measurement.

Increasing energy dissipation appears consistent with decreasing α, but this is not the only possible hypothesis. We may not need to know α to track SoH; measured u alone may suffice. For more certainty relating to how to use u (or a similar measurement) to find θ and α we would need to know I_n and V_n in order to identify their Fourier components and plot impedance spectra based on these [17], but this would move us away from the idea of a simple predictive algorithm that is easily measured *in situ* with minimal hardware and processing power. Moreover, u implies the fitting of an R-CPE model to the data, whereas an R-CPE-CPE model has

been shown to be more appropriate [7, 17], with overall α being dictated by increasing dominance of the second CPE as the battery ages. This is important when building an ECM for a battery, but may not be relevant for simply using u to track SoH.

VI. Conclusion

Energy efficiency u can serve as a marker of SoH in lithium-ion batteries being cycled according to arbitrary waveforms as found in electronic devices being used under real-world conditions. This parameter appears to be related to α, which is defined by the simplest battery ECM, and which declines as the battery wears out. u is described by a very simple algorithm with minimal computing requirements that could be easily incorporated into battery management systems. Further work is needed to confirm (or otherwise) the association of u with phase behavior in a battery, and the significance of this association. The algorithm should also be tested on waveforms from real devices and vehicles in daily use.

References

[1] V. Pop, J. B. Henk, D. Danilov, P. P. L. Regtien, and P. H. L. Notten, *Battery Management Systems: Accurate State-of-Charge Indication for Battery-Powered Applications*. Springer, 2008.

[2] J. A. Osara, O. A. Ezekoye, K. C. Marr, and M. D. Bryant, "A methodology for analyzing aging and performance of lithium-ion batteries: Consistent cycling application," *J. Energy Storage*, vol. 42, p. 103119, Oct. 2021. [Online]. Available: https://linkinghub.elsevier.com/retrieve/pii/S2352152X21008227

[3] C. Pastor-Fernández, T. F. Yu, W. D. Widanage, and J. Marco, "Critical review of non-invasive diagnosis techniques for quantification of degradation modes in lithium-ion batteries," *Renew. Sustain. Energy Rev.*, vol. 109, pp. 138–159, Jul. 2019. [Online]. Available: https://linkinghub.elsevier.com/retrieve/pii/S136403211930200X

[4] L. Ungurean, G. Cârstoiu, M. V. Micea, and V. Groza, "Battery state of health estimation: a structured review of models, methods and commercial devices," *Int. J. Energy Res.*, vol. 41, no. 2, pp. 151–181, 2017.

[5] C. Hendricks, N. Williard, S. Mathew, and M. Pecht, "A failure modes, mechanisms, and effects analysis (FMMEA) of lithium-ion batteries," *J. Power Sources*, vol. 297, pp. 113–120, Nov. 2015. [Online]. Available: https://linkinghub.elsevier.com/retrieve/pii/S0378775315301233

[6] J. Neff, "Tesla Roadster Batteries Are Failing, Revealing End Of Life Symptoms," *INSIDEEVs*, Mar. 2023. [Online]. Available: https://insideevs.com/news/658962/tesla-roadster-ev-battery-end-of-life/

[7] E. Poihipi, J. Scott, and C. Dunn, "Distinguishability of Battery Equivalent-Circuit Models Containing CPEs: Updating the Work of Berthier, Diard, & Michel," *J. Electroanal. Chem.*, vol. 911, p. 116201, Apr. 2022. [Online]. Available: https://linkinghub.elsevier.com/retrieve/pii/S157266572200193X

[8] A. Lasia, "Dispersion of Impedances at Solid Electrodes," in *Electrochemical Impedance Spectroscopy and its Applications*. New York, NY: Springer New York, 2014, pp. 177–201.

[9] V. Farrow, J. Scott, M. Cree, and M. Wilson, "Passive, Fractional, Battery Equivalent-Circuit Model in Time and Frequency Domains Part 1: Linear Model," submitted for publication.

[10] T. T. Hartley, R. J. Veillette, J. L. Adams, and C. F. Lorenzo, "Energy storage and loss in fractional-order circuit elements," *IET Circuits Devices Syst.*, vol. 9, no. 3, pp. 227–235, 2015.

[11] V. Farrow, "Characterisation of rechargeable batteries: addressing fractional ultralow-frequency devices," Master of Engineering, University of Waikato, Hamilton, New Zealand, Sep. 2020.

[12] T. J. Freeborn, B. Maundy, and A. S. Elwakil, "Fractional-order models of supercapacitors, batteries and fuel cells: a survey," *Mater. Renew. Sustain. Energy*, vol. 4, no. 3, p. 9, Sep. 2015.

[13] S. Westerlund and L. Ekstam, "Capacitor theory," *IEEE Trans. Dielect. Electr. Insul.*, vol. 1, no. 5, pp. 826–839, 1994.

[14] R. Morrison, "RC Constant-Argument Driving-Point Admittances," *IRE Trans. Circuit Theory*, vol. 6, no. 3, pp. 310–317, 1959.

[15] S. Seshadri and J. Scott, "Correction to "Compact Nonlinear Model of an Implantable Electrode Array for Spinal Cord Stimulation" [Jun 14 382-390]," *IEEE Trans. Biomed. Circuits Syst.*, vol. 12, no. 4, pp. 963–964, 2018.

[16] M. Wilson, L. Cowie, V. Farrow, M. Cree, and J. Scott, "Simulating Fractional Capacitors With the SPICE Circuit Simulator," 2023. [Online]. Available: https://www.techrxiv.org/account/articles/24156396

[17] C. Dunn and J. Scott, "Achieving Reliable and Repeatable Electrochemical Impedance Spectroscopy of Rechargeable Batteries at Extra-Low Frequencies," *IEEE Trans. Instrum. Meas.*, vol. 71, pp. 1–8, 2022. [Online]. Available: https://ieeexplore.ieee.org/document/9789195/

[18] J. Scott and A. Parker, "Distortion analysis using SPICE," *J. Audio Eng. Soc.*, vol. 43, no. 12, pp. 1029–1040, Dec. 1995.

[19] C. J. Dunn and J. Scott, "Deducing battery impedance from working vehicle voltage and current waveforms," University of Waikato, Hamilton, New Zealand, Oct. 2019.

VII. Biography Section

Christopher Dunn (Student Member, IEEE) received the bachelor's degree from the Portsmouth School of Pharmacy, Portsmouth, U.K., in 1985, the master's degree from the Queen's University of Belfast, Belfast, U.K., in 1993, and the Graduate Diploma in Electronics from The University of Waikato, Hamilton, New Zealand, in 2019, where he is currently pursuing the Ph.D. degree. His background is originally in the pharmaceutical sciences, with past specialization in medicinal chemistry (notably quantitative structure–activity relationships and pharmaceutical analysis), pharmaceutical technology, small-scale and aseptic/sterile manufacturing, and quality assurance. He has also worked in scientific communications and in asset management/inspection and line structure engineering for the power supply industry.

Jonathan Scott (Life Member, IEEE) received the B.Sc., B.E. (Hons), M.Eng.Sc., and Ph.D. degrees from The University of Sydney in 1977, 1979, 1985, and 1997, respectively, and the PGC Management in Higher Education from Waikato University in 2014. From 1998 to 2006, he was with Hewlett-Packard and Agilent Technologies Microwave Technology Center, Santa Rosa, CA, USA, where he was responsible for advanced measurement systems operating from dc to millimeter-wave. In 1997 and 1998, he was the Chief Engineer of RF Technology, Sydney, NSW, Australia. He was with the Department of Electrical Engineering, The University of Sydney, Sydney, prior to 1997. He was the Foundation Professor of electronic engineering with The University of Waikato, Hamilton, New Zealand from 2006 to 2022. He has authored more than 150 refereed publications, several book chapters, and a textbook. He holds numerous patents, several covering active products from microwave and RF to biomedical and battery systems. His educational interests include threshold concepts and their application, particularly across engineering disciplines. His research interests are the characterization and modeling of implantable electrodes, semiconductor devices, batteries, and acoustic systems.

Marcus Wilson received the Honors degree in Physics and Theoretical Physics from the University of Cambridge in 1992, and the Ph.D. degree in Theoretical Solid State Physics from the University of Bristol in 1995. He is a Senior Lecturer in Physics and Chemistry in Te Aka Mātuatua – School of Science at The University of Waikato, Hamilton, New Zealand. He has worked in numerical modeling of physics processes in industry in the U.K. and in academia in New Zealand, the latter since 2004. His research interests include electric properties and dynamics of the human brain, transcranial magnetic stimulation, and more recently batteries.

Vance Farrow received the B.E. degree in 2018 and the M.E. degree in Electronic Engineering at the University of Waikato, Hamilton, New Zealand. His M.E. focused on the prediction of battery life using small-signal measurements. He is currently pursuing the Ph.D. degree, working on battery management systems using fractional-derivative models and extremely low frequency electrochemical impedance spectroscopy measurements, at the University of Waikato.

Chapter 6

Discussion, Conclusions and Future Work

This chapter summarises the key findings, lessons learned, and issues identified by the work described in this thesis. It also discusses briefly aspects such as experimental approaches that were tried but did not work and points of interest that arose from observations during the research.

6.1 The Need For Reliable Measurements in the Frequency Domain

When the work described in this thesis was started, the need for a reliable measurement technique for obtaining ELF impedance data in the frequency domain was an overriding concern for the Battery Modelling Group. Data that could be used with confidence were urgently required to assist battery modelling work (e.g., Poihipi et al. [105]), and a reliable method was needed to allow long-term studies that could be allowed to run for many months in various battery types to start. Even before the work in Chapter 4 was started, it had become clear from the results presented in Chapter 3 [106], and from the failure of the pilot tone method (see below), that control of charge density or rate of current flow was a key determinant of the quality of data, and of any models based on those data.

Some comments on the abandoned pilot tone (or powersweep) method referred to in Section 3.1.1 are warranted. Like bz3p66, this measurement technique was based on a misunderstanding of the form and function of the SEI, and the mistaken idea that there existed in the battery some reversible SEI component (see Section 2.2.5) that was interfering with measurement tones and that could be eliminated with the use of high currents. The pilot tone was in fact a 20 mHz sine wave of magnitude 2 A that was added to 12 measurement tones (1 μHz to 10 mHz). The measurement tones were examined in overlapping sets of four to avoid charge availability and distribution problems caused by the demands of the pilot tone (a disadvantage of this method). The impedance curves obtained were of poor quality (e.g., **Figure 6.1**), with the same erratic phase behaviour at low frequencies as with bz3p66 (see Chapter 3), although bz3p66 had the advantage of allowing all measurement tones to be run at the same time. This is because the high current pulse was applied at intervals, separately from the measurement tones.

Ultimately, the key to good, consistent EIS measurements at ELFs was found to lie with rate of charge movement during the measurement. This was not initially obvious while working in the frequency domain, but became fully apparent as data emerged. Subsequent confirmation was provided by observations in the time domain as described in Chapter 4, and the link made with phenomena such as the cyclic perturbations in voltage response to a constant current stimulus. Such was the success of the bzdcp66 technique that, for the purposes of this thesis, tentative initial plans to explore other types of measurement (e.g., pseudo-random binary

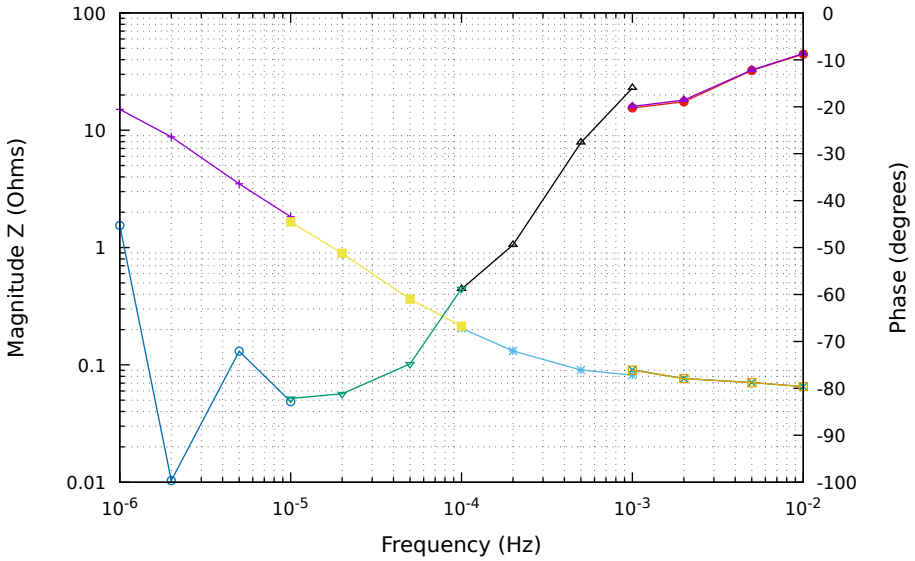

Figure 6.1: Impedance magnitude and phase obtained using a powersweep in a 2.6 Ah lithium ICR 18650 battery. Note that the measurement comprises four sets of four overlapping test frequencies carried out in sequence, each accompanied by a 2 A pilot tone at 20 mHz.

sequences) were not pursued.

The techniques described here also overcome the problem of finding suitable impedance meters with which to carry out EIS measurements at ELFs. It is worth reiterating that all experiments described in this thesis were carried out not with dedicated commercial impedance meters, but rather with basic equipment (including general-purpose programmable power supplies manufactured in the 1990s and controlled by Raspberry Pi computers) obtained at minimal cost. bzdcp66 additionally solves the problem of charge drain that has caused investigators in the past (e.g., [90]) to abandon ELF measurements.

6.2 Connecting the Frequency and Time Domains

The work connecting EIS impedance measurements at ELFs to electrochemistry-related observations in the time domain arose from a realisation of the importance of rate of charge movement that became apparent in Chapter 3, and the association with the perturbations in voltage responses to constant current cycling that smooth out progressively as current magnitude increases.

CV and ICA (and DVA) are usually treated in the literature as entirely different analytical techniques. This is true in terms of the ways in which they are carried out, but the connections between them tend not to be appreciated. The findings presented in Chapter 4 demonstrate that sweep rate in CV is related to charging rate in ICA, that this can be shown mathematically, and that the key underlying factor determining what the investigator sees is rate of movement of charge. Con-

ditions under low rates of charge movement that reveal individual electrochemical characteristics at the electrode in ICA (as opposed to the higher rates that would be associated with a CV scan) create quasi-static conditions that interfere with EIS at ELFs. This in turn ties in with and accounts for the observations in Chapter 3, in which the quality of data obtained with EIS at ELFs was dependent on the presence of adequate charge movement (i.e., current magnitude). Links between CV and ICA in terms of rate of charge movement have been tentatively explored in the literature before (see Section 4.2.3), but here these ideas are greatly extended and are related for the first time to observations during EIS carried out at ELFs.

Of interest, we might expect a power law plus step voltage response in the time domain to a current step if the battery is characterised by a resistance and a CPE (R-CPE). The time series data in Section 4.2 and **Figure 4.1** do indeed appear to show a step (because of R) followed by an upward curve with decreasing gradient (suggesting a power law with power less than one) due to the CPE at higher currents. At low currents this is partly obscured by the regular perturbations in the voltage response as a result of electrochemical processes at the electrode. This idea is potentially supported by logarithmic plots of representative portions of charging data (**Figure 6.2**). Note, however, that the battery is known on the basis of the data summarised in this thesis and from previous work [105] to be better described by an ECM containing two CPEs, and a full and proper analysis of this would be difficult, as explained by Hasan and Scott [60].

6.3 Constant Phase Element Parameters, Energy Efficiency and State of Health

Part of the original motivation for optimising the quality of EIS data at ELFs was the need to improve the estimation of CPE parameters in the battery ECM, most notably fractional order α, which has been linked to SoH (see Section 2.3.1 and Chapter 5). The linking of energy efficiency u to α [65] suggests a means by which battery SoH might be estimated by using a readily measurable quantity that has been associated with a CPE parameter.

While energy efficiency had been linked to α by Hartley et al. [65], this had been done for a single and very specific charge-discharge scenario only. The work presented here confirms the link between u and α for the sine wave case, suggests the same association for other charge-discharge waveforms, and shows that u can be used to track SoH in a lithium-ion battery regardless of waveform.

The D parameter explored in the paper presented in Chapter 5 represents a preliminary attempt to define a general case relating falling u to α as the battery wears out. D was arrived at heuristically, given the difficulty of deriving a general formula for waveforms other than sinusoids (particularly arbitrary waveforms). While it ap-

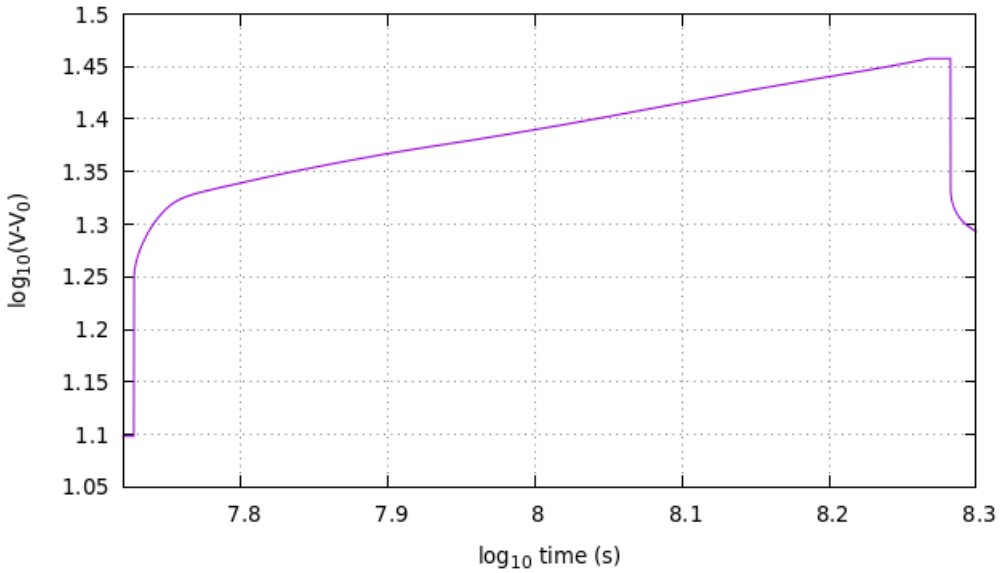

(a) 5 A.

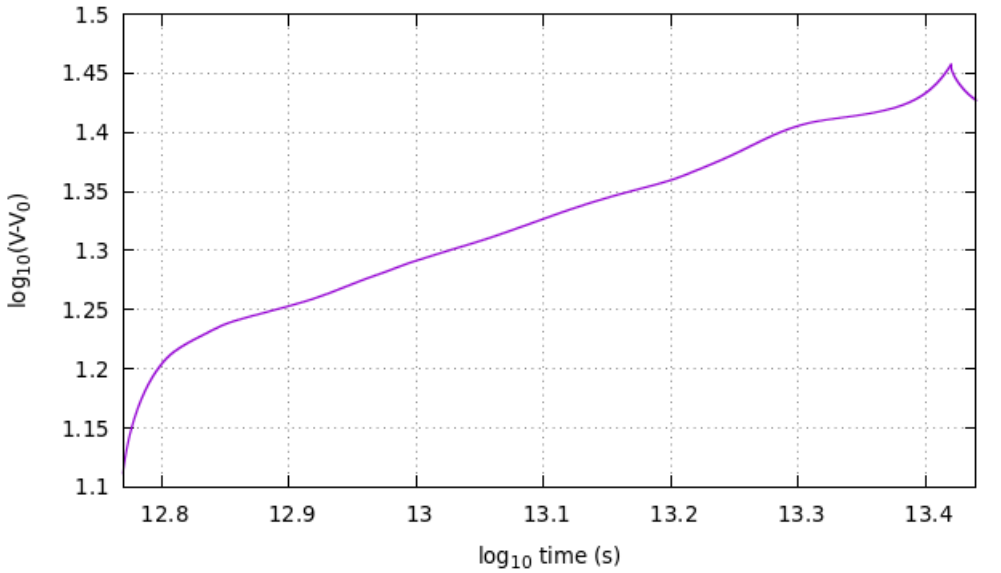

(b) 50 mA.

Figure 6.2: Plots of logarithm of voltage versus logarithm of time for a 4.8 Ah lithium NCA battery cycled with currents of 5 A and 50 mA. A single charge is shown in each case. V_0 is the measured voltage at the start of charging.

peared to offer a means of connecting an u derived from an arbitrary waveform to α, data were widely scattered and linear correlation was weak, although an upward trend mirroring the downward trend in u was visually clearly evident. More work, both mathematical and empirical, would be available here for a future researcher, and it is worth noting that the arbitrary waveform cycling referred to in the paper of Chapter 5 in the NCA 21700 and INR 18650 batteries is ongoing, and will continue

to provide further and longer term data.

Notwithstanding, for the purposes of implementation in a battery management system, defining declining u in terms of a CPE parameter may not be necessary. The GenDrive battery measurement plots depicted in the paper in Chapter 5 show that the total loss in efficiency over 6 months is less than 1%. If that were in a practical application like a cellphone battery, it would be unlikely to be noticed. However, with the simple algorithm described here, we can detect this downward trend quite readily, and have observed it in two batteries with slightly different lithium-based chemistries.

The variation in u (ranging from approximately 0.92 to approximately 0.96 in **Figure 5.5**, Section 5.3) indicates the need for some correction factor in order to standardise u across different wave shapes or stimulus types. Note that this makes sense in light of the findings of Hartley et al. [65], who specified a particular type of pulse stimulus in order to maximise u for any given CPE-based system. Deviation from this stimulus will reduce efficiency (i.e., will change the value of u). We initially believed that this might be achieved by adjusting u for crest factor (CF), a parameter that shows the ratio of the peak values in a waveform to its effective value, thus indicating how extreme the peaks in the waveform are. CF is calculated as the peak amplitude of the waveform divided by its root mean square (RMS) value. A CF of one indicates no peaks (e.g., direct current or square wave); higher CF values indicate peaks. For a sine wave, for example, RMS $= 1/\sqrt{2}$, so CF $= \sqrt{2} \approx 1.414$. Attempts to apply a CF-based correction factor had proved unsuccessful at the time of writing, however. Moreover, the determination of CF for the self-similar waveforms that would be encountered in real-world systems may be excessively difficult.

If values of u corresponding to SoH conditions ranging from brand new to imminent failure could be determined for a given battery type, a battery management system might be programmed to recognise and report these and other intermediate stages in the battery's life (or show ongoing deterioration on a monitor of some kind, such as the health bars in EV dashboard displays). This is discussed further in Section 6.4

6.4 Conclusions

EIS measurements at ELFs in batteries have been shown in this thesis to be feasible and readily achievable without the need for expensive specialised equipment, contrary to prior opinion. Measurement at ELFs reflects real-world battery usage and reveals valuable information, not seen at higher frequencies, about a battery's characteristics and condition. It does this by allowing the investigator to construct a very simple ECM consisting of only a single series resistance and one or two CPEs that captures all necessary impedance magnitude and phase information. Moreover,

rates of charge movement at these microhertz frequencies reveal connections with electrochemical behaviour in the time domain that until now have been unrecognised or poorly described. Additional benefits of the research, accruing from a new appreciation of the importance of rate of charge movement in both frequency and time domains, have included the discovery of a constant-current method for deriving a CV-type analysis from a battery, a procedure that would be hazardous if carried out using a conventional voltage ramp.

While the full details of the relationship of CPE parameters (notably fractional order α) with energy efficiency during charge-discharge cycles remain to be fully and formally described for all waveforms, the relationship between u and SoH, and the utility of this parameter for tracking battery health, has been shown. The work in Chapter 5 demonstrates relationships between u, α and phase that could be utilised in a real-world battery management system *in situ*. For example, full lifetime impedance characterisation of a battery being cycled from new to exhaustion might be carried out by performing EIS at ELFs in the laboratory at regular intervals to provide the "gold standard" reference. During this process u and phase changes could also be tracked. This would give the engineer a full reference set of related parameters and an accurate ECM for that battery.

At least one of these parameters (u, and possibly phase shift) could then be tracked in the time domain in a working device by a management system without the need to remove the battery for testing. Knowledge of how u and phase relate to α, and of what happens to α and phase as the battery ages and approaches end-of-life, would allow us to predict where the battery is in its life cycle and when it is going to be likely to require replacement. This approach would circumvent the practical difficulties inherent in attempting to measure a working battery in the frequency domain at ELFs (notably the need for measurement times of days or even weeks and the absence of a stable, time-invariant and clearly defined waveform for Fourier analysis).

The work is subject to a number of potential limitations, some of which relate to reliance on Fourier transformation of signals in the time domain to obtain information in the frequency domain (particularly in Chapters 3 and 4). To apply a Fourier analysis to a signal we should ideally have an infinitely repeating single-valued function, and the system should be linear and time-invariant (although it is worth noting here that in theory any signal that is physically realisable is Fourier-transformable [107]). None of these requirements can be guaranteed for a battery because it is a finite construct that changes over time. This is unlikely to be significant enough to worry about from an engineering viewpoint, however, as the battery changes its characteristics only very slowly (over months or even years) except when close to failure. Moreover, the measurement software described in Chapters 1 and 3 is capable of tracking and to some extent controlling changes in operating point via setting of voltage and charge movement (referred to as dQmax) limits. Currently

the software aborts a measurement (primarily for safety reasons) if limits set by the user are exceeded, but an option could easily be added to generate a warning (so that closer limits could be set for observational purposes) while allowing the measurement to continue. As described in Chapter 3, Section 3.3, the software already contains a "ramp" option to adjust for charge drift during prolonged measurements.

An alternative approach involves using the Hilbert transform to relate evolving phase differences between $V(t)$ and $I(t)$ to changes in α as the battery deteriorates. This is eminently feasible and straightforward for a simple waveform with predictable periodicity such as the single sinusoid case presented in the paper in Chapter 5, but a working battery *in situ* would not present such a waveform. Rather, a complicated signal that does not repeat in a strictly regular fashion is likely to be encountered, and the Hilbert transform would deliver phase information for every frequency component present in that signal. This would result in considerable fluctuation in phase data that would be likely to obscure relevant information. An example of this can be seen in Figure 7 of the paper presented in Appendix C.

Traditionally, EIS has been used to describe battery degradation in terms of changes in multiple individual aspects of the cell's electrochemistry (see Chapter 2, Section 2.2.3). This approach is exemplified by the work of Westerhoff et al. [52], and the present thesis demonstrates how the investigator may avoid its inherent complexity by relating battery condition and stage of life cycle to impedance phenomena derived from a very simple ECM revealed by EIS measurement at ELFs. This captures the overall consequences of those individual electrochemical degradation mechanisms. There are, however, so-called cell degradation modes that specifically describe capacity loss and power fade in lithium-ion batteries that are of interest to researchers seeking to develop new electrode materials, for example. These mechanisms are loss of lithium inventory, loss of active material, ohmic resistance increase and loss of lithium plating [96]. At first glance, with the exception of ohmic resistance increase, ELF techniques do not appear to capture these. This is a valid criticism that should be addressed here.

Although detailed discussion of electrochemical degradation modes is outside the scope of this thesis, it is worth pointing out that they can be represented by changes in incremental capacity [96]. While Chapter 4 focuses on the relationships between ICA, CV and EIS, the ICA method described therein could in fact be used to track degradation modes. For example, loss of lithium inventory leads directly to capacity fade via a loss of available lithium that accompanies growth of the SEI [108, 109] (see also Chapter 2, Section 2.2.5). Comparison of the work of Anseán et al. [96] with the ICA plot shown in **Figure 4.2** suggests that the sharp and narrow peak at a cell potential of approximately 4.1 V represents electrochemical staging phenomena primarily influenced by lithium ion availability. The shape and position of this peak would be expected to change as the cell ages and available lithium becomes depleted with SEI growth.

6.5 Future Work

EIS at ELFs remains the preferred method for providing standard reference data characterising a battery via a holistic and simple ECM that shows deterioration via impedance phenomena. Experience to date, however, suggests that frequency domain measurements of this type may not be feasible for working batteries *in situ*. This implies in turn that measurement in the time domain would be easier to implement in a practical battery management system, and this has been explored to some extent in Chapter 5 of this thesis.

Following the completion of the draft paper presented in Chapter 5, one of the INR 18650 cells was allowed to continue cycling with tracking of u for a further 6 months. Findings that include this extended period of observation are shown in **Figure 6.3**.

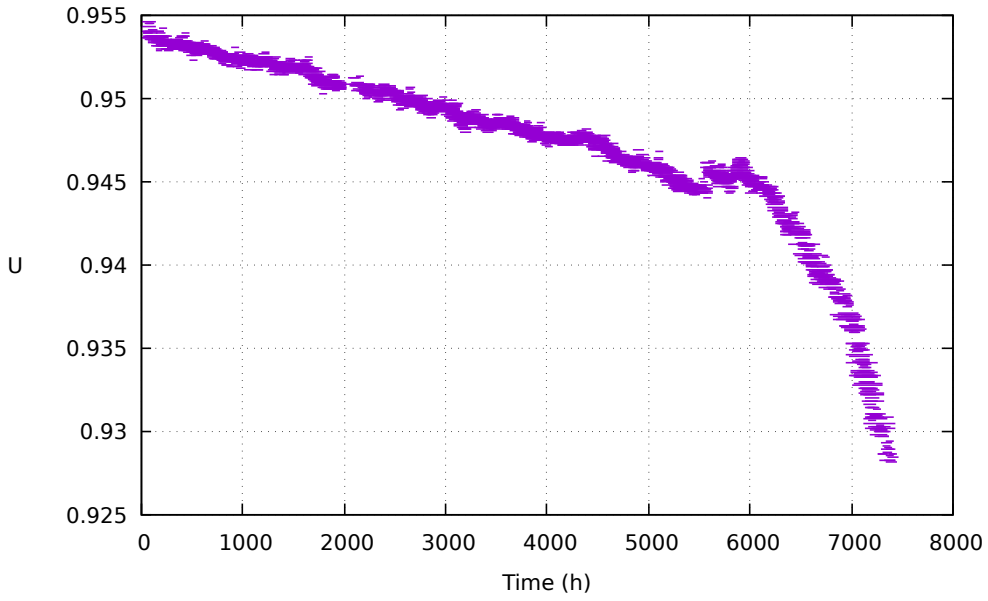

Figure 6.3: Evolution of energy efficiency u against time for an INR 18650 cell charged and discharged using an arbitrary waveform (see Chapter 5). The plotted bars show pseudocycle duration for each calculated u value. Note that cycling was interrupted for EIS measurement at 72 days (1776 hours), 222 days (5328 hours) and 318 days (7632 hours).

Note the increased rate of decline in u after approximately 6000 hours (250 days) of driving. This suggests that time series data could warn of impending failure some weeks in advance of where the user might detect loss of performance, and reinforces confidence in the utility of time domain measurements for future application. Future research should include repetition of this experiment with a range of battery chemistries.

Ideally we would like to characterise battery wearout in terms of the R-CPE-CPE model as shown by EIS performed at ELFs, but to date we are able to relate u

to fractional order α of a CPE mathematically for a single sinusoidal waveform only. For a complicated waveform we might use the Hilbert transform to monitor phase changes over time, but this is not without problems as discussed earlier (Section 6.4). For future development we require a method that is suitable for complicated waveforms that are not strictly repeating. A way forward might be offered by wavelet analysis, an alternative non-parametric technique suitable for time series data [110].

The continuous wavelet transform of a signal $f(t)$ is defined as

$$W_f(a,b) = \int_{-\infty}^{\infty} f(t) \frac{1}{\sqrt{a}} \psi^* \left(\frac{t-b}{a} \right) dt$$

where

- $W_f(a,b)$ is the wavelet coefficient at scale a and translation b,
- $\psi(t)$ is the mother wavelet function,
- $\psi^*(t)$ represents the complex conjugate of the mother wavelet,
- a is the scaling parameter (dilates or compresses the wavelet),
- b is the shift (or translation) parameter (shifts the wavelet in time),
- t is the time variable.

The Fourier transform can obtain the frequency components of a signal, but cannot determine where in time these components occur. By changing the shift parameter b, the wavelet transform can obtain this information, which permits the investigator to generate a three-dimensional time-frequency spectrum. In addition, the availability of the scaling parameter a gives the wavelet transform improved and flexible resolution capabilities in the time-frequency plane [110, 111]. These properties make the wavelet transform a better option for dealing with real-world waveforms as generated by for example electric vehicles or electronic appliances. In short, the wavelet transform can be used to identify power and phase properties of signals at differing frequency scales and to track their changes over time. The information obtained allows the investigator to construct an impedance-like spectrum from $I(t)$ and $V(t)$ data that is directly comparable to an EIS analysis of the same system. The use of wavelet transform techniques therefore merits further investigation in light of the findings presented in this thesis. It may also make possible the transition of the concepts discussed here from the laboratory to working battery management systems.

Appendix A

Poihipi et al.: Distinguishability of Battery Equivalent-Circuit Models Containing CPEs: Updating the Work of Berthier, Diard, & Michel

This paper relates to material presented in Chapter 3 of this thesis, which demonstrated how the use of working currents during EIS measurements at ELFs allows the investigator to increase modelling accuracy when fitting an ECM to a battery. Notably, Poihipi et al. [105] show that a three-element ECM (R-CPE-CPE) is generally sufficient to model real, measured data. This is the level of detail made possible by the use of EIS at ELFs accompanied by a working current as described earlier (Chapter 3) [106].

Contributions made by the present author to this paper included assistance with the drafting of Section 1 “Introduction” and Section 6 “Measured Data”, and provision of measurement data for the latter.

Journal of Electroanalytical Chemistry 911 (2022) 116201

Contents lists available at ScienceDirect

Journal of Electroanalytical Chemistry

journal homepage: www.elsevier.com/locate/jelechem

Distinguishability of Battery Equivalent-Circuit Models Containing CPEs: Updating the Work of Berthier, Diard, & Michel

Eden Poihipi, Jonathan Scott, Christopher Dunn

University of Waikato, Private Bag 3105, Hamilton 3240, New Zealand

ARTICLE INFO

Keywords:
Constant Phase Elements
Equivalent Circuit Model
Battery Model
Frequency Response
EIS

ABSTRACT

This manuscript revisits the assertion of Berthier et al. that competing fractional-element equivalent-circuit models of battery cells are indistinguishable in the presence of noise. Starting with Westerhoff's general equivalent-circuit model (ECM) of 2016 and an idealized impedance spectrum of a lithium battery, a contemporary set of possible ECMs are chosen. Their distinguishability is investigated. Using the extended frequency range recommended by Mauracher & Karden in 1997 or Hasan & Scott in 2019, an approach is presented that permits selection of the appropriate model, even in the presence of noise. For the given frequency range, models with up to five elements or eight real parameters are studied. Fitting to measured data with straightforward numerical methods and choosing the most primitive appropriate sub-circuit is shown to reproduce the data. Typically a three-element, five-parameter ECM is shown to model real, measured data with precision comparable to individual sample error.

1. Introduction

Electrochemists seek the equivalent-circuit model (ECM) of a battery to characterize its internal processes, while electrical engineers seek the same model in order to predict state-of-charge (SoC) and state-of-health (SoH). There is today a vast amount of literature in which models are presented and applied.

Berthier et al. [1] presented a paper in 2001 that set out to determine from an electrochemical perspective whether ECMs containing constant phase elements (CPEs) were numerically distinguishable from one another. These authors used CPEs in models based on electrochemical impedance spectroscopy (EIS) data, and explored their hypothesis by numerically fitting four arbitrary ECMs to synthesized EIS data using the optimization method of Fletcher et al. [2]. They concluded that the ECMs are distinguishable provided that the synthesized EIS data are noise-free. Each circuit was further optimized against noisy synthesized EIS data using 0%, 1%, 2.5% and 5% noise. The authors concluded that circuits became indistinguishable from one another once the noise level exceeded 1%.

Berthier's group used angular frequencies from 100radians/s (16Hz) to 1Mrad/s (160kHz), and displayed results in the form of Argand diagrams (sometimes called Nyquist plots). These frequency bounds and mode of presentation impose significant limitations. Moreover, optimization was applied without delving into details of the process, and equally for each ECM irrespective of its complexity.

Batteries in appliances such as cellphones, computers, and vehicles are commonly cycled as infrequently as once a week or longer, and certainly no more often than every few minutes. These periods equate roughly to frequencies ranging from 1 μHz to 1mHz, or equivalently C-rates from 0.006 to 4. In the case of rechargeable batteries, this implies the need to measure at extra low frequencies (ELFs) to encompass typical usage patterns [3–5].

This manuscript aims to update the work of Berthier and colleagues, with use of an expanded frequency range and presentation of data in Bode plot form. This offers advantages where frequency information is important [6]. In addition, a guided fitting process will be used, and a progressive set of ECMs will be drawn from recent literature [7,8].

2. Battery Equivalent-Circuit Models

Westerhoff and colleagues [7] suggested that there are three ways to characterize a battery, referred to as 'black,' 'gray' and 'white' box models. White box is a theoretical modelling method which returns to fundamental physics and a detailed understanding of the physical chemistry to determine behavior potentially leading to an ECM [9]. For example, [10] starts with white-box methods, than transitions to grey-box models through the fitting of an ECM. Black box modelling, on the other hand, employs a blind empirical modelling method using

https://doi.org/10.1016/j.jelechem.2022.116201
Received 16 December 2021; Accepted 2 March 2022
Available online 5 March 2022

sets of measured data to extract a battery model [11]. This method works best for linear relationships and is not often used on its own [9] since model extraction requires large, accurate, data sets and computationally intensive software [11]. Gray box modelling is the combination of the White and Black methods, using both theoretical understanding of the system and measured data for a more reliable model [10,11].

Westerhoff and colleagues [7] described 'gray' box modeling, in which quantitative ECMs were generated on the basis of experimental data. Westerhoff et al. presented a general battery model (Fig. 1). Like Berthier 15 years before him, Westerhoff includes CPEs, sometimes identified as "fractional capacitors", in his model. Since Randles in 1947 [12], electrochemists have acknowledged the presence of these fractional-derivative functions in their models. Conversely, the engineering literature contains many ECM models that are based at best on second-(integral)-order models [13], despite it having been shown that they are not appropriate[14]. The separate electrical and electrochemical components in a battery are represented by individual circuits, each connected in series with the others. The manuscript suggested that this general model can be simplified leaving fewer sub-circuits while continuing to represent the characteristics of a battery, depending upon the significance of each component to the whole impedance. The authors then compared the output impedance spectra of these sub-circuits to data obtained experimentally. They concluded that the chief determinant of the number of components required for each sub-circuit was the accuracy required for the application in question. Hence, it is possible to reduce the number of components in Fig. 1 without losing the ability to represent the impedance output of a rechargeable battery accurately.

In this manuscript six ECMs will be considered. They will be used in a progressive model fitting approach. The distinguishability and performance of each of the ECM sub-circuits is explored by numerically fitting each one to simulated battery data. The six ECMs appear in Fig. 2.

The first ECM reduces the Westerhoff circuit to its simplest form. This ECM contains two elements: a single CPE and a series resistor. (Fig. 2, upper left circuit.) The impedance of an ideally polarizable liquid electrode (e.g. mercury, amalgam, or indium-gallium) can be modeled by an R-C circuit, but the double-layer capacitance of a solid electrode is not purely capacitative, displays frequency dispersion, and cannot be modeled adequately by an ECM based on capacitors [15]. Instead, CPEs are used to emulate this non-ideally polarizable behavior. The equation for the impedance of a CPE is

$$Z_{CPE} = \frac{1}{C_F s^{\alpha}} \tag{1}$$

where C_F is the CPE value (its pseudo- or fractional capacitance, a constant with the dimensions $Fs^{\alpha-1}$), α is the CPE fractional order exponent, $s = j2\pi f$(where $2\pi f = \omega$, the angular frequency), and f is the frequency in hertz [16]. The total impedance of the R-CPE model can therefore be found by

$$\begin{aligned} Z_{R-CPE} &= R_s + Z_{CPE} \\ &= R_s + \tfrac{1}{C_F s^{\alpha}} \end{aligned} \tag{2}$$

where $R_s$is the series resistance and $Z_{CPE}$is the impedance of the CPE (Eq. 1) in ohms.

It is worth mentioning at this point how the particular six sub-circuits have been selected. Why these six, given the large choice afforded by starting with the circuit of Fig. 1?

The choice is guided by measured impedance data. Fig. 3 shows the magnitude and phase of impedance measured on a small selection of batteries covering different chemistries and capacities. The traces all share a basic shape associated with the base R-CPE circuit. As will become clear below, the other circuits that we have chosen to use in this study correspond to characteristics observed in at least a few measured examples.

The R-CPE model can be extended by the addition of a Warburg element (W) to become the second ECM, R-CPE-W. (Fig. 2, upper right circuit.) Warburg elements are CPEs with an alpha bound to a value of one-half. They famously appeared in the electrode reaction experiments of Randles reported in 1947 [12], and describe Faradaic impedance in the presence of redox processes in semi-infinite linear diffusion systems [6]. Their generalization to arbitrary fractional order yields the CPE described above [17]. The impedance of a Warburg element is given by

$$Z_{\text{Warburg}} = \frac{1}{C_W s^{\frac{1}{2}}} \tag{3}$$

and so the impedance of the R-CPE-W model is given by

$$\begin{aligned} Z_{\text{R-CPE-W}} &= R_s + Z_{CPE} + Z_{\text{Warburg}} \\ &= R_s + \tfrac{1}{C_F s^{\alpha}} + \tfrac{1}{C_W s^{\frac{1}{2}}} \end{aligned} \tag{4}$$

where $R_s$is the series resistance, $Z_{CPE}$is the impedance of the CPE (Eq. 1) and and Z_{Warburg} is the impedance of the Warburg element (Eq. 3).

In practice, assumptions made in the theory that anticipates a Warburg element are often not completely met. The Warburg can be replaced by a CPE to give an extra degree of freedom. (Fig. 2, middle left circuit, and so forth.) The total impedance of this model is given by

$$\begin{aligned} Z_{\text{R-CPE-CPE}} &= R_s + Z_{\text{CPE1}} + Z_{\text{CPE2}} \\ &= R_s + \tfrac{1}{C_F s^{\alpha}} + \tfrac{1}{C_W s^{\alpha 2}} \end{aligned} \tag{5}$$

where $R_s$is the series resistance, and $Z_{\text{CPE1}}$and $Z_{\text{CPE2}}$are the impedances of the two CPEs, and we keep the W subscript to show the origin of the element.

Readers familiar with circuit theory will appreciate that small phase deviations at high and low frequency extents suggest a parallel element in the mix. Additional components can be added in parallel with other elements in an ECM to accommodate deviations in battery phase response. The R-CPE-CPE-Rp subcircuit will have impedance

$$Z_{\text{R-CPE-CPE-Rp}} = R_s + [Z_{\text{CPE1}} + Z_{\text{CPE2}}] \| R_p \tag{6}$$

where R_p is the parallel resistance. This equation can be expanded by noting that the impedance of parallel elements can be written

$$X \| Y = \frac{1}{\frac{1}{X} + \frac{1}{Y}} = \frac{XY}{X+Y} \tag{7}$$

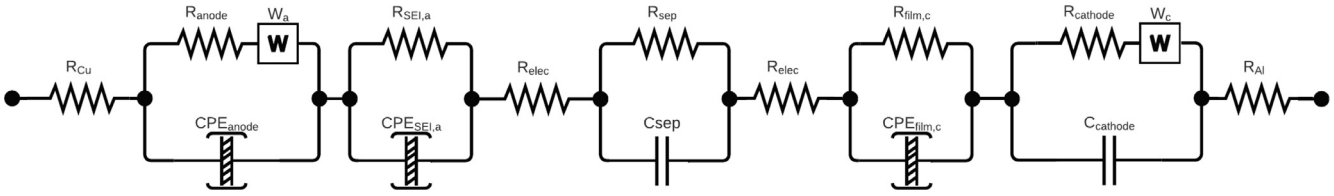

Fig. 1. Potential complete equivalent circuit of a battery according to Westerhoff [7]. Constant phase elements (CPEs) are used to characterize electrochemical behavior at the anode, solid electrolyte interface (SEI), separator (sep), and cathodic thin film (film,c). Note also resistances (R) associated with the copper and aluminium foils (Cu and Al), anode, SEI, electrolyte (elec), separator, thin film and cathode, and capacitances (C) at the separator and cathode. Warburg elements are denoted by W_a and W_c at the anode and cathode, respectively.

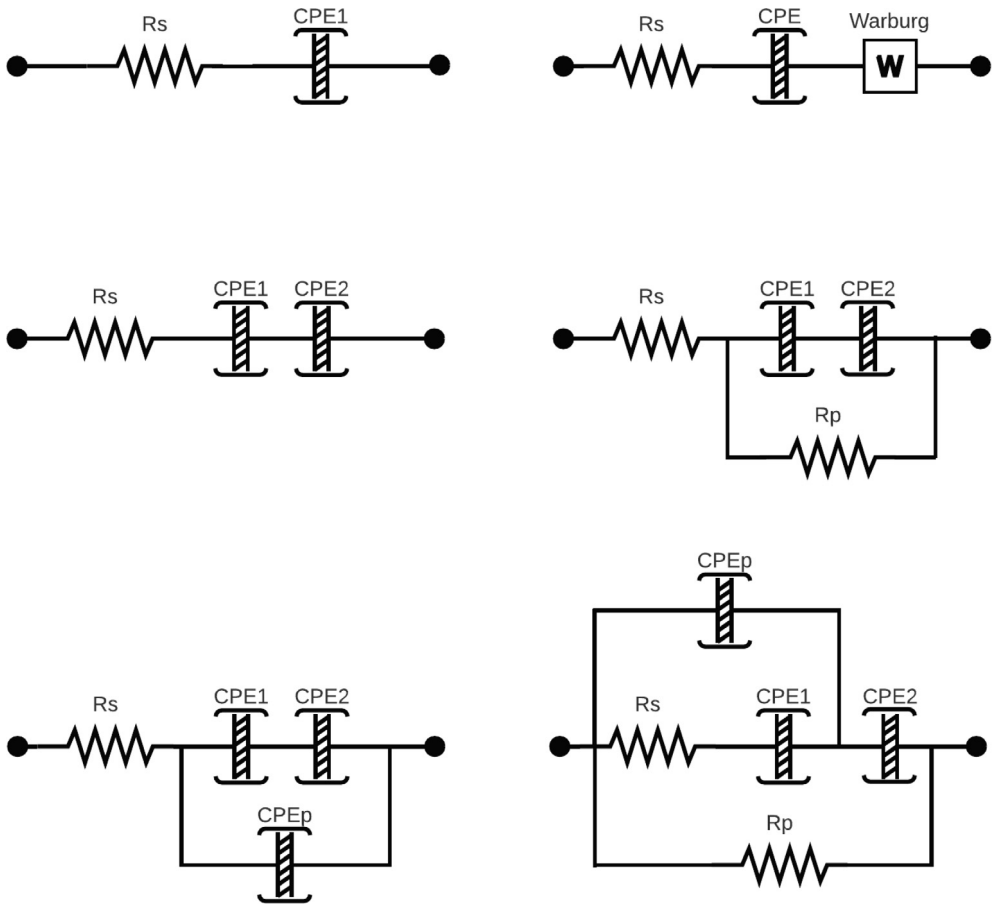

Fig. 2. The equivalent-circuit models (ECMs) considered in this manuscript. For ease of communication we identify them by the sequence of elements. The top left circuit can be identified as "R-CPE", the top right as "R-CPE-W", the middle left as "R-CPE-CPE", middle right as "R-CPE-CPE-Rp", then "R-CPE-CPE-CPEp" and finally "R-CPE-CPE-Rp-CPEp".

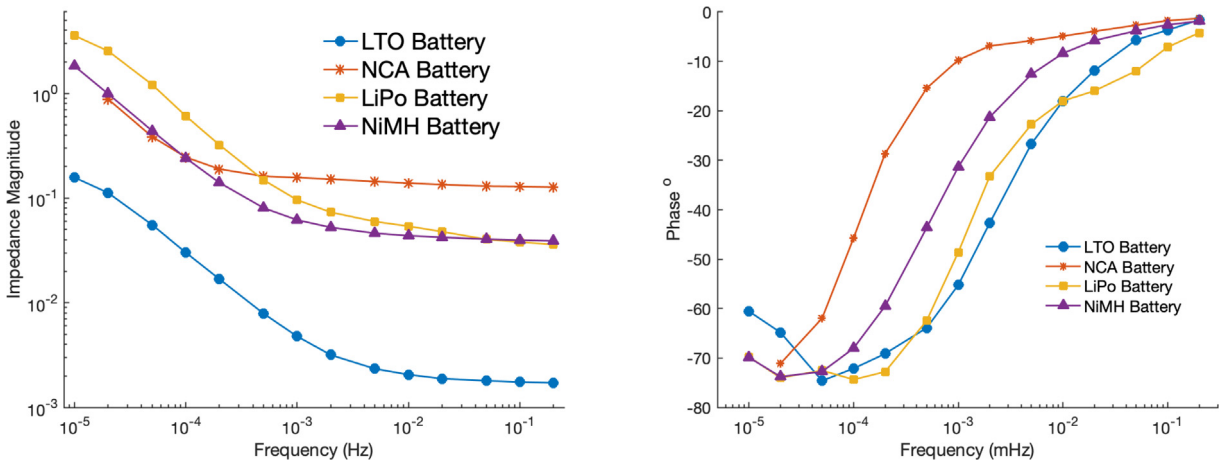

Fig. 3. Impedance magnitude of a selection of rechargeable batteries. LTO is a lithium titanate cell of 40Ah capacity, NCA is a 4.8Ah lithium nickel cobalt aluminium cell, LiPo is a 250mAh lithium polymer cell, and NiMH is a 2.5Ah nickel-metal hydride cell.

leading to

$$Z_{\mathrm{R-CPE-CPE-Rp}} = \frac{[R_s + Z_{\mathrm{CPE1}} + Z_{\mathrm{CPE2}}]R_p}{R_s + Z_{\mathrm{CPE1}} + Z_{\mathrm{CPE2}} + R_p} \tag{8}$$

and then

$$Z_{\mathrm{R-CPE-CPE-Rp}} = \frac{\left[R_s + \frac{1}{C_F s^{\alpha}} + \frac{1}{C_W s^{\alpha_2}}\right]R_p}{R_s + \frac{1}{C_F s^{\alpha}} + \frac{1}{C_W s^{\alpha_2} + R_p}}. \tag{9}$$

The form of (6) is usually preferred by engineers over (9) because it is more intuitive and easier to assimilate. As the expansions rapidly become more onerous we will restrict ourselves to the parallel notation from here onwards.

The final two ECMs to be investigated have impedances Z_5 and Z_6

$$\begin{aligned} Z_5 &= Z_{\mathrm{R-CPE-CPE-CPEp}} \\ &= R_s + [Z_{\mathrm{CPE1}} + Z_{\mathrm{CPE2}}] \| Z_{\mathrm{CPEp}} \\ &= R_s + \left[\tfrac{1}{C_F s^{\alpha}} + \tfrac{1}{C_W s^{\alpha_2}}\right] \| \tfrac{1}{C_P s^{\alpha_P}} \end{aligned} \tag{10}$$

where the $\|$ operator is taken to have precedence over addition, α_p is the order of the parallel CPE, and C_P the proportionality constant of the parallel CPE; and

$$\begin{aligned} Z_6 &= Z_{\mathrm{R-CPE-CPE-Rp-CPEp}} \\ &= \left[[R_s + Z_{\mathrm{CPE1}}] \| Z_{\mathrm{CPEp}} + Z_{\mathrm{CPE2}}\right] \| R_p \\ &= \left[\left[R_s + \tfrac{1}{C_F s^{\alpha}}\right] \| \tfrac{1}{C_p s^{\alpha_p}} + \tfrac{1}{C_W s^{\alpha_2}}\right] \| R_p \end{aligned} \tag{11}$$

3. Fitting Algorithm

Following the lead of Berthier and colleagues [1], data will be generated from one of the ECMs with varying amounts of numerical noise, and each model will be fitted to that data.

3.1. Numerical Optimization Method

The numerical optimizer was created in Matlab, using both the inbuilt toolboxes and previously published examples of real-parameter black box optimization algorithms [18–20]. The optimization method utilizes the downhill simplex algorithm of Nelder & Mead [21,22], a direct-search method which aims to minimize non-linear, multidimensional functions. For a function with *n*dimensions, the optimizer takes a set of $n+1$vertices to create a simplex. The vertices then move iteratively in order to reduce the size of the simplex until a termination value is reached. The main limitation of the Nelder-Mead approximation is potential for convergence of the simplex to local minimum, called a 'saddle', rather than the global minimum.

The method is analogous to multiple skiers on a mountain. As the $n+1$ skiers traverse downward on various paths, they all end up at the lowest point in their environment. However, each skier may end up at different locations and elevations when they reach the 'bottom'. One way to address this problem is to have multiple random starting points and then evaluate which starting point minimized the function the furthest. In some cases we applied this approach using a second program written in C. The C program could apply thousands of random multiple starts with variable range of starting points in a period of about a minute.

The root-mean-square error (RMSE) used as the optimization goal is calculated from the impedances defined in Eqs. (2)–(11) above. Impedance values are complex, and the RMSE is defined as the square root of the average of the squared distance in the complex impedance (Argand) plane. Various alternatives, weighting magnitude and phase differently, etc., were tried, but proved to offer no advantages.

3.2. Fitting Sequence

Choosing the appropriate model to fit given data commences with the simplest ECM, the R-CPE model. The model has only three parameters, converges quickly, and generally finds the global minimum without restarts. The final root-mean-square error (RMSE) reflects how well the model fits the data. If the model perfectly fits ideal data, the RMSE will approach zero. If the model perfectly fits data with a certain amount of random white noise, the RMSE will settle at a value close to that noise level, so that 1% added noise will result in a final RMSE of about 0.01. If the model does not fit the data, the extent of the mismatch also appears in the RMSE.

The second step of the model selection process moves to the next-simplest model, in this case the R-CPE-W model, with four parameters. The fit starts at the model parameter values returned in the R-CPE case. If the previous fit has settled at a point where the RMSE was largely defined by noise in the data, then this attempt will not improve upon the fit, and it may be concluded that the quality of the data does not justify this more complicated model, even if that model might be more correct. However, if the added element results in a lower RMSE, it must be concluded that the extended model does represent the data better.

This process is repeated for the ECMs with increasing degrees of freedom, the R-CPE-CPE model, with five parameters, in the third step, and so on. During the progressive fitting, it is possible for parameter values to be returned that are impossible. For example, α cannot exceed 1.0, and C_p cannot be negative. Such an event signals that the model and fit cannot be appropriate for the data.

4. Simulated Data

A set of model parameter values were chosen for the ECM with eight degrees of freedom, the R-CPE-CPE-Rp-CPEp model. Values appear in Table 1. The magnitude and phase computed using Eq. 11 are plotted in Fig. 4. Also plotted in the figure are the asymptotes corresponding to each of the five elements. This permits the reader to associate regions in the plot with different elements; for example, the horizontal section of the magnitude plot between 1mHz and 1Hz is dominated by the series resistance, R_s, and the straight-line region

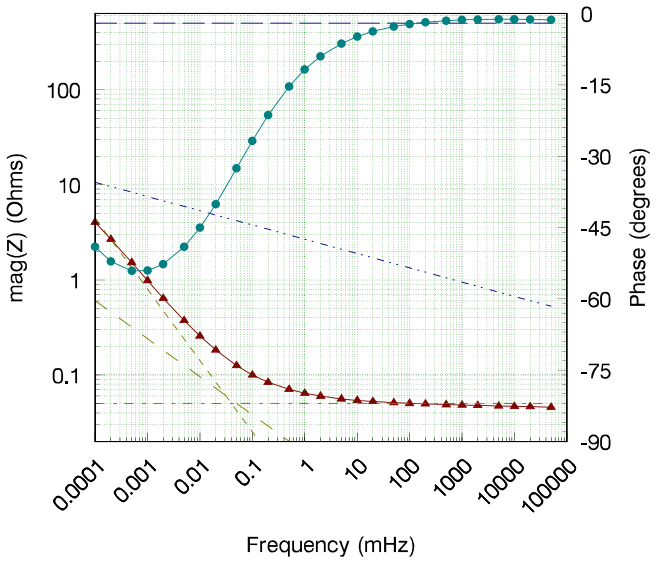

Fig. 4. Plot of magnitude (red triangles) and phase (cyan dots) generated from the eight-parameter model. The additional straight lines represent the impedance of the five elements of the model, three CPEs plus series and parallel pure resistance.

Table 1
Synthetic Model Parameter Values

Parameter	R_s	α	C_F	C_W	$\alpha 2$
Value	0.05	0.75	10,000	500	0.40
Parameter	R_p	α_p	C_p		
Value	500	0.15	0.8		

between 1 μHz and 20 μHz is dominated by the first CPE. A practised eye can pick up other hints about what ECM might be appropriate. For example, the curling up of the phase below 1 μHz hints at a parallel element, and the rounded, gradual nature of the corner at 500 μHz hints at a second fractional series element.

5. Model Discrimination & Selection

Fig. 5 depicts the RMSE obtained fitting each of the ECMs to ideal noiseless data computed according to Section 4. The result is not surprising; only the correct model yields the expected RMSE of zero. Nevertheless, it is also possible to say that the parallel elements are having much less impact on the fit than the three series elements. Also note that the extra degree of freedom acquired when the Warburg is allowed to become a CPE significantly improves the fit, something that might not be expected from the position of its asymptote in Fig. 4.

Adding noise at 1% and 3% leads to the results in Fig. 6. This plot contain a great deal of information. The noiseless data from Fig. 5 is reproduced adjacent to the noisy results for comparison. As expected, adding noise increases the RMSE in all cases. Error bars have been added to the noisy RMSE results. In each case 30 simulations were run with different added noise, and the mean and standard deviation (SD) of the RMSE calculated across these runs. The error bars show the $\pm$1.0SD extents.

Observe that the RMSE results do vary somewhat for given noise contribution, but not greatly. Where different models return RMSE values that lie within the error margins, the conclusion must be that the models are indistinguishable. One way of interpreting this is to say that the quality of the data does not justify the added complexity of the model with a higher number of degrees of freedom. In the example, the R-CPE-CPE-Rp model has six degrees of freedom, the R-CPE-CPE-CPEp model seven, and the R-CPE-CEP-Rp-CPEp model eight. It is clear that the first three models (with three, four, and five degrees of freedom) all fall short of the final three. Amongst the final three, the R-CPE-CPE-Rp model, as the most constrained, is to be preferred. This conclusion is reached both in the case of 1% noise, and 3% added noise. In other words, once noise reaches as little as 1% it becomes impossible to distinguish between the final three models. Given the RMSE with incorrect models but operating with noise-free data, it can be anticipated that the last three models will become indistinct when noise reaches about half a percentage point.

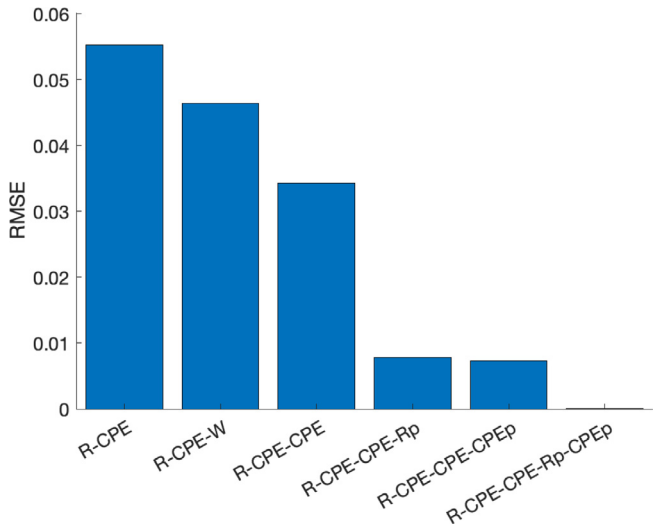

Fig. 5. RMS error obtained fitting the various equivalent-circuit models to ideal (noiseless) synthesized data.

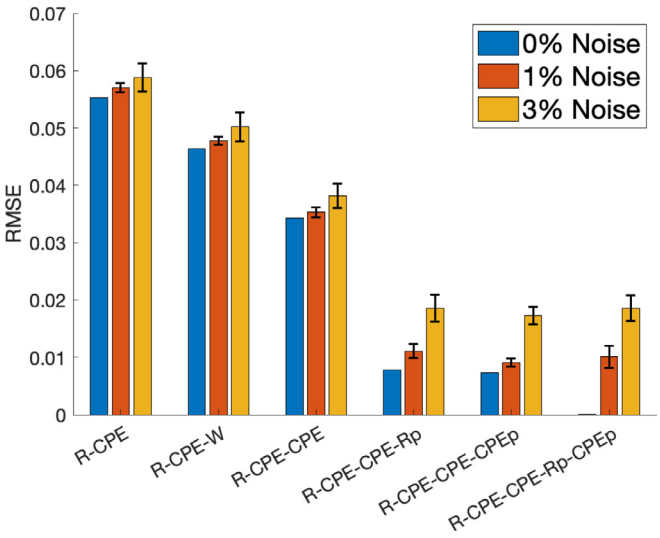

Fig. 6. RMS error obtained fitting the various equivalent-circuit models to ideal (noiseless), 1 percent noise, and 3 percent noise synthesized data. Error bars show 1 standard deviation in expected RMS error.

6. Measured Data

The modelling process described above was applied to impedance magnitude and phase data measured on real batteries. Measured data were obtained for a near-new lithium nickel cobalt aluminium oxide (referred to variously as NCA or NCR) 21700 cell and a used but healthy lithium nickel manganese cobalt oxide (referred to variously as NMC or INR) 18650 cell. Measurements are made with a developed form of the method initially described by Scott and Hasan [4]. For the present experiment, a multiple-sinewave current consisting of multiple frequencies ranging between 0.5 μHz and 2Hz was delivered using a two-quadrant power supply (model 66332A dynamic measurement source) controlled by software developed in-house, written in C, and running on a Raspberry Pi 4 connected via a Prologix-compatible open-source GPIB interface. The 66332A delivers up to 5A of current, and has voltage and current resolutions of 5mV and 1.32mA, respectively. The software can be configured to distribute either current or charge displacement across all frequencies in various fashions.

Impedance, Z, of an electrochemical system around some steady or quasi-steady state can be determined by:

1. applying a small-signal multitonal sinusoidal current, where $I(t) = |I|e^{j(\omega t+\phi_I)}$;
2. measuring the voltage response $V(t) = |V|e^{j(\omega t+\phi_V)}$;
3. calculating $Z(\omega) = \frac{|V|}{|I|}e^{j(\phi_V-\phi_I)}$)[23].

$Z(\omega)$ is made up of real and imaginary parts:

$Z(\omega) = Z_0\cos(\phi) + jZ_0\sin(\phi)$where $Z\prime_{real} = Z_0\cos(\phi)$, the resistance of the system, and $Z\prime\prime_{imag} = Z_0\sin(\phi)$, capacitance and/or inductance, representing energy storage [8]. In this manuscript, we display Bode plots which present magnitude $|Z(\omega)| = |V|/|I|$ and phase $\arg(Z(\omega)) = \phi_V - \phi_I$.

Current and voltage were logged by the 66332A approximately every 0.1s. Magnitudes and phases of both parameters at the frequencies of interest, required to permit the above calculations, were determined using a discrete Fourier transform (DFT) after the method first described by Scott and Parker [24]. The resulting magnitude and phase plots for the batteries used here are shown in Fig. 7.

The results of attempting to fit the various ECMs to these batteries appear in Fig. 8. The associated model parameters appear in Tables 2 and 3.

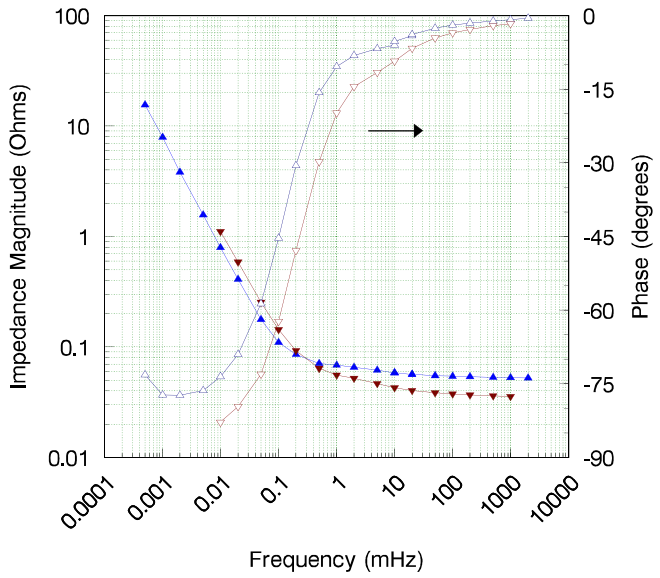

Fig. 7. Plot of measured impedance magnitude (solid blue up triangles) and phase (open blue up triangles) of a lithium nickel cobalt aluminium oxide (NCR/NCA) 2170 cell and magnitude (solid red down triangles) and phase (open red down triangles) measured on a lithium nickel manganese cobalt oxide (INR/NMC) 18650 cell.

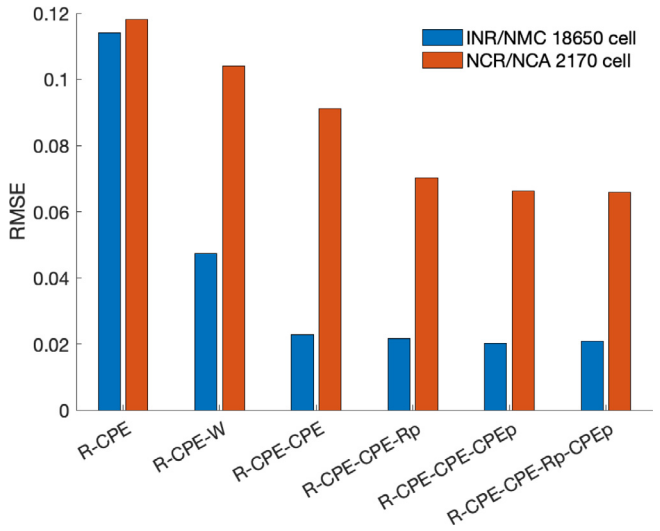

Fig. 8. RMS error obtained fitting each ECM to the two data sets presented in Fig. 7. The left-hand blue bars correspond to the NMC cell.

Table 2
ECM Parameters for NMC 18650 cell

Parameter	R_s	α	C_F	C_W	$\alpha 2$
Value	0.0330	0.99	14,180	187	0.27

Table 3
ECM Parameters for NCA 2170 cell

Parameter	R_s	α	C_F	C_W	$\alpha 2$	R_p
Value	0.0503	0.99	22,230	230	0.272	44

Observing the RMSE for the various models in Fig. 8, it is clear for the NMC cell, for which less data is available, that the R-CPE-CPE model is the appropriate choice. More than five degrees of freedom cannot be justified, and the error in the data is relatively small in measurement terms. In the case of the NCA cell, the noise is much larger, but the data span a greater frequency range. The RMSE settles to a value almost triple that of the other cell. Nevertheless, the data clearly justify a six-parameter model, whose parameters appear in Table 3. The more complex models have very slightly less RMSE, but not by a margin that we consider to warrant the complexity.

7. Conclusion

We have revisited the work of Berthier, employing fractional equivalent-circuit models inspired by recent, extra-low frequency EIS measurements. Our conclusion is that it is possible to distinguish between a selection of ECMs. With real, noisy data there will be models between which it will not be possible to make a reliable selection. We say of these that their extra degrees of freedom are not justified in the face of the quantity and quality of data available. In other words, adding degrees of freedom is not justified if the RMSE does not decrease by an extent greater than the expected uncertainty. Up to that point, the model with more degrees of freedom and lower RMSE is preferred.

The rich literature on gray-box, equivalent-circuit models exposes a disconnect between the work of electrochemists and electrical engineers, the former have great insight into the circuit elements, and the latter the tools to fit and employ them.

It has become clear that a guided fitting approach and multiple restarts in the optimization can help in finding a global minimum, especially in the case of models with more than a few degrees of freedom. When selecting between several ECMs, the most simple is fitted first, and the results of the first fit used as the starting point for fitting the next-most complicated model. Multiple restarts improve the likelihood that the optimization will not be caught in a saddle.

A wide range of frequencies improves the sensitivity of the RMSE to parameters in a given ECM. The frequency range should be chosen appropriately in view of the intended application of the model.

The ability to obtain values for parameters of elements in the ECM of a battery should allow electrochemists to associate internal components of a battery with branches in the ECM. The same ability should allow electrical engineers to observe degradation & ageing in a battery and predict failure well ahead of the event.

Declaration of Competing Interest

The authors declare that they have no known competing financial interests or personal relationships that could have appeared to influence the work reported in this paper.

References

[1] F. Berthier, J.-P. Diard, R. Michel, Distinguishability of equivalent circuits containing CPEs: Part I. Theoretical part, J. Electroanal. Chem. 510 (1) (2001) 1–11. doi:10.1016/S0022-0728(01)00554-X..
[2] R. Fletcher, C. Xu, Hybrid Methods for Nonlinear Least Squares, IMA J. Numer. Anal. 7 (3) (1987) 371–389, https://doi.org/10.1093/imanum/7.3.371. url: https://academic.oup.com/imajna/article-lookup/doi/10.1093/imanum/7.3.371.
[3] P. Mauracher, E. Karden, Dynamic modelling of lead/acid batteries using impedance spectroscopy for parameter identification, J. Power Sources 67 (1–2) (1997) 69–84, https://doi.org/10.1016/S0378-7753(97)02498-1.
[4] J. Scott, R. Hasan, New Results for Battery Impedance at Very Low Frequencies, IEEE Access 7 (2019) 106925–106930, https://doi.org/10.1109/ACCESS.2019.2932094.
[5] R. Hasan, J. Scott, Extending Randles's Battery Model to Predict Impedance, Charge-Voltage, and Runtime Characteristics, IEEE, Access 8 (2020) 85321–85328, https://doi.org/10.1109/ACCESS.2020.2992771.
[6] A. Lasia, Impedance of the Faradaic Reactions in the Presence of Mass Transfer, in: Electrochemical Impedance Spectroscopy and its Applications, Springer New York, New York, NY, 2014, pp. 85–125. doi:10.1007/978-1-4614-8933-7_4..

[7] U. Westerhoff, K. Kurbach, F. Lienesch, M. Kurrat, Analysis of Lithium-Ion Battery Models Based on Electrochemical Impedance Spectroscopy, Energy Technol. 4 (12) (2016) 1620–1630, https://doi.org/10.1002/ente.201600154.
[8] W. Choi, H.-C. Shin, J.M. Kim, J.-Y. Choi, W.-S. Yoon, Modeling and Applications of Electrochemical Impedance Spectroscopy (EIS) for Lithium-ion Batteries, J. Electrochem. Sci. Technol 11 (1) (2020) 1–13, https://doi.org/10.33961/jecst.2019.00528.
[9] B. Sohlberg, E.W. Jacobsen, Grey box modelling – branches and experiences, IFAC Proceedings Volumes 41 (2) (2008) 11415–11420.
[10] L. Nugroho, R. Akmeliawati, Comparison of black-grey-white box approach in system identification of a flight vehicle, Journal of Physics Conference Series, IOP Science 1130 (1)..
[11] J. Brucker, W.G. Bessler, R. Gasper, Grey-box modelling of lithium-ion batteries using neural ordinary differential equations, Energy Informatics 4 (15)..
[12] J.E.B. Randles, Kinetics of rapid electrode reactions, Discuss. Faraday Soc. 1 (1947) 11, https://doi.org/10.1039/df9470100011.
[13] W. Cao, S.-L. Wang, C. Fernandez, C.-Y. Zou, C.-M. Yu, X.-X. Li, A novel adaptive state of charge estimation method of full life cycling lithium-ion batteries based on the multiple parameter optimization, Energy Science and Engineering 7 (5) (2019) 1544–1556.
[14] R. Hasan, J. Scott, Application of Swingler's method for analysis of multicomponent exponentials with special attention to non-equispaced data, in: 2016 IEEE 12th International Colloquium on Signal Processing & Its Applications (CSPA), IEEE, Melaka, Malaysia, 2016, pp. 12–15. doi:10.1109/CSPA.2016.7515794. url:http://ieeexplore.ieee.org/document/7515794/.
[15] A. Lasia, Dispersion of Impedances at Solid Electrodes, in: Electrochemical Impedance Spectroscopy and its Applications, Springer, New York, New York, NY, 2014, pp. 177–201, https://doi.org/10.1007/978-1-4614-8933-7_8.
[16] S. Westerlund, L. Ekstam, Capacitor theory, IEEE Trans. Dielect. Electr. Insul. 1 (5) (1994) 826–839, https://doi.org/10.1109/94.326654.
[17] T.T. Hartley, J.-C. Trigeassou, C.F. Lorenzo, N. Maamri, Energy Storage and Loss in Fractional-Order Systems, J. Comput. Nonlinear Dyn. 10 (6) (2015), https://doi.org/10.1115/1.4029511 061006.
[18] N. Hansen, Benchmarking the Nelder-Mead downhill simplex algorithm with many local restarts, in: Proceedings of the 11th Annual Conference Companion on Genetic and Evolutionary Computation Conference: Late Breaking Papers, Association for Computing Machinery, Montreal, Québec, Canada, 2009, pp. 2403–2408. url:https://doi.org/10.1145/1570256.1570335.
[19] U.M. Sundar, Numerical Optimization Using MATLAB (2015). url:https://www.mathworks.com/content/dam/mathworks/mathworks-dot-com/solutions/automotive/files/in-expo-2015/numerical-optimization-using-matlab.pdf..
[20] A. Parkhomenko, (2017). url:https://www.andrii-parkhomenko.net/files/Numerical%20optimization%20in%20Matlab.pdf..
[21] J.A. Nelder, R. Mead, A Simplex Method for Function Minimization, Comput. J. 7 (4) (1965) 308–313, https://doi.org/10.1093/comjnl/7.4.308.
[22] W.H. Press, Numerical recipes in C : the art of scientific computing, 2nd Edition,., Cambridge University Press, Cambridge [England], 1992.
[23] C. Zou, L. Zhang, X. Hu, Z. Wang, T. Wik, M. Pecht, A review of fractional-order techniques applied to lithium-ion batteries, lead-acid batteries, and supercapacitors, J. Power Sources 390 (2018) 286–296, https://doi.org/10.1016/j.jpowsour.2018.04.033.
[24] J. Scott, A. Parker, Distortion analysis using SPICE, J. Audio Eng. Soc. 43 (12) (1995) 1029–1040.

Appendix B

Wilson et al.: Measuring Electrical Properties of Batteries at Ultra-long Timescales

The following paper by Wilson et al. [92] draws on work presented in the present thesis, and gives a broad and succinct overview of ELF battery measurement and its place in the overall work of the Battery Modelling Group at the University of Waikato. Section 3 of the paper "Measuring Impedance" relates to Chapter 3, and Sections 4 "Time-Domain Measurements at Constant Current" and 5 "Relationship to Cyclic Voltammetry and Incremental Capacity Analysis" to Chapter 4. The author provided experimental data for use in these sections.

Measuring Electrical Properties of Batteries at Ultra-long Timescales

M. T. Wilson[1], C. Dunn[2], V. Farrow[2], M. Mucalo[1], J. B. Scott[2]

Abstract: Quantifying battery behavior is critical to development of new battery technologies and energy storage systems. While it is straightforward to measure properties such as impedance at short timescales (i.e. frequencies larger than ~1 Hz) the relevance of this is questionable since rechargeable batteries in normal usage are often cycled on timescales of hours or days. Making measurements at these timescales, for example impedance measurements below ~1 mHz, is more challenging. In this paper we discuss approaches to quantifying battery behavior at timescales from hours to weeks (frequency scales of ~0.1 mHz down to ~1 µHz). We present frequency domain measurements and time domain measurements, achieved through four-point measurements with a Keysight 66332A at around 100 mA RMS. At low frequencies significant charge is shifted in a measurement cycle, complicating interpretation. The digitization of a sine-wave may introduce errors such as constant current offsets that build in significance with time. The operating point (DC voltage level) of the battery should be controlled since it influences impedance at the lowest frequencies as a result of the voltage-dependent nature of different electrochemical processes. We relate the voltage-dependent effects to time-domain measurements such as cyclic voltammetry and incremental capacity analysis.

1. Introduction

Rechargeable batteries are becoming increasingly important in energy storage applications, such as electric cars. Reliably measuring battery performance parameters such as state-of-charge and state-of-health is critical. Failing to identify state-of-health reliably results in waste as batteries are disposed of when they still have useful life remaining, or ugly surprises for a user when a battery fails unexpectedly. In the case of medical implants, replacing a battery involves risky surgery—knowing exactly when to do this would save many surgical procedures.

Batteries are frequently described by equivalent circuit models (ECMs) [1, 2, 3]. A variety of electronic circuit elements, typically capacitors and resistors but also constant-phase elements, are put together to form an equivalent circuit. These are useful for modeling battery response in different situations, but have limitations. It is difficult to distinguish one circuit model from another, particularly when data have been measured over a limited frequency range [3]. While laboratory-based measurements might be carried out using frequencies of order hertz (timescales of order seconds), batteries in practice operate at much longer timescales—often days between charging periods.

In this paper we discuss ways in which battery performance over long timescales may be characterized, in both the frequency domain and time-domain. We first discuss some general principles of rechargeable batteries. We then discuss the process of measuring battery impedance, highlighting some subtleties. Then we move to considering time-domain measurements, specifically charge-discharge cycles and their relationship to cyclic voltammetry. Finally, we put our findings into a broader context for battery measurement.

2. General Principles

2.1 Equivalent Circuit Models

Numerous ECMs have been proposed in the literature [1]. ECMs allow prediction of the voltage response to different current profiles, facilitating investigation of battery properties such as state-of-charge (the charge held by the battery

Corresponding Author
M. T. Wilson
Te Aka Mātuatua – School of Science, University of Waikato
marcus.wilson@waikato.ac.nz
https://orcid.org/0000-0001-6214-7727
https://doi.org

[1] Te Aka Mātuatua – School of Science, University of Waikato, Private Bag 3105, Hamilton 3240, New Zealand
[2] School of Engineering, University of Waikato, Private Bag 3105, Hamilton 3240, New Zealand

relative to its maximum charge capacity) and state-of-health (often defined as the charge capacity relative to its capacity when first manufactured).

Numerous ECMs have been proposed for batteries, including the historical model of Randles [5], the physical model of Westerhoff [2] with 16 elements to describe explicitly various battery electrochemical processes, and the phenomenological model proposed in reference [4], Figure 1.

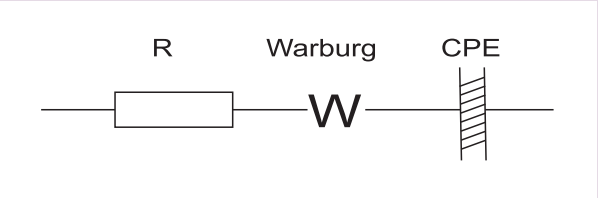

Figure 1. One of the battery ECMs proposed in [4], consisting of a resistor, Warburg element and constant-phase element (CPE).

2.2 Fractional Elements

The CPE and Warburg are components whose impedance Z is a non-integer power of frequency, and whose phase is a constant, $Z = 1/(j\omega)^{\alpha}C_F$, where ω is the angular frequency, 2π times frequency, α is a constant between 0 and 1, and C_F is a constant known as the fractional capacitance. A pure capacitor has α=1; a pure resistor has α=0. The special case of α=1/2 gives a 'Warburg' element, often associated with ion-diffusion mechanisms.

An unpleasant feature of fractional elements is that their behavior is non-local—their voltage depends not just on their state now but on how they reached that state. Their behavior may be modeled mathematically in the time domain through fractional calculus [6].

2.3 Frequency Domain and Time Domain

Typically electrical measurements are carried out (a) in the frequency domain, using sine-wave currents of constant frequency, or (b) in the time domain using controlled pulses of current. For linear systems, the two are connected via Fourier or Laplace transforms. For realistic systems, there is often discrepancy between the two forms of measurement, e.g. [7, 8], due to nonlinearities.

3. Measuring Impedance

3.1 General Principles

Impedance of a component is often measured using a four-point impedance meter. This equipment sets a controlled current through the device under test (DUT) and then monitors the voltage over the DUT. Often impedance meters will produce AC signals of frequencies of the order 1 Hz at the low end, though some will go much lower. For example, the Solartron 1260A will measure down to 10 μHz. But to work at still lower frequencies, programmable supplies are required, such as a Keysight 66332A.

Low frequency measurements demand long timescales and are slow to make. Impedance measurements are often non-repeatable unless carried out carefully. Battery impedance decreases after cycling and takes many days to re-equilibrate [9]. Several periods are required to acquire a good quality measurement. This long timescale means that the battery's operating point (state-of-charge) might change during the course of the measurement, complicating the interpretation of the result.

3.2 Measuring at Multiple Frequencies

If a DUT behaves linearly, it is practicable to measure impedance at several frequencies simultaneously. This superposition will speed up measurement of an impedance spectrum considerably, by constructing a current waveform that exhibits multiple frequencies, carried on a lower frequency that ensures the battery is always actively working [9]. The amplitude of the carrier waveform should be kept low in order that the battery does not charge or discharge significantly during the measurements. Spectral windowing (e.g. Hann windowing) should be applied to the collected data before a discrete Fourier transform is applied to recover a spectral response. Linearity should be checked by repeating with a different current amplitude.

Alternatively, multiple frequencies may be applied on top of a square carrier wave of several-milliampere current; the carrier wave ensures that the battery is always in a 'working' condition when measured [9, 10]. Figure 2 shows a section of the voltage and current in an example measurement on a Li-ion battery.

3.3 Analogue-to-Digital Conversion

Impedance meters will construct sine-wave signals digitally. Some analogue-to-digital converters (ADCs) will round towards zero, but others may round up or round down. This rounding may cause difficulties. Figure 3 illustrates the error when an ADC rounds down. The solid black line shows a sine wave. The solid blue line shows this wave converted (four-bit ADC) into a digital form. The dashed blue line is the average of the digitally constructed sine wave—this average is not zero. A consequence of this non-zero average is that the battery will slowly discharge during the measurement period. For short periods this is unlikely to be problematic, but at ultra-long periods this will result in a significant movement in charge during the measurement period even with 12-bit resolution—meaning that the battery's operating point is different by the end of the measurement period. This error may be corrected by monitoring and adjusting charge drift throughout a measurement.

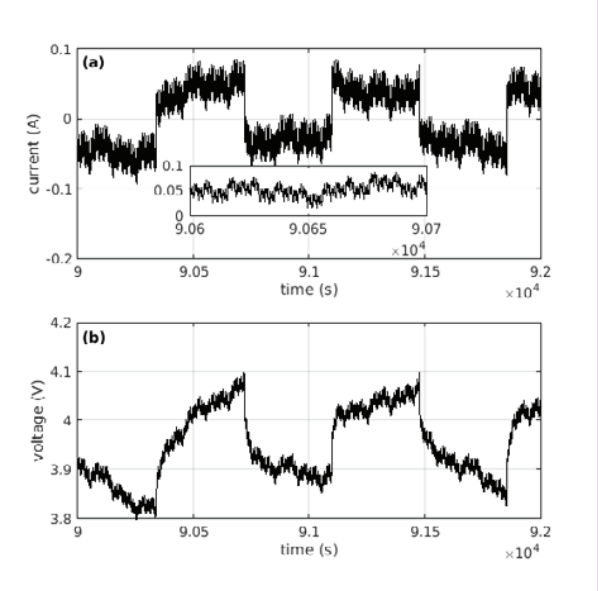

Figure 2. Using a square wave of 0.00132 Hz to ensure a battery is continually working (charging or discharging) during an impedance measurement using several frequencies. (a) The current against time, as set by the measurement machine. The inset is a close-up of one section showing multiple frequencies in the time domain. (b) The voltage against time, as measured.

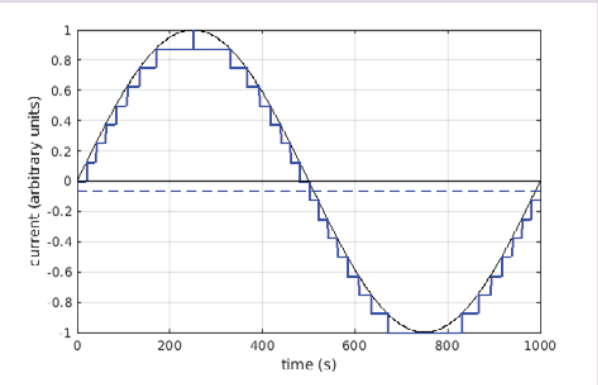

Figure 3. An illustration of an error introduced by an ADC. The black line is a sine wave; the blue line a digitally-reconstructed sine wave where the ADC has rounded down. The average of the digital reconstruction is not zero (blue dashed line).

3.4 Example Impedance Plot

An example impedance plot is shown in Figure 4. These data were collected with a Keysight 66332A four-point dynamic measurement source with a current of up to 100 mA (lower at lower frequencies), with 12 bits of ADC. Current waveforms were digitally constructed at single frequencies and the resulting voltage measured over three periods. Waveforms were then Hann-windowed and a discrete Fourier transform applied and Z recovered at the applied frequency [3].

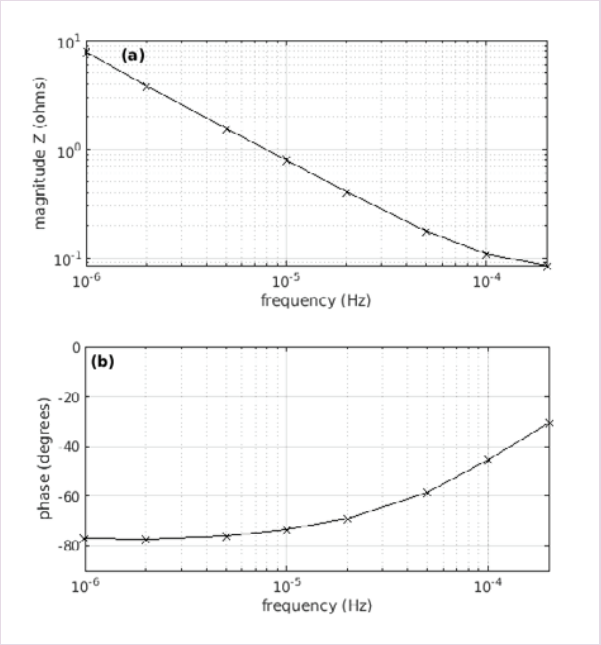

Figure 4. A plot of (a) magnitude and (b) phase of impedance against frequency for a 4.8 A h NCA battery, for sub-millihertz frequencies. The lowest and highest frequencies shown correspond to periods of 11.6 d and 1.4 h respectively.

4. Time-Domain Measurements at Constant Current

One may also analyze time-domain measurements. Here, one may cycle a battery (charge and discharge) several times. One option is a constant current (CC) protocol: here we charge at a constant current until the voltage reaches a defined upper limit, then discharge at a constant current, which is often same as the charge current, until the voltage reaches a defined lower limit, and then repeat. The voltage response $V(t)$ then contains information about the battery in a complementary manner to the impedance measurements. Another well-used alternative, which is more akin to battery charging protocols used in practice, is constant current–constant voltage (CC–CV). Here one begins by charging at constant current until the voltage reaches a defined upper limit, then holding the voltage constant, which means that the current reduces, before applying a constant discharge current.

With time domain data we may typically analyze (a) the *charge capacity*, that is how much charge the battery takes during a charge cycle, equal to I_0T for a constant current I_0 charge over a time T, (b) the *discharge capacity*, how much charge the battery gives out in a discharge cycle (which might not equal the charge capacity [11]), and (c) the shape of the voltage response $V(t)$. For a battery, the charge-discharge capacities vary with timescale (longer periods give higher capacities), a phenomenon labeled *capacity offset*.

Practically, CC or CC–CV measurements at long timescales require careful consideration. A programmable supply such as the Keysight 66332A or Keithley 2400-series Source Measurement Unit will put out a current at the requested level subject to an analogue to digital conversion. Thus the actual current applied will differ from the requested current. With a resolution of around 1 mA this will result in a significant error in calculated charge passed over timescales of hundreds of days. E.g. for an eight-day charge period this error results in 0.2 A h of extra charge, a significant fraction of the capacity of a 4 A h battery. It is important to use the actual applied current in calculations of charge capacity.

We have performed CC measurements for a lithium nickel-cobalt-aluminium-oxide (NCA) battery, rated at 4.8 A h charge capacity and 17.1 W h energy capacity [7]. Specifically, we have charged and discharged the battery at currents of 5 A, 2 A, 1 A, 0.5 A, 0.2 A, 0.1 A and 0.05 A in that order.

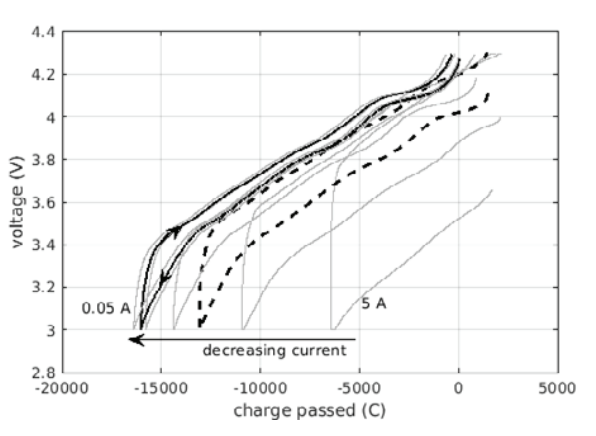

Figure 5. A plot of voltage against charge for currents from 5 A down to 50 mA for a 4.8 A h NCA battery cycled under CC.

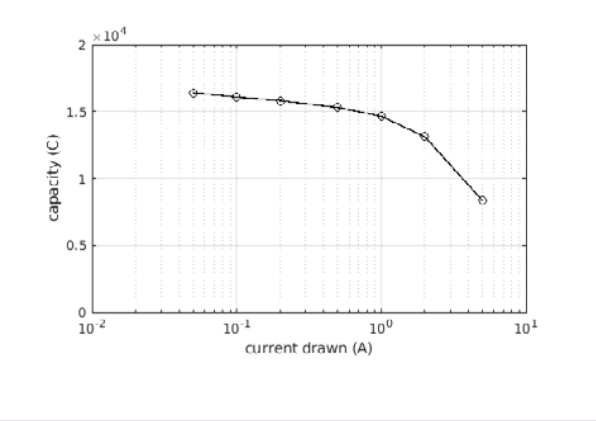

Figure 6. A plot of discharge capacity against time for a 4.8 A h NCA battery.

Charging is considered complete when the voltage reaches 4.30 V; discharging is considered complete when the voltage drops to 3.00 V. The lowest current gives a charging period of about 4 days. Figure 5 shows V against q plots for selected currents. Figure 6 shows the discharge capacity as a function of current drawn.

Figure 5 shows that, at lower discharge currents, the charge capacity is greater and the hysteresis is reduced (less area in a charge-discharge loop, meaning less energy is dissipated as heat). Also, there are pronounced 'wiggles' in the $V(q)$ curves at the higher voltages, for the lower discharge currents, where $\mathrm{d}V/\mathrm{d}q$ fluctuates significantly from low (a 'plateau') to high, as the battery approaches fully charged. Figure 6 demonstrates the phenomenon of 'capacity offset', where charge capacity increases as the rate of charge-discharge (current drawn) reduces.

5. Relationship to Cyclic Voltammetry and Incremental Capacity Analysis

The wiggles of Figure 5 may be related to cyclic voltammetry (CV), an experimental method commonly used to characterize and identify electrochemical reactions [12]. In CV, the voltage across a cell is swept up (increasing V) at a constant rate and the resulting current is recorded; the voltage is then swept down at the same rate to complete the cycle. A plot of i against V typically shows a series of peaks which correspond to various electrochemical reactions and phase transitions.

If we assume for a battery voltage is a function of charge, $V=V(q)$, then the relationship between Figure 5 and CV becomes clear. Differentiating with respect to time gives:

$$\frac{dV}{dt} = \frac{dV}{dq}\frac{dq}{dt} = \left(\frac{dV}{dq}\right) i \qquad (1)$$

and hence $i = V_{\mathrm{rate}}/(\mathrm{d}V/\mathrm{d}q)$ where $V\mathrm{rate}=\mathrm{d}V/\mathrm{d}t$ is the voltage slew rate. The peaks of current in CV thus correspond to regions of low $\mathrm{d}V/\mathrm{d}q$. That is, broadly the plateaus of Figure 5 correspond to the peaks in CV. This is a simplistic assessment, since for a battery, V is not a strict function of q, since it has memory effects. However, it is reasonable to assume that the plateaus (wiggles) of the V against q plot are associated with specific electrochemical processes in the battery.

One may reconstruct a pseudo-CV from the time-domain data via Eq. (1); for example, the CV reconstructed from the 0.1 A data of Figure 5 (the solid black line) is shown in Figure 7 below.

A study of a cyclic voltammogram suggests why electrical impedance spectroscopy (EIS) will sometimes produce highly variable results. If the battery is operating near a peak, voltage will vary little with a given change in current (thus impedance is low), but away from a peak the same change in current requires a much greater change in voltage and thus

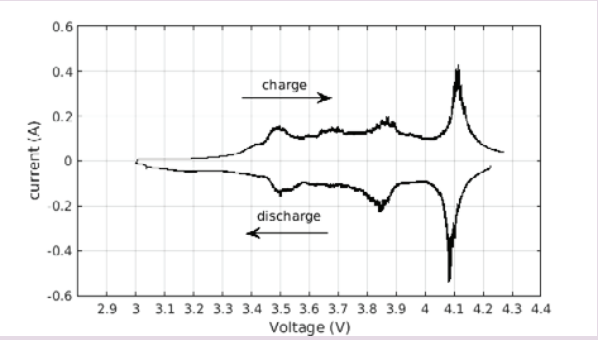

Figure 7. A reconstruction of a CV from constant-current data for a NCA battery cycled at 0.1 A (corresponding to the solid black line in Figure 5).

a higher impedance measurement. Operating point is thus significant, for example Figure 7 suggests that at around 4.05 V a small change in operating point would give a significant change in measured impedance. Using a square carrier wave for impedance measurements (Figure 2) may help reduce these fluctuations by varying the operating point during measurement.

A related experimental technique is incremental capacity analysis (ICA) [13]. During ICA, voltage is increased in small steps ΔV and a measurement of the charge ΔQ passed in order for the battery to re-equilibrate is made. A plot of $\Delta Q/\Delta V$ against V then yields similar information to Figure 7.

6. Discussion and Conclusion

We have presented frequency and time domain measurements of batteries, at ultra-long timescales (several days). At such scales, battery behavior may be modeled through fractional calculus, using ECMs containing fractional elements. These elements lead to measurable phenomena such as capacity offset. Measurements should to be made carefully since errors in current, e.g. due to ADC, will accumulate into a considerable error in charge over a long time period. Batteries have nonlinear $V(q)$ characteristics at high and low states of charge and it is advisable to make impedance measurements away from these regions to ensure repeatability. Even so, reconciling time-domain and frequency-domain measurements is difficult. If done well, frequency and time domain measurements allow identification of plausible ECMs and component values, thus allowing a battery to be described with meaningful, and measurable parameters. At long timescales, the complexities of battery electrochemistry become evident and plots of $V(q)$ demonstrate patterns that link with cyclic voltammetry.

7. References

[1] Hidalgo-Reyes J, Gómez-Aguilar J F, Escobar-Jiménez R F, Alvarado-Martínez V M, & López-López M, "Classical and fractional-order modeling of equivalent electrical circuits for supercapacitors and batteries, energy management strategies for hybrid systems and methods for the state of charge estimation: A state of the art review", *Microelectronics Journal*, **85**, 109-128, (2019).

[2] Westerhoff U, Kurbach K, Lienesch F & Kurrat M, "Analysis of lithium-ion battery models based on electrochemical impedance spectroscopy", *Energy Technology*, **4**(12), 1620-1630, (2016).

[3] Scott J B & Hasan R, "New results for battery impedance at very low frequencies", *IEEE Access*, **7**, 106925, (2019).

[4] Poihipi E, Scott J & Dunn C, *"Distinguishability of battery equivalent-circuit models containing CPEs: updating the work of Berthier, Diard & Michel"*, Journal of Electroanalytical Chemistry, **911**, 116201 (2022).

[5] Randles J E B, "Kinetics of rapid electrode reactions", Discussions of the Faraday Society, **1**, 11, (1947). doi:10.1039/df9470100011

[6] Samko S G & Kilbas A A, *Fractional Integrals and Derivatives: Theory and Applications*, (CRC Press), 1993.

[7] Wilson M T, Farrow V, Pyne C J & Scott J B, "Charge capacity characteristics of a Lithium Nickel-Cobalt-Aluminium Oxide battery at ultra-slow time scales show fractional-derivative behaviour", *Communications in Nonlinear Science and Numerical Simulation*, under review, (2022).

[8] Budde-Meiwes, H, Kowal J, Sauer D U & Karden E. "Influence of measurement procedure on quality of impedance spectra on lead-acid batteries", *Journal of Power Sources*, **196**, 10415–10423, (2011).

[9] Dunn C & Scott J, "Achieving reliable and repeatable electrochemical impedance spectroscopy of rechargeable batteries at extra-low frequencies", I*EEE Transactions on Instrumentation and Measurement*, **71**, 8003808 (2022).

[10] Farrow V, "Characterisation of rechargeable batteries: Addressing fractional ultralow-frequency devices," *M.E. thesis, University of Waikato*, (Hamilton, New Zealand), (2020).

[11] Hartley T T, Veilette R J, Adams J L & Lorenzo C F. "Energy storage and loss in fractional-order circuit elements", *IET Circuits Devices and Systems*, **9**(3), 227, (2015).

[12] Elgrishi N, Rountree K J, McCarthy B D, Rountree E S, Eisenhart T T & Dempsey J L, "A practical beginner's guide to cyclic voltammetry", *Journal of Chemical Education*, **95**(2), 10415, (2011).

[13] Anseán D, García V M, González M, Blanco-Viejo C, Viera J C, Pulido Y F & Sánchez L, "Lithium-ion battery degradation indicators via incremental capacity analysis", *IEEE Transactions on Industry Applications*, **35**(3), 2992-3002, (2019).

Appendix C

Wilson et al.: Efficiency of Cycled Batteries Analyzed Through Voltage-Current Phase Differences

The paper presented in this appendix [102] was published in early 2024, after the initial version of the present thesis was sent out for examination. The paper consolidates and builds on the concepts developed in the draft paper of Chapter 5, and shows how use of the phase-efficiency relationship opens up the possibility of monitoring battery SoH by analysing time domain data acquired while the device under test is *in situ*.

While EIS remains the "gold standard" for characterising battery ageing, the very low frequencies (and subsequently long measurement times) needed when describing the battery in terms of the simple R-CPE circuit model are likely to render the method impractical for in-use devices. Time series analysis of *in-situ* voltage and current measurements may provide a solution to this problem and represent the way forward.

IEEE Access
Multidisciplinary ⋮ Rapid Review ⋮ Open Access Journal

Received 13 February 2024, accepted 28 February 2024, date of publication 7 March 2024, date of current version 13 March 2024.

Digital Object Identifier 10.1109/ACCESS.2024.3374339

METHODS

Efficiency of Cycled Batteries Analyzed Through Voltage-Current Phase Differences

MARCUS T. WILSON[1], CHRISTOPHER J. DUNN[2], (Student Member, IEEE), VANCE FARROW[2], MICHAEL J. CREE[2], (Senior Member, IEEE), AND JONATHAN B. SCOTT[2], (Life Senior Member, IEEE)

[1]Te Aka Mātuatua—School of Science, The University of Waikato, Hamilton 3240, New Zealand
[2]School of Engineering, The University of Waikato, Hamilton 3240, New Zealand

Corresponding author: Marcus T. Wilson (marcus.wilson@waikato.ac.nz)

ABSTRACT Ageing of rechargeable batteries is routinely characterized in the frequency domain by electrochemical impedance spectroscopy, but the technique requires laboratory measurements to be made on a time scale of days. However, the normal cycling of a battery as it is used *in situ* provides equivalent information in the time domain, though extracting robust frequency information from a time series is challenging. In this work, we explore, in the time domain, the relationship between instantaneous voltage-current phase difference and cycle efficiency. Moreover, we demonstrate that phase measures can be used to identify battery ageing. We have cycled a 250 mA h Nickel-Cobalt cell several hundred times and used Hilbert Transforms to identify phase difference between voltage and current. This phase difference becomes closer to zero as the battery ages, commensurate with a drop in energy cycle efficiency. In another experiment, we applied a synthetic current profile mimicking behaviour of an electric car cell, to a 3.2 A h $LiNiMnCoO_2$ cell, for ∼100 days. For this more complicated profile with a wide range of frequency content, we used wavelet analysis to identify changes in phase difference and impedance as the battery aged. For this cell, drop in cycle efficiency was associated with a rise in internal resistance. The results imply that time-series analysis of *in situ* measurements of voltage and current, when applied with equivalent circuit models and underlying theory, can identify markers of battery ageing.

INDEX TERMS Battery, constant phase element, efficiency, fractional capacitance, time-series analysis.

I. INTRODUCTION

Battery state of health (SoH) is a loose term generally used to describe of the performance of a battery when compared to an equivalent 'new' battery [1]. State of Health can manifest itself in various ways, such as charge or energy capacity, energy cycle efficiency and ability to deliver power, and can be estimated in numerous ways in practical applications [2]. Degradation is associated with many different failure mechanisms [3], [4] and can show itself through many ways, such as increased charge transfer and diffusion resistance, reduced current density, decreased voltage, and heat generation [5]. Frequently, battery ageing is clearly demonstrated through changes in impedance spectrum [6], [7], [8], [9] but electrochemical impedance spectroscopy (EIS) often requires long measurement times in the laboratory, and thus is impractical for many battery applications, although in some cases more rapid measurements are possible [10].

Equivalent circuit models, using an array of capacitors, resistors, and constant phase elements (CPEs), have been well used to describe batteries [11], [12], [13]. Variations in different circuit elements will lead to variations in energy cycle efficiency, charge capacity, *etc.*, and it is attractive to seek to describe ageing of batteries in terms of these elements. Indeed, Farrow has used measurements of impedance spectrum to show a change in circuit elements as ageing occurs [8], and Mauracher & Karden have used electrochemical impedance spectroscopy to model changes in lead-acid batteries [14]. Significantly, combining EIS with time domain measurements, Messing et al. have identified

The associate editor coordinating the review of this manuscript and approving it for publication was Bo Pu.

changes in circuit elements with ageing from relaxation effects [15].

In this work we demonstrate that a change in order of a constant phase element in an equivalent circuit influences cycle energy capacity, via a change of phase between the voltage and current. Changes in phase have been previously recognized as underlying signals for SoH of lithium-ion batteries [2]. Importantly the phase changes can be extracted from time-series data acquired while the battery is cycled. We first relate phase and energy efficiency for a CPE, through a theoretical analysis, as shown in Sec. II. We demonstrate that, for a CPE, we expect a relationship between cycle energy efficiency and phase between V and I. We then, in Sec. III, describe and analyze with Hilbert transforms and wavelet analysis the results of three experiments, using different batteries and charging-discharging cycles, that elucidate the relationship between phase and cycle efficiency. We demonstrate that for one of these experiments, changes in efficiency as the battery ages are related to phase changes. However, for another experiment, they are related to an increase in resistance. Finally, in Sec. IV, we put these results into the context of equivalent circuit models and suggest how time-series analysis of voltage and current can be used to elucidate changes in SoH.

II. THEORY

A. CONSTANT PHASE ELEMENTS

A constant phase element (CPE) or fractional capacitor can be defined through the fractional derivative relationship between current I and voltage V:

$$I(t) = C_f \frac{d^\alpha V}{dt^\alpha}, \tag{1}$$

where t is time, C_f is the fractional capacitance, and d^α/dt^α denotes the fractional derivative of order α, where $0 < \alpha < 1$. Fractional calculus has a secure mathematical base [16] including for application to batteries [17]. For the purposes of this work, the relationship is best discussed in terms of a response to a sine wave stimulus. For a sine wave current input, the voltage responds as a sine wave, but with a phase difference determined by the fractional order α. Specifically, constructing the impedance as the complex voltage (amplitude and phase) divided by the complex current, we have:

$$Z(\omega) = \frac{1}{C_f (j\omega)^\alpha} \tag{2}$$

where ω is the angular frequency ($= 2\pi f$ where f is the frequency) and $j^2 = -1$. Of importance is the phase (argument of Z), which is $\arg(j^{-\alpha}) = -\pi\alpha/2$. This phase is independent of frequency, hence the term 'constant phase element'. In the limit of $\alpha \to 1$ the CPE behaves as a capacitor; in the limit of $\alpha \to 0$ the CPE behaves as resistor. The special case of $\alpha = 0.5$ describes a Warburg element, commonly used in modelling of electrochemical processes, for example with the Randles circuit [18].

CPEs have been commonly used in models of batteries. For example, the model of Westerhoff et al. which explicitly considers the physical behaviour of the various structures of a battery, contains three CPE elements in addition to two Warburg elements, two capacitors and nine resistors [12]. Westerhoff's model associates electronic components with physical processes. However, for practical purposes, many fewer elements are needed to describe a battery [13], [19], with Poihipi et al. using just two CPEs and a resistor to effectively model experimental results [11]. Such a reduced phenomenological model makes attribution of changes in electronic component values to particular chemical and physical processes difficult. Indeed, experimental measurements of impedance [8], [20], [21], [22] suggest that in many cases simply a single CPE may be sufficient in series with a resistor might be a sufficient equivalent circuit to describe a battery.

B. ENERGY EFFICIENCY OF CPE

For a rechargeable battery, the energy efficiency of a cycle, ϵ, defined as the energy taken out of the battery during a discharge divided by the energy put in during a charge, is of significance. For a pure capacitor ($\alpha = 1$) there is no energy loss and $\epsilon = 1$; in contrast for a pure resistor ($\alpha = 0$) there is no energy stored and $\epsilon = 0$. In general, the efficiency of a battery cycle will depend on the shape of the cycle. In some special cases, it is possible to derive the efficiency mathematically.

The case of a single rectangular charge and discharge pulse (where charging and discharging currents are both constant, but not necessarily equal) has been analyzed by Hartley et al. [23], [24]. By setting the charge and discharge currents and times to maximize energy efficiency, one obtains an efficiency directly related to the fractional order α:

$$\epsilon = \left(2^\alpha - 1\right)^2. \tag{3}$$

While efficiency is dependent on α, the actual values of energy into the battery during the charge and the energy taken out of the battery during the discharge, depend on the currents and cycle times.

A second case in which we can explicitly derive the efficiency of a CPE is that of a continuous sine wave input. In the analysis below, we derive the efficiency under a sine wave stimulus for the case of a CPE in series with a resistor (denoted CPE-R), which is a reasonable circuit model for many batteries [8], [11]. A CPE-R model has a knee angular frequency defined where $|Z(\omega)| = R$; below this angular frequency the CPE dominates the impedance. We use the standard convention for batteries that *positive* and *negative* currents correspond to *charging* and *discharging* of the battery respectively. For the case of a sine wave current,

$$I(t) = I_0 \sin(\omega t), \tag{4}$$

the voltage across the CPE, assuming there is a constant starting voltage offset V_0 as a result of charging a CPE a long

time in the past, responds as:

$$V_{CPE}(t) = V_0 + V_a \sin(\omega t + \theta) \tag{5}$$

where $V_a = |Z(\omega)|I_0$ is the amplitude of the a.c. part of the waveform, and $\theta = -\alpha\pi/2$ is the phase, *i.e.* the voltage trails the current by $\alpha\pi/2$. Note that V_a depends on frequency through $|Z|$. The voltage across the resistor, R, is simply IR, and thus the total voltage over the CPE-R elements is

$$V(t) = V_0 + V_a \sin(\omega t + \theta) + I_0 R \sin(\omega t). \tag{6}$$

We assume that $V(t)$ is always positive. For rechargeable batteries in normal operation, this will always be the case. Then the sign of the instantaneous power, $P(t) = V(t)I(t)$, is determined by the sign of the current $I(t)$, positive in the first half-cycle and negative in the second. The energy into the CPE-R circuit in the first half-cycle is given by:

$$E_{in} = \int_{t=0}^{T/2} V(t)I(t)dt. \tag{7}$$

Writing out $V(t)$ and $I(t)$ explicitly leads to

$$\begin{aligned} E_{in} = &\int_{t=0}^{T/2} V_0 I_0 \sin(\omega t)dt \\ &+ \int_{t=0}^{T/2} V_a I_0 \sin(\omega t)\sin(\omega t + \theta)dt \\ &+ \int_{t=0}^{T/2} I_0^2 R \sin^2(\omega t)dt \end{aligned} \tag{8}$$

where T is the period of the sine wave. Performing the integrals yields

$$E_{in} = \frac{V_0 I_0 T}{\pi} + \frac{V_a I_0 T \cos\theta}{4} + \frac{I_0^2 RT}{4}. \tag{9}$$

The energy put *into* the CPE in the *second* half-cycle is given by:

$$E_{in}^{(2)} = \int_{t=T/2}^{T} V(t)I(t)dt \tag{10}$$

which is

$$\begin{aligned} E_{in}^{(2)} = &\int_{t=T/2}^{T} [V_0 + V_a \sin(\omega t + \theta) \\ &+ I_0 R \sin(\omega t)]\, I_0 \sin(\omega t)dt. \end{aligned} \tag{11}$$

The quantity $E_{in}^{(2)}$ is *negative*, since $I(t)$ is negative during the second half-cycle. We can perform the integration to give:

$$E_{in}^{(2)} = -\frac{V_0 I_0 T}{\pi} + \frac{V_a I_0 T \cos\theta}{4} + \frac{I_0^2 RT}{4}. \tag{12}$$

The energy taken *out* of the CPE in the second half-cycle, is the negative of the energy put in, that is $E_{out} = -E_{in}^{(2)}$.

Thus we can define the efficiency as being $\epsilon = E_{out}/E_{in}$ which is:

$$\epsilon = \frac{V_0 I_0 T/\pi - V_a I_0 T \cos\theta/4 - I_0^2 RT/4}{V_0 I_0 T/\pi + V_a I_0 T \cos\theta/4 + I_0^2 RT/4}. \tag{13}$$

Multiplying numerator and denominator by $\pi/V_0 I_0 T$, and writing the voltage over the resistor as $V_r = I_0 R$ gives:

$$\epsilon = \frac{1 - \pi V_a \cos\theta/4V_0 - \pi V_r/4V_0}{1 + \pi V_a \cos\theta/4V_0 + \pi V_r/4V_0}. \tag{14}$$

In the limit of $\alpha \to 1$, and $R \to 0$, in other words the CPE-R equivalent circuit of the battery becoming a pure capacitor, $\cos\theta \to 0$ and $V_r \to 0$, and thus $\epsilon \to 1$ as we expect.

C. APPLYING EFFICIENCY MEASURES TO REALISTIC SITUATIONS

We emphasize that Eq. (14) applies to a sine wave current stimulus delivered to a single CPE in series with a resistor. In the limit of small currents (long charge/discharge times) any resistive effects will become small. For example, if the battery were described by a CPE in series with a resistor, the energy dissipated over the resistor would become negligible as the charge/discharge currents were reduced. Therefore, as one reduces the charge/discharge current, the final term in the numerator and denominator of Eq. (14) will become negligible.

In practice, the current can be far from sinusoidal. A realistic waveform will consist of non-harmonic periods of charge and discharge, over a range of different frequency scales. We note however that Eq. (14) gives a value of ϵ that is *independent of frequency* and depends only on (a) the phase angle $\theta = \pi\alpha/2$ and (b) the ratio of the amplitude of the voltage variation over the CPE, V_a, to the constant offset term V_0, and, if the current is large enough, (c) the ratio of the amplitude of the voltage over the resistor, V_r, to the constant offset term V_0. It is therefore reasonable to hypothesize that efficiency in realistic (non-sinusoidal) situations will depend most significantly on these dimensionless terms. In typical situations cycling of a battery is performed between prescribed voltage limits and thus V_a and V_0 will be defined independently of charging rate.

If the ratio of V_a to V_0 is rather less than one (which practically would likely be the case, *e.g.* for a battery cycled between 2.9 V and 3.3 V one can attribute V_0 = 3.1 V and V_a as 0.2 V), and the current is small so that V_r/V_0 is negligible, the binomial theorem approximates Equation (14) as:

$$\epsilon \approx 1 - \frac{\pi V_a \cos\theta}{2V_0}. \tag{15}$$

We note here that V_a is the amplitude of the assumed sine-wave and V_0 the mean voltage. We emphasize that Eq. (15) applies rigorously only for the case of a low-current sine wave stimulus, but rigorous generalization for more complicated waveforms is mathematically challenging. Nevertheless, the analysis demonstrates a relationship between cycle energy efficiency and phase differences — thus we expect in a general case a loss of cycle energy efficiency, for example due to ageing, to be accompanied by a changes in phase between V and I where the battery can be described as a CPE. Note however that if resistance R is significant, which will be the case at the higher frequencies, changes in cycle efficiency could also be attributed to changes in R.

III. EXPERIMENTAL METHODS AND ANALYSIS

We have carried out three separate experiments in order to demonstrate and confirm the relationship between efficiency to the fractional order, including in realistic battery operating conditions.

In the first experiment, we have cycled a battery using rectangular current pulses, at ever-decreasing currents. In the limit of zero current one would expect the effect of any series resistance to disappear, and we would be left with the behaviour of the CPE. Specifically, we expect that a plot of current and voltage would show hysteresis and the energy efficiency would be related to α. We confirm this is the case.

In the second experiment, we have cycled a battery over several weeks in an attempt to wear it out, using some standardized charge-discharge cycles. We extract the energy efficiency over each cycle and show it is related to the phase difference between the voltage and current signals. In particular, as the battery ages, the energy efficiency drops while the phase between voltage and current moves towards zero in the manner expected.

Finally, we have cycled another battery over several weeks with a current profile more akin to what would be expected for an electric vehicle (EV), consisting of a time of rapidly-changing, mostly negative currents (corresponding to the EV being in use), followed by a time of zero current (corresponding to the EV being parked), and then a time of constant positive current (corresponding to charging), repeated over many days with small variations. We have extracted ϵ for these cycles, and have used the Multiscale Oscillatory Dynamics Analysis (MODA) toolbox of Lancaster University [25], [26], available at github.com/luphysics/moda to identify the phase relationship between voltage and current. All experiments were performed in an air-conditioned room where ambient temperature was kept between 21.0–22.5°C. Raw data is available from the authors on request.

A. LOW FREQUENCY CYCLING

1) EXPERIMENTAL METHOD

In the first experiment we cycled a 4.8 A h, 3.7 V, $LiNiCoAlO_2$ (NCA) 21650 cell using a constant-current charge followed by a constant-current discharge using the same current as for the charge. Specifically, for a given current, we cycled the battery several times between lower and upper voltage limits of 3.0 V and 4.3 V respectively. We used currents of 5 A, 2 A, 1 A, 0.5 A, 0.2 A, 0.1 A and 0.05 A in that order, recording voltage and current as a function of time. We have evaluated the energy in and energy out for each of the cycles using Eqs. (7) and (10) respectively, and thus found the efficiency. From the efficiency in the low current limit we estimate α using Eq. (15) and compare the result to a value of α measured from an impedance spectrum obtained using the method of Dunn et al. [9], [20].

2) RESULTS

Figure 1 shows a plot of voltage against charge for the various charge-discharge currents. At the lowest currents hysteresis remains, indicating that there is energy loss. The voltage against charge plot is roughly linear over much of the voltage range, although it shows some regular fluctuation particularly at the higher voltages and a rapid increase in gradient at both ends of the voltage range. We ignore these tails in our processing, and identify a voltage range here of 3.4 V to 4.2 V for the linear portion. We also note that the charge capacity of the cell increases as current decreases, consistent with a fractional element being involved [27].

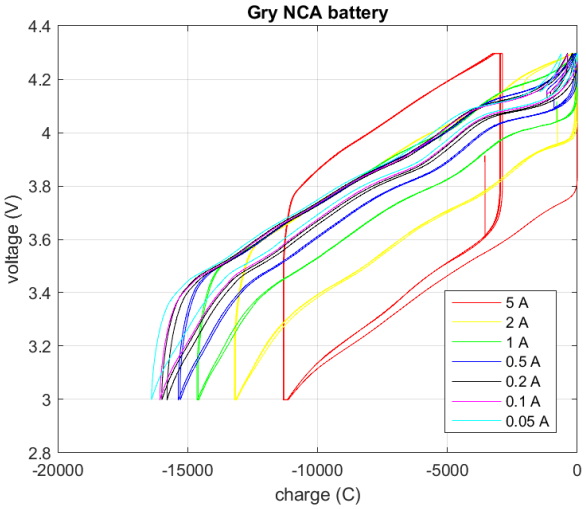

FIGURE 1. A plot showing hysteresis in the NCA battery at various constant charge-discharge currents. The currents used are given in the legend. Adapted from [27].

3) ANALYSIS

The energy in and out of the cell during the charge and discharge half-cycles, found by integrating $V(t)I(t)$ over time, are shown in Table 1. In the limit of zero current, the efficiency approaches 0.988; this is close to 1 indicating that the cell is very like a capacitor but is clearly less than 1 showing that loss mechanisms are present. Applying Eq. (15) with voltage limits of 3.4 V and 4.2 V (thus $V_0 = 3.8$ V and $V_a = 0.4$ V) with a measured efficiency of 0.988 gives us $\theta = 1.497\ rad = 85.8°$, and hence $\alpha = 0.954$.

We can verify the value for the fractional order α from the impedance spectrum. Figure 2 shows a plot of the of the impedance of the cell against frequency, on logarithmic axes, as (a) magnitude and (b) phase. Fitting a straight line to the lowest seven frequency points of (a) yields a gradient of $-0.976(8)$ and hence we infer a value of α from the impedance measurement of 0.976(8), larger but close to that estimated through the efficiency.

In the limit of zero current, we expect that any resistive loss becomes negligible. By attributing the energy loss to a CPE, we have estimated an order for the CPE of 0.954. This is slightly lower than that found by measuring an impedance spectrum.

We note that we have estimated the order of the CPE, α, using Eq. (15) which strictly only applies to a CPE-R model driven by a sine-wave stimulus, in the limit of low currents.

TABLE 1. The energy in and out of the battery, E_{in} and E_{out} respectively, and the cycle efficiency ϵ, at different charge-discharge currents during the battery cycling of Fig. 1.

Current (A)	E_{in} (kJ)	E_{out} (kJ)	ϵ
5	34.14	28.54	0.836
2	51.86	47.64	0.919
1	57.10	54.39	0.953
0.5	58.97	57.40	0.973
0.2	60.77	60.04	0.988
0.1	61.78	61.04	0.988
0.05	62.89	62.13	0.988

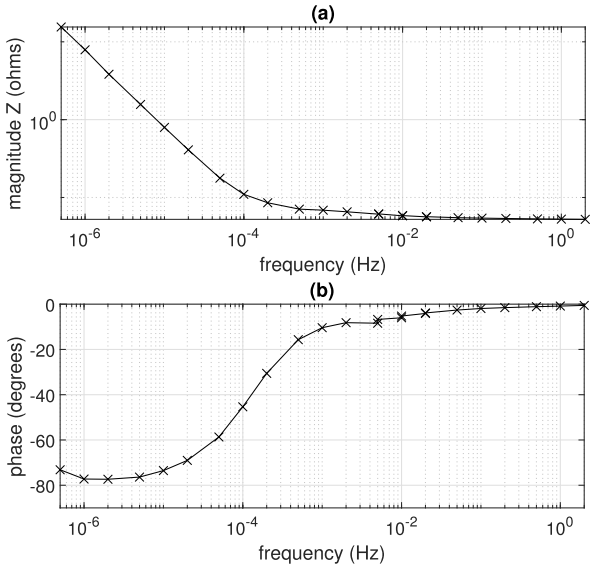

FIGURE 2. The impedance spectrum of the NCA battery, presented as (a) magnitude and (b) phase.

The experimental cycling has been carried out, for practical reasons, with a rectangular stimulus and so the calculated value of α should be seen as an estimate only. Nevertheless, it is encouraging that the value estimated from energy efficiency and the value from the impedance spectrum, two very different methods, are roughly in agreement.

B. STEREOTYPED CYCLES

The second experiment consists of ageing a battery by performing repetitive charge-discharge cycles. The cycle efficiency is monitored and related to phase difference between voltage and current. A repetitive but non-sinusoidal cycle can be analyzed using Hilbert Transforms in order to extract the phase difference between voltage and current. For example, Hilbert Transforms have been used in the context of batteries to validate electrochemical impedance spectrum measurements [28] and to detect disturbances in power systems via phase changes [29].

1) EXPERIMENTAL METHOD

A 250 mA h INR Nickel-Cobalt cell was cycled in the laboratory using sets of 30 charge-discharge cycles, each of a particular form of constant-current-constant-voltage (CC-CV) cycling. In CC-CV, a constant charging current I_{ch} is applied to bring the voltage to a specified upper voltage V_h.

TABLE 2. The different cycle types used, defined in terms of the charge current I_{ch}, discharge current I_{dis}, upper voltage V_h, lower voltage V_l, lower bound on charging current during the constant voltage phase I_{low}, and time spent at zero current t_0.

Type	I_{ch} (A)	I_{dis} (A)	$V_{\rm h}$ (V)	$V_{\rm l}$ (V)	I_{low} (A)	t_0 (s)
Cyc	0.16	-0.16	4.3	3.3	0.03	600
Shal	0.16	-0.16	4.0	3.3	0.03	600
Float	0.16	-0.16	4.3	3.3	0.003	600
Asym	0.04	-0.16	4.3	3.3	0.01	600
Mysa	0.16	-0.04	4.3	3.3	0.03	600
Slow	0.08	-0.08	4.3	3.3	0.03	600

TABLE 3. The sequence of CC-CV cycling, in sets of 30 cycles.

Sequence	Cycle set	Cycle type	Cumulative cycles
1	1	Cyc	310
2		Shal	340
3		Float	370
4	2	Cyc	400
		Impedance measurement	
5	3	Cyc	430
6		Asym	460
7		Mysa	490
8	4	Cyc	520
		Impedance measurement	
9		Slow	550
10	5	Cyc	580
11		Shal	610
12		Float	640
13		Slow	670
14		Asym	700
15		Mysa	730
16	6	Cyc	760

Then the battery is held at this voltage by reducing the current, until the current decays to a specified lower value I_{low}. The battery is then discharged with a constant discharge current I_{dis}, until its voltage reaches a specified lower bound V_l. Then a period of zero current is applied for a defined time period t_0. The cycle is then repeated. Six different variations of the CC-CV cycling were used, as outlined in Table. 2 and applied in the sequence shown in Table. 3. The forms of cycle differed in terms of maximum and minimum voltage, charge and discharge currents, and the lower current bound to end the constant voltage phase. A standard cycle, denoted here by 'Cyc' was returned to several times in order to allow a direct evaluation of ageing effects. The current characteristics of a standard cycle, along with a voltage response, are shown in Fig. 3. Before this experiment, the cell had already been cycled approximately 280 times in various ways. At two points in the experiment the cycling was interrupted to perform a measurement of impedance on the cell [9]. The experiment took nine weeks total duration.

We discarded the first three cycles of each set of 30 cycles to allow the voltage signals to stabilize. Cycle efficiency ϵ was evaluated for each cycle, and averaged over the remaining 27 cycles in each set. We also, for the time period spanned by the final 27 cycles, calculated the Hilbert Transforms of current and voltage using Matlab. The phase $\phi_I(t)$ of the current waveform was then extracted as:

$$\phi_I[I(t)](t) = \tan^{-1}\left(\frac{H[I(t)](t)}{I(t)}\right), \tag{16}$$

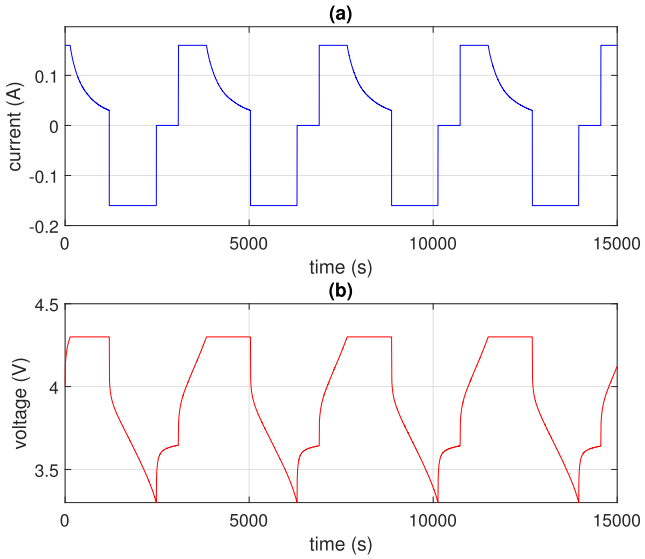

FIGURE 3. The current (top, blue) and voltage response (bottom, red) for a few standard 'Cyc' cycles.

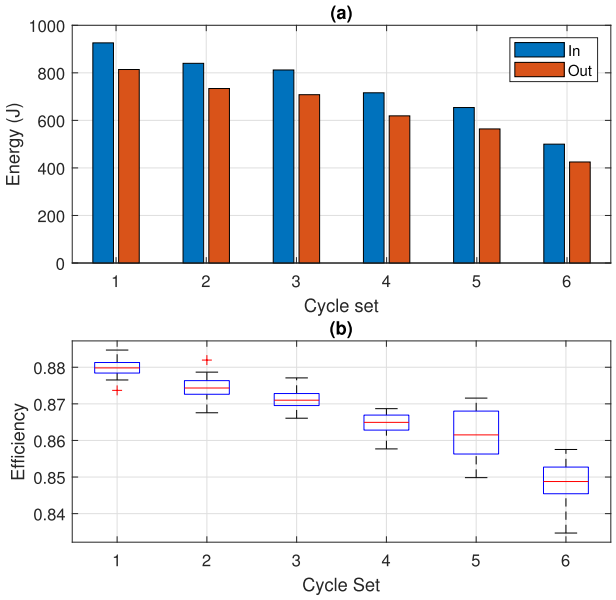

FIGURE 4. (a) The mean energy in and out of the battery during each of the six sets of standard cycles (excluding the first 3 cycles in each set). (b) The distribution of the cycle efficiencies for each set. The red line shows the median; the boxes show lower quartile and upper quartile; the extending lines showing the range of the data. Outliers are marked with red crosses. Note how *both* the energy capacity and the efficiency drop with age.

where $H[I(t)](t)$ denotes the Hilbert transform of $I(t)$ and the inverse tangent is evaluated using the signs of the numerator and denominator using the 'atan2' function in order to be continuous from $-\pi$ to π. The phase $\phi_V(t)$ was similarly extracted for the voltage waveform $V(t)$. The phase angle $\phi(t) = \phi_V(t) - \phi_I(t)$ was found, representing an instantaneous phase difference between $V(t)$ and $I(t)$. The mean phase difference over the final 27 cycles of each 'Cyc' set was calculated.

2) RESULTS

In Fig. 4(a) we show, for each of the six sets of 30 'Cyc' cycles, the mean energy into the cell during the charge periods (averaged across the final 27 cycles), and the mean energy out of the cell during the discharge periods (similarly averaged over the final 27 cycles). In Fig. 4(b) we show the distribution of cycle efficiencies for the six 'Cyc' sets.

Figure 5 shows the distribution of phase differences between V and I over each of the six 'Cyc' sets, as found through the Hilbert transform. The second and subsequent sets are displaced downwards by 0.1 on the y-axis for clarity. It is immediately evident that the phase distribution moves towards zero as the battery ages.

3) ANALYSIS

Figures 4 and 5 show that as the battery ages, (i) the cycle efficiency drops and (ii) the distribution of phase differences becomes less negative. These changes are summarized in Table. 4. Furthermore, we have used Eq. (15) with $V_0 = 3.8$ V and $V_a = 0.5$ V, in order to estimate the phase angle θ from the measured efficiencies; these are shown in Tab. 4 as θ_{est}. These can be compared with the mean measured phase differences as found via the Hilbert transforms, indicated as θ_H.

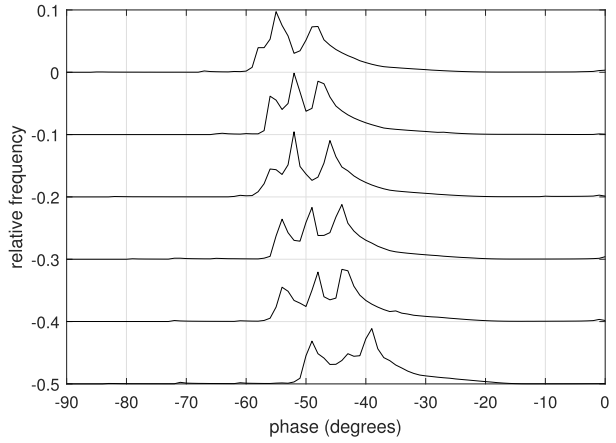

FIGURE 5. The phase between voltage and current as distributed over each of the six sets of cycles, as calculated using Hilbert transforms. The first set is shown in the top trace; the second and subsequent sets are displaced downwards by 0.1 for clarity.

TABLE 4. For each of the six standard cycle sets, we show the cumulative number of times the battery has been cycled by the end of the set, the mean measured efficiency ϵ, the phase difference estimated from the measured efficiency θ_{est}, and the mean measured phase difference from the Hilbert transform, θ_H.

Set	Cumulative cycles	$\epsilon(\%)$	ϕ_{est} (rad)	ϕ_{H} (rad)
1	310	87.9(5)	−0.945	−0.837
2	400	87.5(6)	−0.921	−0.816
3	430	87.2(5)	−0.904	−0.794
4	520	86.5(6)	−0.860	−0.771
5	580	86.2(13)	−0.840	−0.754
6	760	84.8(13)	−0.745	−0.681

We note that the measured efficiency drops as the battery ages and as a consequence θ_{est} moves closer to zero. Additionally, the measured phase θ_H also moves towards

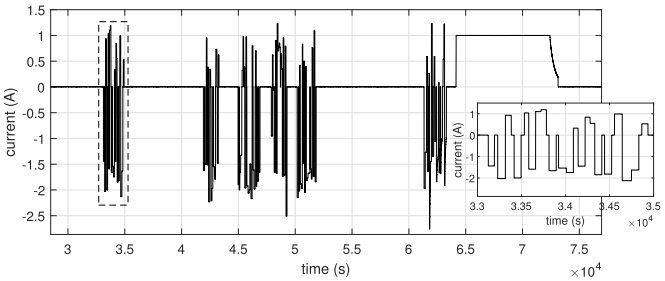

FIGURE 6. A section of the current input to the cell. The inset is a close-up of one of the period of activity indicated by the dashed box.

zero. The ratio of the two, ϕ_{est}/ϕ_H, is roughly constant across the six sets, ranging from 0.87 (for set 5) to 0.91 (for set 6). We do not expect them to be exactly the same since Eq. (15) applies rigorously only for a sine wave stimulus, but nevertheless the two measures are similar. These result also suggest that a move in order of the CPE is responsible for a significant part of the ageing-related drop in efficiency.

C. SYNTHETIC DRIVE PATTERN FOR ELECTRIC CAR

The previous two examples have used simple, repeated current waveforms. For the third situation, we now consider more complicated current waveforms, more akin to the currents that would be experienced by an EV battery, and have used wavelet analysis in order to identify phase differences. An advantage of a complicated waveform is that it contains frequency components across the spectrum and can help distinguish between efficiency changes due to changes in α and those due to changes in R.

1) EXPERIMENTAL METHOD

A synthetic current profile $I(t)$, lasting around three months, was created using the method described below. The profile is designed to mimic electric vehicle activity. It shows several hours of constant-current charging (representing a vehicle being charged overnight), followed by a period of a few hours inactivity (when the charging is complete but the vehicle is not in use), then about an hour of charge/discharge activity at high currents (corresponding to a morning commute), then several hours of inactivity followed by about an hour of charge/discharge activity at high currents (corresponding to an evening commute). Randomness is included so that the function is not periodic. A section of the profile is shown in Fig. 6.

Before the profile was applied, the impedance spectrum of an UBCO 3.2 A h 3.6 V 18650 INR $LiNi_xMn_yCo_{1-x-y}O_2$ cell was measured using the method of [9]. The synthetic profile was then applied to the cell using a Hewlett Packard 66332A precision current-voltage supply. The actual current applied and the voltage of the battery were monitored continuously. Data were recorded with a sample rate of 8.6 Hz.

2) RESULTS

Since the cycles are not periodic, efficiency has been defined over a pseudo-cycle. Specifically, we have identified a pseudo-cycle as starting at a time when the charge (time-integrated current) drops to 50% of its range (*i.e.* is at 50% of the way from its minimum to its maximum), and then ends after it has risen to at least 90% of its range and then dropped again to 50%. Over each pseudo-cycle we have evaluated the energy supplied to the battery E_{in} by integrating $I(t)V(t)$ where I is positive, and evaluated the energy taken out E_{out} by integrating $I(t)V(t)$ where current is negative, and constructing the efficiency $\epsilon = E_{out}/E_{in}$.

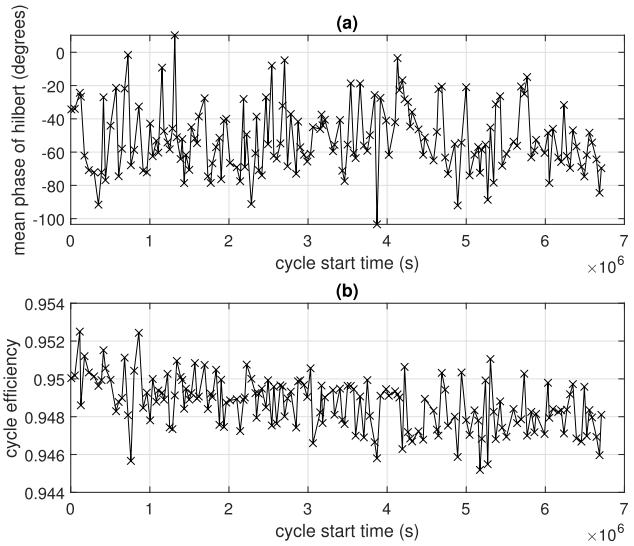

FIGURE 7. (a) The average phase difference between *V* and *I* as calculated via a Hilbert Transform (Sec. III-B) over each pseudocycle. (b) The energy efficiency for each pseudocycle.

Efficiency has been evaluated for each pseudo-cycle. Figure 7(b) shows the efficiency of each successive pseudo-cycle.

3) ANALYSIS

The results of the Hilbert Transform method of Sec. III-B to find the mean phase difference between $V(t)$ and $I(t)$ over a pseudocycle are shown in Fig. 7(a). The results fluctuate considerably because of the many frequency components present in the signal. This is in contrast to the regular cycling results in Sec. III-B where the periodicity of the cycle is much better defined. The cycle efficiencies also fluctuate considerably for similar reasons, Fig. 7(b), but in this case there is a clear trend to reduced efficiencies as the battery ages, with efficiency ϵ dropping from about 0.950 to 0.948. This is a relative increase in $1-\epsilon$ of 4%.

To proceed we need to use a method appropriate for complicated waveform shapes and for waveforms that are not strictly repeating. We have analyzed the data with a wavelet-based approach, using the Multiscale Oscillatory Dynamics Application (MODA) toolbox produced by Lancaster University github.com/luphysics/moda [25], [26]. The time-series data $V(t)$ and $I(t)$ were split into six equal sections, each 17 days long. To ensure file sizes were sufficiently small for analysis on an Intel i5-1145G7 2.6 GHz processor with 16.0 GB RAM, both $V(t)$ and $I(t)$ were downsampled by a

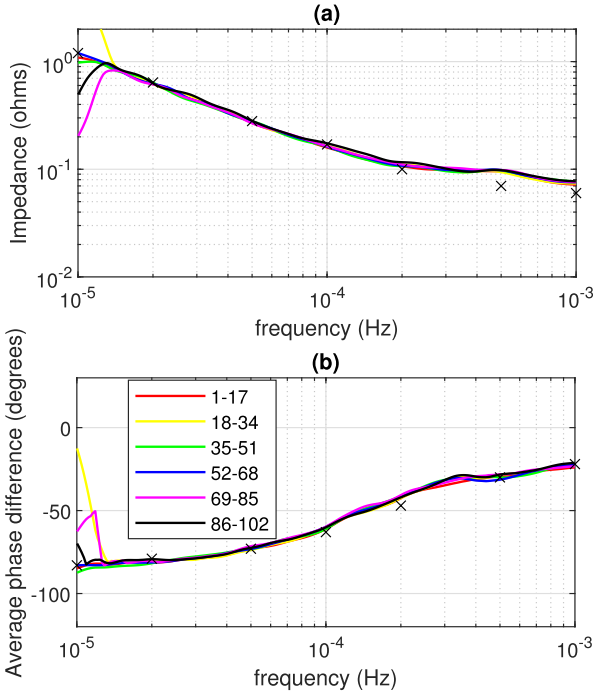

FIGURE 8. (a) The magnitude $\hat{Z}(f)$ and (b) the phase $\phi(f)$ of the wavelet-constructed impedance spectrum at low frequencies, averaged over six seventeen-day sections. The legend shows the start and end day for each section. The black crosses show the results from the impedance measurement at the start of the experiment.

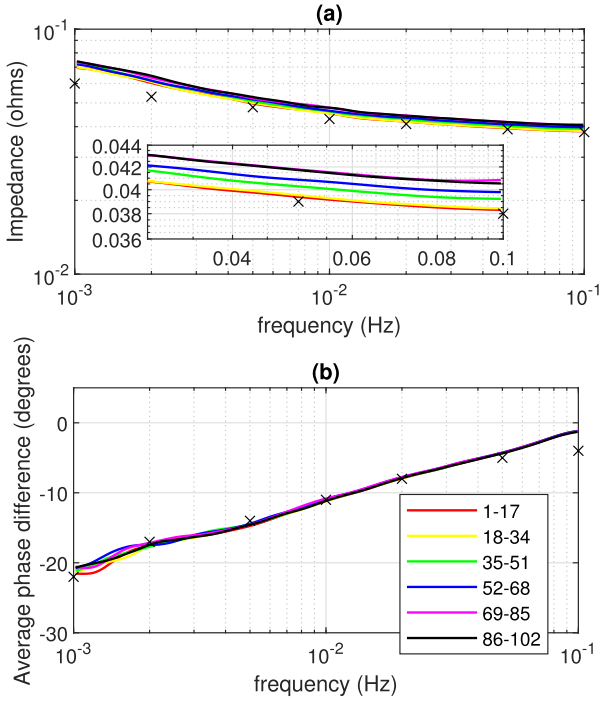

FIGURE 9. (a) The magnitude $\hat{Z}(f)$ and (b) the phase $\phi(f)$ of the wavelet-constructed impedance spectrum at high frequencies, averaged over six seventeen-day sections. The inset on (a) shows the highest frequencies on a finer scale, indicating a small but discernable rise in impedance magnitude as the battery ages. The legend shows the start and end day for each section. The black crosses show the results from the impedance measurement at the start of the experiment.

factor 40, to 0.215 Hz. A wavelet transform using a lognorm wavelet was applied to both voltage and current waveforms in each section, to give a spectrogram of voltage $\tilde{V}(f,t)$ and current $\tilde{I}(f,t)$ against both frequency f and time t in that section. Frequency ranges of 10^{-5} Hz to 10^{-3} Hz were initially used, to emphasize the low-frequency region where the CPE impedance is likely to dominate the resistive impedance. Impedances were constructed using $\tilde{Z} = \tilde{V}/\tilde{I}$ (note these are complex quantities) from which an impedance magnitude $|\tilde{Z}(f,t)|$ and phase $\arg[\tilde{Z}(f,t)]$ constructed. The magnitude and phase were both averaged over time t to give a spectrum for magnitude $\hat{Z}(f) = \left\langle |\tilde{Z}(f,t)| \right\rangle_t$ and phase $\phi(f) = \left\langle arg[\tilde{Z}(f,t)] \right\rangle_t$ for each section. The magnitudes and phases are plotted in Fig. 8. Also shown is the result of the impedance measurement at the start of the experiment. The higher frequency range was also examined — the analysis was repeated but this time for a frequency range of 10^{-3} Hz to 10^{-1} Hz; results are shown in Fig. 9.

First, we note that the impedance spectra reconstructed from the wavelet analysis, in particular day 1–17, are very similar to the impedance spectrum measured directly at the start of the experiment, providing some confidence in the wavelet analysis. Figures 8 shows no obvious differences in the impedance spectra for the 17-day periods considered at frequencies below about 10^{-3} Hz. The variation in $\hat{Z}$ at the very lowest frequencies is likely to be uncertainty due to having only a few periods in the datastream at the lowest frequencies, and is ignored. In the 10^{-5} Hz to 10^{-4} Hz region, the impedance shows CPE-like behaviour, having a constant slope on the $\hat{Z}(f)$ graph and roughly constant phase $\phi(f)$. In contrast to the results of Sec. III-B, there is no indication of a change in phase of the impedance despite Fig. 7(b) showing a small but clear reduction in the energy efficiency. For this particular cell under the conditions tested, the underlying changes responsible for the loss in efficiency with ageing do not appear to be a result of a change in the properties of this CPE.

However, the impedance spectrum at higher frequencies, Fig. 9, shows a clear gain in impedance magnitude as the cell ages. At 10^{-1} Hz, the magnitude of impedance rises from about 38.25 mΩ to about 41.00 mΩ from the first and second seventeen-day range to the fifth and sixth, an increase of 2.8% In this spectral region, the impedance is resistor-like as evidenced by the phase difference close to zero. The 2.8% increase in resistance is roughly commensurate with the experimental change in $1-\epsilon$ of about 4% from Fig. 7(b); we would expect the two to be linearly related through Eq. (14).

The implication is that under the tested conditions, this cell demonstrates ageing through increases in its internal resistance R, as opposed to changes in its CPE characteristics.

IV. DISCUSSION

We have used time-series analysis of voltage and current data to probe the changes in batteries as they age. We have assumed that a battery can be described through a CPE-R

equivalent circuit model. For the special case of a sine wave stimulation, we have shown theoretically that cycle energy efficiency is related to (i) the order of the CPE, α, which manifests through a phase difference between voltage and current, and (ii) the resistance, R.

The theory has been tested for three cases. In Sec. III-A we have used different charge and discharge currents to cycle a battery, and shown that the order of the CPE element predicted by applying the theory to measured cycle efficiency matches that independently measured through Electrochemical Impedance Spectroscopy.

For the case of regular repetitive cycling of a battery in Sec. III-B, the cycle energy efficiency has been measured as the battery ages and the theory applied to predict a move in phase difference towards zero. Analysis of the V and I time-series with Hilbert Transforms have been able to provide another measure of phase difference which is in broad agreement with that predicted from the efficiency measurements, as shown in Table 1.

In the third experiment in Sec. III-C, irregular cycling with a wide range of frequency components has been applied for around 100 days. The analysis in this case is more complicated, since (i) it is difficult to define a cycle, and (ii) the use of a Hilbert Transform is dubious. To identify the change of energy efficiency with ageing, we have needed to use pseudo-cycles — with start and end points being based on returning a battery to a defined state of charge following a significant discharge. This has introduced considerable variation in the results, but cycle energy efficiency still shows a clear downward trend, as shown in Fig. 7(b). For complicated signal patterns, wavelet analysis, for example used to detect disturbances in electrical power systems [29], offers a wave forward. We have used wavelet analysis with V and I time-series to identify changes in phase and impedance with ageing. For the battery tested, the ageing manifests as a rise in impedance at high frequency rather than a change in phase difference.

An implication is that the two batteries, of Secs III-B and III-C, are likely ageing in different ways. While both are reducing in energy cycle efficiency, the underlying mechanisms appear to be different. We emphasize that our theory in Sec. II, and in particular the relationship between cycle energy efficiency and phase of the CPE, Eq. (15), has been derived using only a sine wave stimulus. Our application of it to more complicated signals is therefore not rigorous, but is still insightful. The development of more general theory is mathematically challenging. While we have aimed to keep ambient temperature constant, we finally note that even fluctuations of the size of 1.5°C, which are experienced, may be sufficient to make measurable differences to efficiency and may partly be the cause for the fluctuations in Fig. 7.

V. CONCLUSION

By considering phases between voltage and current traces, we have demonstrated that the energy efficiency of a cell relates to the order of a CPE element in its equivalent circuit. In the case of the measured Nickel-Cobalt cell, the drop of efficiency of the cell as it ages can be attributed to a change in the phase difference between voltage and current. Moreover, the analysis has been performed in the time domain, rather than requiring frequency domain measurements such as EIS. The phase-efficiency relationship opens up the possibility of monitoring the state-of-health of a battery from time domain data acquired while a battery is *in situ* in its normal operation.

ACKNOWLEDGMENT

The authors would like to thank Aneta Stefanovska and Juliane Bjerkan for valuable discussion regarding the MODA toolbox and wavelet analysis.

REFERENCES

[1] V. Pop, J. B. Henk, D. Danilov, P. P. L. Regtien, and P. H. L. Notten, *BatteryManagement Systems: Accurate State-of-Charge Indication for Battery-Powered Applications*. Cham, Switzerland: Springer, 2008.

[2] M. Huotari, S. Arora, A. Malhi, and K. Främling, "Comparing seven methods for state-of-health time series prediction for the lithium-ion battery packs of forklifts," *Appl. Soft Comput.*, vol. 111, Nov. 2021, Art. no. 107670.

[3] J. A. Osara, O. A. Ezekoye, K. C. Marr, and M. D. Bryant, "A methodology for analyzing aging and performance of lithium-ion batteries: Consistent cycling application," *J. Energy Storage*, vol. 42, Oct. 2021, Art. no. 103119.

[4] C. Pastor-Fernández, T. F. Yu, W. D. Widanage, and J. Marco, "Critical review of non-invasive diagnosis techniques for quantification of degradation modes in lithium-ion batteries," *Renew. Sustain. Energy Rev.*, vol. 109, pp. 138–159, Jul. 2019.

[5] C. Hendricks, N. Williard, S. Mathew, and M. Pecht, "A failure modes, mechanisms, and effects analysis (FMMEA) of lithium-ion batteries," *J. Power Sour.*, vol. 297, pp. 113–120, Nov. 2015.

[6] Y. Fu, J. Xu, M. Shi, and X. Mei, "A fast impedance calculation-based battery state-of-health estimation method," *IEEE Trans. Ind. Electron.*, vol. 69, no. 7, pp. 7019–7028, Jul. 2022.

[7] T. Murariu and C. Morari, "Time-dependent analysis of the state-of-health for lead-acid batteries: An EIS study," *J. Energy Storage*, vol. 21, pp. 87–93, Feb. 2019. [Online]. Available: https://www.sciencedirect.com/science/article/pii/S2352152X18303712

[8] V. Farrow, *Characterisation of Rechargeable Batteries: Addressing Fractional Ultralow-frequency Devices: Master of Engineering*. Hamilton, New Zealand: University of Waikato, 2020.

[9] C. Dunn, J. B. Scott, and V. Farrow. (2019). *A Multitone Current Sink for Measuring Impedance of In-Use Batteries*. Univ. Waikato, Hamilton, New Zealand. [Online]. Available: https://hdl.handle.net/10289/13149

[10] E. Locorotondo, V. Cultrera, L. Pugi, L. Berzi, M. Pierini, and G. Lutzemberger, "Development of a battery real-time state of health diagnosis based on fast impedance measurements," *J. Energy Storage*, vol. 38, Jun. 2021, Art. no. 102566.

[11] E. Poihipi, J. Scott, and C. Dunn, "Distinguishability of battery equivalent-circuit models containing CPEs: Updating the work of Berthier, Diard, & Michel," *J. Electroanal. Chem.*, vol. 911, Apr. 2022, Art. no. 116201.

[12] U. Westerhoff, K. Kurbach, F. Lienesch, and M. Kurrat, "Analysis of lithium-ion battery models based on electrochemical impedance spectroscopy," *Energy Technol.*, vol. 4, no. 12, pp. 1620–1630, Dec. 2016.

[13] F. Berthier, J.-P. Diard, and R. Michel, "Distinguishability of equivalent circuits containing CPEs," *J. Electroanal. Chem.*, vol. 510, nos. 1–2, pp. 1–11, Sep. 2001.

[14] P. Mauracher and E. Karden, "Dynamic modelling of lead/acid batteries using impedance spectroscopy for parameter identification," *J. Power Sour.*, vol. 67, nos. 1–2, pp. 69–84, Jul. 1997.

[15] M. Messing, T. Shoa, and S. Habibi, "Estimating battery state of health using electrochemical impedance spectroscopy and the relaxation effect," *J. Energy Storage*, vol. 43, Nov. 2021, Art. no. 103210. [Online]. Available: https://www.sciencedirect.com/science/article/pii/S2352152X21009087

[16] O. I. M. Stefan, G. Samko, and A. A. Kilbas, *Fractional Integrals and Derivatives: Theory and Applications*. Boca Raton, FL, USA: CRC Press, 1993.
[17] M. E. Fouda, A. S. Elwakil, A. G. Radwan, and A. Allagui, "Power and energy analysis of fractional-order electrical energy storage devices," *Energy*, vol. 111, pp. 785–792, Sep. 2016. [Online]. Available: https://www.sciencedirect.com/science/article/pii/S036054421630723X
[18] J. E. B. Randles, "Kinetics of rapid electrode reactions," *Discuss. Faraday Soc.*, vol. 1, p. 11, 1947.
[19] T. J. Freeborn, B. Maundy, and A. S. Elwakil, "Fractional-order models of supercapacitors, batteries and fuel cells: A survey," *Mater. Renew. Sustain. Energy*, vol. 4, no. 3, p. 9, Sep. 2015.
[20] C. Dunn and J. Scott, "Achieving reliable and repeatable electrochemical impedance spectroscopy of rechargeable batteries at extra-low frequencies," *IEEE Trans. Instrum. Meas.*, vol. 71, pp. 1–8, 2022.
[21] R. Hasan and J. Scott, "Extending Randles's battery model to predict impedance, charge–voltage, and runtime characteristics," *IEEE Access*, vol. 8, pp. 85321–85328, 2020.
[22] J. Scott and R. Hasan, "New results for battery impedance at very low frequencies," *IEEE Access*, vol. 7, pp. 106925–106930, 2019.
[23] T. T. Hartley, J.-C. Trigeassou, C. F. Lorenzo, and N. Maamri, "Energy storage and loss in fractional-order systems," *J. Comput. Nonlinear Dyn.*, vol. 10, no. 6, Nov. 2015, Art. no. 061006.
[24] T. T. Hartley, R. J. Veillette, J. L. Adams, and C. F. Lorenzo, "Energy storage and loss in fractional-order circuit elements," *IET Circuits, Devices Syst.*, vol. 9, no. 3, pp. 227–235, May 2015.
[25] P. Clemson, G. Lancaster, and A. Stefanovska, "Reconstructing time-dependent dynamics," *Proc. IEEE*, vol. 104, no. 2, pp. 223–241, Feb. 2016.
[26] P. T. Clemson and A. Stefanovska, "Discerning non-autonomous dynamics," *Phys. Rep.*, vol. 542, no. 4, pp. 297–368, Sep. 2014.
[27] M. T. Wilson, C. Dunn, V. Farrow, M. Mucalo, and J. B. Scott, "Measuring electrical properties of batteries at ultra-long timescales," *NCLSI Measure J. Meas. Sci.*, vol. 15, no. 2, pp. 12–16, 2023.
[28] W. Ehm, H. Göhr, R. Kaus, B. Röseler, and C. A. Schiller, "The evaluation of electrochemical impedance spectra using a modified logarithmic Hilbert transform," *Models Chem.*, vol. 137, nos. 2–3, pp. 145–157, Jan. 2000.
[29] V. Sharma and L. Gidwani, "Recognition of disturbances in hybrid power system interfaced with battery energy storage system using combined features of stockwell transform and Hilbert transform," *AIMS Energy*, vol. 7, no. 5, pp. 671–687, 2019.

MARCUS T. WILSON received the degree (Hons.) in physics and theoretical physics from the University of Cambridge, in 1992, and the Ph.D. degree in theoretical solid state physics from the University of Bristol, in 1995. He is currently a Senior Lecturer in physics and chemistry with the Te Aka Mātuatua—School of Science, The University of Waikato. He has worked in numerical modeling of physics processes in industry in the U.K. and in academia in New Zealand, since 2004. His research interests include the electric properties and dynamics of the human brain, transcranial magnetic stimulation, and more recently batteries.

CHRISTOPHER J. DUNN (Student Member, IEEE) received the bachelor's degree from Portsmouth School of Pharmacy, Portsmouth, U.K., in 1985, the master's degree from Queens University Belfast, Belfast, U.K., in 1993, and the Graduate Diploma degree in electronics from The University of Waikato, Hamilton, New Zealand, in 2019, where he is currently pursuing the Ph.D. degree. His background is originally in the pharmaceutical sciences, with past specialization in medicinal chemistry (notably quantitative structureactivity relationships and pharmaceutical analysis), pharmaceutical technology, small-scale and aseptic/sterile manufacturing, and quality assurance. He has also worked in scientific communications and in asset management/inspection and line structure engineering for the power supply industry.

VANCE FARROW received the degree (Hons.) in electronic engineering from The University of Waikato, in 2018, and the M.E. degree in prediction of battery life using small-signal measurements, in 2020. He is currently pursuing the Ph.D. degree with The University of Waikato, working on battery management systems using fractional-derivative models and extremely-low frequency electrochemical impedance spectroscopy measurements. In 2018, he worked with Nyriad, Cambridge, New Zealand.

MICHAEL J. CREE (Senior Member, IEEE) received the B.Sc. degree (Hons.) in physics and the Ph.D. degree in electrical and electronic engineering from the University of Canterbury, Christchurch, New Zealand, in 1990 and 1994, respectively. He is currently an Associate Professor in electrical and electronic engineering with The University of Waikato, Hamilton, New Zealand. His research interests include medical imaging, computer vision, the time-of-flight range imaging, and more recently, the equivalent circuit modeling of batteries.

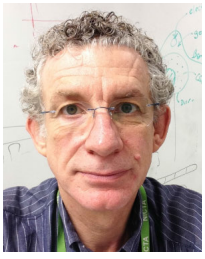

JONATHAN B. SCOTT (Life Senior Member, IEEE) is currently the Foundation Professor of Electronic Engineering with The University of Waikato, New Zealand. From 1998 to 2006, he was with the Hewlett-Packard and Agilent Technologies Microwave Technology Center, Santa Rosa, CA, USA, where he was responsible for advanced measurement systems operating from DC to millimetre-wave. In 1997 and 1998, he was a Chief Engineer with RF Technology, Sydney. He was with the Department of Electrical Engineering, The University of Sydney, prior to 1997. He holds five degrees, he has authored over 150 refereed publications, several book chapters and a textbook, and he holds a dozen patents, several covering active products. His educational interests include threshold concepts and their application, particularly across engineering disciplines. His research interests include characterization and modeling, particularly applied to implantable electrodes, batteries, semiconductor devices, and acoustic systems.

Appendix D

Co-Authorship Forms

THE UNIVERSITY OF WAIKATO
Te Whare Wānanga o Waikato

Postgraduate Studies Office
Student and Academic Services Division
Wahanga Ratonga Matauranga Akonga
The University of Waikato
Private Bag 3105
Hamilton 3240, New Zealand
Phone +64 7 838 4439
Website: http://www.waikato.ac.nz/sasd/postgraduate/

Co-Authorship Form

This form is to accompany the submission of any PhD that contains research reported in published or unpublished co-authored work. **Please include one copy of this form for each co-authored work.** Completed forms should be included in your appendices for all the copies of your thesis submitted for examination and library deposit (including digital deposit).

Please indicate the chapter/section/pages of this thesis that are extracted from a co-authored work and give the title and publication details or details of submission of the co-authored work. Chapter 3, Achieving Reliable and Repeatable Electrochemical Impedance Spectroscopy of Rechargeable Batteries at Extra-Low Frequencies, pp46-53 Dunn C, Scott J. Achieving Reliable and Repeatable Electrochemical Impedance Spectroscopy of Rechargeable Batteries at Extra-Low Frequencies. IEEE Trans Instrum Meas 2022;71:1-8	
Nature of contribution by PhD candidate	Conceptualization; Methodology; Software; Formal analysis; Investigation; Writing – Original Draft; Writing – Review & Editing; Visualization
Extent of contribution by PhD candidate (%)	90%

CO-AUTHORS

Name	Nature of Contribution
Jonathan Scott	Conceptualization; Supervision; Methodology; Software; Resources; Writing – Review and Editing

Certification by Co-Authors

The undersigned hereby certify that:

- the above statement correctly reflects the nature and extent of the PhD candidate's contribution to this work, and the nature of the contribution of each of the co-authors; and

Name	Signature	Date
Jonathan Scott	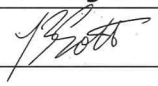	28 November 2023

THE UNIVERSITY OF WAIKATO
Te Whare Wānanga o Waikato

Co-Authorship Form

Postgraduate Studies Office
Student and Academic Services Division
Wahanga Ratonga Matauranga Akonga
The University of Waikato
Private Bag 3105
Hamilton 3240, New Zealand
Phone +64 7 838 4439
Website: http://www.waikato.ac.nz/sasd/postgraduate/

This form is to accompany the submission of any PhD that contains research reported in published or unpublished co-authored work. **Please include one copy of this form for each co-authored work**. Completed forms should be included in your appendices for all the copies of your thesis submitted for examination and library deposit (including digital deposit).

Please indicate the chapter/section/pages of this thesis that are extracted from a co-authored work and give the title and publication details or details of submission of the co-authored work.	Chapter 4, Incremental Capacity and Voltammetry of Batteries, and Implications for Electrochemical Impedance Spectroscopy, pp62-69 Dunn C, Scott J, Wilson M, Mucalo M, Cree M. Incremental Capacity and Voltammetry of Batteries, and Implications for Electrochemical Impedance Spectroscopy (as originally submitted to IEEE Trans Instrum Meas)
Nature of contribution by PhD candidate	Conceptualization; Methodology; Software; Formal analysis; Investigation; Writing – Original Draft; Writing – Review & Editing; Visualization
Extent of contribution by PhD candidate (%)	80%

CO-AUTHORS

Name	Nature of Contribution
Jonathan Scott	Conceptualization; Supervision; Methodology; Software; Resources; Writing – Review & Editing
Marcus Wilson	Supervision; Writing – Review & Editing
Michael Mucalo	Conceptualization; Writing – Review & Editing
Michael Cree	Conceptualization; Writing – Review & Editing

Certification by Co-Authors

The undersigned hereby certify that:

- the above statement correctly reflects the nature and extent of the PhD candidate's contribution to this work, and the nature of the contribution of each of the co-authors; and

Name	Signature	Date
Jonathan Scott		28 November 2023
Marcus Wilson		28 November 2023
Michael Mucalo	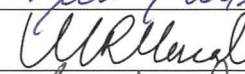	28 November 2023
Michael Cree	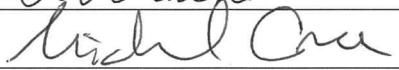	28 November 2023

THE UNIVERSITY OF WAIKATO
Te Whare Wānanga o Waikato

Co-Authorship Form

Postgraduate Studies Office
Student and Academic Services Division
Wahanga Ratonga Matauranga Akonga
The University of Waikato
Private Bag 3105
Hamilton 3240, New Zealand
Phone +64 7 838 4439
Website: http://www.waikato.ac.nz/sasd/postgraduate/

This form is to accompany the submission of any PhD that contains research reported in published or unpublished co-authored work. **Please include one copy of this form for each co-authored work.** Completed forms should be included in your appendices for all the copies of your thesis submitted for examination and library deposit (including digital deposit).

Please indicate the chapter/section/pages of this thesis that are extracted from a co-authored work and give the title and publication details or details of submission of the co-authored work. Chapter 5, New Theory and Efficient Algorithm for Tracking Lithium Battery State of Health, pp87-96 Dunn C, Scott J, Wilson M, Farrow V. New Theory and Efficient Algorithm for Tracking Lithium Battery State of Health. Manuscript as originally drafted for IEEE Trans Instrum Meas	
Nature of contribution by PhD candidate	Conceptualization; Methodology; Software; Formal analysis; Investigation; Writing – Original Draft; Writing – Review & Editing; Visualization
Extent of contribution by PhD candidate (%)	65%

CO-AUTHORS

Name	Nature of Contribution
Jonathan Scott	Conceptualization; Supervision; Methodology; Software; Resources; Writing – Review & Editing
Marcus Wilson	Conceptualization; Supervision; Methodology; Writing – Review & Editing
Vance Farrow	Resources; Methodology

Certification by Co-Authors

The undersigned hereby certify that:

- the above statement correctly reflects the nature and extent of the PhD candidate's contribution to this work, and the nature of the contribution of each of the co-authors; and

Name	Signature	Date
Jonathan Scott		28 November 2023
Marcus Wilson		28 November 2023
Vance Farrow		28 November 2023

THE UNIVERSITY OF WAIKATO
Te Whare Wānanga o Waikato

Co-Authorship Form

Postgraduate Studies Office
Student and Academic Services Division
Wahanga Ratonga Matauranga Akonga
The University of Waikato
Private Bag 3105
Hamilton 3240, New Zealand
Phone +64 7 838 4439
Website: http://www.waikato.ac.nz/sasd/postgraduate/

This form is to accompany the submission of any PhD that contains research reported in published or unpublished co-authored work. **Please include one copy of this form for each co-authored work.** Completed forms should be included in your appendices for all the copies of your thesis submitted for examination and library deposit (including digital deposit).

Please indicate the chapter/section/pages of this thesis that are extracted from a co-authored work and give the title and publication details or details of submission of the co-authored work. Appendix A, Poihipi et al.: Distinguishability of Battery Equivalent-Circuit Models Containing CPEs: Updating the Work of Berthier, Diard, & Michel, pp109-115 Poihipi E, Scott J, Dunn C. Distinguishability of Battery Equivalent-Circuit Models Containing CPEs: Updating the Work of Berthier, Diard, & Michel. J Electroanal Chem 2022;911:116201	
Nature of contribution by PhD candidate	Writing – Original Draft; Investigation
Extent of contribution by PhD candidate (%)	10%

CO-AUTHORS

Name	Nature of Contribution
Eden Poihipi	Conceptualization; Methodology; Software; Formal analysis; Investigation; Writing – Original Draft; Writing – Review & Editing; Visualization
Jonathan Scott	Conceptualization; Supervision; Methodology; Software; Writing – Original Draft; Writing – Review & Editing

Certification by Co-Authors

The undersigned hereby certify that:

- the above statement correctly reflects the nature and extent of the PhD candidate's contribution to this work, and the nature of the contribution of each of the co-authors; and

Name	Signature	Date
Eden Poihipi	E. Poihipi	28 November 2023
Jonathan Scott	J Scott	28 November 2023

THE UNIVERSITY OF WAIKATO
Te Whare Wānanga o Waikato

Co-Authorship Form

Postgraduate Studies Office
Student and Academic Services Division
Wahanga Ratonga Matauranga Akonga
The University of Waikato
Private Bag 3105
Hamilton 3240, New Zealand
Phone +64 7 838 4439
Website: http://www.waikato.ac.nz/sasd/postgraduate/

This form is to accompany the submission of any PhD that contains research reported in published or unpublished co-authored work. **Please include one copy of this form for each co-authored work**. Completed forms should be included in your appendices for all the copies of your thesis submitted for examination and library deposit (including digital deposit).

Please indicate the chapter/section/pages of this thesis that are extracted from a co-authored work and give the title and publication details or details of submission of the co-authored work.

Appendix B, Wilson et al.: Measuring Electrical Properties of Batteries at Ultra-long Timescales, pp119-123

Wilson M T, Dunn C, Farrow V, Mucalo M, Scott J B. Measuring Electrical Properties of Batteries at Ultra-long Timescales. NCSL Int Meas 2023;15:12-16

Nature of contribution by PhD candidate	Investigation; Resources; Visualization
Extent of contribution by PhD candidate (%)	20%

CO-AUTHORS

Name	Nature of Contribution
Marcus Wilson	Conceptualization; Methodology; Formal analysis; Investigation; Writing – Original Draft; Writing – Review & Editing; Visualization
Vance Farrow	Software; Investigation; Resources
Michael Mucalo	Resources
Jonathan Scott	Software; Investigation; Resources

Certification by Co-Authors

The undersigned hereby certify that:

- the above statement correctly reflects the nature and extent of the PhD candidate's contribution to this work, and the nature of the contribution of each of the co-authors; and

Name	Signature	Date
Marcus Wilson		28 November 2023
Vance Farrow		28 November 2023
Michael Mucalo		28 November 2023
Jonathan Scott	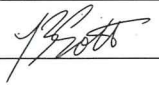	28 November 2023

THE UNIVERSITY OF WAIKATO
Te Whare Wānanga o Waikato

Co-Authorship Form

Postgraduate Studies Office
Student and Academic Services Division
Wahanga Ratonga Matauranga Akonga
The University of Waikato
Private Bag 3105
Hamilton 3240, New Zealand
Phone +64 7 838 4439
Website: http://www.waikato.ac.nz/sasd/postgraduate/

This form is to accompany the submission of any PhD that contains research reported in published or unpublished co-authored work. **Please include one copy of this form for each co-authored work.** Completed forms should be included in your appendices for all the copies of your thesis submitted for examination and library deposit (including digital deposit).

Please indicate the chapter/section/pages of this thesis that are extracted from a co-authored work and give the title and publication details or details of submission of the co-authored work. Appendix C, Wilson et al., Efficiency of Cycled Batteries Analyzed Through Voltage-Current Phase Differences, pp127-136 Wilson M T, Dunn C J, Farrow V, Cree M J, Scott J B. Efficiency of Cycled Batteries Analyzed Through Voltage-Current Phase Differences. IEEE Access 2024;12:36202-36211	
Nature of contribution by PhD candidate	Making experimental measurements, development of theory, data interpretation
Extent of contribution by PhD candidate (%)	15%

CO-AUTHORS

Name	Nature of Contribution
Marcus Wilson	Conceptualization of work, development of theory, analysis of experimental data, data interpretation, leading writing
Vance Farrow	Writing software, data interpretation
Michael Cree	Overall guidance
Jonathan Scott	Conceptualization of work, overall guidance, contribution to writing

Certification by Co-Authors

The undersigned hereby certify that:

- the above statement correctly reflects the nature and extent of the PhD candidate's contribution to this work, and the nature of the contribution of each of the co-authors; and

Name	Signature	Date
Marcus Wilson		29 August 2024
Vance Farrow		29 August 2024
Michael Cree		29 August 2024
Jonathan Scott	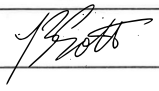	29 August 2024

References

[1] L. Ulrich, "State of charge," *IEEE Spect.*, vol. 49, no. 1, pp. 56–59, 2012.

[2] M. Malewski, D. M. J. Cowell, and S. Freear, "Review of battery powered embedded systems design for mission-critical low-power applications," *Int. J. Electron.*, vol. 105, no. 6, pp. 893–909, 2018.

[3] S. M. Rezvanizaniani, Z. Liu, Y. Chen, and J. Lee, "Review and recent advances in battery health monitoring and prognostics technologies for electric vehicle (EV) safety and mobility," *J. Power Sources*, vol. 256, pp. 110–124, 2014.

[4] "Battery and energy technologies: state of health (SOH) determination." [Online]. Available: https://www.mpoweruk.com/soh.htm

[5] J. Scott and A. Parker, "Distortion analysis using SPICE," *J. Audio Eng. Soc.*, vol. 43, no. 12, pp. 1029–1040, Dec. 1995.

[6] R. Xiong, L. Li, and J. Tian, "Towards a smarter battery management system: A critical review on battery state of health monitoring methods," *J. Power Sources*, vol. 405, pp. 18–29, 2018.

[7] L. Ungurean, G. Cârstoiu, M. V. Micea, and V. Groza, "Battery state of health estimation: a structured review of models, methods and commercial devices," *Int. J. Energy Res.*, vol. 41, no. 2, pp. 151–181, 2017.

[8] M. V. Micea, L. Ungurean, G. N. Cârstoiu, and V. Groza, "State-of-health assessment for battery management systems," *IEEE Trans. Instrum. Meas.*, vol. 60, no. 6, pp. 1997–2006, 2011.

[9] K. S. Ng, C.-S. Moo, Y.-P. Chen, and Y.-C. Hsieh, "Enhanced coulomb counting method for estimating state-of-charge and state-of-health of lithium-ion batteries," *Appl. Energy*, vol. 86, no. 9, pp. 1506–1511, 2009.

[10] B. Divakar, K. Cheng, H. Wu, J. Xu, H. B. Ma, W. Ting, K. Ding, W. Choi, B. F. Huang, and C. Leung, "Battery management system and control strategy for hybrid and electric vehicle," *3rd International Conference on Power Electronics Systems and Applications (PESA)*, pp. 1–6, 2009.

[11] T. Sasaki, Y. Ukyo, and P. Novák, "Memory effect in a lithium-ion battery," *Nat. Mater.*, vol. 12, no. 6, pp. 569–575, 2013.

[12] S. Westerlund, "Dead matter has memory!" *Phys. Scr.*, vol. 43, no. 2, pp. 174–179, 1991.

[13] "BU-303: Confusion with Voltages," May 2017. [Online]. Available: https://batteryuniversity.com/learn/article/confusion_with_voltages

[14] C. Weng, Y. Cui, J. Sun, and H. Peng, "On-board state of health monitoring of lithium-ion batteries using incremental capacity analysis with support vector regression," *J. Power Sources*, vol. 235, pp. 36–44, 2013.

[15] C. Weng, J. Sun, and H. Peng, "A unified open-circuit-voltage model of lithium-ion batteries for state-of-charge estimation and state-of-health monitoring," *J. Power Sources*, vol. 258, pp. 228–237, 2014.

[16] Y. Xing, W. He, M. Pecht, and K. L. Tsui, "State of charge estimation of lithium-ion batteries using the open-circuit voltage at various ambient temperatures," *Appl. Energy*, vol. 113, pp. 106–115, 2014.

[17] W. Waag, C. Fleischer, and D. U. Sauer, "Adaptive on-line prediction of the available power of lithium-ion batteries," *J. Power Sources*, vol. 242, pp. 548–559, 2013.

[18] Z. Guo, X. Qiu, G. Hou, B. Y. Liaw, and C. Zhang, "State of health estimation for lithium ion batteries based on charging curves," *J. Power Sources*, vol. 249, pp. 457–462, 2014.

[19] "Battery Performance Characteristics - How to specify and test a battery." [Online]. Available: https://www.mpoweruk.com/performance.htm

[20] "Peukert's law," Mar. 2021, page Version ID: 1012718468. [Online]. Available: https://en.wikipedia.org/w/index.php?title=Peukert%27s_law&oldid=1012718468

[21] A. Eddahech, O. Briat, and J.-M. Vinassa, "Determination of lithium-ion battery state-of-health based on constant-voltage charge phase," *J. Power Sources*, vol. 258, pp. 218–227, 2014.

[22] M. Dubarry and B. Y. Liaw, "Identify capacity fading mechanism in a commercial $LiFePO_4$ cell," *J. Power Sources*, vol. 194, no. 1, pp. 541–549, 2009.

[23] M. Dubarry, B. Y. Liaw, M.-S. Chen, S.-S. Chyan, K.-C. Han, W.-T. Sie, and S.-H. Wu, "Identifying battery aging mechanisms in large format Li ion cells," *J. Power Sources*, vol. 196, no. 7, pp. 3420–3425, 2011.

[24] T. R. Ferguson and M. Z. Bazant, "Phase Transformation Dynamics in Porous Battery Electrodes," *Electrochim. Acta*, vol. 146, pp. 89–97, Nov. 2014. [Online]. Available: https://linkinghub.elsevier.com/retrieve/pii/S0013468614017174

[25] X. Han, M. Ouyang, L. Lu, J. Li, Y. Zheng, and Z. Li, "A comparative study of commercial lithium ion battery cycle life in electrical vehicle: Aging mechanism identification," *J. Power Sources*, vol. 251, pp. 38–54, 2014.

[26] Y. Li, M. Abdel-Monem, R. Gopalakrishnan, M. Berecibar, E. Nanini-Maury, N. Omar, P. van den Bossche, and J. Van Mierlo, "A quick on-line state of health estimation method for Li-ion battery with incremental capacity curves processed by Gaussian filter," *J. Power Sources*, vol. 373, pp. 40–53, 2018.

[27] C. Weng, X. Feng, J. Sun, and H. Peng, "State-of-health monitoring of lithium-ion battery modules and packs via incremental capacity peak tracking," *Appl. Energy*, vol. 180, no. C, pp. 360–368, 2016.

[28] J. Tian, R. Xiong, and Q. Yu, "Fractional-Order Model-Based Incremental Capacity Analysis for Degradation State Recognition of Lithium-Ion Batteries," *IEEE Trans. Ind. Electron.*, vol. 66, no. 2, pp. 1576–1584, 2019.

[29] L. Wang, C. Pan, L. Liu, Y. Cheng, and X. Zhao, "On-board state of health estimation of $LiFePO_4$ battery pack through differential voltage analysis," *Appl. Energy*, vol. 168, pp. 465–472, 2016.

[30] C. Zou, L. Zhang, X. Hu, Z. Wang, T. Wik, and M. Pecht, "A review of fractional-order techniques applied to lithium-ion batteries, lead-acid batteries, and supercapacitors," *J. Power Sources*, vol. 390, pp. 286–296, 2018.

[31] W. Choi, H.-C. Shin, J. M. Kim, J.-Y. Choi, and W.-S. Yoon, "Modeling and Applications of Electrochemical Impedance Spectroscopy (EIS) for Lithium-ion Batteries," *J. Electrochem. Sci. Technol*, vol. 11, no. 1, pp. 1–13, 2020.

[32] Y.-H. Liu and Y.-F. Luo, "Search for an Optimal Rapid-Charging Pattern for Li-Ion Batteries Using the Taguchi Approach," *IEEE Trans. Ind. Electron.*, vol. 57, no. 12, pp. 3963–3971, 2010.

[33] Y.-H. Liu, C.-H. Hsieh, and Y.-F. Luo, "Search for an Optimal Five-Step Charging Pattern for Li-Ion Batteries Using Consecutive Orthogonal Arrays," *IEEE Trans. Energy Convers.*, vol. 26, no. 2, pp. 654–661, 2011.

[34] H. E. Perez, X. Hu, S. Dey, and S. J. Moura, "Optimal Charging of Li-Ion Batteries With Coupled Electro-Thermal-Aging Dynamics," *IEEE Trans. Veh. Technol.*, vol. 66, no. 9, pp. 7761–7770, 2017.

[35] J. S. Richman and J. R. Moorman, "Physiological time-series analysis using approximate entropy and sample entropy," *Am. J. Physiol. Heart Circ. Physiol.*, vol. 278, no. 6, pp. H2039–H2049, Jun. 2000. [Online]. Available: https://www.physiology.org/doi/10.1152/ajpheart.2000.278.6.H2039

[36] G. L. Plett, "Dual and Joint EKF for Simultaneous SOC and SOH Estimation," in *Proceedings of the 21st Electric Vehicle Symposium (EVS21)*, 2005, pp. 1–12.

[37] W. Waag, S. Käbitz, and D. U. Sauer, "Experimental investigation of the lithium-ion battery impedance characteristic at various conditions and aging states and its influence on the application," *Appl. Energy*, vol. 102, pp. 885–897, 2013.

[38] M. Wohlfahrt-Mehrens, C. Vogler, and J. Garche, "Aging mechanisms of lithium cathode materials," *J. Power Sources*, vol. 127, no. 1, pp. 58–64, 2004.

[39] R. Fu, S.-Y. Choe, V. Agubra, and J. Fergus, "Modeling of degradation effects considering side reactions for a pouch type Li-ion polymer battery with carbon anode," *J. Power Sources*, vol. 261, pp. 120–135, 2014.

[40] Y. Zhang and C.-Y. Wang, "Cycle-life characterization of automotive lithium-ion batteries with $LiNiO_2$ cathode," *J. Electrochem. Soc.*, vol. 156, no. 7, pp. A527–A535, 2009.

[41] A. Lasia, *Electrochemical Impedance Spectroscopy and its Applications*. New York, NY: Springer New York, 2014.

[42] N. Meddings, M. Heinrich, F. Overney, J.-S. Lee, V. Ruiz, E. Napolitano, S. Seitz, G. Hinds, R. Raccichini, M. Gaberšček, and J. Park, "Application of electrochemical impedance spectroscopy to commercial Li-ion cells: A review," *J. Power Sources*, vol. 480, p. 228742, Dec. 2020. [Online]. Available: https://linkinghub.elsevier.com/retrieve/pii/S0378775320310466

[43] J. E. B. Randles, "Kinetics of rapid electrode reactions," *Discuss. Faraday Soc.*, vol. 1, p. 11, 1947.

[44] A. Lasia, "Dispersion of Impedances at Solid Electrodes," in *Electrochemical Impedance Spectroscopy and its Applications*. New York, NY: Springer New York, 2014, pp. 177–201.

[45] K. S. Cole and R. H. Cole, "Dispersion and Absorption in Dielectrics I. Alternating Current Characteristics," *J. Chem. Phys.*, vol. 9, no. 4, pp. 341–351, 1941.

[46] G. Brug, A. van den Eeden, M. Sluyters-Rehbach, and J. Sluyters, "The analysis of electrode impedances complicated by the presence of a constant phase element," *J. Electroanal. Chem. Interf. Electrochem.*, vol. 176, no. 1-2, pp. 275–295, 1984.

[47] S. Westerlund and L. Ekstam, "Capacitor theory," *IEEE Trans. Dielect. Electr. Insul.*, vol. 1, no. 5, pp. 826–839, 1994.

[48] J. Jacquelin, "The Phasance Concept," *Curr. Top. Electrochem.*, vol. 4, pp. 127–136, 1997.

[49] S. M. Gateman, O. Gharbi, H. Gomes De Melo, K. Ngo, M. Turmine, and V. Vivier, "On the use of a constant phase element (CPE) in electrochemistry," *Curr. Opin. Electrochem.*, vol. 36, p. 101133, Dec. 2022. [Online]. Available: https://linkinghub.elsevier.com/retrieve/pii/S2451910322001983

[50] "Randles circuit," May 2021, page Version ID: 1021468208. [Online]. Available: https://en.wikipedia.org/w/index.php?title=Randles_circuit&oldid=1021468208

[51] A. Lasia, "Impedance of the Faradaic Reactions in the Presence of Mass Transfer," in *Electrochemical Impedance Spectroscopy and its Applications.* New York, NY: Springer New York, 2014, pp. 85–125.

[52] U. Westerhoff, K. Kurbach, F. Lienesch, and M. Kurrat, "Analysis of Lithium-Ion Battery Models Based on Electrochemical Impedance Spectroscopy," *Energy Technol.*, vol. 4, no. 12, pp. 1620–1630, 2016.

[53] P. Gao, C. Zhang, and G. Wen, "Equivalent circuit model analysis on electrochemical impedance spectroscopy of lithium metal batteries," *J. Power Sources*, vol. 294, pp. 67–74, 2015.

[54] B. T. Habte and F. Jiang, "Effect of microstructure morphology on Li-ion battery graphite anode performance: Electrochemical impedance spectroscopy modeling and analysis," *Solid State Ion.*, vol. 314, pp. 81–91, 2018.

[55] H. Nara, D. Mukoyama, R. Shimizu, T. Momma, and T. Osaka, "Systematic analysis of interfacial resistance between the cathode layer and the current collector in lithium-ion batteries by electrochemical impedance spectroscopy," *J. Power Sources*, vol. 409, pp. 139–147, 2019.

[56] D. W. Abarbanel, K. J. Nelson, and J. R. Dahn, "Exploring Impedance Growth in High Voltage NMC/Graphite Li-Ion Cells Using a Transmission Line Model," *J. Electrochem. Soc.*, vol. 163, no. 3, pp. A522–A529, 2016.

[57] F. Berthier, J.-P. Diard, and R. Michel, "Distinguishability of equivalent circuits containing CPEs: Part I. Theoretical part," *J. Electroanal. Chem.*, vol. 510, no. 1, pp. 1–11, 2001.

[58] S. Buteau, D. C. Dahn, and J. R. Dahn, "Explicit Conversion between Different Equivalent Circuit Models for Electrochemical Impedance Analysis of Lithium-Ion Cells," *J. Electrochem. Soc.*, vol. 165, no. 2, pp. A228–A234, 2018.

[59] S. Buteau and J. R. Dahn, "Analysis of Thousands of Electrochemical Impedance Spectra of Lithium-Ion Cells through a Machine Learning Inverse Model," *J. Electrochem. Soc.*, vol. 166, no. 8, pp. A1611–A1622, 2019.

[60] R. Hasan and J. Scott, "Application of Swingler's method for analysis of multicomponent exponentials with special attention to non-equispaced data," in *2016 IEEE 12th International Colloquium on Signal Processing & Its Applications (CSPA)*. Melaka, Malaysia: IEEE, Mar. 2016, pp. 12–15. [Online]. Available: http://ieeexplore.ieee.org/document/7515794/

[61] ——, "Measurement for fractional characteristic of lithium batteries," in *2019 IEEE International Instrumentation and Measurement Technology Conference (I2MTC)*. Auckland, New Zealand: IEEE, May 2019, pp. 1–5. [Online]. Available: https://ieeexplore.ieee.org/document/8826948/

[62] X. Wang, X. Wei, and H. Dai, "Estimation of state of health of lithium-ion batteries based on charge transfer resistance considering different temperature and state of charge," *J. Energy Storage*, vol. 21, pp. 618–631, 2019.

[63] Y. Cui, P. Zuo, C. Du, Y. Gao, J. Yang, X. Cheng, Y. Ma, and G. Yin, "State of health diagnosis model for lithium ion batteries based on real-time impedance and open circuit voltage parameters identification method," *Energy*, vol. 144, pp. 647–656, 2018.

[64] Q. Yang, J. Xu, X. Li, D. Xu, and B. Cao, "State-of-health estimation of lithium-ion battery based on fractional impedance model and interval capacity," *Int. J. Electr. Power Energy Syst.*, vol. 119, p. 105883, 2020.

[65] T. T. Hartley, R. J. Veillette, J. L. Adams, and C. F. Lorenzo, "Energy storage and loss in fractional-order circuit elements," *IET Circuits Devices Syst.*, vol. 9, no. 3, pp. 227–235, 2015.

[66] E. Locorotondo, V. Cultrera, L. Pugi, L. Berzi, M. Pierini, and G. Lutzemberger, "Development of a battery real-time state of health diagnosis based on fast impedance measurements," *J. Energy Storage*, vol. 38, p. 102566, 2021.

[67] R. Mingant, J. Bernard, and V. Sauvant-Moynot, "Novel state-of-health diagnostic method for Li-ion battery in service," *Appl. Energy*, vol. 183, pp. 390–398, 2016.

[68] C. J. Dunn and J. Scott, "Deducing battery impedance from working vehicle voltage and current waveforms," University of Waikato, Hamilton, New Zealand, 2019, poster presented at the Engineering Design Show, October 15-17.

[69] J. Jiang, Z. Lin, Q. Ju, Z. Ma, C. Zheng, and Z. Wang, "Electrochemical Impedance Spectra for Lithium-ion Battery Ageing Considering the Rate of Discharge Ability," *Energy Procedia*, vol. 105, pp. 844–849, 2017.

[70] J. Kim, L. Krüger, and J. Kowal, "On-line state-of-health estimation of Lithium-ion battery cells using frequency excitation," *J. Energy Storage*, vol. 32, p. 101841, 2020.

[71] Y.-B. He, M. Liu, Z.-D. Huang, B. Zhang, Y. Yu, B. Li, F. Kang, and J.-K. Kim, "Effect of solid electrolyte interface (SEI) film on cyclic performance of $Li_4Ti_5O_{12}$ anodes for Li ion batteries," *J. Power Sources*, vol. 239, pp. 269–276, 2013.

[72] M. B. Pinson and M. Z. Bazant, "Theory of SEI Formation in Rechargeable Batteries: Capacity Fade, Accelerated Aging and Lifetime Prediction," *J. Electrochem. Soc.*, vol. 160, no. 2, pp. A243–A250, 2013.

[73] S. Zhang, K. Xu, and T. Jow, "EIS study on the formation of solid electrolyte interface in Li-ion battery," *Electrochim. Acta*, vol. 51, no. 8-9, pp. 1636–1640, 2006.

[74] L. Wang, A. Menakath, F. Han, Y. Wang, P. Y. Zavalij, K. J. Gaskell, O. Borodin, D. Iuga, S. P. Brown, C. Wang, K. Xu, and B. W. Eichhorn, "Identifying the components of the solid–electrolyte interphase in Li-ion batteries," *Nat. Chem.*, vol. 11, no. 9, pp. 789–796, 2019.

[75] V. A. Agubra and J. W. Fergus, "The formation and stability of the solid electrolyte interface on the graphite anode," *J. Power Sources*, vol. 268, pp. 153–162, 2014.

[76] Y. Liu, Q. Liu, Z. Li, Y. Ren, J. Xie, H. He, and F. Xu, "Failure Study of Commercial LiFePO $_4$ Cells in over-Discharge Conditions Using Electrochemical Impedance Spectroscopy," *J. Electrochem. Soc.*, vol. 161, no. 4, pp. A620–A632, 2014.

[77] K. M. Shaju, F. Jiao, A. Débart, and P. G. Bruce, "Mesoporous and nanowire Co $_3$ O $_4$ as negative electrodes for rechargeable lithium batteries," *Phys. Chem. Chem. Phys.*, vol. 9, no. 15, pp. 1837–1842, 2007.

[78] K.-A. Kwon, H.-S. Lim, Y.-K. Sun, and K.-D. Suh, "α-Fe $_2$ O $_3$ Submicron Spheres with Hollow and Macroporous Structures as High-Performance Anode Materials for Lithium Ion Batteries," *J. Phys. Chem. C*, vol. 118, no. 6, pp. 2897–2907, 2014.

[79] S. Xu, C. M. Hessel, H. Ren, R. Yu, Q. Jin, M. Yang, H. Zhao, and D. Wang, "α-Fe $_2$ O $_3$ multi-shelled hollow microspheres for lithium ion battery anodes with superior capacity and charge retention," *Energy Environ. Sci.*, vol. 7, no. 2, pp. 632–637, 2014.

[80] D. Chen, H. Quan, J. Liang, and L. Guo, "One-pot synthesis of hematite-graphene core-shell nanostructures for superior lithium storage," *Nanoscale*, vol. 5, no. 20, p. 9684, 2013.

[81] Y. Xiao, X. Wang, W. Wang, D. Zhao, and M. Cao, "Engineering Hybrid between MnO and N-Doped Carbon to Achieve Exceptionally High Capacity for Lithium-Ion Battery Anode," *ACS Appl. Mater. Interfaces*, vol. 6, no. 3, pp. 2051–2058, 2014.

[82] A. Lasia, "Definition of Impedance and Impedance of Electrical Circuits," in *Electrochemical Impedance Spectroscopy and its Applications*. New York, NY: Springer New York, 2014, pp. 7–66. [Online]. Available: http://link.springer.com/10.1007/978-1-4614-8933-7_2

[83] P. Mauracher and E. Karden, "Dynamic modelling of lead/acid batteries using impedance spectroscopy for parameter identification," *J. Power Sources*, vol. 67, no. 1-2, pp. 69–84, 1997.

[84] J. Scott and R. Hasan, "New Results for Battery Impedance at Very Low Frequencies," *IEEE Access*, vol. 7, pp. 106 925–106 930, 2019.

[85] R. Hasan and J. B. Scott, "Impedance measurement of batteries under load," Auckland, New Zealand, May 2019. [Online]. Available: https://hdl.handle.net/10289/12840

[86] J. B. Scott and P. Single, "Compact nonlinear model of an implantable electrode array for spinal cord stimulation (SCS)," *IEEE Trans. Biomed. Circuits Syst.*, vol. 8, no. 3, pp. 382–390, 2013.

[87] S. Seshadri and J. Scott, "Correction to "Compact Nonlinear Model of an Implantable Electrode Array for Spinal Cord Stimulation" [Jun 14 382-390]," *IEEE Trans. Biomed. Circuits Syst.*, vol. 12, no. 4, pp. 963–964, 2018.

[88] R. Morrison, "RC Constant-Argument Driving-Point Admittances," *IRE Trans. Circuit Theory*, vol. 6, no. 3, pp. 310–317, 1959.

[89] V. Farrow, "Characterisation of rechargeable batteries: addressing fractional ultralow-frequency devices," Master of Engineering, University of Waikato, Hamilton, New Zealand, Sep. 2020.

[90] H. Budde-Meiwes, J. Kowal, D. U. Sauer, and E. Karden, "Influence of measurement procedure on quality of impedance spectra on lead–acid batteries," *J. Power Sources*, vol. 196, no. 23, pp. 10 415–10 423, 2011.

[91] M. Schroeder, "Synthesis of low-peak-factor signals and binary sequences with low autocorrelation," *IEEE Trans. Inform. Theory*, vol. 16, no. 1, pp. 85–89, 1970.

[92] M. T. Wilson, C. Dunn, V. Farrow, M. Mucalo, and J. B. Scott, "Measuring Electrical Properties of Batteries at Ultra-long Timescales," *NCSL Int. Meas.*, vol. 15, no. 2, pp. 12–16, 2023.

[93] L. Zheng, J. Zhu, D. D.-C. Lu, G. Wang, and T. He, "Incremental capacity analysis and differential voltage analysis based state of charge and capacity estimation for lithium-ion batteries," *Energy*, vol. 150, pp. 759–769, May 2018. [Online]. Available: https://linkinghub.elsevier.com/retrieve/pii/S0360544218304213

[94] V. Ovejas and A. Cuadras, "Battery Aging Impedance Spectroscopy and Incremental Capacity Analysis," Chemnitz, Germany, Sep. 2017.

[95] E. Talaie, P. Bonnick, X. Sun, Q. Pang, X. Liang, and L. F. Nazar, "Methods and Protocols for Electrochemical Energy Storage Materials Research," *Chem. Mater.*, vol. 29, no. 1, pp. 90–105, Jan. 2017. [Online]. Available: https://pubs.acs.org/doi/10.1021/acs.chemmater.6b02726

[96] D. Anseán, V. M. García, M. González, C. Blanco-Viejo, J. C. Viera, Y. F. Pulido, and L. Sánchez, "Lithium-Ion Battery Degradation Indicators Via Incremental Capacity Analysis," *IEEE Trans. Ind. Appl.*, vol. 55, no. 3, pp. 2992–3002, May 2019. [Online]. Available: https://ieeexplore.ieee.org/document/8603757/

[97] Y. Ye, H. Xie, Y. Yang, Y. Xie, Y. Lu, J. Wang, X. Kong, S. Jin, and H. Ji, "Solid-Solution or Intermetallic Compounds: Phase Dependence of the Li-Alloying Reactions for Li-Metal Batteries," *J. Am. Chem. Soc.*, p. jacs.3c08711, Nov. 2023. [Online]. Available: https://pubs.acs.org/doi/10.1021/jacs.3c08711

[98] N. Elgrishi, K. J. Rountree, B. D. McCarthy, E. S. Rountree, T. T. Eisenhart, and J. L. Dempsey, "A Practical Beginner's Guide to Cyclic Voltammetry," *J. Chem. Educ.*, vol. 95, no. 2, pp. 197–206, Feb. 2018. [Online]. Available: https://pubs.acs.org/doi/10.1021/acs.jchemed.7b00361

[99] D. Y. W. Yu, C. Fietzek, W. Weydanz, K. Donoue, T. Inoue, H. Kurokawa, and S. Fujitani, "Study of $LiFePO_4$ by Cyclic Voltammetry," *J. Electrochem. Soc.*, vol. 154, no. 4, p. A253, 2007. [Online]. Available: https://iopscience.iop.org/article/10.1149/1.2434687

[100] A. Quiroga, "Cyclic Voltammetry - Chemistry LibreTexts." [Online]. Available: https://chem.libretexts.org/Bookshelves/Analytical_Chemistry/Supplemental_Modules_(Analytical_Chemistry)/Instrumentation_and_Analysis/Cyclic_Voltammetry?readerView

[101] C. Bracher, H. Robson, and M. Reinhardt, "Cyclic Voltammetry Basic Principles, Theory & Setup." [Online]. Available: https://www.ossila.com/pages/cyclic-voltammetry

[102] M. T. Wilson, C. J. Dunn, V. Farrow, M. J. Cree, and J. B. Scott, "Efficiency of Cycled Batteries Analyzed Through Voltage-Current Phase Differences," *IEEE Access*, vol. 12, pp. 36 202–36 211, 2024. [Online]. Available: https://ieeexplore.ieee.org/document/10462108/

[103] M. Wilson, L. Cowie, V. Farrow, M. Cree, and J. Scott, "Simulating Fractional Capacitors With the SPICE Circuit Simulator," 2023. [Online]. Available: https://www.techrxiv.org/account/articles/24156396

[104] C. J. Dunn, "Deducing Battery Impedance From Working Vehicle Voltage and Current Waveforms," Capstone Project Dissertation, School of Engineering, University of Waikato, Hamilton, New Zealand, Oct. 2019.

[105] E. Poihipi, J. Scott, and C. Dunn, "Distinguishability of Battery Equivalent-Circuit Models Containing CPEs: Updating the Work of Berthier, Diard, & Michel," *J. Electroanal. Chem.*, vol. 911, p. 116201, Apr. 2022. [Online]. Available: https://linkinghub.elsevier.com/retrieve/pii/S157266572200193X

[106] C. Dunn and J. Scott, "Achieving Reliable and Repeatable Electrochemical Impedance Spectroscopy of Rechargeable Batteries at Extra-Low Frequencies," *IEEE Trans. Instrum. Meas.*, vol. 71, pp. 1–8, 2022. [Online]. Available: https://ieeexplore.ieee.org/document/9789195/

[107] S. S. Haykin, *Introduction to analog and digital communications*, 2nd ed. Hoboken, NJ: Wiley, 2007.

[108] M. Dubarry, C. Truchot, and B. Y. Liaw, "Synthesize battery degradation modes via a diagnostic and prognostic model," *J. Power Sources*, vol. 219, pp. 204–216, Dec. 2012. [Online]. Available: https://linkinghub.elsevier.com/retrieve/pii/S0378775312011330

[109] C. R. Birkl, M. R. Roberts, E. McTurk, P. G. Bruce, and D. A. Howey, "Degradation diagnostics for lithium ion cells," *J. Power Sources*, vol. 341, pp. 373–386, Feb. 2017. [Online]. Available: https://linkinghub.elsevier.com/retrieve/pii/S0378775316316998

[110] A. N. Akansu, W. A. Serdijn, and I. W. Selesnick, "Emerging applications of wavelets: A review," *Phys. Commun.*, vol. 3, no. 1, pp. 1–18, Mar. 2010. [Online]. Available: https://linkinghub.elsevier.com/retrieve/pii/S1874490709000482

[111] R. Du, X. Wang, H. Dai, X. Wei, and P. Ming, "Online impedance spectrum measurement of fuel cells based on Morlet wavelet transform," *Int. J. Hydrog. Energy*, vol. 46, no. 47, pp. 24 339–24 352, Jul. 2021. [Online]. Available: https://linkinghub.elsevier.com/retrieve/pii/S0360319921016918